

Contents

Articles

X-Ray Lithography Mask Metrology: Use of Transmitted Electrons in an SEM for Linewidth Measurement	Michael T. Postek, Jeremiah R. Lowney, Andras E. Vladar, William J. Keery, Egon Marx, and Robert D. Larrabee	415
Interlaboratory Study on the Lithographically Produced Scanning Electron Microscope Magnification Standard Prototype	Michael T. Postek, Andras E. Vladar, Samuel N. Jones, and William J. Keery	447
Phase Equilibria and Crystal Chemistry in Portions of the System SrO-CaO-Bi ₂ O ₃ -CuO, Part IV – The System CaO-Bi ₂ O ₃ -CuO	B. P. Burton, C. J. Rawn, R. S. Roth, and N. M. Hwang	469

Conference Reports

COMPASS '93, Eight Annual Conference on Computer Assurance	Dolores R. Wallace and Elizabeth B. Lennon	517
Workshop on Aging, Dimensional Stability, and Durability Issues in High Technology Polymers	Cynthia Arnold-McKenna and Gregory B. McKenna	523

News Briefs

GENERAL DEVELOPMENTS	535
Electrical Potential: Israel, United States Agree on Standard CRADA Partners Focus on Improving Laser Lenses NIST Observes One Electron in 10 Billion	
Research Partners Seek Better Infrared Radiometry CRADA Partners to Evaluate Advanced Insulations Standard Addresses CNC Performance Evaluations Integrated Optic Laser Emitting at 905, 1057, and 1356 nm Trapped Neutral Atom Methodology Applied to High-Accuracy Wavelength Reference for Optical Communications	536
Industry, NIST Collaborate to Study Overlay Measurements NIST Provides Leadership for DARPA Infrared Detector Materials Program Young's Interference Experiment Using Two Atoms	537

Holographic Measurements of Atomization and Spray Forming AMRL Supports the Metric Conversion of AASHTO Materials Standards New SRM for Calibrating Infrared Spectrophotometers	538
NIST Sponsors Mammography Workshop Thermal Conductivity of HCFC-Filled Polymer Foams Computer Graphics Metafile Generator Test Service Initiated NIST/ASA/NSF Fellow Develops New Model for Controlling Measurement Processes	539
NIST Publishes IGES Hybrid Microcircuit Application Protocol Improved Method Developed for Characterizing HgCdTe Infrared Detectors NIST Develops Improved Sensor for High AC and Pulsed Currents	540
Industry Focuses on Traceability Needs at NIST/DOE Gear Metrology Workshop Photopatterning of Alkylthiol Self-Assembled Monolayers Atmospheric Sampling in Saudi Arabia	541
Collaborative Research Elucidates Carbon Monoxide and Soot Oxidation NIST Supports Computer-Aided Acquisition and Logistic Support (CALIS) Initiative in Computer Graphics Spoken Language Technology and Applications Day Held “Trapped” Ions Provide First View of Light Property	542
Partners Plan Device for Clearer Protein Images CRADA Seeks Better Factory Systems Integration U.S./Hungarian Team to Refine pH Standards Eleven Inventions Ready for Licensing	543
Wall Designers Get Help Avoiding the “Draft” NIST Intends to Grant Exclusive DSA License Aerospace Alloys Consortium Launched	544
Consortium to Advance Polymer Blends Processing CRADA May Improve Microwave Measurements Activities Report Highlights 1992 for NIST Lab New CRADA to Improve On-Line CVD Monitoring Report Reviews 1992 Achievements of NIST Lab	545
“Hash” Standard for Digital Signatures Approved New Algorithm Sharpens Images, Damps Noise A STEP Toward Competitive “Made-to-Measure” Primer Tells What’s Cool (and Trapped) with Lasers	546
Examiners Needed for 1994 Baldrige Award NIST Measurements Confirm Quantum Hall Devices as Intrinsic Standards of Resistance NIST Work Enables Micromachine Designers to Fabricate Devices Through Foundry Processing	547
“Lift-Mode” Magnetic-Force Microscopy Deconvolves Magnetic Information from Surface Topology NIST Develops Reference Specimens to Improve Critical-Current Measurements on High-Temperature Superconductors Workshop on Thermochemical Data Needs for CVD Modeling	548

New Monograph of Thermocouple Reference Functions and Tables Based on the ITS-90 Now Available Technology to Fabricate Nanometer-Size Surface Test Structures Developed	549
Observation of Strain-Induced Microcracks in High T_c Superconductor Composite Wire Incommensurate Spin Density Waves in Metallic $V_{2-y}O_3$ High-Speed Spatial Scanning Pyrometer Developed	550
Computer Graphics Metafile (CGM) and POSIX FIPS Revised Overview of First Text REtrieval Conference Published NIST Sponsors Users' Forum on Application Portability Profile (APP) and Open System Environment (OSE) NIST Explains Role of Measurements in the Competitive Stance of the U.S. Electronics Industry	551
NIST-Industry Collaboration Developing Needed Fine-Scale Test Structures Private Laboratories to Use NIST Princeton Engine Video Supercomputer NIST Provides Leadership in International VAMAS Superconductor Standards Activities	552
NIST Leads Team Demonstrating Concept of Electronic Business Reply Card Sensing Surface Finish Ultrasonically Chromium in Coal Fly Ash Using Microwave	553
NIST/SEMATECH Gas Flow Round Robin Program CRADA with Private Company on Spray Flames X-Ray Goniometer Developed for Use in Ultra High Vacuum	554
New Technique Reveals Unexpected Phenomenon in Electron-Ion Excitation Materials Evaluation in Support of Superconducting Magnetic Energy Storage New Hg Superconductors	555
Measurements for Polymer Processing Consortium Optical and Ultrasonic Sensors for Polymer Processing	556
Reliability of Glass Aircraft Windows Ultrasonic Resonance Spectroscopy Using EMATs NIST Develops Building and Ventilation Characterization Protocols for Indoor Air Quality Investigations	557
Expert System for Highway Concrete NIST and the Department of the Treasury Sign Memorandum of Understanding (MOU) in Information Technology Security Revision of Federal Information Processing Standards (FIPS) for Database Language SQL Guidance on Improving Software Quality Issued Conference on Extreme Value Theory and Its Applications	558

STANDARD REFERENCE MATERIALS

559

Tin-Lead Coating Thickness Standards 60% Sn-40% Pb

Standard Reference Material 886 – Refractory Gold Ore

Standard Reference Materials 2556 and 2557 – Used Automobile Catalysts

STANDARD REFERENCE DATA

560

Russian Rocket-Space Technology Data Available

Database Details Atomic-Scale Surface Structures

X-Ray Lithography Mask Metrology: Use of Transmitted Electrons in an SEM for Linewidth Measurement

Volume 98

Number 4

July–August 1993

Michael T. Postek, Jeremiah R. Lowney, Andras E. Vadar, William J. Keery, Egon Marx, and Robert D. Larrabee

National Institute of Standards and Technology,
Gaithersburg, MD 20899-0001

X-ray masks present a measurement object that is different from most other objects used in semiconductor processing because the support membrane is, by design, x-ray transparent. This characteristic can be used as an advantage in electron beam-based x-ray mask metrology since, depending upon the incident electron beam energies, substrate composition and substrate thickness, the membrane can also be essentially electron transparent. The areas of the mask where the absorber structures are located are essentially x-ray opaque, as well as electron opaque. This paper shows that excellent contrast and signal-to-noise levels can be obtained using the transmitted-electron signal for mask metrology rather than the more commonly collected secondary electron signal. Monte Carlo modeling of the transmitted electron signal was used to support this work in order to determine the optimum detector position and characteristics, as well as in determining the location of the edge in the image profile. The comparison be-

tween the data from the theoretically-modeled electron beam interaction and actual experimental data were shown to agree extremely well, particularly with regard to the wall slope characteristics of the structure. Therefore, the theory can be used to identify the location of the edge of the absorber line for linewidth measurement. This work provides one approach to improved x-ray mask linewidth metrology and a more precise edge location algorithm for measurement of feature sizes on x-ray masks in commercial instrumentation. This work also represents an initial step toward the first SEM-based accurate linewidth measurement standard from NIST, as well as providing a viable metrology for linewidth measurement instruments of x-ray masks for the lithography community.

Key words: lithography; metrology; secondary electron; SEM; transmitted electron; x ray.

Accepted: March 2, 1993

1. Introduction

Optical and electrical linewidth measurements have been the traditional methods of monitoring and controlling microelectronics fabrication processes. As the feature sizes in these processes approached and ultimately became smaller than the wavelength of the light used in the optical measurements, the industry turned to the scanning electron microscope (SEM) for this monitoring. The SEM solved some problems limiting accuracy

in linewidth metrology, but also introduced some new problems of its own [1,2]. This paper describes a nonconventional transmission-mode of the SEM as applied to x-ray masks that reduces the impact of some of the metrological problems of accurate linewidth metrology in the SEM. However, at the present time, there are few process control applications within the semiconductor industry where the transmission electron detection mode can be used.

Many of the concepts described here can be eventually employed in these other applications since the concepts of the transmitted electron detection (TED) mode form the basis for future accurate backscattered and secondary electron metrology. The utility of this mode for metrology arises from the relative insensitivity to the inevitable approximations that must be made in the modeling of electron scattering and detection required for accurate edge detection [3,4]. The present work should be of particular interest to the SEM metrologist who is concerned with either feature size measurement or the detection of defects in the x-ray mask structure and contamination on its surface. The utility for inspection arises from the fact that the transmission of electrons through the mask for lithography is, in some ways, analogous to the transmission of x rays through the mask.

Perhaps the three most important unsolved measurement issues in controlling the processes of fabricating integrated circuits by optical lithography are: 1) accurate measurement of linewidth, 2) detection and characterization of geometrical faults, and 3) measurement of mask-to-mask pattern placement errors. The same three issues will undoubtedly be important in x-ray lithography. This paper addresses the problem of measuring linewidth and line spacing (i.e., pitch) on x-ray masks by making use of the transmission electron detection mode of the scanning electron microscope [4,5,6] referred to as the transmitted scanning electron detection mode (TSEM). This technique utilizes a TED system which is mounted below the sample. The application of TSEM is made possible by the presence of a relatively thin supporting membrane composing these masks which is essentially electron transparent for beam energies as low as about 15 keV (for the present samples and detector arrangement). The TSEM mode is also useful for inspecting x-ray masks for defects because, to a first approximation, the electrons interact with the mask in much the same way as the x rays do in producing their transmission-mode image. For example, defects such as a small void inside an x-ray absorber line will be seen in transmission by both x rays and electrons. However, they will not be seen by visible light, perhaps not by conventional secondary-electron SEM imaging, and certainly not by scanning probe imaging.

X-ray lithography process engineers want accurate dimensional measurements, but accuracy is an elusive concept that everyone would like to deal with by simply calibrating their measurement system by using a NIST developed standard. Unfortu-

nately, it is not easy either for NIST to calibrate submicrometer standards or for the engineer to use standards in calibrating instruments. Accurate feature-size measurements require accurate determination of the left and right edges of the feature being measured. The determination of edge location presents difficulties for all current measurement technologies because x-ray mask features are generally not thin compared to the wavelength of light in the optical microscope [1], or the electron scattering range in the SEM [2], or the size of the probe in scanning probe systems such as the atomic force microscope [7]. Since linewidth is a left-edge-to-right-edge measurement, an error in absolute edge position in the microscopic image of an amount ΔL will give rise to an error in linewidth of $2 \Delta L$. If any technique could be found that produces a step-function response at the location of the geometric edge in its image, there would be no problem in identifying that edge position. However, to date, no such technique has been found. This paper demonstrates that the TSEM images can have a relatively rapidly changing intensity in the vicinity of the true edge position and, therefore, can be made inherently less sensitive than the conventional SEM modes to this source of error in linewidth measurements. The TSEM technique is not inherently more or less accurate than other SEM modes for pitch measurements because pitch measurements are not subject to this type of error (if the two lines in question have similarly shaped left and right edges). Therefore, the present paper will concentrate on TSEM-based linewidth measurements.

Conventional transmission-electron-mode (TEM) operation of a scanning electron microscope utilizes an electron detector with a very narrow cone-angle of acceptance designed to detect only the unscattered component of the transmitted electron beam. An alternative would be the dark-field mode where only the scattered electrons are collected. The reverse is true for the present TSEM technique where a broad acceptance angle detector is used to detect as many of the transmitted electrons as possible (i.e., whether scattered or not) that have an energy above some predetermined threshold which is usually several keV. Then, the electrons are physically filtered both by the signal threshold characteristics of the detector and a physical filter in front of the detector. This greatly improves the contrast level over the conventional TEM mode for this type of application, and greatly simplifies the required Monte Carlo modeling. It is, in fact, this change in electron detection philoso-

phy (compared to more conventional TEM operation) that makes the present TSEM approach so attractive for dimensional metrology and inspection of x-ray masks. Therefore, the TSEM mode should be attractive to both NIST (for use in calibrating future x-ray mask standards) and the x-ray lithographic community (for use in metrology instruments to minimize inherent sources of inaccuracy).

The results of measuring the widths of nominal 0.25, 0.35, 0.5, and 0.75 μm wide lines and pitch arrays on actual x-ray masks with the TSEM mode of operation of the NIST Metrology SEM [8] are presented. The results of Monte Carlo simulations of these measurements are also presented and compared to the experimental data. These Monte Carlo results predicted a definite characteristic notch in the transmission-mode image profile as the electron beam traverses the sloping edges of an ideal trapezoidal shaped line. The measured lines actually were, to a first approximation, trapezoidal but with rough sloping surfaces that made observation of the notch difficult, but not impossible. This paper reports on the theoretical existence of this notch, its observation, and discusses metrological significance that makes the TSEM mode even more attractive than indicated above.

The x-ray mask work presented here represents one method under development at NIST to measure, and ultimately certify x-ray mask linewidth standards for the x-ray lithography community when the interest and need arises. However, the use of the TSEM mode is also recommended for use by that community for its routine metrology, inspection and repair of x-ray masks.

2. Metrology Issues and Implementation

2.1 X-Ray Masks

Masks utilized in x-ray lithography are of various constructions depending upon the manufacturing process employed. However, except for the thickness (affecting electron transparency) of the supporting membrane and chromium coating, this variability should have little bearing on the present technique. Test masks for this study were obtained from IBM Corporation¹ [9]. A drawing of the over-

all mask can be seen in Fig. 1a. The masks are composed of a support membrane of approximately 2.5 μm of boron-doped silicon upon which 1.7 μm of polyimide is placed (Fig. 1b); other masks manufactured later in this work had the polyimide layer removed (Fig. 1c). The absorber structure was patterned in a layer of gold approximately 0.7 μm thick over a 5 nm chromium plating base. Other types and designs of x-ray masks available from other manufacturers that differ somewhat from these figures are not addressed in this work. The patterned features of the test mask used for this work have some edge irregularities (Fig. 2a) which limit the measurement precision and increase the measurement uncertainty. The edges of the absorber are slightly rounded and are reasonably vertical in cross section but have a slight slope (discussed later) which can also influence edge detection (Fig. 2b).

2.2 Scanning Electron Microscopes

Imaging and measurements for this work were done by using the NIST metrology instrument based on an AMRAY 1610 scanning electron microscope equipped with a lanthanum hexaboride filament. Supplemental imaging and beam-scanned metrology was also done by using a field emission Hitachi S-4000 scanning electron microscope (FESEM).

2.2.1 NIST Metrology Instrument The fundamental construction aspects of the NIST metrology instrument have been published previously [8]. This instrument, as most standard laboratory scan-

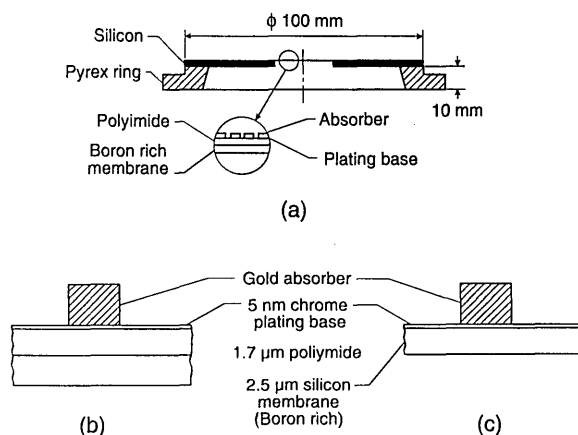
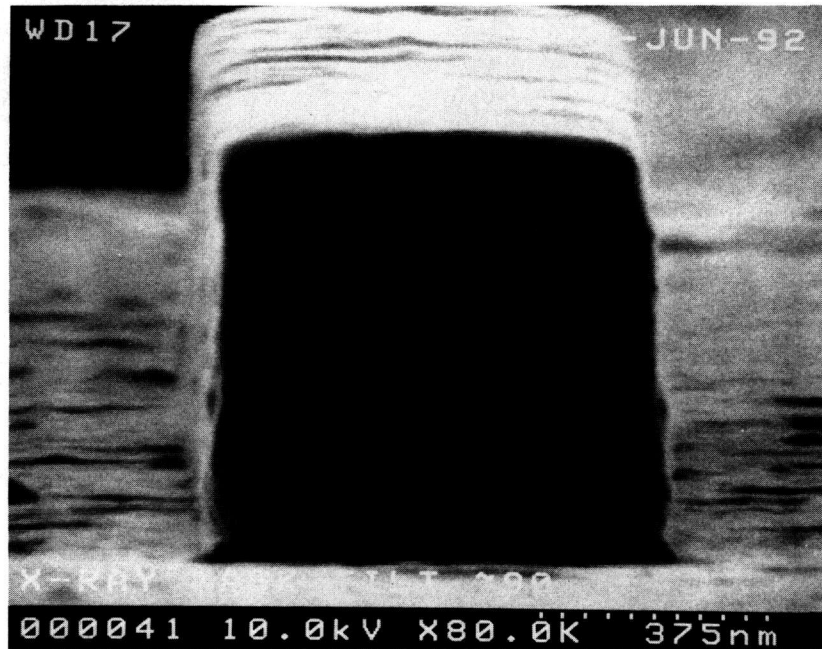
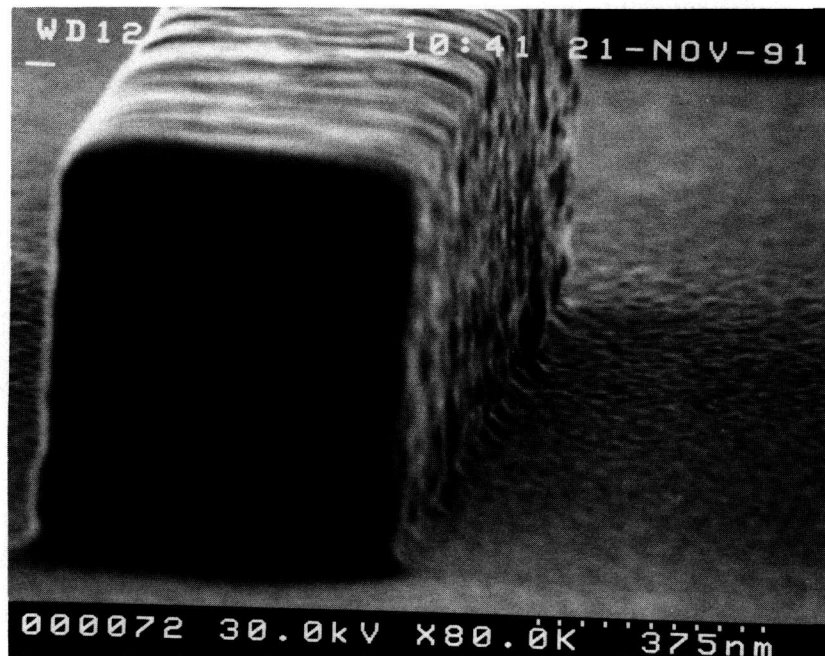


Fig. 1. Diagram showing an enlarged cross section of the x-ray mask studied in this work. (a) View of the entire mask assembly. (b) Diagram of the original membrane-absorber cross section. (c) Diagram of the modified version without the polyimide.

¹ Certain commercial equipment, instruments, or materials are identified in this paper to specify adequately the experimental procedure. Such identification does not imply recommendation or endorsement by the National Institute of Standards and Technology, nor does it imply that the materials or equipment identified are necessarily the best available for the purpose.



a



b

Fig. 2. Scanning electron micrographs of the gold absorber lines at high tilt. (a) High tilt near a cross sectional view. Note the edge roughness and irregularity. (b) Micrograph similar to (a) but including some sample rotation in order to further observe the sidewall structure.

ning electron microscopes, was factory-equipped with a maximum 30 kV accelerating voltage. This system was later modified to have a computer-controlled, cathode-stabilized 30 kV power supply system [10]. One important experiment performed with the instrument was to retrofit in the field a 50 kV accelerating voltage power supply system, in order to test the potential advantages (and disadvantages) afforded by the higher accelerating voltage on TED metrology, imaging, and resolution on the x-ray masks. Most typical SEMs operate at or below 30 kV accelerating voltage but other types of electron beam instrumentation, notably the typical scanning transmission electron microscopes (STEM) can operate at much higher accelerating voltages. The comparison work (between 30 and 50 kV), is discussed below and in our earlier work [4]. This work demonstrated that there was no advantage in doing the metrology at accelerating voltages over 30 kV for the design of x-ray masks investigated in this work. This means that most standard commercial SEMs can be converted to x-ray mask metrology systems with no major instrument modifications. Therefore, the NIST metrology instrument was returned to the computer-controlled 30 kV configuration.

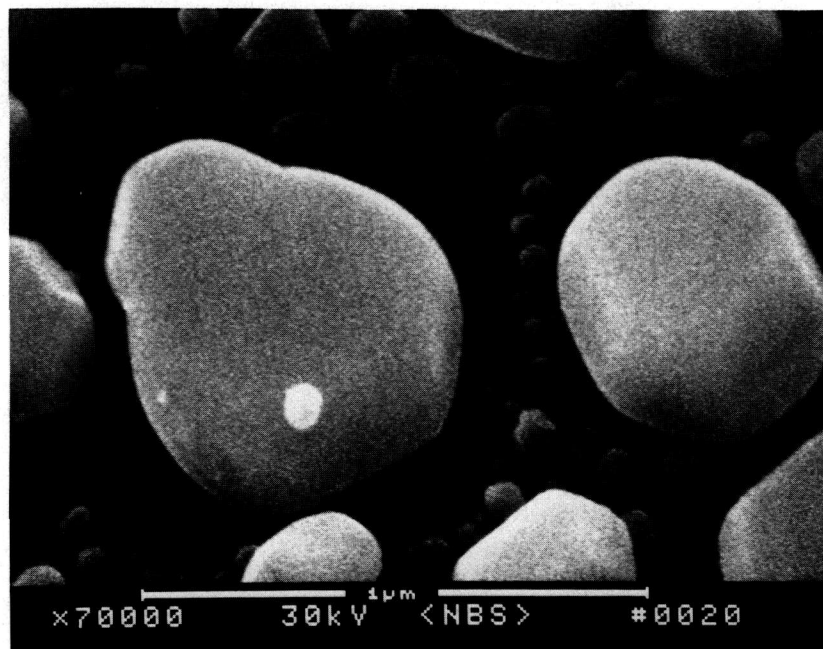
2.2.2 Fundamental Metrology Instrument Operation In operation, the sample area to be measured is visually positioned by using the standard raster scan. Then the electron beam of the metrology instrument is "fixed" in position by switching into spot mode. The electron beam acts as the reference point for the measurement. The philosophy behind this technique has been discussed previously [11]. The object to be measured is then translated beneath the electron beam by an electromechanically-scanned stage [12,13]. The linear displacement of the stage is precisely determined by use of a commercial optical interferometric measurement system. As the sample is scanned, the collected electron signal is stored simultaneously with the data from the interferometer system by a dedicated microcomputer system. The output of the system is a graph of the measured transmitted signal plotted against the interferometrically determined scan position (i.e., the image profile). Subsequent analysis of this image profile and its comparison to the profiles determined from the Monte Carlo modeling determine the location of, and the distance between, the left and right edges of the line being measured.

2.2.3 Laser Interferometer Stage A precise laser-interferometer piezo-flex stage, custom fitted to the SEM chamber, was developed in order to

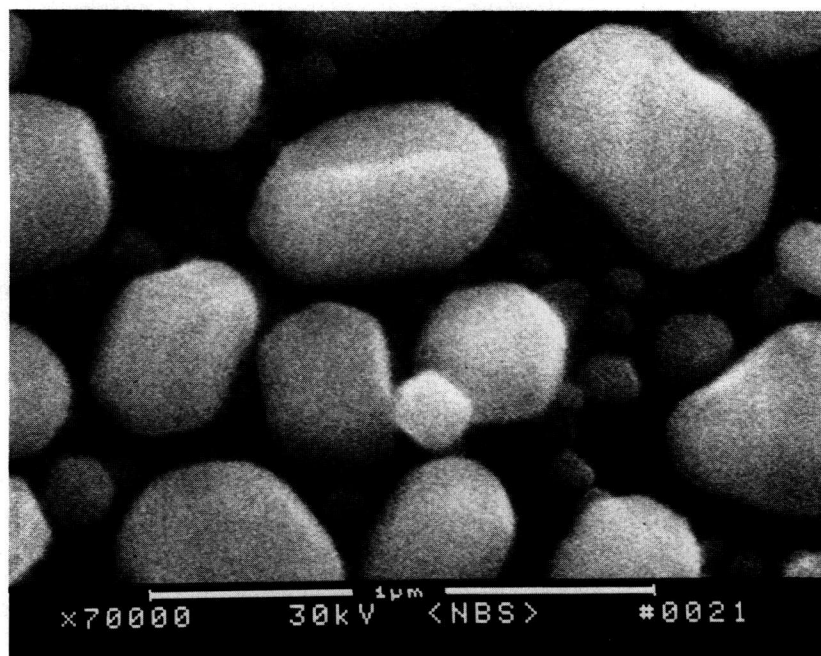
accurately monitor the specimen motion to within a few nanometers under computer control. The original stage [8] was modified extensively for the measurements of the x-ray masks. These modifications were necessary to facilitate the large x-ray mask reticle and pyrex support ring as well as the transmitted-electron detector scheme employed for this work. This mask was far larger than any sample originally envisioned for measurement in this instrument. The metrology stage used in this instrument is similar in principle, but not in practice, to the stage used in the other NIST metrology instrument currently used to certify the SEM magnification standard SRM 484 [14]. The total range of travel of the present piezo-flex stage is limited to about 70 μm , but this can be circumvented by the 100 mm range of coarse stage. Therefore, the larger samples generally associated with the semiconductor community can be accommodated as long as the area of interest is positioned in the center of the wafer or mask. Limited fine-positioning motion is available in both the X and Y directions. Currently the maximum measurement distance is limited by the maximum piezo stage travel although staging and software changes are planned to extend this motion to include the mechanical stage motion.

The laser interferometer stage is designed so that the sample resides at a fixed 12 mm working distance below the final lens polepiece of the instrument. This long working distance has the unfortunate effect of limiting the resolution of the instrument from the specified and demonstrated 4 nm resolution to about 10 to 15 nm ultimate resolution under these conditions. The effect of the working distance on image sharpness is shown in Fig. 3 by using a standard gold-on-carbon resolution specimen. The only major instrument parameter changed between the two micrographs was the working distance. The image was then refocused and re-astigmated. These micrographs demonstrate that the reduction in sharpness is directly related to the increased working distance.

The stage motion is tracked by optical laser interferometry. The interferometers for both the X and Y measurements are dual-pass plane mirror (quad-beam) Michelson-type interferometers [15], with a least-count of 2.5 nm. The interferometer is mounted directly in the vacuum chamber in order to minimize both the dead-path and any environmental influences. The laser source is a Zeeman-stabilized He-Ne laser which emits reference and measurement beams of orthogonal linear polarization separated by a frequency of about 2 MHz. The



a



b

Fig. 3. Scanning electron micrographs of a standard gold-on-carbon resolution sample using the NIST LaB₆ metrology instrument. (a) Short working distance (i.e., 4 mm) and (b) long working distance (i.e., 12 mm) where the sample on the laser interferometer stage resides. Note the loss of sharpness in the long working distance micrograph.

mirrors reflecting the laser beam back are mounted in X and Y above the piezo stage in direct line with the sample. This position minimizes any Abbé-offset errors. Displacement of the mirrors in either the X or the Y directions appears as phase information on a radio-frequency carrier and is detected by standard heterodyne techniques. The entire laser-interferometer stage unit is composed of two joined sections: 1) the laser, the directing optics and the receivers which are all external to the vacuum; and 2) the interferometer optics, stage assembly and sample which are all in the vacuum space of the electron microscope. The entire stage is removable from the vacuum as a unit in order to facilitate all alignments before being installed within the microscope chamber. All the adjustments have locks so that once the stage has been placed into the vacuum no change in alignment occurs.

Prior to the x-ray mask work, the laser-interferometer metrology stage was designed around secondary and backscattered electron detection and measurement by using a microchannel-plate electron detection system [16]. As part of the extensive modifications to the stage for the x-ray mask metrology, a TED facility was also included as described below.

2.2.4 Stage Control and Data Acquisition Software The stage control for positioning and data acquisition is fully controlled by a Hewlett Packard model 320 microcomputer system connected through a Hewlett Packard model 3852 data acquisition system. This system is programmed to generate a stair-stepped voltage ramp to drive the piezo-flex stage and move the sample area under the stationary SEM beam. At the highest of the four resolution settings available, the system is capable of three to four thousand steps per micrometer of travel. After the operator's choices have been made, such as direction and length of scan, the sample is visually positioned and then the scan is started and measurement data are taken. A count from the laser system electronics and a voltage reading from the electron detector electronics are taken simultaneously at each step of the ramp and stored by the data acquisition system. At the completion of the scan, all data are transferred to the microcomputer and the raw laser counts are converted to micrometers. This original set of data pairs may be graphically displayed on the computer for review.

The construction of the piezo stage coupled with the relatively heavy assembly of mirrors, sample holder, and sample which it carries, causes it to be subject to some vibration effects, especially during sample motion. Considerable effort went into reducing the effects due to external sources of vibration, and measurements confirm that these are held to plus or minus one laser count (i.e., 2.5 nm). However, under stage drive, there is a vibrational motion superimposed onto the desired linear motion. The resulting plot of voltage signal versus laser position is not a smooth curve. This is not a serious concern as long as the data for the image profile are made simultaneously and reflect the position and signal at the same time. A method of smoothing the raw data and reducing the total amount of data to be analyzed was adopted. The data were first sorted by increasing value of laser reading (position) and then multiple voltage values (signal intensity) at each different laser reading were averaged and replaced by this single value. This is equivalent to making several readings at a single point and then reporting only the average as a means of increasing the apparent signal-to-noise ratio. In practice, this means that a raw scan of over 20 000 data points over several micrometers (such as in a pitch measurement) is reduced to about 2 000 data points by this procedure. Both the original and this reduced data set may be printed, stored for future use, recorded on floppy disk, or transmitted to a larger computer for analysis and computation.

A second data measurement program for the computer has been developed [17] and is still undergoing further development. This program, in addition to providing for control of the stepper motor driven stages, can read the stored data files and display the resultant curves. On these plots, the regions between movable gates may be expanded to show line edges in greater detail. Cursors may be moved along the curve with a display of the laser position and corresponding voltage shown below the plot. With this program, the edges of the feature being measured are not determined subjectively by moving the cursors over the displayed image profile (as done by most current measurement algorithms), but by the results of the modeling of the measured x-ray masks as described below. Using the model-derived edge criterion and the plots in this program, edge locations were manually determined and appropriate widths and pitches reported. Future modifications to this program will facilitate automated operation.

2.3 SEMs and Data Acquisition

2.3.1 AMRAY Measurement Systems Comparison measurements were made of TED mode image profiles from the digitally-acquired video data from two sources: 1) the commercial AMRAY beam scan linewidth measurement system accurately calibrated to NIST SRM 484, and 2) the laser interferometer stage described above. Since the transmitted electron detection system can be common between the two measurement systems, comparison measurements can be made with little difficulty. However, the pixel resolution between the two systems differs significantly.

2.3.2 Hitachi Measurement System The same sample holder and TED system (described in Sec. 2.4.2) was carefully inserted into the Hitachi S-4000 field emission instrument. Only slight modifications to the amplification system were required. The Hitachi field emission SEM was also equipped with the Hitachi keyboard measurement system accessory and was accurately calibrated by using NIST SRM 484 at high accelerating voltage. This instrument was also useful in the determination of the edge precision of the absorber lines at high magnification and resolution on broken mask pieces. It was also used to measure the wall angle. But, since these data are unable to be directly transferred to an ancillary computer system for image analysis, precise measurements could not be obtained directly from this instrument and a secondary system described below was developed.

2.3.3 ISAAC Image Analysis System A computer-based measurement system christened "Isaac" was developed for analysis of the digital images from the Hitachi S-4000 SEM or other video input [18]. The images are captured with a high-speed frame-grabber called a PIXEL PIPELINE [19]. The software generally used on the system is a commercially available image analysis program called IP Lab Spectrum [20] and also the public domain program named "Image" of the National Institutes of Health [21]. The display rate is 30 frames/s (real time video on the computer screen), the spatial resolution is 640×480 pixels with 256 gray levels. Further improvements of this system for high resolution digitization (4048×4048) have also been implemented.

The video signal for the Isaac system was acquired at TV rates or scanned into the computer using the scanner and then stored and processed in the computer. The pixels of both the scanner and the Isaac have been calibrated with precise linear scales. With the Image and the IP Lab Spectrum

Programs, there is the capability to control the frame-grabber card, and the capability to use the built-in tools, modifications, pseudocolorization, calculations, and measurements. The IP Lab Spectrum program also has an extension developed by Signal Analytics [20] in collaboration with NIST specially designed for linewidth or pitch measurements used in this work.

2.4 Electron Detection System

The development of the electron detection system used in this work was divided into three parts. The first was the electron scattering modeling used to study the geometry of the TED detection system. The second was the experimentation necessary to compare different detection systems available and adaptable for use. The third was to determine the optimum conditions for the measurements.

2.4.1 Geometry of the Electron-Detector System Monte Carlo modeling of the transmitted-electron signal showed that the angle subtended by the detector should be maximized to obtain a large enough signal with good edge contrast. This required the development of a special detection system, a highly-efficient transmitted electron detector, and high-gain and low-noise amplifiers that would fit within the limited space available in the instrument. A semiconductor diode detector was selected for this that had a threshold detection energy of about 3–5 keV (Fig. 4a) and therefore was insensitive to the secondary or low-energy transmitted electrons. This insensitivity was an advantage for this work. The main causes of this insensitivity are a gold surface barrier (the ohmic contact) on the diode and a thin dead layer above the real detecting p-n junction. Therefore, those relatively low-energy electrons having undergone high-energy loss because of inelastic collisions, but with a trajectory leading to the detector, are filtered from the measured signal. In addition, placement of electron barriers such as pre-filtration grids or metallic foils can reduce the highly-scattered fraction even more. A very thin (approximately 0.5 μm) copper foil was placed above the detector ensuring that the electrons having less than about 10 keV energy are not detected (Fig. 4b). Since the number of electrons reaching the transmitted electron detector through the filter is rather small, in this particular application, the gain and performance of the detector/amplification system must be high.

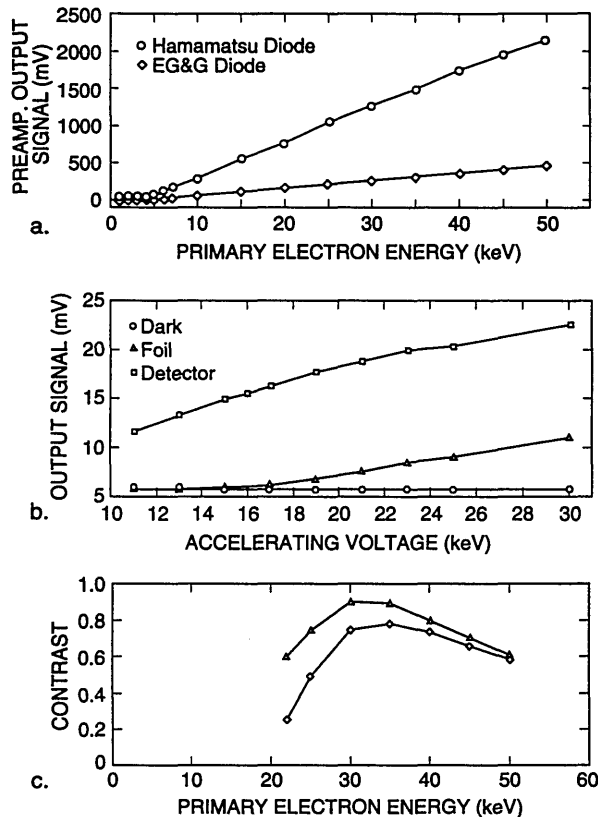


Fig. 4. Semiconductor diode detector. (a) Comparison of the cut-off energy for two types of diodes tested and used as transmission electron detectors. Note the cut-off energy is at about 5 keV. (b) Comparison of the unfiltered signal of the transmission electron detector to the same detector equipped with a thin copper foil filter. Note the minimum energy reaching the detector to generate signal is now about 16 keV. (c) Comparison of the response of two detector types within the range of 20–50 keV. Note that the contrast peaks in about the 30–35 keV region.

2.4.2 Selection of the Semiconductor Diode Detector The first detector used as a transmitted electron detector for this work, was a HUV 4000B photo diode/operational amplifier combination [22]. The HUV 4000B, consists of an approximately 11 mm outside diameter silicon diode with an active area of 100 mm which was ordered without the passivation layer to maximize the sensitivity. This diode has a built-in FET first-stage amplifier with a feedback resistor. The frequency range is DC - 0.1 MHz (gain bandwidth product). This detector proved to be adequate to demonstrate the utility of the transmitted electron collection and evaluation of the technique. Early experimental work was done using this detection system. Later, a new detector/amplifier was designed and assembled with a discrete detector and preamplifier [23]. This detector, a S3590-02 type, PIN silicon photo diode was specially advantageous because it has large, 10×10

mm photon sensitive and thus electron sensitive area. Two preamplifier stages are also mounted at the detector, consisting of two OPA 637 BP type integrated circuits [24]. This design showed better signal-to-noise ratio and wider bandwidth than the previous design (Fig. 4c), allowing it to work with picoampere primary beam current, therefore permitting the condenser lens smallest spot size setting and high non-TV scan rate. In the design of the detector/amplifier, it was important to take into account the following considerations (as well as those discussed above):

- 1) *Available Space.* There is a relatively narrow (11 mm) space underneath the x-ray mask where a detector could be placed, (Fig. 1a).
- 2) *Weight of the detector amplifier assembly.* The total weight of the assembly must be as small as possible and the wiring used must be as flexible as possible to minimize any vibration transmitted to the stage assembly.
- 3) *Location Flexibility.* The detector itself should be easily moveable underneath the mask to be able to place the most sensitive area in the correct location beneath the pattern.
- 4) *Power Consumption.* The detector/amplifier should be a low-power type to eliminate any possible heat dissipation.
- 5) *Cleanliness.* The design must meet the requirement of cleanliness and high-vacuum compatibility.

The sample holder/detector design as shown in Fig. 5 fulfills the necessary requirements for this detector assembly and is currently in use. All the measurement work was done with this detector although some of the experimental work shown may have been done with the other experimental designs.

The detector/amplifier assembly is constructed on lightweight Vector board. This board is an epoxy glass panel having holes in a raster of a tenth of an inch that it is easy to position and mount the components on it and to place the detector to the required position. The ICs are powered with only ± 6 V to minimize the power consumption and thus heat dissipation. The detector and the integrated circuits are in thin, special, gold-plated sockets and the components are soldered on the back side. After the final assembly, the circuitry was carefully cleaned and dried and the detector and the active elements were inserted in place. The detector has no passivation layer and is kept in vacuum so that it remains clean and free of any noise-causing moisture or dirt.

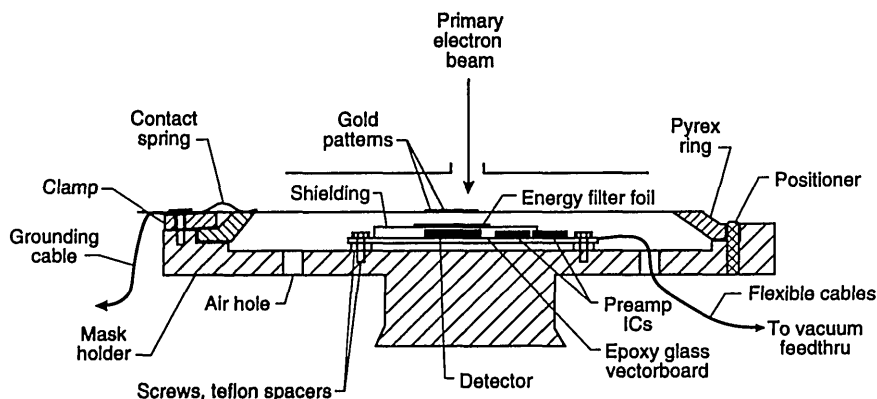


Fig. 5. Cross section diagram of the detector/mask holder assembly developed for the NIST metrology instrument.

The wiring is made of a specially-flexible shielded cable similar to that used in record turntable tonearms. These wires are flexible enough not to transmit disturbing mechanical forces to the stage and do not act as small springs. The cables terminate in plug-in receptacles allowing simple mounting and removal for sample exchange. When the mask holder is in place, fastened on the piezo-electrical stage and the cables are connected, the assembly is ready for operation.

2.4.3 Optimal Conditions The third part of this study was to find the suitable, optimal conditions for the measurement. Beyond the obvious choices like the small spot size for good resolution, the parameters of bandwidth, signal conditioning to improve the signal-to-noise ratio and the optimum of energy filtering had to be found. Fortunately, since the laser interferometer stage information is taken slowly, the bandwidth of the amplification system does not contribute to the measurement. The contrast distributions established experimentally show the best accelerating voltage region of the primary electron beam to be in the range of 20–30 keV, the maximum necessary, in this case, being about 30 keV. Figure 4c shows the ratio of signals on the gold stripes and on the membrane for the two different detector/amplifiers demonstrating a peak in this range. Thus, the metrology instrument was operated and the measurements made at 30 keV accelerating voltage.

2.5 Monte Carlo Electron Beam Modeling

Electron beam modeling done on the NIST Cray super computer was used to support the experimental work in several areas of this study. This work is used to compare experimental and theoret-

ical results in order to suggest new approaches for the measurements, and to help in the interpretation of the experimental results. The Monte Carlo code used in this work produces predictions of the number of backscattered, secondary, transmitted, and filtered transmitted electrons as a function of the location of the incident electron beam from the simulated trajectories of electrons. Only the high-energy (filtered) transmitted electron data is of interest for this work. Input variables include: the electron energy, electron beam diameter, location of the incident beam on the sample relative to the feature of interest, the thickness of the component layers of the x-ray mask, and the characteristics of the solid-state diode detector.

The Monte Carlo computer code was based on the code generated by D. Newbury and R. Myklebust of NIST [25] based on the earlier work by Curgenvin and Duncumb [26]. This code was modified for this work to model the particular configuration of the x-ray mask and to gather statistics about the electrons that are collected by the detector. This computer model has been used to determine the transmission of electrons through lithographically-produced gold lines on silicon substrates. A thin (5 nm) chrome layer, which improves the interface properties between the gold and the silicon, has been included. The Monte Carlo code is based on a screened Rutherford model for the atomic scattering. The scattering cross sections have been multiplied by the factor $(1 + Z/300)$, where Z is the atomic number, in order to improve agreement with measured backscattering coefficients. This factor is a zero-th order way to account for the differences between the screened Rutherford [27] and the more exact Mott cross sections [28]. A low energy cut-off has been

included in the transmission coefficient because a filter is placed in front of the detector that eliminates electrons with energies below a known value (e.g., 16 keV). A total of 20 000 trajectories has been used in these calculations to reduce the level of error to less than 1%. The code allows the user to follow closely the changes in the number of transmitted electrons as the simulated electron beam traverses the mask from the substrate to the gold absorber strip. This modeling effort is currently being extended to include other concerns, such as the proximity effects of neighboring lines, detector geometry, detector sensitivity, and other geometric effects.

The Monte Carlo code was specifically modified to solve for the special case of the x-ray mask, that is, the transmission of electrons through gold absorber lines on thin silicon membranes. In this work, a gold line is modeled as a strip with trapezoidal cross section on an otherwise uniform plane. If an electron crosses the boundary of the line, then a backward step must be taken so that the previous step terminates at the intersection with that boundary. Energy losses are thus computed only up to this point. The calculations then proceed in the new layer (or in vacuum) until a predetermined stopping condition is reached. When the energy of an electron falls below a preassigned minimum value it is removed from further consideration. The energy losses are determined from the theory of Bethe [29]. Note that the specific energy losses due to secondaries are included in the Bethe formula and are not subtracted from the primary electrons, which would constitute double counting. The number of backscattered, secondary, and transmitted electrons are determined with the inclusion of a possible energy filter associated with the electron detector. The results are then printed as a function of the position of the incoming electron beam.

The primary emphasis of this work is to model the electron transmission near the edge of gold lines in order to identify the edge locations and thereby obtain a value for the linewidths. The transmission varies greatly as the electron beam crosses the edge. In principle, the edge may be found by superimposing the normalized measured and calculated transmission-electron image profiles and, if they agree with each other, the edge locations in the model profile are taken as the real edge locations. The model was used to simulate the behavior of 100 electrons for different incident lo-

cations on the x-ray mask as shown in Fig. 6. The incident electrons in this case are modeled to have an energy of 20 keV and a Gaussian spatial distribution with a diameter of 2 nm. The gold structure is modeled with a perfectly vertical wall. The electron beam in Fig. 6a is shown incident on the membrane far away from the gold absorber strip; in Fig. 6b the electron beam is shown incident at the center of the gold absorber strip; and in Fig. 6c the beam is shown incident at the edge of the absorber. A comparison of the electron behavior for 10 keV is shown in Fig. 6d where no electrons are transmitted. The figures shown are limited to a field width of 5 μm , although electrons are actually followed by the model out to a much larger distance. These electron trajectory plots illustrate the degree of electron scatter as the electron beam traverses the mask.

Figure 7 shows the fraction of the electrons that are expected to be transmitted and collected by a detector with a diameter of 12.5 mm located 5 mm from the lower surface of the membrane, with a diode cutoff energy of 4 keV, as a function of the position of the incident beam. No energy filter was included in this calculation. The energy of the incident electrons is 22 keV in Fig. 7a and 50 keV in Fig. 7b (10 000 trajectories were simulated for each point). As demonstrated in these diagrams, the contrast at the edge is better for the lower accelerating voltage electrons in spite of the fact that only about 10% of the electrons are collected by the detector, compared to over 90% for 50 keV. The reason is that practically no electrons are transmitted when the beam is incident on the center part of the strip for an incident energy of 22 keV, as opposed to about 30% collected electrons passing through the absorber at 50 keV. The change in the number of transmitted electrons as the beam passes over the edge is quite sharp, leading to a precise value of the width (as discussed later). Modeling also can provide the fraction of the maximum number of transmitted electrons that corresponds to the edge of the strip. It is apparent that a trade-off between contrast and resolution is necessary. By the addition of the copper filter we were able to increase the accelerating voltage to improve instrument resolution, but at the same time maintain high contrast. For the metrology work a beam diameter of 10 nm has been used and an accelerating voltage of 30 kV with a copper foil filter having a cut-off at about 16 keV. The 16 keV cut-off was determined experimentally as shown in Fig. 4b.

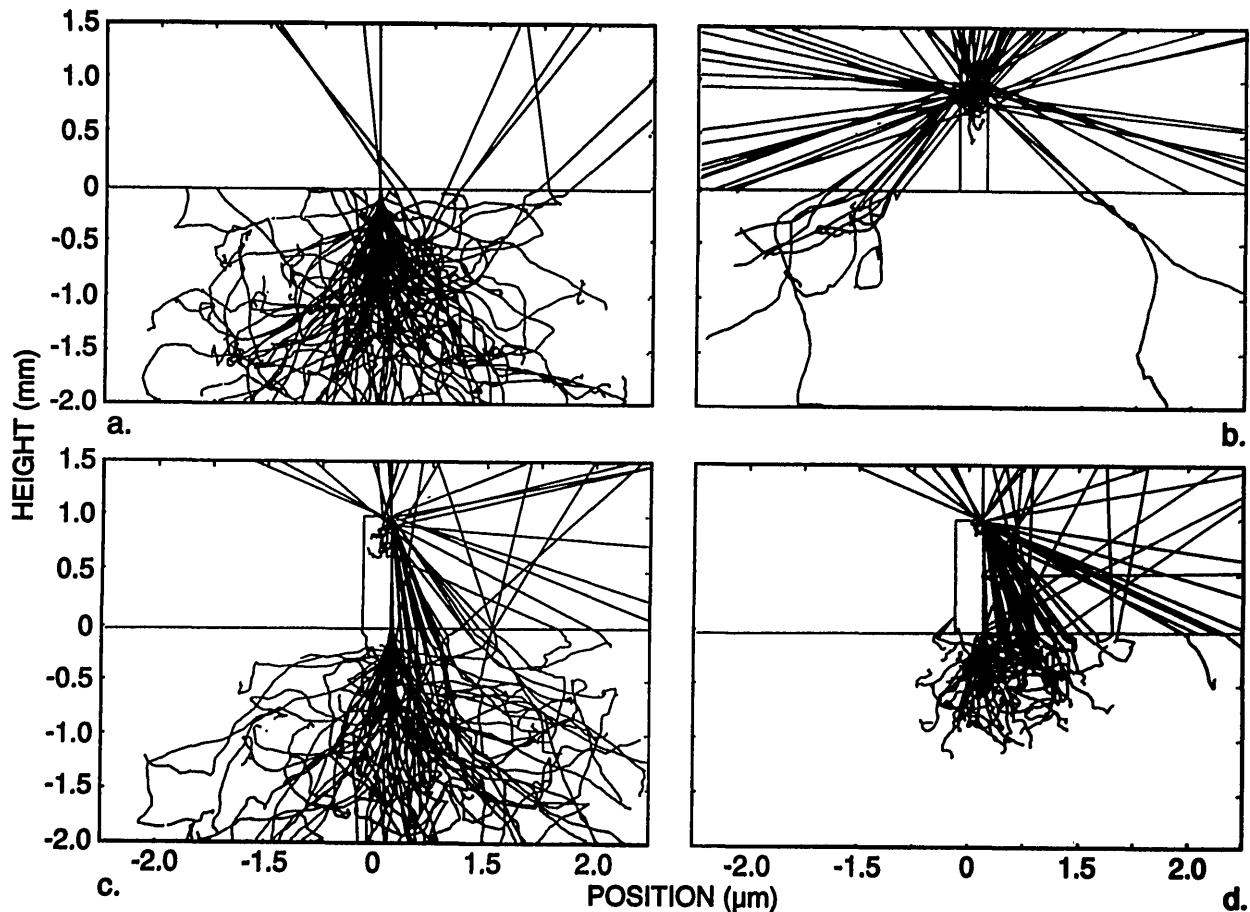


Fig. 6. Monte Carlo modeling of the x-ray mask. (a) Simulated behavior of the electron beam incident on the membrane region. The primary electron beam is incident at the 0,0 position of the graph. Electrons leaving the membrane at height -2.0 are not shown in the figure, but pass on to the electron detector. (b) Simulated behavior of the electron beam incident on the center of the absorber structure. (c) Simulated behavior of the electron beam incident at the edge of the absorber structure (20 keV electron beam accelerating voltage and a vertical wall absorber). (d) Comparison of the simulated behavior of the electron beam incident at the edge of the absorber, but at 10 keV accelerating voltage where there is no electron transmission.

2.5.1 Detector Placement In many typical transmission electron applications in which high-energy electrons are aimed at a target with the purpose of detecting cellular ultrastructure (or other types of samples), the optimum type of detector is one placed at a relatively long distance from the sample. Such a detector covers a small solid angle and collects electrons that have gone through the material essentially undeflected through a very thin sample. Contrast of the ultrastructure is enhanced by insertion of an aperture preceding the detector. This would be the typical philosophy adopted by those commonly working with a scanning transmission electron microscope (STEM), where the entrance angle to the electron detector is typically about 1×10^{-4} rad. The overall construction of the STEM instrument permits more flexibility in the detector and aperture placement than the SEM, although often at the expense of a limited sample

size. This limited-solid-angle approach to the detector was the initial philosophy adopted in the early x-ray mask metrology study based on the typical TSEM geometry [5,6]. In that work, the electron detector had an entrance angle of about 1.7×10^{-2} rad. This resulted in a poor signal-to-noise ratio and thus limited the ability to achieve small spot diameters. This also resulted in a very limited field of view as well as excessive noise amplification (60 Hz) in the signal.

X-ray mask metrology presents a different situation from that described above. A very small fraction of the electrons, only a few in 10 000, satisfy the conditions that allow them to be collected by a small-angle detector unless the beam energy is much higher than 50 keV. As shown in Fig. 6, the electrons in the modeled energy range suffer multiple scattering events. Those that emerge from the lower surface of the membrane may or may not be

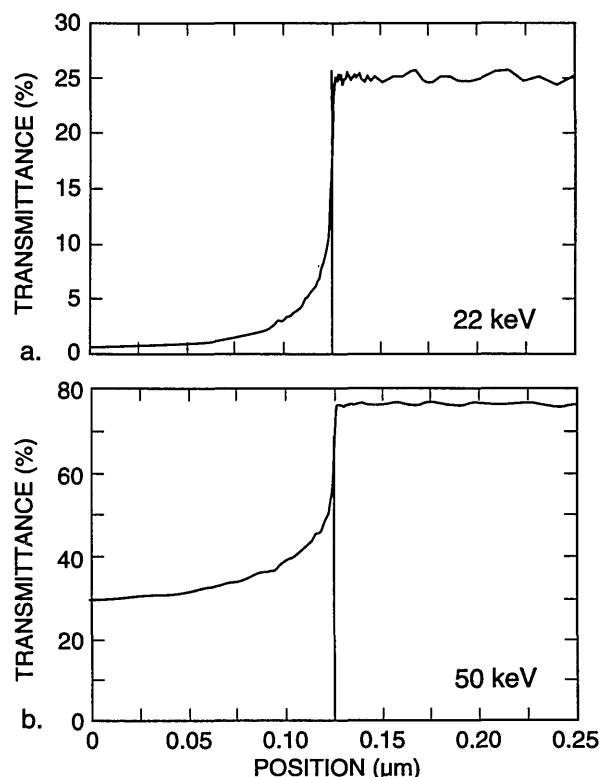


Fig. 7. Monte Carlo modeling of the electron fraction transmitted through the x-ray mask. (a) 22 keV electron beam. (b) 50 keV electron beam.

collected by the detector. A detector with a large acceptance angle, located close to the lower surface will collect a significant fraction of the transmitted electrons. The edge region is characterized by a rapid change in the total number of transmitted electrons as the beam passes over the edge of the gold strip, as shown in Fig. 7.

As the incident energy decreases from 50 keV, the ratio of the two on-feature and off-feature current levels in Fig. 7 increases until it reaches a maximum in the neighborhood of 22 keV (unfiltered), and then sharply decreases again as the number of electrons transmitted through the membrane alone becomes very small (i.e., the signal decreases to zero) near 20 keV. Therefore, for this particular metrological application which differs from the customary STEM or TSEM application, it is favorable to collect as large a fraction of the transmitted electrons as possible. Consequently, a large, wide-angle detector was located close to the sample (as described below). Within the practical limitations due to the configuration of the scanning electron microscope, this strategy leads to stronger signal and good images of the structure(s) of interest. The excellent signal-to-noise ratio demonstrated by

this configuration permits minimum spot diameters and thus, potentially higher resolution of the edge and lower edge uncertainty than with the original commercial configuration used for this purpose. It is also possible to obtain solid-state diodes such as the one currently under test as large as 12.5 mm in diameter. Thus, much of the x-ray mask pattern can be viewed directly even at low magnifications. However, it should be noted that diode uniformity and bandwidth limitations require further investigation. Alternatively multiple diode detectors, microchannel-plates or scintillator detectors could be used. However, due to our special space limitations, the diode detector proved to be the most appropriate.

Early work [4] demonstrated an experimental comparison between the two types of detector configurations. The difference between the conventional detector configuration and the one where there is a wide solid angle of acceptance and placement is about 5 mm from the sample was shown to be significant. There was increased contrast without any degradation of edge definition in the close detector arrangement. In fact, in this mode of electron collection, the signal was so great with the commonly used primary electron-beam currents for this type of work, that the gain of the amplifier required substantial reduction to avoid saturation effects. Under these conditions the spot diameter of the SEM could be reduced to the minimum possible, still with acceptable contrast. These results were first predicted by the modeling work and subsequently confirmed experimentally. This is the type of detector used throughout this work.

2.6 Specimen Charging

Specimen charging is always a concern in scanning electron microscopy. The x-ray mask used in this study has the chrome plating base left in place. This provides a grounded conductive layer under the isolated structures and over the insulating layers (Fig. 1). Unfortunately, the chromium coating can have structure. This structure adds to the "noise" in the measurement scan (discussed later).

The surface of the mask was also carefully grounded by using a grounding clip. The potential effects of specimen charging were also tested by partially coating a test mask and comparing with the data. For this work it was determined that where this specific all-conductive mask construction was concerned, specimen charging was not a major concern. For the development of standards, often it is necessary to optimize the sample for the

metrology. X-ray masks constructed without insulating layers might circumvent charging problems if suitably grounded. However, no masks without the chromium layer were tested. X-ray masks with insulating membranes (e.g., silicon nitride) could have greater charging problems as well as those masks that have another insulating layer above the support membrane and absorber.

3. Results

3.1 Electron Beam Interaction Modeling

There are currently no standardized x-ray mask fabrication techniques. This area is currently undergoing evaluation and experimentation regarding the most effective construction of the masks. This evolution process necessitated the development of reasonably flexible computer modeling code. Changes in the mask structure during this work necessitated that the modeling be run with the polyimide layer in place for early test masks, as well as removed (actually with this layer still included, but with zero thickness) for the later ones. The results, as expected were similar, but varied from the original by an absolute increase in the level of electron transmission of about 14% in the membrane region and 2–3% in the absorber region (Fig. 8). The fundamental characteristics of the transmission profiles did not change significantly within the “noise” of the modeling. Therefore, the results described here pertain to either mask design (unless specifically indicated). The modeling parameters used for Fig. 8 were those described previously for metrology as well as a slight wall slope (as described below).

Figure 9 shows the modeling results for a 0.25 and a 0.5 μm line with vertical walls. If a perfect vertical wall structure could be manufactured, the determination of the edge would be quite straightforward. Unfortunately due to the fact that we are dealing with “real world” structures and not the ideal structures assumed in computer models, it is not so straightforward. Figure 10 is a plot of the experimental data obtained from the metrology SEM from a 0.5 μm line. It can be seen from comparison of Figs. 9 and 10 that the experimental data obtained are broader than the computed profile for a vertical wall. A substantial amount of effort was expended in order to determine the major factors causing variations in the line profile from the computed values. Some of the contributing factors found to cause a deviation from the ideal are discussed in the following sections.

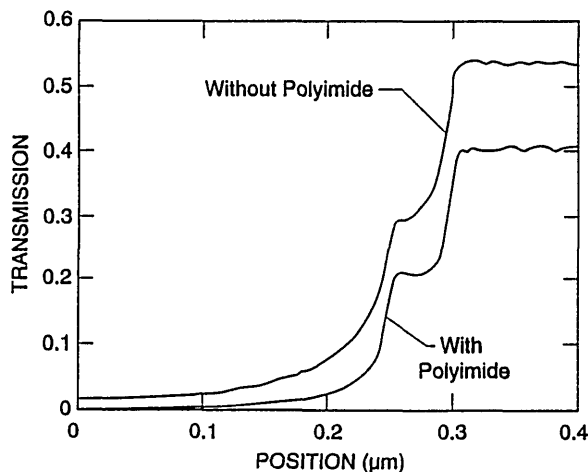
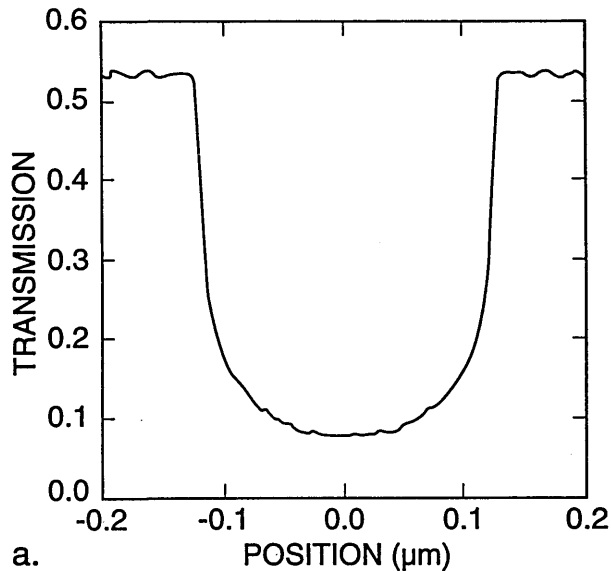


Fig. 8. Comparison of the modeled transmitted electron line profile with a 4° wall slope with (dash) and without (solid) the polyimide layer.

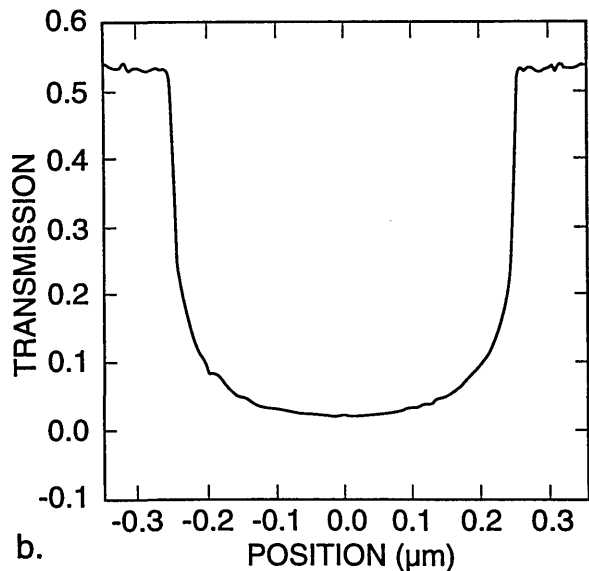
3.1.1 Wall Verticality With the best conditions and stage capabilities possible in the NIST field-emission SEM, it was determined that the wall slope of a line on a broken piece of the x-ray membrane is about 2°–3° (Fig. 11). Because of fundamental FESEM stage limitations, only broken pieces of the mask could be viewed at high tilt. The numbers are obtained from non-cross sectioned samples since to cross section an x-ray mask would require the development of precise metallurgical-like mounting and polishing techniques (which was not part of this study). Therefore, since compound angles are involved in the micrographs, these angles are not exact but are assumed to be reasonable.

The TSEM method is very sensitive to wall slope. Small angular deviations from vertical result in significant changes in the profile. Monte Carlo modeling of a 2° sloped-absorber wall (Fig. 12) begins to approach the experimental data, as shown, in Fig. 10.

Wall verticality issues are not only associated with structure fidelity but also surface flatness. Surface flatness measurements made with a WYKO 6000 Phase Measuring Interferometer [30] on several of the test masks, have shown that there is on average a 0.5 μm peak-to-valley variation across the surface of the mask within the measured window (Fig. 13). This variation could also contribute to the inaccuracy of the measured result. Local waviness across the x-ray mask can result in variations in local surface tilt which can then be translated to differences in the resulting video profile and eventually the measurement.



a.



b.

Fig. 9. Monte Carlo image profile of absorber lines with perfectly vertical walls. (a) 0.25 micrometer line and (b) 0.5 micrometer line both computed with 0° slope to the wall.

A third factor associated with wall verticality is that of positioning within the measurement instrument. The surface of the mask must be perfectly perpendicular to the electron beam. If the SEM sample stage itself were to demonstrate a 2° tilt from normal to the beam this is added to the 2° already present on the structure. This effectively results in a vertical wall on one edge and a 4° slope on the other edge. This effect has been able to be demonstrated experimentally as shown in Fig. 14. This concept is essentially equivalent to tool in-

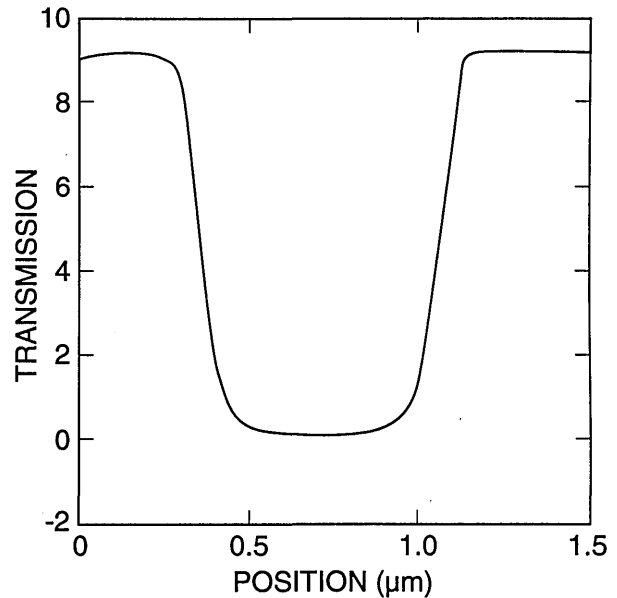


Fig. 10. Experimental data obtained from the NIST metrology instrument of a $0.5 \mu\text{m}$ nominal line obtained by using the methods described in the text.

duced shift (TIS) found in other forms of measurement equipment. The effect was verified by reversing the application of the angle by 180° as done in standard TIS testing. This stage wobble factor underscores the need for extremely precise SEM stage construction in inspection instruments with this technique. A stage accommodating a 12.7 cm (5 in) x-ray mask may need to travel up to 25.4 cm (10 in) to view and measure all the structures necessary. Such a stage must be aligned perpendicular to the electron beam well within 1° for the entire travel. The stage must also demonstrate roll during travel of less than 1° as seen by the sample as it travels or the roll will translate into tilt on the sample. Measurements using the secondary or backscattered electron techniques will also be affected, but the magnitude of the effect was not a part of this study.

3.1.2 Wall Edge Roughness There is about a 7–16 nm edge wall roughness that can be attributed to the structure or graininess of the gold absorber and other factors as seen in Fig. 2 and measured by the digital beam scan measurement in Fig. 15. This surface roughness randomly affects the effective slope of the edge as seen by the electrons and can increase the apparent deviation from vertical by about 2° from its estimated geometrical value. This makes the effective wall slope, as seen by the electrons in the NIST metrology SEM, to be about 4° (explained later).

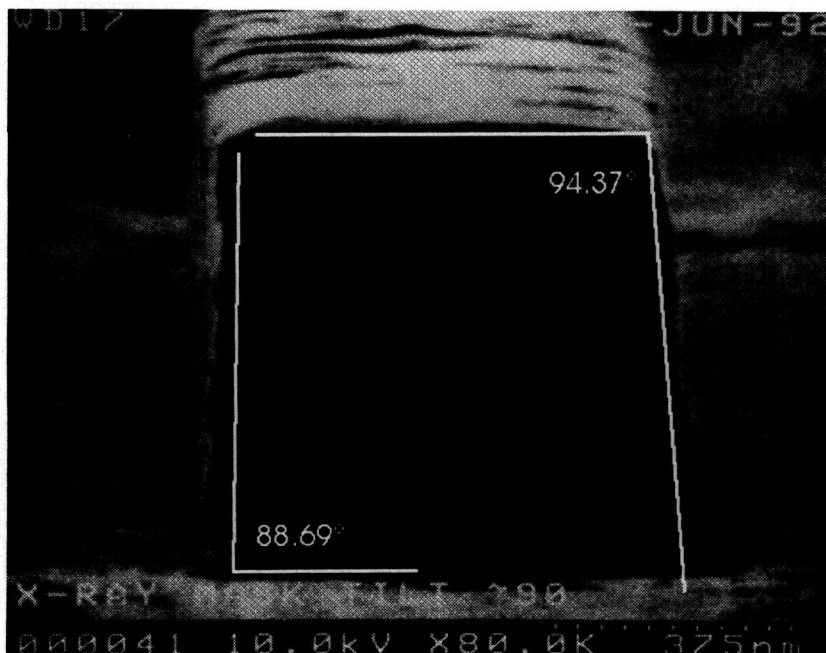


Fig. 11. Scanning electron micrograph that has been scanned into the Isaac image analysis system demonstrating the approximate 3° slope to the sidewalls.

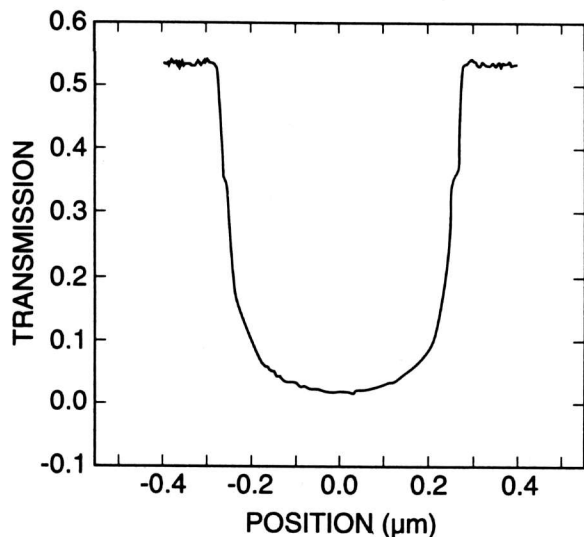


Fig. 12. Monte Carlo image profile of a 0.5 μm gold line with a 2° wall slope.

3.1.3 Edge Rounding The edge of the absorber is rounded and not sharply delimited as shown in Fig. 2. This affects the transmission profile in those regions where these rounded edges are interacting with the electron beam (e.g., when the electron beam is incident on the top of the line near the edge). Edge rounding is not serious *vis-a-vis* determining the edge location in the present

measurements. However, it should be included in future versions of the Monte Carlo modeling.

3.1.4 Wall Foot Many of the “real-world” structures have a foot associated at the base which can be as large as 30 nm in size (Fig. 16a). The effects of this foot to the measurement are similar to edge rounding and is most evident when the electron beam is incident on or near the foot. The material composition of this foot is not known but it is presumed to be material left over from previous processing steps. Like edge rounding, it appears not to be a serious limitation for the present measurements. This structure (depending upon its composition) could become a problem especially if truly vertical walls were fabricated.

3.1.5 Chromium Structure The chromium can have a structure as evidenced by high resolution SEM imaging (Fig. 16b). This structure adds noise to the measurement but seems to have little effect on the metrology.

3.1.6 Contamination Hydrocarbon contamination of the sample deposited by the electron beam measurement can contribute to the measurement imprecision in two ways. First the buildup of the contamination appears initially at the base of the absorber structure, therefore broadening the base of the measurement profile (Fig. 17). Second, contamination build-up can tend to attenuate the

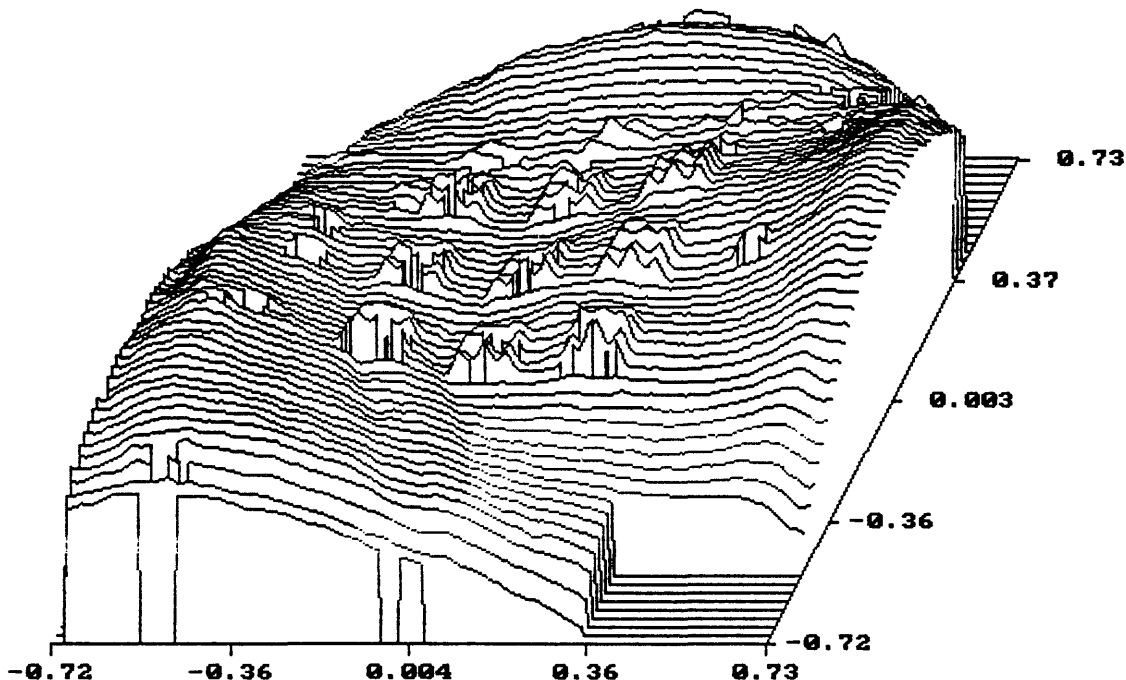


Fig. 13. WYKO 6000 Phase measuring interferometer flatness measurement of the x-ray mask surface demonstrating a 0.5 μm peak-to-valley variation across the surface of the mask (courtesy of Mr. Chris Evans).

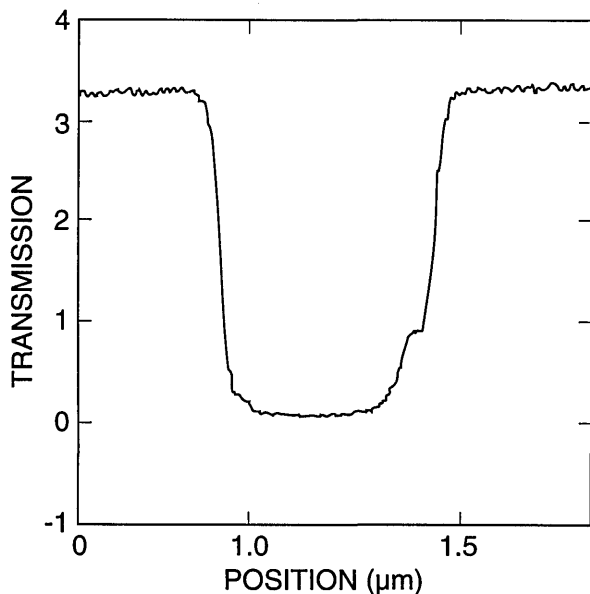


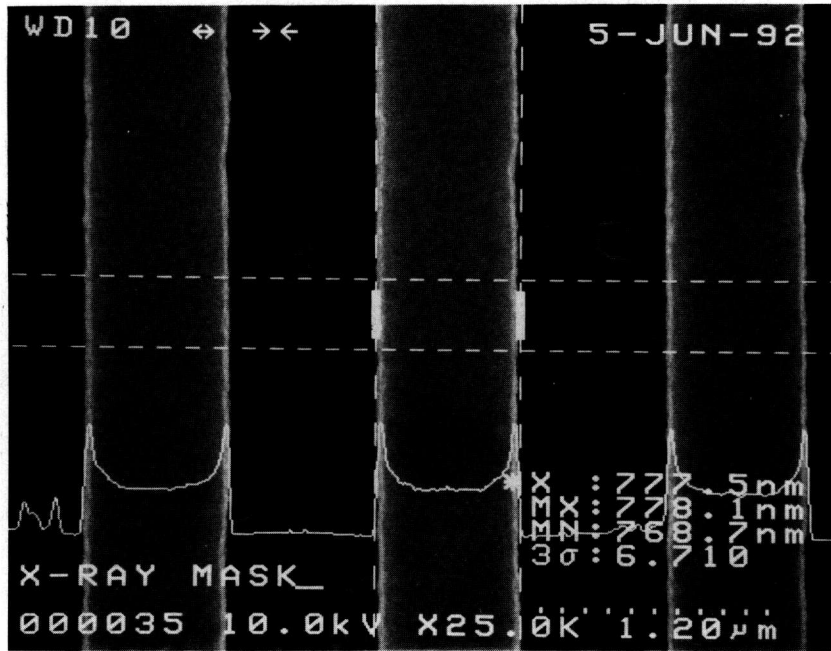
Fig. 14. NIST metrology instrument measurement scan of an absorber line which has had 4° of experimentally induced angle into the position of the mask. Note the prominence of the notch on the right side of the graph. If the induced angle is placed 90° from the first measurement the notch appears on the opposite side. Also notice that the verticality of the opposite side of the scan approaches the modeled data for the 0° case since the composite wall angle has been compensated by the shimming of the mask.

collected transmitted electron signal and thus alter the actual measurement threshold. The figures shown were intentionally contaminated for an extended period of time. Under normal measurement conditions this should not be a problem.

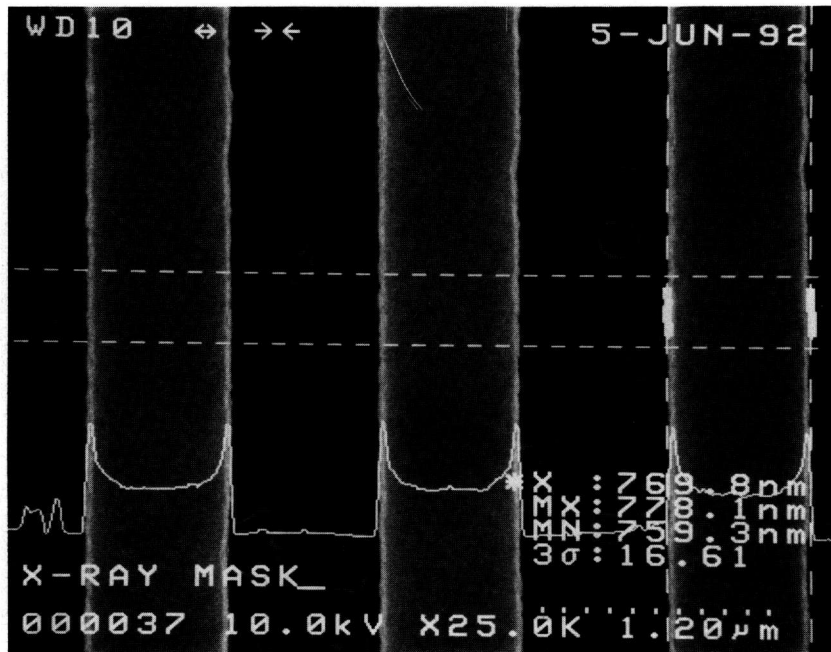
3.2 Analysis

The six factors described above, with the first two (wall verticality and edge roughness) being the dominant ones, contribute to the differences seen between the observed transmission line profile obtained with the TSEM technique on “real world” samples and the Monte Carlo modeling result for an ideal line under the same conditions of measurement. It was therefore necessary to model a line for each case with the measured geometrical slope of 2°, as well as one with an effective slope of 4° for the various cases. Figure 18 shows the data for the 0.5 micrometer line with the two wall slopes superimposed for each case.

It has been shown that the edge of the absorber line is not a perfect vertical wall. Instead there is a widening at the bottom which results from its trapezoidal shape as well as rounding and roughness. The computer modeling code, for this case, is based on a simple trapezoidal line with known height, measured to be 0.7 μm, and variable wall

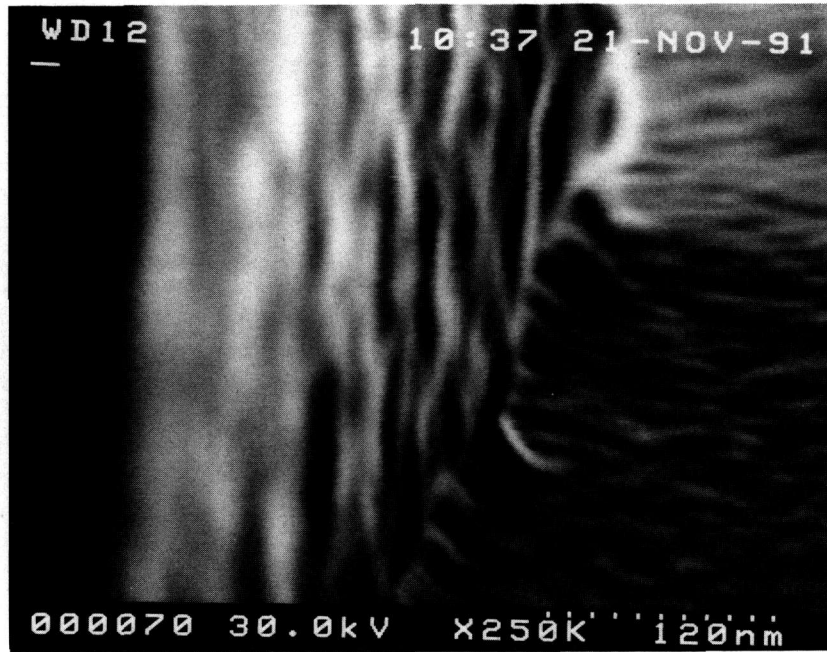


a

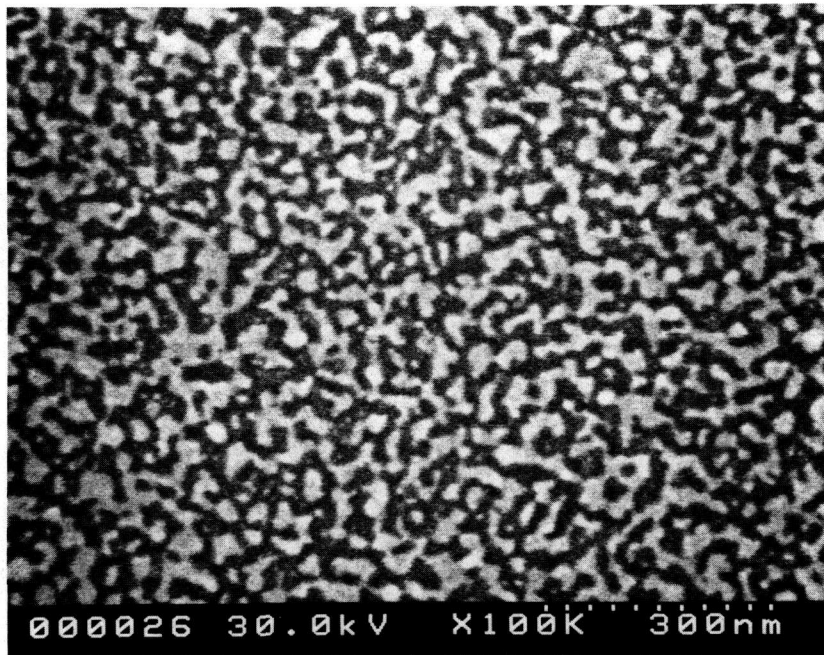


b

Fig. 15. Scanning electron micrographs and beam scanned measurements of the gold absorber lines demonstrating the edge precision of the lines. (a) Position 1 and (b) Position 2. Note that depending upon the position on the absorber line where the measurement is taken, the 3σ value for the precision varies from 6.7–16.6 nm.

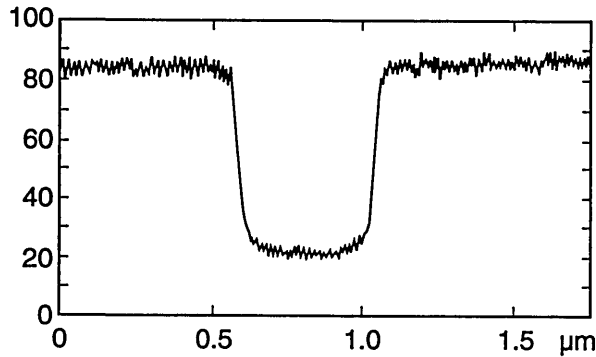


a

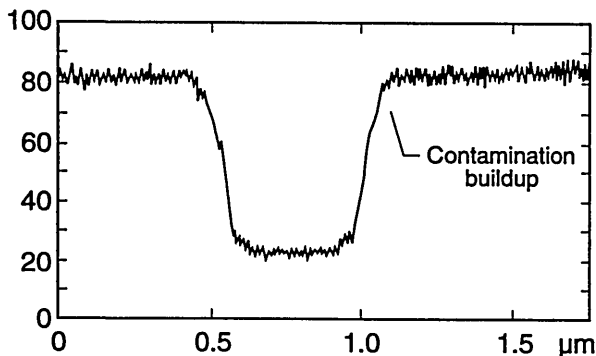


b

Fig. 16. Scanning electron micrographs of the x-ray mask structure. (a) Wall foot showing the material at the base. (b) Structure of the chromium.



a.



b.

Fig. 17. Effects of sample contamination on the measured profile. (a) Original scan. (b) Scan after intentionally allowing the sample to become contaminated.

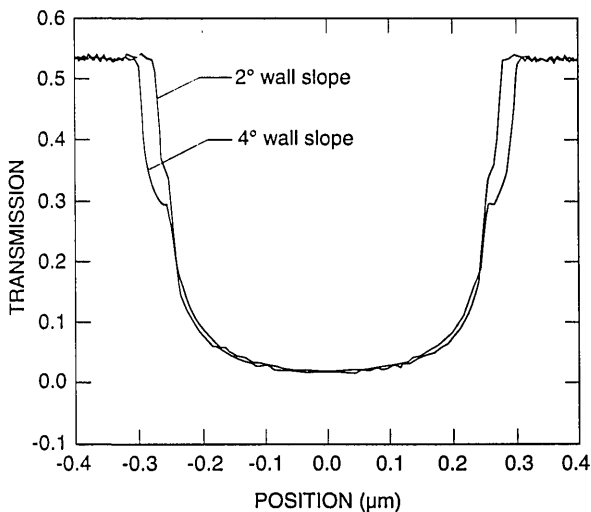


Fig. 18. Monte Carlo modeled data for $0.5\ \mu\text{m}$ gold line with a 2° wall slope and a 4° wall slope superimposed.

angle. The measured wall angle was about 2° , but a best fit to the measured lines was with an angle of 4° . The extra angle is a way to include the effects of roughness and rounding, which make the variation of transmission more gradual. Thus, there is an ambiguity in interpreting the predicted position of the edge. One can either make a best fit with the measured 2° slope and take the position of the edge from it or one can use the better fit with the 4° slope and take the edge from it. The former method attributes disagreement in fit to the non-ideality of the trapezoidal line and then assumes that the edge is still properly determined by neglecting these effects. The latter method attempts to incorporate these effects in the model and extract an edge position that in some sense includes them. Both approaches have been used and the results from the two methods are expected to bracket the true edge position.

A very interesting phenomenon was observed in the simulation of the transmission across the edge of an absorbing gold line on a silicon membrane. When the beam lies wholly on the sloping edge of the trapezoidal line, the electron transmission remains relatively constant especially along the upper half of the slope. The signal constancy is enhanced by the removal of lower energy electrons by the copper detector filter. This effect occurs because the electrons that strike a steeply sloping edge can escape easily from the surface and continue down to the detector. In a sense, the electrons are reflecting off the surface. The point of contact along the face is then not very important because the phenomenon is nearly the same at all points. Figure 19a is a trajectory plot of 20 electron trajectories showing how the electrons exhibit this behavior. The height and width of the modeled line are both $0.7\ \mu\text{m}$, and the beam intersects the middle of the 4° trapezoidal face. The beam diameter is $10\ \text{nm}$. Many of the electrons exit from the face to form the stream that is then collected by the detector. This phenomenon can be used to determine the position of the edge if it can be seen in the measured TED mode image. If the necessary spatial resolution can be achieved, then this signature can be observed provided that the surface is not so rough that it is completely blurred. The effect of this phenomenon on the modeled electron transmission, as compared to the structure of Fig. 19a, is shown in Fig. 19b. This figure shows the right-hand edge of the line. The line center is taken as the left-hand edge in the figure. The transmission becomes relatively constant when the beam is wholly

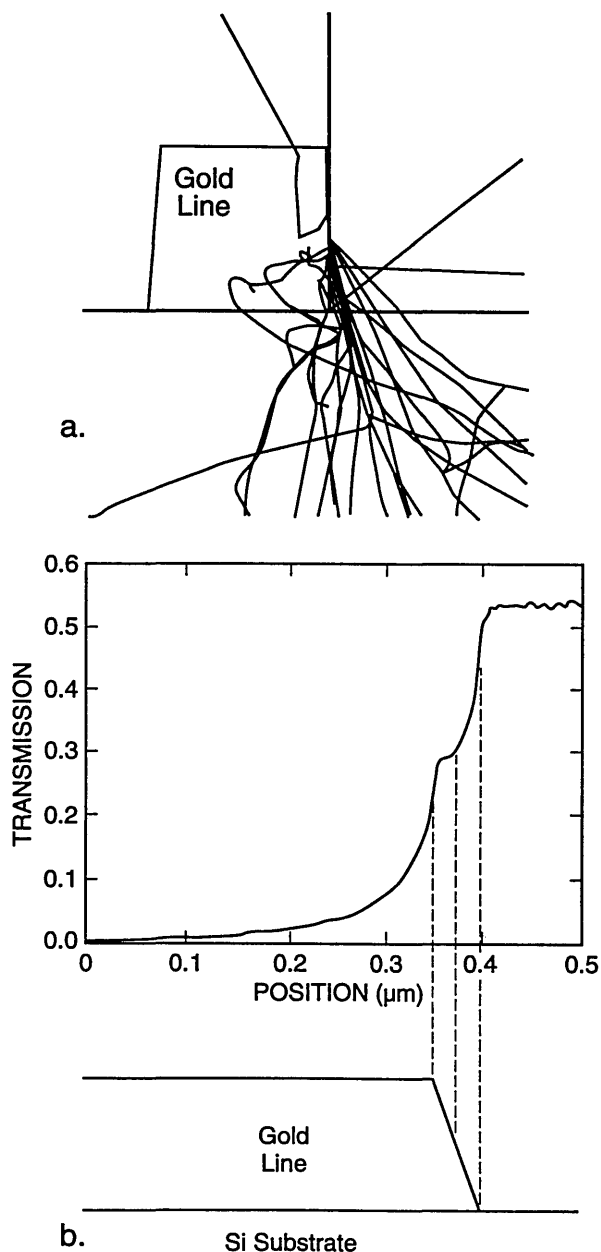


Fig. 19. The effects of the electron scatter from a sloped edge of the absorber. (a) Trajectory plot showing the reflection of electrons from a 4° sloped surface. (b) Diagram showing the reflection of electrons from the edge as related to the structure and modeled profile.

on the face and not much below the center of the face. Further modeling of the edge roundedness and the effect of the foot at the base would help to understand better the transition points before and after this notched region. The same effect occurs in the backscattered electron signal and it may also become useful in finding the edge in this method of electron collection as well (Fig. 20) but has yet to

be confirmed experimentally. This phenomenon is currently being explored further.

As the wall angle increases from vertical to 4° (and beyond), this characteristic notch begins to appear as a ledge in the model profiles. This is an important observation because the model tells us that this ledge occurs when the electron beam is incident on the sloping edge of the assumed trapezoidal line. This is confirmed in the experimental results shown in Fig. 14 where the effective vertical wall of the right side with no notch contrasts with the 4° slope of the left side which has a prominent notch. Just as in the model, as the wall slope decreases, the position of this notch moves up the profile to ultimately become obscured at verticality. If the actual laser interferometer/SEM data is fit to the 4° modeled data, excellent agreement is obtained (Fig. 21)—except in the region of the actual notch. Perfect agreement of the experimental data obtained from the NIST instrument to the modeled data, in this region, is difficult for two reasons: 1) the current NIST instrument has a flat final lens and is operating at a relatively long (12 mm) working distance to accommodate the laser interferometer stage assembly. Under these conditions the instrument operates at about 10-nm (or poorer) ultimate resolution previously shown in Fig. 3. Unfortunately, the size of the notch is approximately 8–10 nm within the 4° slope range (less for 2°) and thus is not always resolved; and 2) the factors associated with surface roughness and rounding of the edge are random and the notch may appear on one

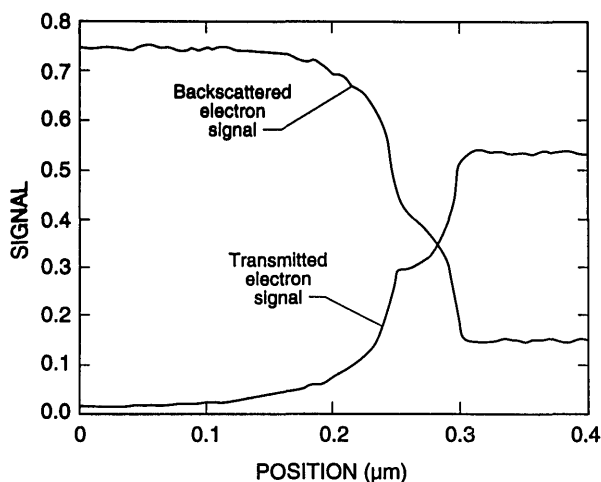


Fig. 20. Monte Carlo modeled data of the transmitted electron signal and the backscattered electron signal showing the appearance of the characteristic notch in both modes of electron detection.

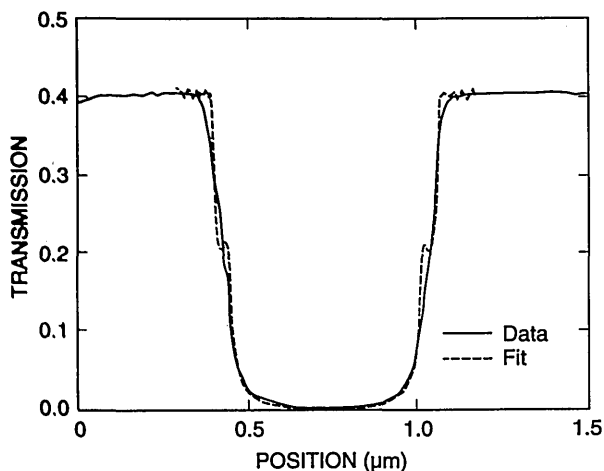


Fig. 21. Comparison of the Monte Carlo modeled data for a 4° wall slope to the actual fitted experimental data.

edge of the profile but not on the other and can be blurred. Then the question becomes: is the character found on the measured profile real or is it noise? Indeed, the characteristics of the notch are within the resolution capabilities of a good field-emission SEM. The notch then can sometimes be unambiguously detected by its consistency from scan to scan whereas the noise is not consistent (see continued discussion on this point below).

3.3 Measurement Criteria

For the purposes of the present study, it will be assumed that the effective linewidth for x-ray masking purposes is the width at a point 50% down the slope of the absorber line. This assumption could be refined in the future by comparison of linewidths on x-ray masks measured by the present technique and linewidths actually produced by using the measured masks. Fortunately, 50% down a line is geometrically the same on a 2° or 4° edge slope. However, the modeling reveals that the notch position on the video profile (and thus the position of the edge on the profile) is a function of **both** edge slope **and** linewidth for linewidths less than about 2.0 μm. This is due to the fact that as the linewidth decreases below about 2.0 μm, the minimum transmission increases because of leakage of electrons out from both edges. This means that as the linewidth decreases, more transmission occurs and the baseline level of the profile increases (Fig. 22a). Even an infinitely large gold line will have some base level of transmission (0.002% of incident electrons) and as the line decreases in size this will rapidly increase as shown in Fig. 22b. This means that there would also be a vertical shift

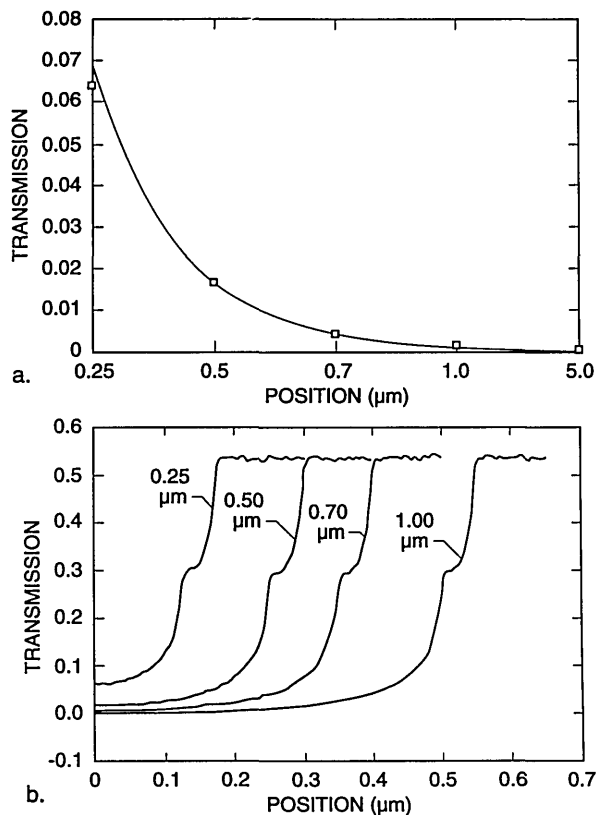


Fig. 22. Effect of electron transmission on the location of the edge. (a) Relationship between the percent minimum transmission as related to the size of the absorber structure as modeled. (b) Monte Carlo modeled plots of the threshold variation as a function of structure size for 0.25, 0.5, 0.7 and 1.0 μm width lines with a 4° sloped wall. Both the 0.35 and 0.75 μm thresholds have been interpolated from these data.

in position of the “edge” location as interpreted from the model. Furthermore, the absolute transmission at the edge depends on edge slope for any linewidth because the amount of leakage out the edge depends on the slope (Fig. 23).

The criteria for determining the edge position, for the masks used in this study are summarized in Table 1. These are determined from the modeling results as follows: the 50.0% point of the face of the slope is located at the 52.0% transmission point on the TSEM profile of a 0.25 μm line with a 4° effective slope and at the 61.7% point for a 2° sloped line. Since we can argue for both 2° (real) slopes and for 4° (effective) slopes, we average these values to obtain an “edge” criterion at the 56.9% point. For a 0.5 μm line with a 4° effective slope the position is at the 56.2% point while for a 2° slope the point is at 65.0% (Fig. 23a). The average is 60.6% and is where the measurement is made (Fig. 23b).

Table 1. Gold absorber edge location

Nominal line (μm)	Edge location (%)
0.25	56.85
0.35	58.35
0.50	60.60
0.70	61.55
0.75	61.60
1.00	61.75

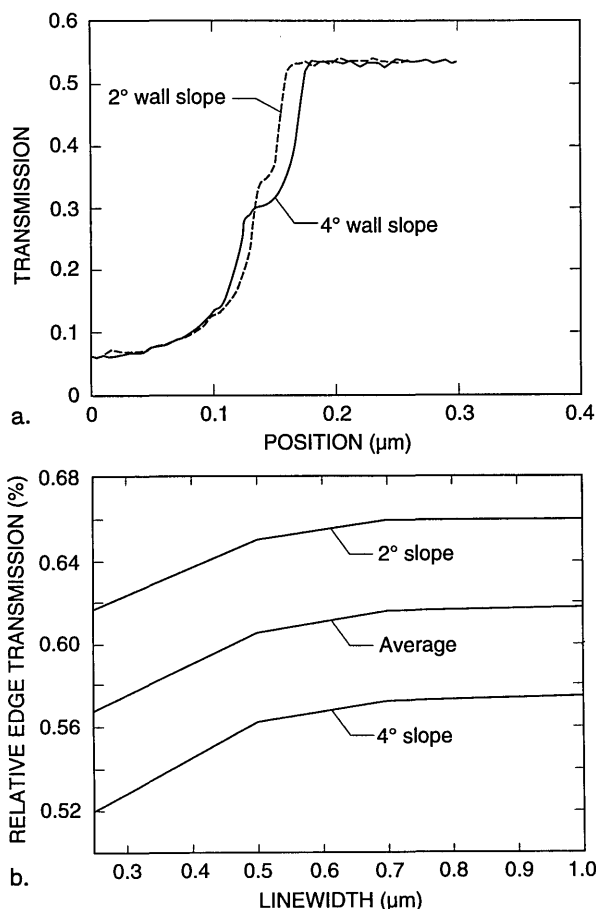


Fig. 23. Relative edge transmission. (a) Plot of the relative edge transmission for a 0.25 μm line as related to the nominal linewidth for the 2° wall case (dashed line) and the 4° wall case (solid line). (b) Plot of the calculated relative edge transmission of various width lines from 0.25 to 1.0 μm and the average between the two where the measurements were made.

The resulting difference in linewidth between the 2° slope percentages and 4° slope percentages is accepted as a systematic unknown component of inaccuracy. This difference is estimated to be less than 10 nm for each linewidth measurement for edges defined at 50% down the absorber line and

does not contribute to errors in the pitch measurements since it is a self-compensating measurement. This component of inaccuracy would decrease for smoother walls and/or smaller edge slopes.

3.3.1 Measurements A series of x-ray masks were measured by using the metrology SEM and the criteria, as described above for the edge location. Example measurements are shown in Table 2. Examples of representative 0.5 μm lines for pitch and width measurements are shown in micrographs of Fig. 24 a–d and the profiles of these lines are shown in Fig. 25 a and b. The pitch measurements of these lines represent about 25 000 original data points per measurement and the width measurements represent about 8000 original data points per measurement handled in the manner described previously. The above measurements compare favorably with the beam scanned data from the same measurement instrument for a 0.5 μm line depending upon the threshold setting chosen (Fig. 26).

Table 2. X-ray mask measurements

Nominal line (μm)	Actual measurement (μm)	Standard deviation (μm)
0.25	0.237	0.00015
0.35	0.363	0.00070
0.50	0.487	0.00280
0.75	0.740	0.00070

The measurement results, to date, are quite encouraging and indicate that the present technique has resulted in an estimated edge-location uncertainty as low as 10 nm with the modeling. This performance could be further improved by improvement in the wall edge verticality and the surface roughness. Increases in the number of pixel points available for the measurement, in the use of high-brightness, high-resolution field-emission electron optics, or the development of measurement algorithms based on the electron-beam modeling would improve the data handling but would not improve the uncertainty of this measurement. This occurs because for the level of accuracy required, the physical limitation imposed by the measurement subject is the limiting factor.

3.4 “To Notch or Not to Notch”

The question “can the notch be resolved?” was also studied. The complete “test” mask on the TED assembly was carefully installed in the NIST

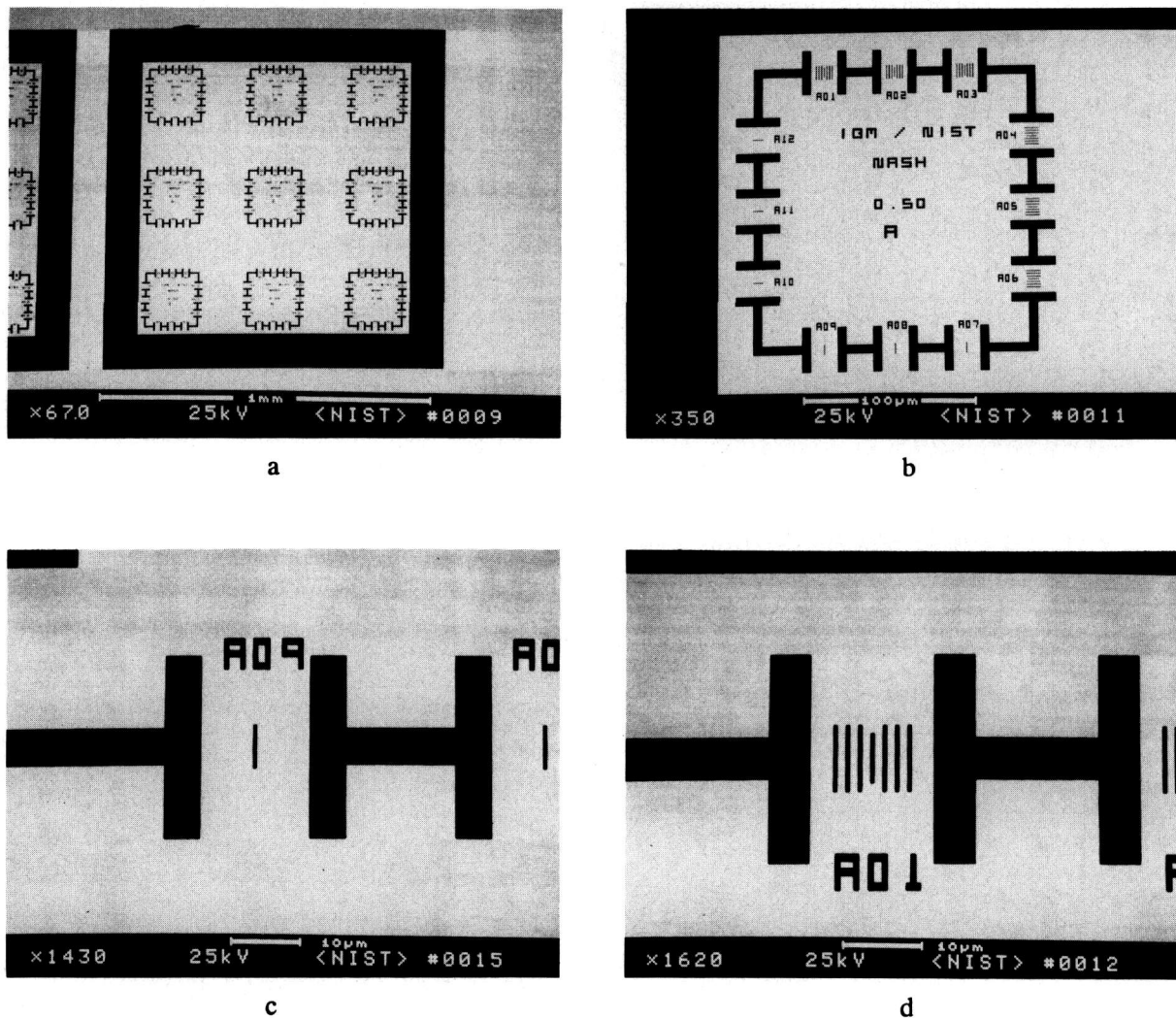


Fig. 24. Measurement data. Micrographs of a representative x-ray mask feature having a nominal $0.5\ \mu\text{m}$ absorber structure measured in the NIST metrology SEM. (a) Low magnification image showing absorber pattern array. (b) Individual pattern with nominal $0.5\ \mu\text{m}$ absorber structures. (c) Isolated absorber line. (d) Pitch array of the absorber lines.

FESEM and the characteristics of the image of the transmitted electrons studied by using the standard beam scanning mode. This image was then transferred and stored in the Isaac image analysis system. When the resolution and signal-to-noise level are adequate (as they are in the FESEM) a notch was resolved (Figs. 27 and 28).

Figure 28 shows that the resolution of the notch structure is sometimes only on one edge due to local grain interference, rounding or roughness, which complicates matters somewhat and can be seen to vary as the beam is scanned across the line. This characteristic is good for precise metrology if this notch can be precisely imaged in the measurement instrumentation and algorithms developed to

exploit this characteristic. We are unable to image this notch routinely (as discussed previously), in the metrology SEM, but our beam-scanned measurements with the FESEM demonstrate its location in the profile (Figs. 27 and 28).

3.5 Imaging and Particle Detection

The high contrast image obtained in this mode of electron detection lends itself to less ambiguity regarding the location of the structures of interest. Figure 29a shows a low magnification image of a test pattern, and Fig. 29b displays the pattern at higher magnification, showing the presence of an electron-dense particle. Such dense particles could

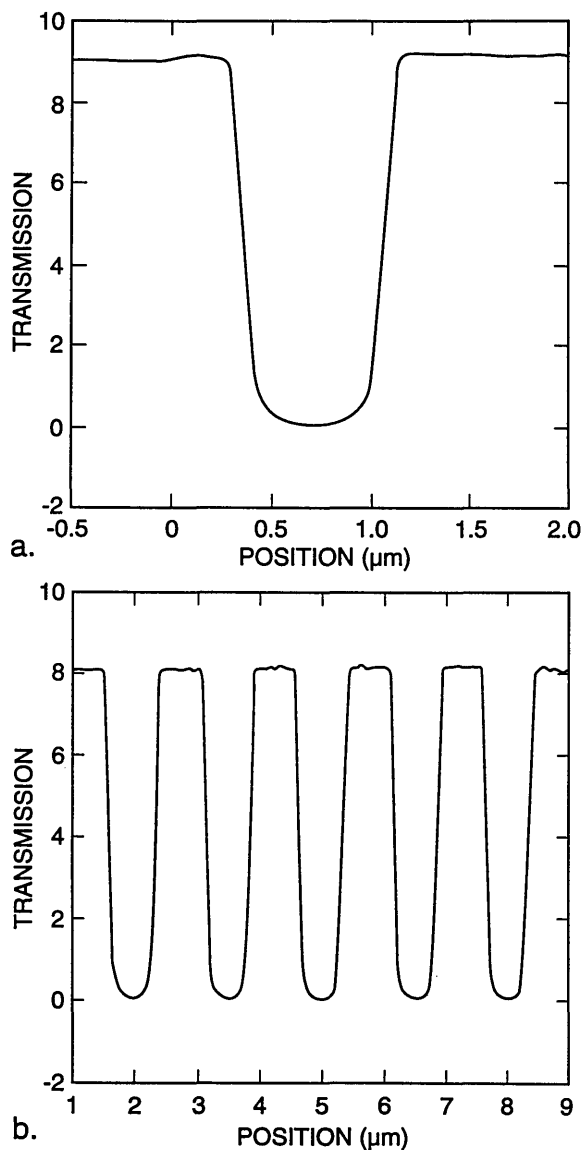


Fig. 25. Measurement data. Actual laser stage data, using the TED mode, from the NIST metrology instrument of the $0.5\ \mu\text{m}$ absorber structures. (a) Isolated line used for width measurement. (b) Array of lines used for both width and pitch measurements.

result in defects on the exposed wafer. Inspection in the secondary electron imaging mode could tend to exaggerate the importance of such a small contaminant particle because of enhanced topographic contrast or particle contrast. In secondary electron detection, a low atomic weight contaminant such as a carbonaceous or siliceous particle could appear bright and thus be misinterpreted as being of a higher atomic number (i.e., a particle of gold) yet, in actuality be relatively transparent to the x rays. The TSEM technique described here yields an im-

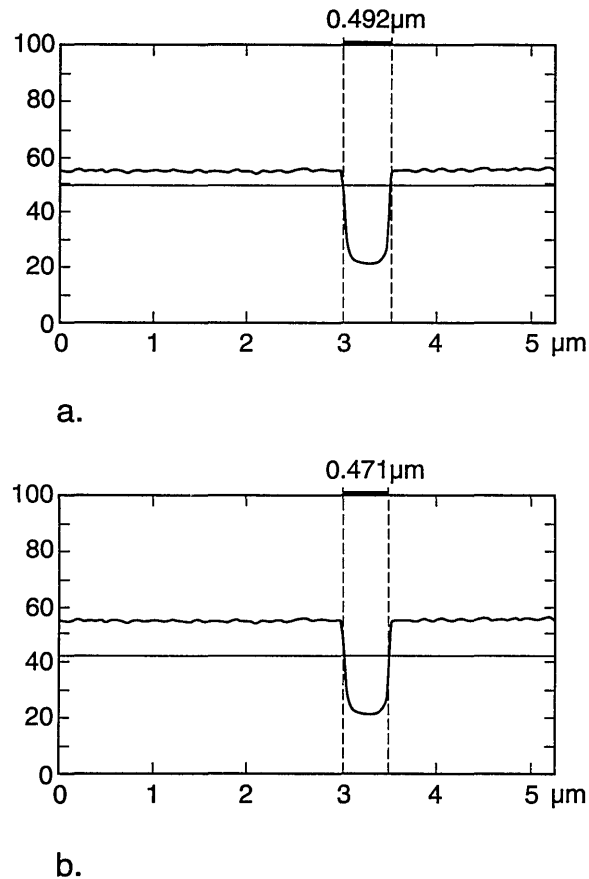


Fig. 26. Beam scanned comparison measurement using the classic AMRAY A-90 measurement system installed on the NIST metrology SEM: (a) 20% negative autothreshold setting and (b) 40% negative autothreshold setting.

age of the x-ray mask similar to the view the wafer has of the x rays passing through the mask during exposure. Overlay comparison of this image in a die-to-database or die-to-standard image could readily detect such particles by high-speed computer systems and image analysis. Another area where the TSEM technique has proven useful has been in x-ray mask repair. Fig. 30 shows micrographs of x-ray masks that have been intentionally modified by focused ion beam milling showing that this technique can be used to find and view mask defects prior to their repair as well as inspect the actual repair work.

4. Conclusions

This work has shown that, given the appropriate specimen, novel approaches to metrology issues can result from using the SEM. One appropriate specimen is an x-ray mask which allows the use of the

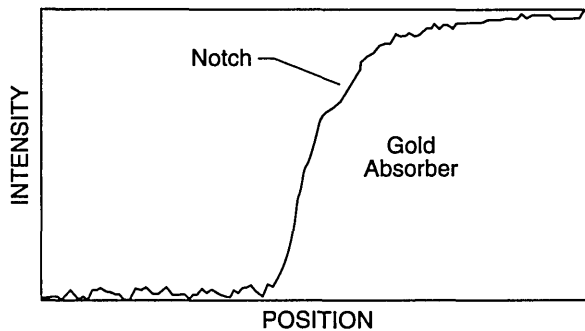


Fig. 27. Digitized field emission scanning electron micrograph demonstrating the presence of the characteristic notch on one side of the profile. Note that the data have been inverted.

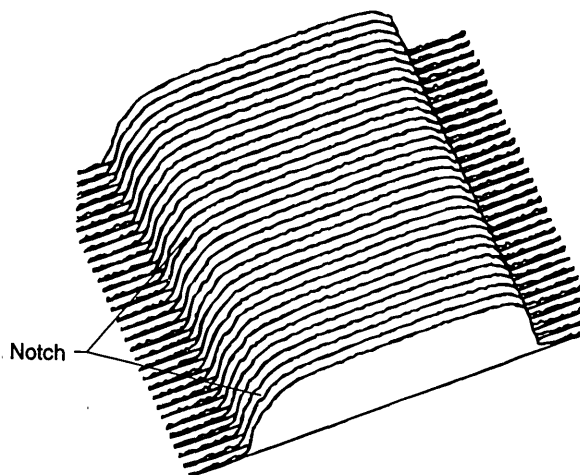


Fig. 28. Image analysis of the digital field emission scanning electron micrograph demonstrating multiple line scans down a gold line showing the presence or absence of the characteristic notch along the left edge depending on the surface roughness. Note that the data have been inverted.

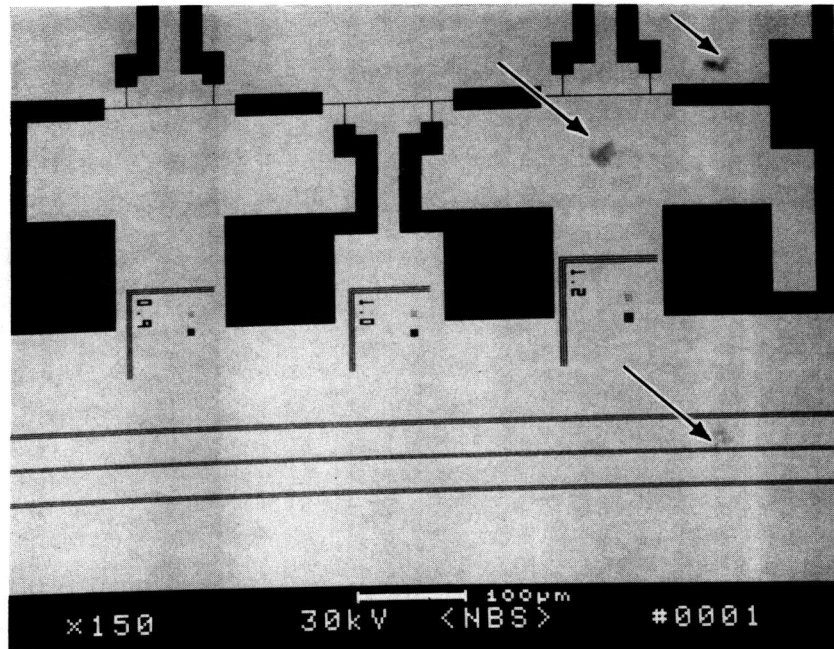
TSEM mode for accurate linewidth metrology. Although not the primary motivation of this work, this technique also lends itself to high-speed x-ray mask defect inspection. Secondary electron imaging is unable to detect large voids within the absorber (even if they are large enough to affect x-ray absorption), whereas these voids could be observed as contrast variations in the transmission electron image. Furthermore, in transparent areas of the mask, secondary electron detection tends to exaggerate the importance of a small contaminant particles because of enhanced topographic contrast or particle contrast. In secondary electron detection, a low atomic weight contaminant such as a carbonaceous or siliceous particle could appear bright and thus be misinterpreted as being of a higher atomic

number (i.e., a particle of gold) yet, in actuality be relatively transparent to the x rays. The technique described here yields a clear image of the x-ray mask similar to the view the wafer has of the x rays passing through the mask during exposure. Unfortunately, metrology based on the transmitted-electron image is not readily adaptable to totally opaque specimens such as photoresist on silicon wafers where the need for standards and precise measurements is presently the greatest. However, experiments currently underway can elucidate this problem further. Another question that can only be answered by further experimentation is the magnitude of process bias or the difference between nominal and actual structure that will exist in the final product once an x-ray mask is measured in the SEM and then is used for exposing wafers with the x rays. In addition, since no standards currently exist for the following measurement of the thick layer structures present on the processed wafer, accurate critical dimension verification is not possible.

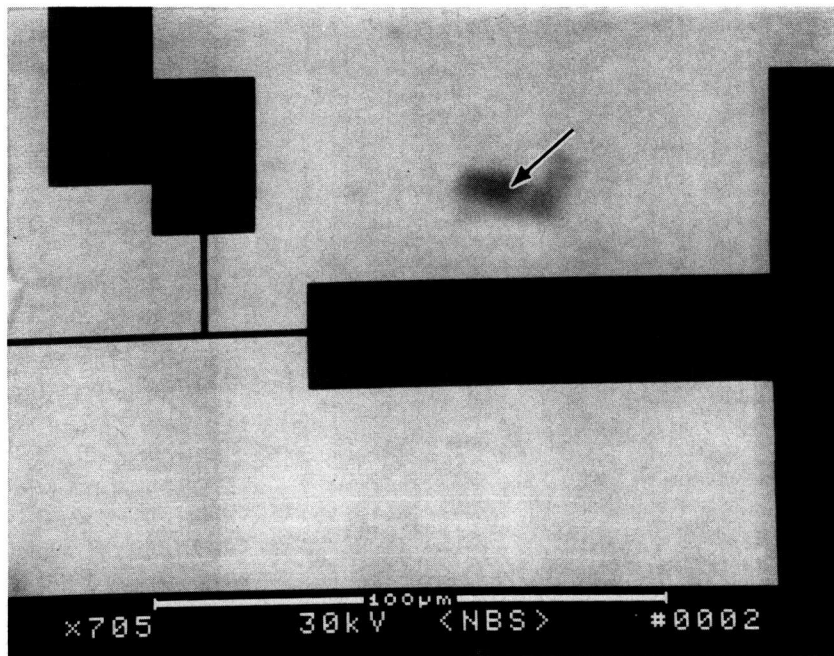
One advantage of the present TSEM mode for dimensional metrology is its relative insensitivity to some of the major contributors to imprecision of dimensional measurements in the more conventional SEM and TEM modes. Clearly, the axial alignment of the broad-area TSEM detector and the detector-feature spacing are not critical and thereby make the mode more robust to reasonable amounts of misalignment. The broad-area type detector developed for this work also collects more electrons than the narrow-angle type detector and thus improves the signal-to-noise ratio. The signal-to-noise ratio is further enhanced by the large number of data points taken by the laser interferometer system and the averaging of the data points for the same location.

Contamination of the sample by the electron beam is always a potential problem in the SEM, but due to the high beam energies required for the TSEM technique, contamination is not a first order metrology problem in this instance, because any reasonable amount of low atomic-number contamination (carbon, for example) is easily penetrated by the beam electrons (and x rays). However, it should be noted that contamination build-up over time can cause measurement imprecision because of contamination build-up at the base of the absorber which broadens the profile and can also attenuate the signal thus altering the threshold point of the measurement.

The ability to use a high accelerating voltage for the TSEM technique permits the use of smaller beam diameters and thus higher resolution than is

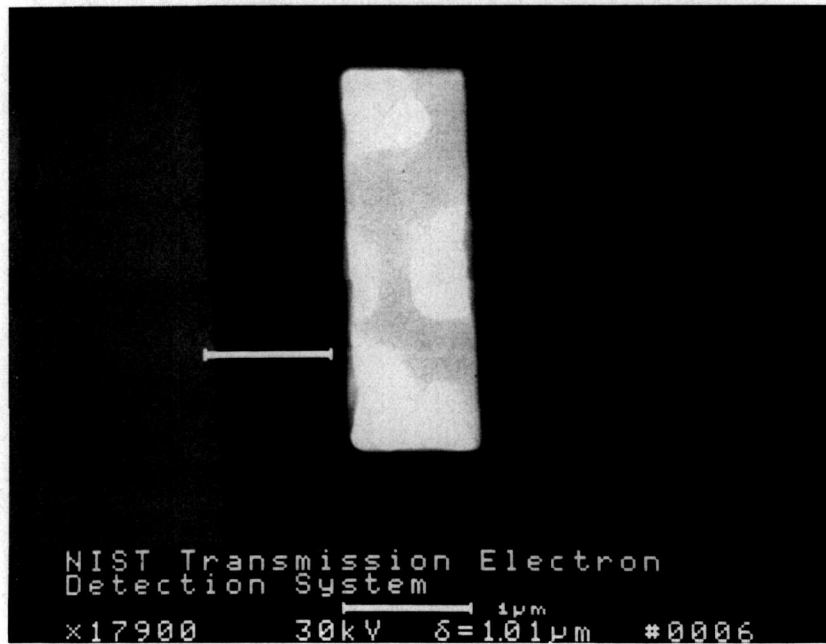


a



b

Fig. 29. Particle detection using transmitted electron detection. (a) Low magnification micrograph demonstrating a test pattern with several particulate defects. (b) Higher magnification of the area with the defect.



a



b

Fig. 30. TED mode as applied to x-ray mask repair. (a) Micrograph with intentionally ion-beam-milled windows positioned 1 micrometer from the edge using the Micron ion beam mask repair system. (b) Defect in the absorber to be repaired.

possible with low accelerating-voltage instruments. Therefore, as long as the resolution is better than the horizontal projection of the sloping trapezoidal edges of the features being measured, the notch in the transmission that occurs along the edge is theoretically observable. However, in order to make the notch observable in practice it may be necessary to improve: 1) the signal-to-noise ratio by longer observation times at each pixel point of the line profile, 2) improve the smoothness of the sloping edges of the specimen, and/or 3) improve the alignment of the specimen normal to the SEM column axis. Therefore, given these potential advantages with no overriding disadvantages, the expectation is that the TSEM mode can be made as precise, or more precise, than conventional SEM modes of operation with the added advantage afforded by the modeling, which is accuracy.

The major components of potential inaccuracy in contemporary SEM metrology are: 1) imprecision; 2) inability to determine the location of the edge; 3) inadequately calibrated magnification and/or nonlinearity in beam-scanned instruments (or its equivalent in interferometric-stage instruments), and 4) rough edge geometries that not only tend to obscure observation of the notch in the TED mode, but also cloud the very definition of linewidth for any mode of operation.

Edge roughness should be considered an undesirable attribute of the sample, and not necessarily a fundamental metrology problem with the TSEM technique. The treatment of roughness used in this paper should be considered as only a first approximation because the justification for treating the roughness as being equivalent to an added component of effective smooth trapezoidal slope is almost totally phenomenological. The "linewidth" in this approximation was defined to be the average of two calculated linewidths determined by two different methods: 1) by using the theoretical notch positions for a smooth-edge trapezoidal specimen with the measured (in an SEM) geometrical edge slope, and 2) by using the notch positions determined theoretically for smooth edges, but with a larger phenomenological slope that gave better all-over agreement with the experimentally observed profiles. Fortunately, the two "linewidths" so determined were not too different (less than or equal to 10 nm for the 0.25 μm width line). This linewidth difference is clearly a component of systematic inaccuracy of this approximation. A better approach would be to actually model the effects of edge roughness and thereby calculate a more accurate notch position in the presence of edge roughness.

Uncertainty in the measurement process is the combination of the two conceptually different quantities: imprecision and inaccuracy. A conservative approach to uncertainty (i.e., a possible overestimate) will be taken because there is no guarantee that all sources of imprecision and inaccuracy have been identified or were under control. This conservative approach is to simply algebraically add the observed 3 standard deviation imprecision of the measurement to the above quoted value of inaccuracy. This results in an uncertainty of 10 nm for 0.25 μm wide lines because the standard deviation is negligible (see Table 2). The uncertainty in other measurements may be more or less than these values because of different specimens, different SEMs, and the use of different methods of calculating uncertainty. However, the present values of uncertainty do indicate the general magnitude of the uncertainties one might expect to achieve by using the TSEM technique on actual x-ray masks, and that is all that was intended. There remain several issues that should be studied to improve this work even further. One major issue is the development and modification of the computer model to include the edge rounding and surface roughness. A second area of study would be the comparison of the secondary, backscattered and transmitted electron images. This should also be done to evaluate the potential of more conventional SEM modes for x-ray mask metrology. The handling of the data and automatic measurement algorithms are another area that can now be improved. Currently it takes about 4 h to obtain one data set composed of pitch and width data of one nominal line size in both the X and Y directions.

The measurement of x-ray masks with the TED mode presents a unique opportunity to obtain precise and, ultimately, accurate measurements of these samples. This "opens the door" for the development and issuance of NIST traceable standards. This also provides the x-ray lithography community with the only calibrated SEM linewidth standard.

Acknowledgments

The authors would like to thank and acknowledge the following for their assistance during the course of this work: Mr. Steve Nash and Mr. Michael Trybendis of IBM Corporation, General Technology Division, Burlington, VT; Mr. John Frank of SEMATECH, Austin, TX; Drs. Dale Newbury and Robert Myklebust of NIST for their assistance in the electron beam modeling program; AMRAY, Inc., Bedford, MA for their continued

assistance in the modification of the NIST Metrology Instrument; Mr. Joe Stella of J. Stella Engineering and Design, Amherst, NH for the re-design work on the laser interferometer stage, and Edward J. Fjeld of E. J. Fjeld Company, Billerica, MA for the fabrication and implementation of the laser stage modifications. The authors would also like to thank Mr. Michael Mort of Signal Analytics Co., Vienna, VA for cooperation in modifications to IP Lab Spectrum necessary for this work; and Mr. Leon Carroll for his assistance in the laser stage program development; Mr. Chris Evans for his assistance in the flatness measurements; Mr. Raymond Mele of the Program Office for his graphics arts work, and Mr. Samuel Jones for supplemental SEM work, all of NIST.

5. References

- [1] D. Nyyssonen and R. D. Larrabee, Submicrometer Linewidth Metrology in the Optical Microscope, *J. Res. Natl. Bur. Stand. (U.S.)* **92**(3), 187–204 (1987).
- [2] M. T. Postek and D. C. Joy, Submicrometer Microelectronics Dimensional Metrology: Scanning Electron Microscopy, *J. Res. Natl. Bur. Stand. (U.S.)* **92**(3), 205–228 (1987).
- [3] M. G. Rosenfield, Analysis of Backscattered Electron Signals for X-ray Mask Inspection, Scanning Electron Microscopy SEM/1985/II SEM, Inc., AMF O'Hare, IL 60666, pp. 605–615 (1985).
- [4] M. T. Postek, R. D. Larrabee, W. J. Keery, and E. Marx, The Application of Transmission Electron Detection to X-ray Mask Calibrations and Inspection, *SPIE Proceedings 1464, Integrated Circuit Metrology, Inspection and Process Control V* (1991) pp. 35–47.
- [5] M. T. Postek, R. D. Larrabee, and W. J. Keery, A New Approach to Accurate X-ray Mask Measurements in a Scanning Electron Microscope, *IEEE Trans. Electron Devices* **36**(11), 2452–2457 (1989).
- [6] M. T. Postek, R. D. Larrabee, and W. J. Keery, An Approach to Accurate X-ray Mask Measurements in a Scanning Electron Microscope, *NISTIR 89-4047* (1989) pp. 1–8.
- [7] D. A. Grigg, P. E. Russell, J. E. Griffith, M. J. Vasile, and E. A. Fitzgerald, Probe Characterization for Scanning Probe Metrology, *Ultramicroscopy*, **42-44**, 1616–1620 (1992).
- [8] M. T. Postek, Scanning Electron Microscope-based Metrological Electron Microscope System and New Prototype Scanning Electron Microscope Magnification Standard, *Scanning Microscopy* **3**(4), 1087–1099 (1989).
- [9] IBM Corporation General Technology Division (Burlington, VT).
- [10] M. T. Postek, W. J. Keery, and A. E. Vladar, Modification of a Commercial SEM with a Computer-Controlled Cathode-Stabilized Power Supply, in preparation.
- [11] D. Nyyssonen and M. T. Postek, SEM-based System for the Calibration of Linewidth SRM's for the IC Industry, in *Micron and Submicron Integrated Circuit Metrology*, *Proc. SPIE* **565** (1985) pp. 180–186.
- [12] F. Scire and E. C. Teague, Piezo-Driven 50 Micrometer Range Stage with Subnanometer Resolution, *Rev. Sci. Instr.* **49**, 1735–1740 (1978).
- [13] R. D. Young, Moving Stage Improves Accuracy of Microcircuit Measuring Technique, *Res. Development* **4**, 4–6 (1984).
- [14] G. G. Hembree, A Metrology Electron Microscope System, G. W. Bailey, ed., *Proc. EMSA*, San Francisco Press, CA (1956) pp. 644–645.
- [15] R. R. Baldwin and G. J. Siddall, A Double Pass Attachment for the Linear and Plane Mirror Interferometer, in *Integrated Circuit Metrology*, *Proc. SPIE* **480** (1984) pp. 78–83.
- [16] M. T. Postek, W. J. Keery, and N. V. Frederick, Low-Profile High-Efficiency Microchannel-plate Electron Multiplier Detector for Scanning Electron Microscopy Applications, *Rev. Sci. Instrum.* **61**(6), 1648–1657 (1990).
- [17] Mr. Leon Carroll of the NIST Precision Engineering Division.
- [18] The Isaac system is based on an Apple Macintosh II fx computer equipped with 8 MB RAM, two (1.2 & 1.44 MB) floppy drives, a 200 MB hard disk, a 650 MB magneto-optical drive, a Sharp JX-320 Color scanner (max. 600 × 600 dpi and 256 gray level resolution), and an Apple LaserWriter II printer.
- [19] Perceptics Co., P.O. Box 22991 Pellissippi Parkway, Knoxville, TN 37933-0991. The PIXEL PIPELINE is a full size NuBus board with four independent, software controlled, RS 170 or PAL standard inputs.
- [20] Signal Analytics Co. 374 Maple Ave. East Suite #204, Vienna, VA 22180.
- [21] Wayne Rasband, National Institutes of Health Building 36 2A03, 9000 Rockville Pike, Bethesda, MD 20892 (Internet, BitNet: wayne@helix.nih.gov).
- [22] EG&G Judson, 221 Commerce Drive, Montgomeryville, PA 18936.
- [23] Hamamatsu, 360 Foothill Road Box 6910, Bridgewater, NJ 08807-0910.
- [24] Burr Brown, P.O. Box 400, Tucson, AZ 85706.
- [25] R. L. Myklebust, D. E. Newbury, and H. Yakowitz, NBS Monte Carlo Electron Trajectory Calibration Program, K. Heinrich, D. Newbury, and H. Yakowitz, ed., *Natl. Bur. Stand. (U.S.) Special Publication 460* (1976) p. 105.
- [26] L. Curgenvan and P. Duncumb, Simulation of electron trajectories in a solid target by a simple Monte Carlo Technique, Tube Investments Research Laboratories, Report No. 303, Hinxton Hall, Saffron Walden, Essex, England (1971).
- [27] L. Reimer, *Scanning Electron Microscopy, Physics of Image Formation and Microanalysis*, Springer-Verlag, NY (1985).
- [28] N. F. Mott and H. S. W. Massey, *Theory of Atomic Collision*, Oxford University Press, London, England (1965).
- [29] H. A. Bethe, Zür Theorie des Durchganges Schneller Korpuskularstrahlen durch Materie, *Ann. Phys.* **5**(5), 325–400 (1930).
- [30] Mr. Chris Evans of the NIST Precision Engineering Division.

About the authors: Michael Postek is a physical scientist and the project leader for scanning electron microscopy metrology in the Microelectronics Dimensional Metrology Group of the Precision Engineering Division at NIST. His main interest is the development of

dimensional standards for the scanning electron microscope. Jerry Lowney is a theoretical physicist in the Semiconductor Electronics Division specializing in electron interactions in solids. Andras Vladar is an electrical engineer and Guest Scientist from the Research Institute for Technical Physics of the Hungarian Academy of Sciences currently working in the Microelectronics Dimensional Metrology Group. William Keery, now retired from NIST, is an electronics engineer and currently a Guest Scientist in the Microelectronics Dimensional Metrology Group. Egon Marx is a theoretical physicist in the Surface and Particle Metrology group of the Precision Engineering Division specializing in electromagnetic theory and optical and electron scattering theory. Robert Larrabee is the Group Leader of the Microelectronics Dimensional Metrology Group. This group has the responsibility for submicrometer SEM and optical metrology and the supporting standards. The National Institute of Standards and Technology is an agency of the Technology Administration, U.S. Department of Commerce.

Interlaboratory Study on the Lithographically Produced Scanning Electron Microscope Magnification Standard Prototype

Volume 98

Number 4

July–August 1993

Michael T. Postek, Andras E. Vladar, Samuel N. Jones, and William J. Keery

National Institute of Standards and Technology,
Gaithersburg, MD 20899-0001

NIST is in the process of developing a new scanning electron microscope (SEM) magnification calibration reference standard useful at both high and low accelerating voltages. This standard will be useful for all applications to which the SEM is currently being used, but it has been specifically tailored to meet many of the particular needs of the semiconductor industry. A small number of test samples with the pattern were prepared on silicon substrates using electron beam lithography at the National Nanofabrication Facility at Cornell University. The structures were patterned in titanium/palladium with maximum nominal pitch structures of approximately 3000 μm scaling down to structures with minimum nominal pitch of 0.4 μm . Eighteen of these samples were sent out to a total of 35 university, research, semiconductor and other industrial laboratories in an interlaboratory study. The purpose of the study was to test the SEM instrumentation and to review the suitability of the

sample design. The laboratories were asked to take a series of micrographs at various magnifications and accelerating voltages designed to test several of the aspects of instrument performance related to general SEM operation and metrology. If the instrument in the laboratory was used for metrology, the laboratory was also asked to make specific measurements of the sample. In the first round of the study (representing 18 laboratories), data from 35 instruments from several manufacturers were obtained and the second round yielded information from 14 more instruments. The results of the analysis of the data obtained in this study are presented in this paper.

Key words: calibration; linewidth; lithography; magnification; pitch; scanning electron microscope; SEM; standard.

Accepted: March 8, 1993

1. Introduction

NIST is in the process of developing a new low accelerating voltage SEM magnification calibration reference standard [1]. This standard will be useful for all applications to which the SEM is currently being used, but it has been specifically tailored to meet many of the particular needs posed by the semiconductor industry. These needs have been outlined previously [2] but, specifically, include the need of the industry for sub-half micrometer cali-

bration structures that are able to be used to calibrate the instrumentation at low accelerating voltages. The standard must be able to be inserted into and be used on the dedicated on-line wafer inspection instruments. The current NIST SEM magnification standard, Standard Reference Material (SRM) 484 was not designed for this purpose and does not meet all of these fundamental semiconductor industry needs. It should be noted, how-

ever, the new standard is not intended to replace SRM 484 but to supplement it where the need exists. The overall characteristics of the new prototype standard have been published previously [1,2] and since this description and proof of concept were published, work has been done to have this sample fabricated in bulk quantities. For this interlaboratory study, a number of test samples were contracted by NIST to be fabricated on silicon substrates using electron beam lithography at the National Nanofabrication Facility (NNF) at Cornell University. The prototype samples were patterned in titanium/palladium with maximum nominal pitch structures of approximately 3000 μm scaling down to structures with minimum nominal pitch of 0.4 μm (Fig. 1). It was necessary for the samples (for this study) to be fabricated in the titanium/palladium and at a larger minimum pitch geometry (0.4 μm) than the originally desired 0.2 μm minimum pitch because of processing limitations at the NNF when this batch of samples was made. This compromise was not deemed a limitation to the interlaboratory study since the main purpose of the study was to have the pattern design reviewed in order to determine if any instrument specific modifications should be made to the pattern. Eighteen of the samples were sent out to a variety of university, research, semiconductor, and other industrial laboratories. This was done in two rounds since there were two sets of patterns

available for testing on each sample. Thus, data were obtained from a total of 49 instruments.

This study is referred to as an interlaboratory study rather than a "round robin" because multiple test samples were used. The purpose of the study was to test the instrumentation and to determine the suitability of the sample design. The laboratories chosen were asked to submit to NIST a series of micrographs at specific magnifications and accelerating voltages designed to test several aspects of instrument performance related to SEM operation and metrology. If the instrument in the laboratory was used for metrology, the laboratory was also asked to make specific measurements of the sample.

2. Materials and Methods

2.1 Scanning Electron Microscopes

Imaging and measurements, for this work, were done by the participants on a variety of instrument types. The list of instrumentation is shown in Table 1, however; the performance of the instruments, as well as, the participants in the study will remain anonymous. This cross section of SEMs represented instruments as old as 15 years to modern instrumentation. Sample inspection and comparison work supporting this study at NIST was done with a Hitachi S-4000 field emission scanning

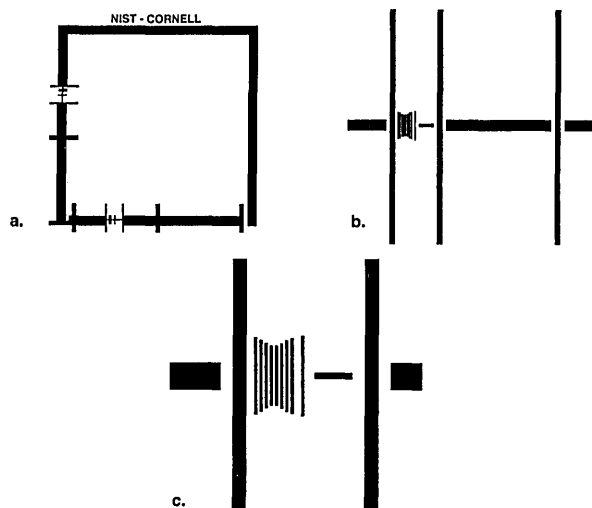


Fig. 1. Drawings of the NIST prototype SEM pattern as written by the electron beam writing system for this study. (a) 1 mm pattern. (b) Medium magnification pitch pattern. (c) Highest magnification pitch pattern showing the 0.4 μm pitch. The large 3 mm pattern is not shown.

Table 1. List of instruments

<u>AMRAY</u>	<u>HITACHI</u>	<u>JEOL</u>
1000B	S-800 (3)	JSM-35 CF
1610	S-4000 (2)	T-330 A
1645 (2)	S-4100 (1)	JSM 848 A(2)
1850 FE	S-7000 (3)	JSM IC 845 (3)
1860 FE	S-6820	JSM 840 FE(2)
1880 FE	S-6100	JSM 6400 FE (2)
<u>BIORAD</u>	S-6000 (5)	JSM 6400
800 FE	S-6600	JSM 5400
	S-900	
<u>Cambridge</u>	<u>TOPCON (ISI)</u>	<u>NANOMETRICS</u>
S-200 (3)	CC-CD	Cwikscan III
S-250	DS-130 FE	<u>PHILIPS</u>
	DS-130	XL-30
<u>ETEC</u>		
OMNISCAN		

electron microscope (FESEM).¹ Measurements of the video signal were done on the FESEM using the beam scanned mode because the NIST metrology instrument [2] was unavailable during much of this study since being specially modified and equipped for x-ray mask measurements [3].

A limited amount of sample data was obtained from the NIST metrology instrument. The instrument was used in the stationary beam, sample scanned mode of operation described previously [2] with new software and hardware modifications [3]. For this work, the electron signal was collected using a solid state backscattered electron detector at high accelerating voltage (30 kV) and the measurement data were taken in the backscattered electron detection mode [4].

2.1.1 FESEM System The prototype samples were sent out to the participants of the first round without initial SEM inspection in order to minimize any initial sample contamination. Upon their return, the samples were mounted on standard specimen stubs and carefully inserted into the Hitachi S-4000 instrument. Each sample was viewed at low accelerating voltage in order to assess the contamination level on the surface. The sample was then measured and photographed at high accelerating voltage. The image was also taken and stored in the "Isaac" System (described below) for image analysis. Any sample with excessive contamination was not sent out in the second round.

The FESEM was accurately calibrated using NIST SRM 484 at high accelerating voltage (20 keV) with a procedure developed at NIST using the Hitachi keyboard measurement system accessory. Adjustment of this instrument resulted in a calibration $\pm 1\%$ of the certified value for SRM 484 as shown in Fig. 2.

Unfortunately, with the instrument currently equipped, any imaging or measurement data were unable to be directly transferred to an ancillary computer system for image analysis. This transfer was necessary in order to analyze all the data (participants data and NIST data) in the same manner using the same algorithms. This necessitated the development of the system described below.

¹ Certain commercial equipment, instruments, or materials are identified in this paper to specify adequately the experimental procedure. Such identification does not imply recommendation or endorsement by the National Institute of Standards and Technology, nor does it imply that the materials or equipment identified are necessarily the best available for the purpose.

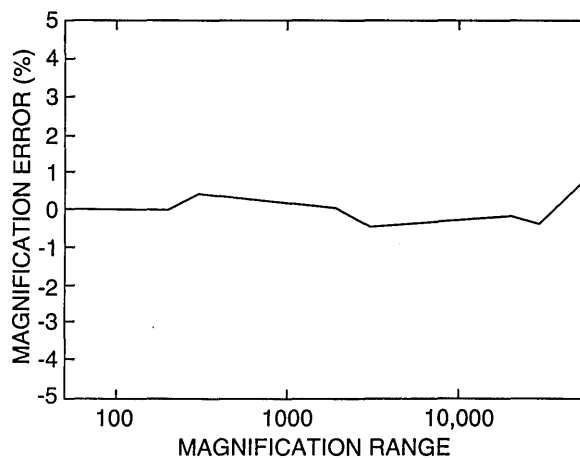


Fig. 2. Plot of the magnification calibration error of the NIST SEM as related to the certified SRM 484 value.

2.1.2 "Isaac" Image Analysis System A computer based measurement system christened "Isaac" was developed to analyze the SEM images from the Hitachi S-4000 FESEM, as well as other "scanned-in" or digitally obtained data.

Hardware This system is based on an Apple Macintosh IIfx computer [5]. The images are captured with a high speed frame grabber, PIXEL PIPELINE card [6]. The video signal for the Isaac system is grabbed at TV frequency from the SEM (512×512) or scanned at 600 dots per 25.4 mm (600 dpi) into the computer using the scanner and then stored and manipulated in the computer system. The pixels of both the scanner and the Isaac have been calibrated with accurate NIST certified linear scales. A typical 512×512 SEM digital storage system functions at about 100 DPI. This means that in comparison, the scanned image is operating with about 5 times the pixel density. Barring any "blooming" of the photographic emulsion this provides a highly precise representation of the images submitted by the participants.

Software The software generally used on the system is a commercially available scientific image analysis program called IP Lab Spectrum [7]. The IP Lab Spectrum program also has an extension developed by Signal Analytics in collaboration with NIST specially designed for linewidth or pitch measurements used in this work. The public domain program named "Image" of the National Institutes of Health [8] was also useful in this work. With Image and IP Lab Spectrum, there is the capability to control the frame grabber card, and then use the built-in tools, modifications, pseudo-

colorisation, calculations, measurements and other features. For control of the image scanning the commercially available program "Adobe Photoshop" was used.

Further improvements of both the hardware and the software the Isaac system for higher resolution digitization are currently in progress.

2.2 Experiment

2.2.1 Instrument Conditions Scanning electron microscopes are operated in a variety of manners depending on the laboratory. Some are exclusively low voltage instruments such as many of those used in the semiconductor industry for on-line inspection while others are exclusively high voltage instruments. Many general laboratory instruments operate through both extremes depending on the work to be done. Because of the variety of participants chosen for this study several experimental possibilities were offered. The participants were asked either to do the high accelerating voltage set of micrographs, a low accelerating voltage set of micrographs or both sets of micrographs. The instrument was expected to be operating with conditions optimized for the chosen operation range. All of the micrographs and/or measurements were to be done at 0° tilt (normal incidence to the electron beam).

2.2.2 Accelerating Voltage All micrographs or measurements were to be made at nominal (what the instrument indicates) 1 and 5 kV for the low accelerating voltage set and nominal 10 and 30 kV for the high accelerating voltage set.

2.2.3 Magnification Ranges Example micrographs of the requested pattern sites at the magnifications requested were provided for each accelerating voltage set. The eight magnification ranges established are shown in Table 2. These ranges were chosen to demonstrate the decade

magnification calibration of the instruments [2] and the two sets of accelerating voltage were chosen to demonstrate any magnification variation due to failure of the instrument compensation system to correct for changes in accelerating voltage. Lens hysteresis effects on the magnification would be minimized, in this particular study, if the participants followed the directions provided and worked from low accelerating voltage to high accelerating voltage and not the converse.

If the instrument was not able to operate at the higher accelerating voltages (5 kV and above), such as in the newer wafer inspection instruments, the participant was asked to do the 1 kV work and then use the highest accelerating voltage available (i.e., still provide two sets of data). Since performance between the various classes of instruments varied, it was fully understood and appreciated that some instruments were not capable of doing all of the experimental magnifications requested (i.e., an instrument equipped with a tungsten filament would not be expected to provide a good Range 8 or 100 000× micrograph at 1 kV). All the participants were requested to provide the best quality micrographs for the evaluation.

2.2.4 Measurement System If the instrument was equipped with a linewidth type measurement system the participants were asked to provide a hardcopy of the measurement data for each micrograph and wherever possible an ASCII dump of the data for NIST analysis on disk (IBM or Macintosh compatible).

2.3 Prototype Standard

2.3.1 Magnification Standards Currently, the only certified magnification standard available for calibration of the magnification of an SEM is NIST SRM 484. SRM 484 is composed of thin gold lines separated by layers of nickel providing a series of pitch structures ranging from nominally 1 to 50 μm [9] (depending on the version). This standard is still very viable for many SEM applications. Certain limitations presented by this standard for the semiconductor industry have been published previously [2]. The prototype standard in this test was designed to minimize or eliminate the limitations of SRM 484 for calibration of instruments used in the semiconductor industry. Since this was an interlaboratory comparison study and not the issuance of a standard, the samples were carefully measured only in the FESEM using beam scanning mode and the images acquired into the Isaac system in slow scan mode. The FESEM (and the Isaac) was calibrated accurately in slow scan mode

Table 2. Magnification ranges

Magnification range	Nominal magnification	Measured pitch dimension (μm)
1	60×	500
2	600×	50
3	2000×	25
4	6000×	10
5	15 000×	5
6	30 000×	2.5
7	50 000×	1.2
8	100 000×	0.8

using the NIST SRM 484 at high accelerating voltage. This provided a computed calibration error for the SEM in the “X” direction of only about $\pm 1\%$ as compared to the certified measurements on SRM 484 (Fig. 2). This error could be reduced by finer steps in the electronics of the magnification calibration system. All the comparison measurements of the participant’s samples were made at the same FESEM calibrated accelerating voltage and working distance. Measurement with the FESEM of the samples returned to NIST using this procedure resulted in a measurement precision with a standard deviation of no greater than about +1 pixel width over the entire measurement range (Fig. 3). Each new standard, when issued, will be individually calibrated using the NIST metrology SEM thus providing a certified, NIST traceable measurement of the spacing (or pitch) between the various lines making up the standard.

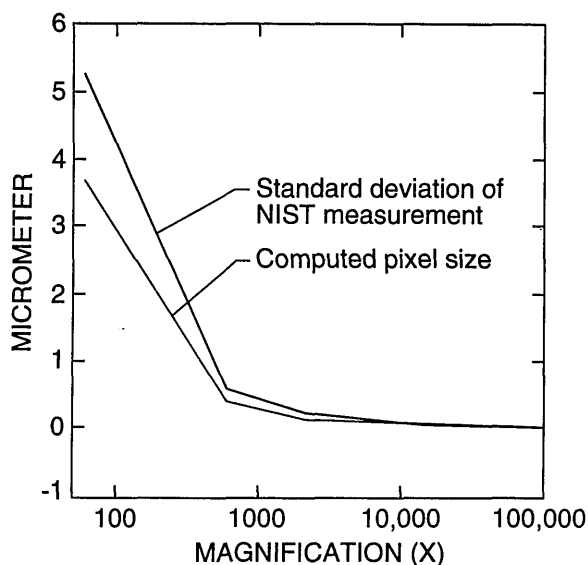


Fig. 3. Plot of the standard deviation of the NIST instrument measurement of all the samples successfully returned to the computed pixel size relative to the magnification ranges surveyed.

2.3.2 Measurement Criteria Most modern scanning electron microscopes provide an alphanumeric display of the magnification and a micrometer bar on the viewing screen. These data are also recorded on the micrograph. Measurement data are obtained directly from the image, the micrograph (as a unit) or from a digital measurement system. The confidence we can place on the accuracy of those readouts depends upon

many factors—the main one being magnification (column scan) calibration. The semiconductor industry today, relies greatly upon the measurements made in scanning electron microscopes to control million dollar process lines. However, the correctness of the answer to the question of “How big is it?” relates directly to two major factors in the SEM, as well as a whole host of lesser factors [10]. The first and foremost factor is the accurate magnification calibration of the SEM. Magnification, in an SEM, is essentially defined as the ratio between the area scanned by the electron beam on the specimen to the area displayed or photographed or measured. It is imperative that the distance being scanned by the electron beam be accurately calibrated.

The second factor relating to SEM measurements is the effect on the image induced by the electron beam/specimen interaction. This factor cannot be ignored. Fortunately it can be minimized by the use of a “pitch” type magnification calibration sample, such as SRM 484, or this new standard when it is issued. These standards are both based on the measurement of “pitch.” A pitch is the distance from the edge of one portion of the sample to a similar edge some distance away from that first edge (Fig. 4). In Fig. 4, a measurement of the pitch would be the distance from A to C or from B to D. In a pitch standard, that distance is certified and it is to that certified value that the

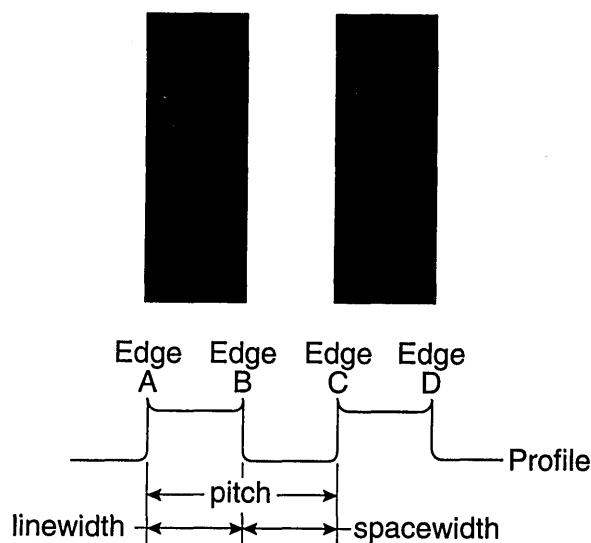


Fig. 4. Graphic comparison between the measurement of pitch and width. Measurement of A to C or measurement of B to D defines the pitch of the sample. Measurement of A to B or C to D defines the linewidth of the sample and measurement of B to C defines the spacewidth.

magnification calibration of the SEM is set. If we consider two lines separated by some distance, the measurement of the distance from the leading edge of the first line to the leading edge of the second line defines the pitch. Many systematic errors included in the measurement of the pitch are equal on both of the leading edges; these errors, including the effect of the specimen beam interaction, cancel. This form of measurement is therefore self-compensating. The major criteria for this to be a successful measurement is that the two edges measured must be similar in all ways. SEM magnification can be easily and accurately calibrated to a pitch using SRM 484, the NIST certified magnification calibration standard or this standard when issued.

The measurement of a width of one of the lines, on the other hand, (A to B or C to D on Fig. 4), is complicated in that many of the errors (vibration, electron beam interaction effects, etc.) are now additive. Therefore, errors from both edges are included in the measurement. SEM magnification should not be calibrated to a width measurement since these errors vary from specimen to specimen due to the differing electron beam/sample interaction effects. Effectively, with this type of measurement we do not know the accurate location of an edge in the video image and more importantly it changes with instrument conditions (this can be seen later in Sec. 3.4). The determination of the edge location requires electron beam modeling of the interactions occurring both in the sample and the specimen chamber, as well as, modeling of the electron collection. This is the ultimate goal of this program and recently has been shown to be successful for special samples such as x-ray masks measured in the SEM [3].

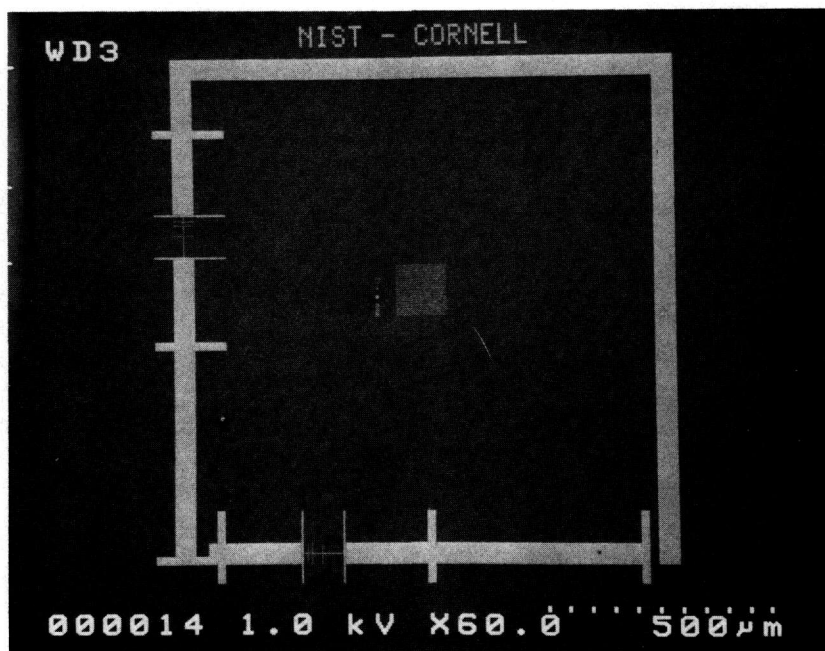
2.3.3 “X” and “Y” Magnification Calibration The “X” and the “Y” scans of an SEM must be independently calibrated in order that round objects appear round and square objects appear square. That is to say, measurements of a defined pitch in the X direction must agree with measurements of the same structure (physically rotated by 90°) in the Y direction. For this study, all measurements were to be made in the “X” direction. The first group of participants were only concerned with the pattern located in the “X” direction. Therefore, no direct determination of the squareness of the X to Y calibration was done by the participants. However, these data could be obtained from the lowest magnification images supplied (see Sec. 3). The pattern in the “X” direction is defined as the one parallel to the NIST-CORNELL label

(see Fig. 1). The second group using the same samples were asked to measure the features located in the “Y” direction which is perpendicular to the label (since these presumably had not been contaminated by previous scans), but measured in the “X” direction by inserting the pattern and physically rotating it into position.

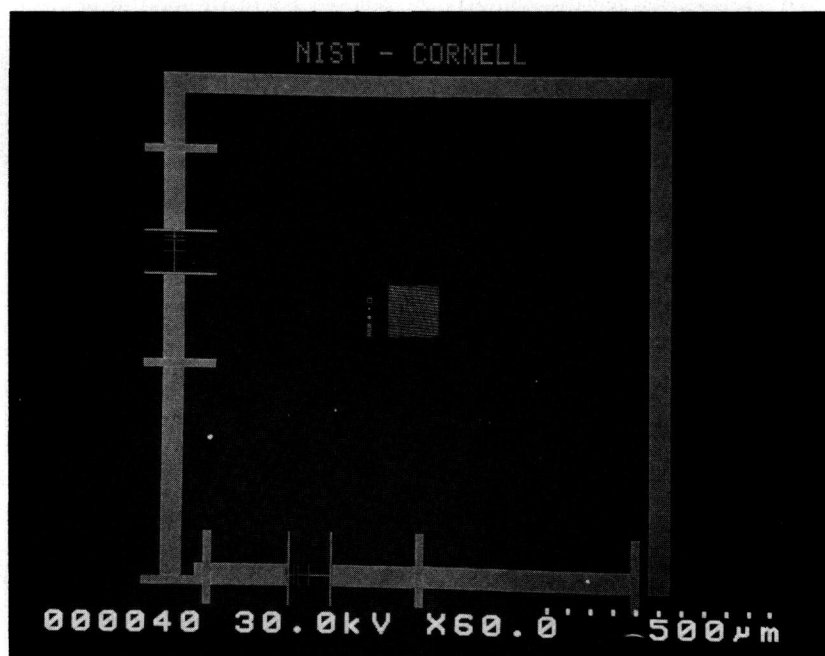
2.3.4 Sample Materials The NIST sample was lithographically produced with an electron beam at the National Nanofabrication Facility at Cornell University. This sample was composed of titanium (10 nm) and palladium (50 nm) for a nominal thickness of about 60 nm on a standard silicon wafer. Future samples will be fabricated of the preferred heavy metal silicide. The sample works well at both high and low accelerating voltages (Fig. 5).

2.3.5 Pattern The prototype sample is composed of a large, approximately 3 mm (nominal) outer pattern and a smaller 1 mm inner pattern. Embedded in the smaller pattern is an array of calibration lines (Fig. 1) reducing in pitch, in steps, to a nominal 0.2 μm pitch. The large pattern is used to calibrate the SEM in the lower decades of the magnification range; whereas, the smaller patterns (as shown in Fig. 1) are used for the upper decades. Various combinations of these patterns might be used in a typical instrument calibration (Table 2). For a full instrument calibration of most instruments, several measured pitches of various structures would be used from the calibration sample. For the full range of magnifications to be properly calibrated, several steps progressing from low magnification to high magnification may require adjustment first—then the offset calibrated at a high magnification step. This procedure will vary with the instrument design. The current prototype sample has calibration patterns written in both the “X” and the “Y” directions in order to permit the full calibration of the X and the Y scans of the SEM without physical sample rotation. Raster rotation is not a proper procedure for use during magnification calibration because this circuitry can, in some instances, distort the X and the Y scans.

The NIST prototype sample was designed for use in the standard “post-lens type” SEM where the sample is found below the lens. This is typical of most laboratory and many production instruments. Special “in-lens type” SEMs where the sample is inserted into the final lens, generally require smaller samples since the available space within the lens is quite restricted. The prototype sample was viewed in one in-lens type instrument, but, the placement of the sample within the instrument



a



b

Fig. 5. NIST prototype SEM magnification sample. (a) Low accelerating voltage image at 1 kV. (b) High accelerating voltage image at 30 kV.

required breaking the sample into a smaller piece. For the in-lens type instruments, future versions of this magnification sample could be made having only the inside 1 mm calibration pattern. This would significantly reduce the size and would not compromise the calibration function since low magnification operation (where calibration using the larger 3 mm pattern is needed) in these microscopes is not possible.

Included in the center of the 1 mm pattern, is a matrix of small crosses used to focus and correct the astigmatism of the electron beam. These structures are used for instrument set-up; then the field is moved over to the actual pattern for the final measurement work (Fig. 6).

2.3.6 Sample Mounting The NIST sample was pre-diced from the wafer into approximately 12 mm squares each holding a single complete pattern. For standard inspection or research-type SEMs, the sample was mounted, with carbon-based adhesive, on any platform or stub required by the particular instrument.

Mounting of the sample for the new dedicated wafer inspection instruments presented a slightly more difficult problem. Placement of the sample on the surface of a wafer the proper size for the instrument was acceptable if the added thickness of the NIST sample did not compromise the working distance/magnification compensation system of the instrument. This means that if the instrument expects the wafer to always be at a certain working distance for focus (and therefore magnification compensation and computation) it may not be able to accommodate the difference in the magnification resulting from the added thickness of the specimen/wafer. If there was any question, the participants were asked to contact the SEM manufacturer. Alternatively, a specially prepared sample was inserted into a conductive 150 mm (6 in) wafer, flush with the surface. This sample holder was made available to the participants upon request.

2.3.7 Specimen Contamination It was inevitable that the samples would become contaminated from handling and from the vacuum system of the instrument. Sample contamination is especially troublesome at low accelerating voltages. Therefore, those participating in the low accelerating voltage aspects of the study were asked to make the low accelerating voltage micrographs first (starting at low magnification) and then work up in the proper steps to the high accelerating voltages and magnifications. In order to minimize contamina-

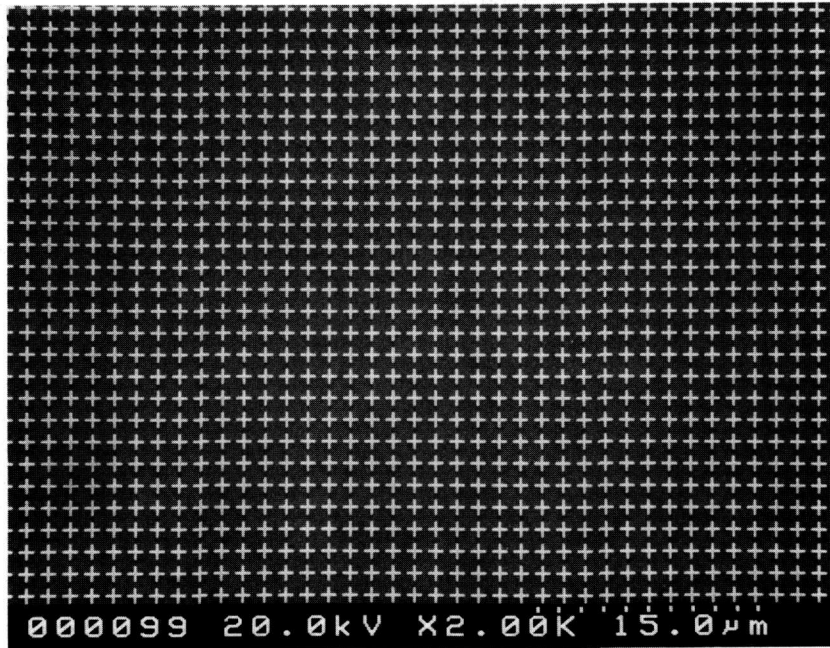
tion during the inspection phase, the NIST FESEM was equipped with a special liquid nitrogen cold trap and a nitrogen leak system.

3. Results

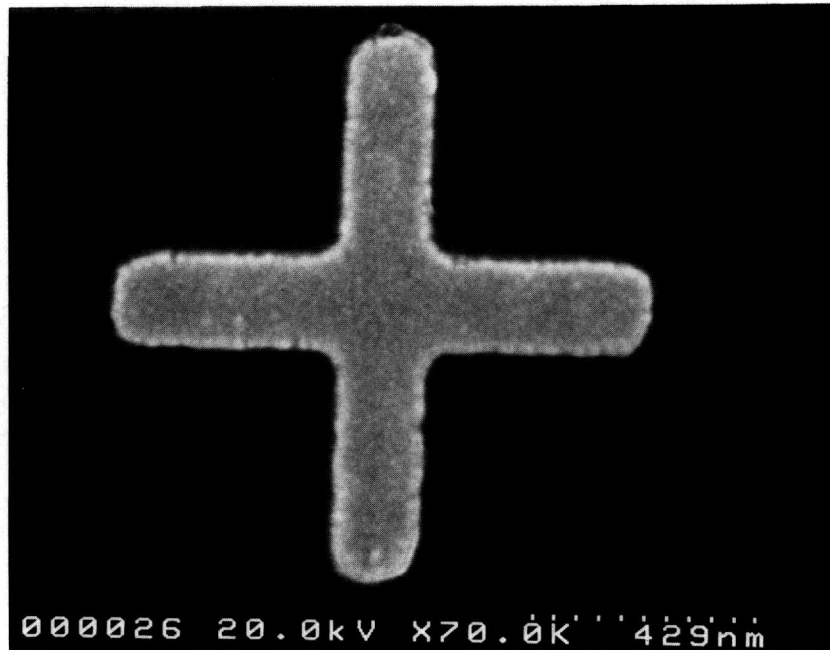
The participants of the study provided NIST with micrographs and data in several formats. In some instances the data were supplied in as varied media as "instant" film, video prints and optical disks. Except for the digital storage (which may have its own artifacts in the form of digitization noise), it is fully understood that the recording of the data in these formats can introduce artifacts. For example it is reasonably well known that "instant" film can shrink and change dimensions during the development process. However, it was necessary to work with the data and media provided. This is also sensible since, in common operation, many important conclusions are based on the same type of data format.

Two major studies were done on the data submitted. The first was an analysis of the μm marker length to the measured image of the prototype sample from the micrograph. Depending upon the magnification range, a pitch structure of some dimension was available in the micrograph, for measurement and comparison (Table 2). The second study was a comparison of the measured image to the NIST (FESEM) measurements of the same structure on the same sample.

There are three fundamental calibrations that alter either the SEM magnification or the apparent magnification for many "laboratory" scanning electron microscopes. These calibrations, therefore, have direct bearing upon the results of this study. The first and foremost is the adjustment of the X and Y column scans. This adjustment is often done manually with calibration potentiometers at the board level by the field service engineer to some type of standard. In the more modern instruments, some of these adjustments may be under software control but usually there is at least one manual potentiometer adjustment. This adjustment sets the column scans (i.e., magnification); and this adjustment is often, but not always performed in decades, such as: lowest magnification to $250\times$; $260\times$ to $2500\times$ and so on throughout the range. The transition between decades must be made as smooth as possible within the adjustability of the potentiometer or software step. Otherwise gross or "sawtooth" jumps in magnification can be seen as



a



b

Fig. 6. Focus and astigmatism correction structures located in the center of the 1 mm pattern
(a) Low magnification. (b) High magnification.

the magnification is increased or decreased (Fig. 7). For the decade transition to be smooth, measurement of the pitch of a defined structure at the high end of the lower decade (i.e., $2400\times$) should equal the pitch measurement of the same defined structure at the low end of the next decade (i.e., $2500\times$). The graphical magnification data from the participants shown here in this report would best be represented as decade jumps—if the transition points were known for all instruments. Unfortunately, this information is not known for all the instruments, so the data are plotted with a line connecting the points. Thus, any large jumps in magnification between data points are not emphasized.

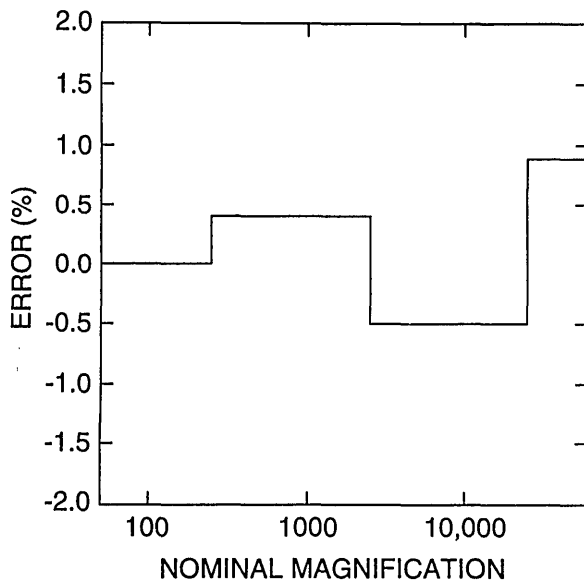


Fig. 7. Schematic plot of the decade magnification of an SEM showing a distinct transition between the decade points leading to large jumps in the magnification at the transition points when miscalibrated.

The standards used for the calibration of the instruments used by the participants in this study were quite varied. By far the majority (over 50%) used NIST SRM 484 but other “standards” included: latex spheres, in-house standards, and copper transmission electron microscope grids. Of course, some participants used no standards or did not know if their instrument was calibrated to a standard sample.

The ratio of the calibration measurement of the X to the Y scan should be 1:1. Deviation from this relationship makes round structures appear oblong and square structures appear rectangular. In this paper, this characteristic is referred to as the

squareness of the image. This definition does not take into account any other factors that could also distort the image such as pincushion distortion or skew. A measurement of the X and the Y magnification calibration was obtained from the lowest magnification images ($60\times$) provided by the participants. Figure 8 shows the results of that measurement. Plotted is the measured error (%) from the expected value for both X and Y. Few instruments involved in this study had the X to Y ratio at (or even near) the desired 1:1. A perfect calibration would fall in the center of the graph (0,0). It is apparent that at low magnification, the basic calibration of the squareness of an SEM is inadequate. One reason for this problem is that it is very difficult to match the proper X and Y potentiometer settings due to insensitivity (coarseness) of the adjustment potentiometers. A second problem is that the calibrated lines of NIST 484 are too small to be used to adjust the low magnifications and no large pitch dimension is available. Therefore, a secondary calibration standard such as a transmission electron microscope grid is often used for the low magnification calibration. This is why the approximately 3 mm low magnification pattern was included in the new prototype standard used in this study.

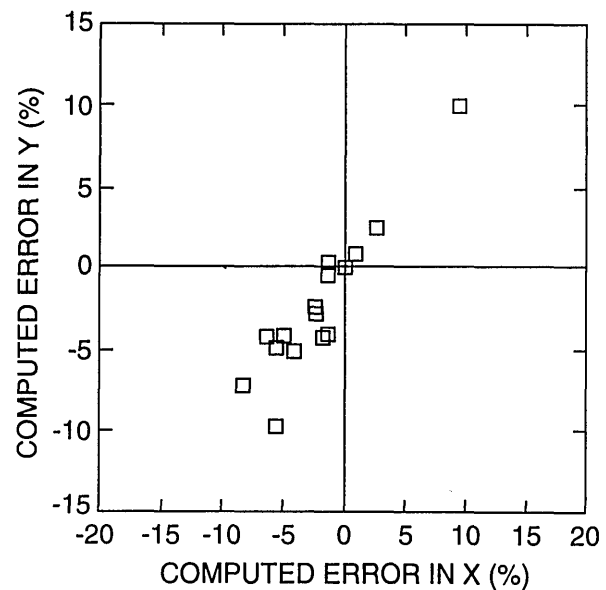


Fig. 8. A plot of the measurement of the X and the Y magnification calibration error for high accelerating voltage operation obtained from the low magnification images. Plotted is the computed error (%) from the expected value for X plotted against the computed error (%) from the expected value for Y. Perfect X and Y calibration would place the boxes representing the data points in the center of the graph (0,0).

The second calibration of interest is the adjustment of the photographic CRT. Since, for many laboratory SEMs, the final record is the micrograph, the calibration of the photographic CRT is critical. The major calibration of the photographic CRT is associated with the adjustment of the alphanumeric especially the micrometer marker. The micrometer marker is generally the measurement fiducial used by the recipient of the micrograph to determine the size of structures in the micrograph. Even if the column scan calibrations are correct, erroneous measurement data can be generated if the micrometer marker is incorrectly calibrated. Figure 9 shows a micrograph where the micrometer marker (represented as a series of small white squares) has been adjusted to be exactly 30 mm in pitch from the left edge of the far left block to the left edge of the far right block. Based upon this, the length of that marker should be equal to 600 nm at a correctly calibrated magnification of $50\,000\times$. This adjustment was very accurately done using the Isaac system, but field service engineers do not have the availability of such systems for calibrations on-site in most SEM laboratories.

The third calibration step is the adjustment of the visual CRTs so that the image viewed and focused is reasonably equivalent to the photographed

image. This calibration has no bearing upon the column magnification per se but is aesthetically necessary so that the visual image field that the SEM operator sees is equivalent to that which is photo-graphed.

The dedicated "linewidth measurement" instruments or those with linewidth measurement computer systems also have an added calibration in the software of the measurement function. This places a user defined "offset" or "correction" factor into the system. This offset can be determined from measurement of an internal standard, NIST standard or even the pitch of the actual device. Unfortunately, this offset usually does not effect the actual column scans or any of the above mentioned calibrations—only the "computer" measurement made directly with that system. Therefore, digital measurements made with the computer system may be relatively correct, but micrographs taken with that system may be out of calibration by several percent. This software adjustment is really a point calibration in that it is usually done in the decade where the measurement is to be made. Erroneous results can also occur if the magnification is changed from that "calibrated" decade without rechecking the point calibration for that new decade.

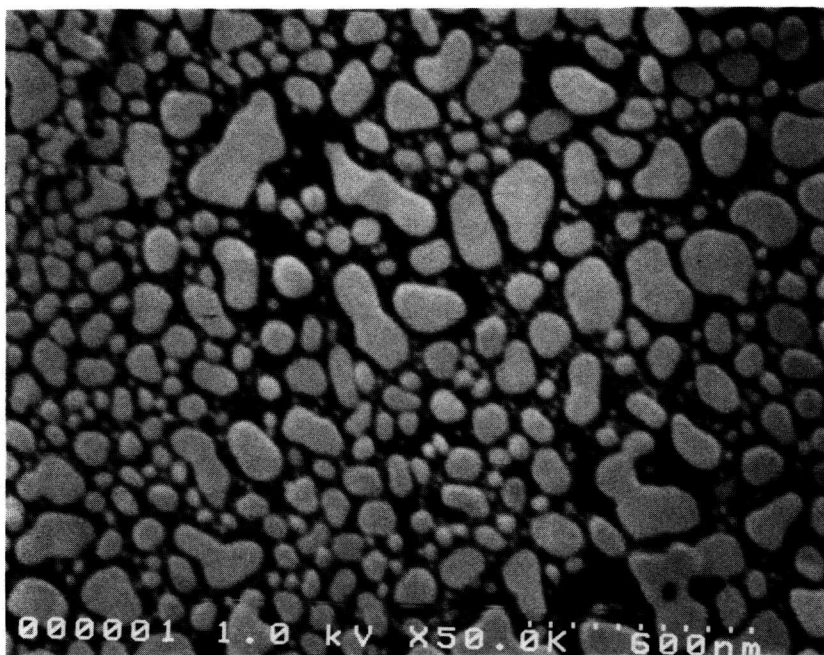


Fig. 9. Micrograph showing the calibrated μm marker represented here as series of small white squares. The pitch between the first and the last square represents 600 nm, as discussed in the text. (Reductions during the publication process may change the value.)

3.1 Image Magnification/Micrometer Marker

Overall, all the SEMs involved in this study demonstrated some error in the adjustment of the micrometer bar. This is a very difficult adjustment to make since it is made directly from the micrograph, often from a relatively short fiducial line (often 10-30 μm in length). Box plots of the percent error demonstrated by all the instruments of this study relative to the magnification range (for all accelerating voltages reported) are shown in Fig. 10a. The box of the plot shown encompasses the 25th through the 75th percentiles of the data. The lines making up the box plot represent the 10th, 25th through 75th, and the 90th percentiles. Data of either the 5th and 95th percentiles are shown as a symbol (0) above or below the 10% and 90% lines. The mean of the error of these measurements was 2.23% with a standard deviation of $\pm 13.01\%$. The individual means and standard deviations for each magnification range are shown in Fig. 10b. Where these data are concerned, it could be argued that statistically, the mean may not be the most appropriate description since the distribution is nonsymmetric. But, for this study, the mean has been adopted since it is the most common manner to describe this type of data. It should be understood that the calibration of the micrometer bar is extremely important because even if an SEM is properly calibrated for the column scan magnification, measurement results can be in error if they are obtained from a comparison to a miscalibrated micrometer bar. In general, this represents a slight offset (either positive or negative) to the NIST measurements (discussed below) depending upon how far the micrometer bar calibration is miscalibrated (Fig. 11).

3.2 Image Magnification/ NIST Measurements

NIST SRM 484 has an uncertainty of about 0.05 μm for the nominal 1 μm pitch or about 5%; therefore, for these comparisons a +5% upper tolerance (UT) and a -5% lower tolerance (LT) was established leading to an overall 10% possible "acceptable" error range. Until recently, SEM manufacturer's specifications for magnification calibration within 10% were considered to be acceptable because no calibration sample better than this was available. With the new SEM magnification prototype sample, sufficient structure is available to test the entire magnification range of most SEMs with a high degree of accuracy.

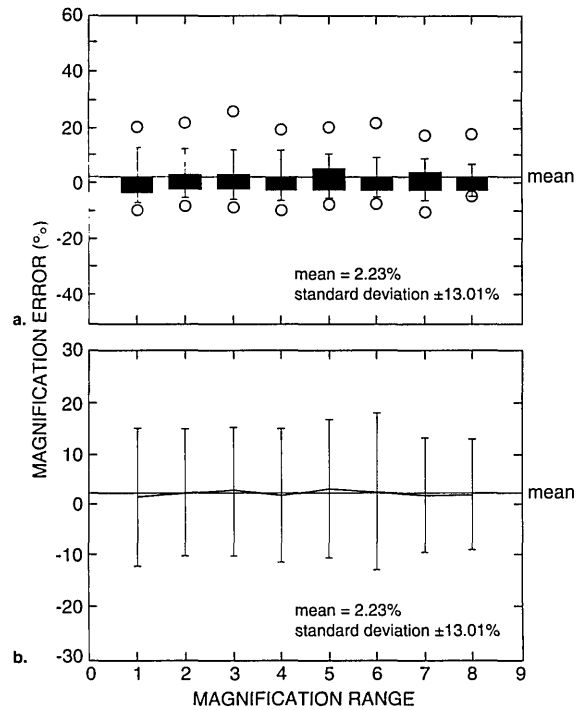


Fig. 10. Micrometer bar error. (a) Box plots and (b) scatter plots of the percent error of the measured structure in the micrograph to the length of the μm bar for the eight magnification ranges, all instruments at all accelerating voltages.

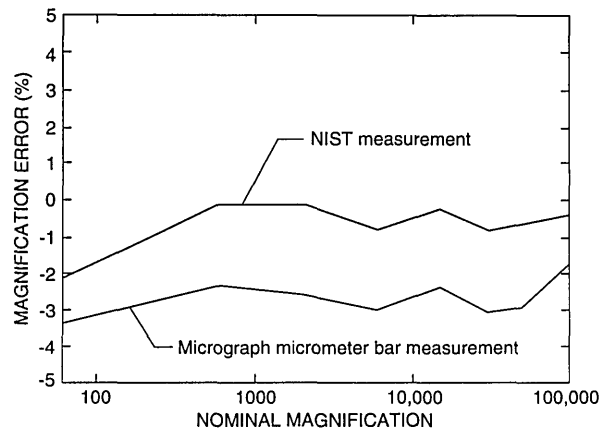


Fig. 11. Micrometer bar error. Plot showing the relationship typical of the error of the micrometer bar measurement to the NIST measurement of the same structure for one set of data.

Data obtained from a new instrument are shown in Fig. 12a. This instrument was recently installed, and it is unlikely that any magnification checks were run on the instrument. This instrument is

demonstrating a systematic offset in magnification of, on average about, +9% up to about 30 000 \times and slightly less error above 30 000 \times . With calibration, a similar model instrument submitted by another participant is shown to be calibrated within about $\pm 1\%$ or well within the above defined “common” specification (Fig. 12b). Differences of sensitivities between the resistors of the decades and care taken during the adjustment procedure still leave some irregularities in the profile, but, this performance compares favorably with the NIST instrument calibration (Fig. 2).

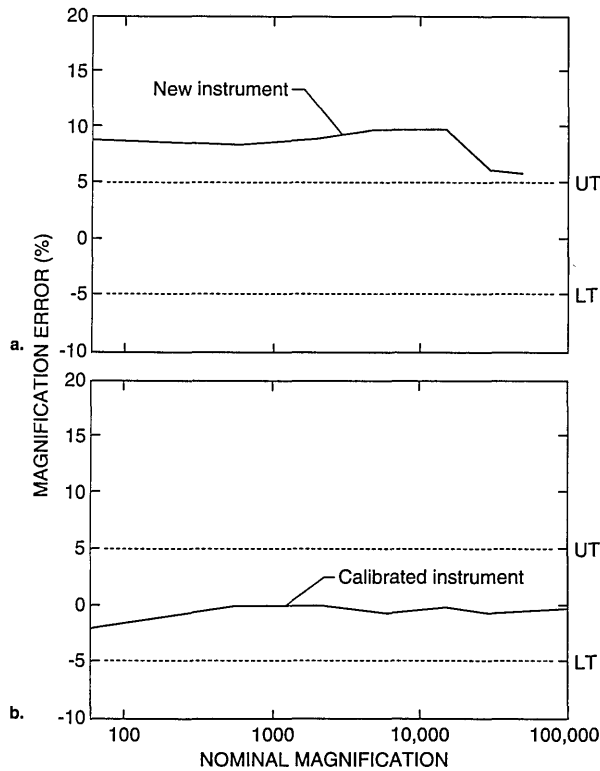


Fig. 12. Magnification calibration. (a) Newly delivered instrument demonstrating the uncalibrated nature of the instrument. (b) Well calibrated instrument of the same model from a different laboratory.

Comparison of the magnification of instruments from a single site can be seen in Fig. 13. Figure 13a shows the results from two instruments from the same laboratory using the same data conditions. From the graph it can be seen that the two instruments vary nearly 10% in magnification from each other. Another site is shown in Fig. 13b where there is a reasonably tight agreement between the four instruments tested and the entire group of instruments generally fell within the acceptable

range. It is apparent from this plot that these four instruments would provide similar results between the range of 1000 \times to about 20 000 \times magnification.

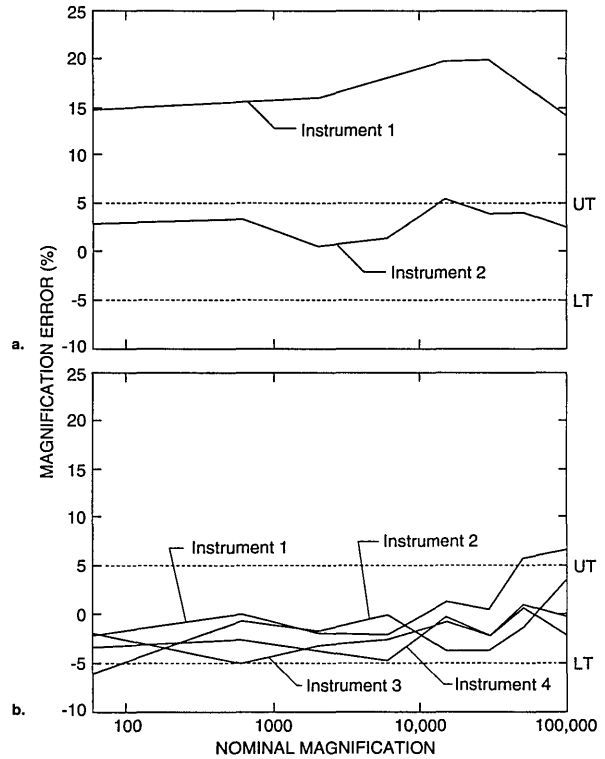


Fig. 13. Comparison of the magnification calibration of instruments from the same site. (a) Site where two instruments are not in agreement with each other. (b) Site where a good deal of agreement exists between instruments.

The graphical representation of the magnification error as compared to the NIST measurements (relative to the magnification ranges for all the instruments tested in this study) are shown in Fig. 14. Figure 14a represents box plots of the magnification error data obtained from all the instruments. In this figure, the mean of the error of these measurements was 1.77% with a standard deviation of $\pm 12.03\%$. The individual mean and standard deviation for each magnification range is shown in Fig. 14b. This figure is directly comparable to the data set of Fig. 10.

The data described above in Fig. 14 can be separated and compared relative to the instrument's accelerating voltage performance, as shown in Figs. 15 and 16. Figure 15a represents box plots of the data obtained from the highest accelerating voltage reported from each instrument. In this figure, the

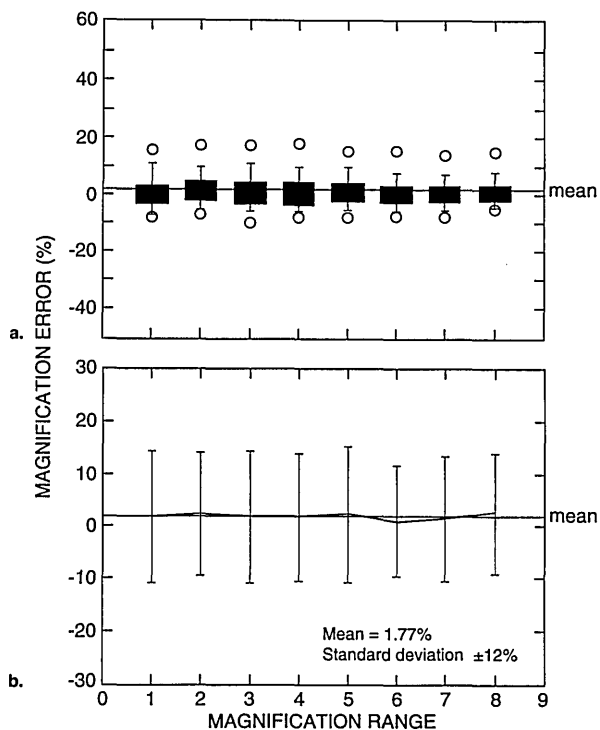


Fig. 14. Magnification calibration error. (a) Box plots and (b) scatter plots of the magnification error for all the ranges as compared to the NIST measurements for all instruments and accelerating voltages.

mean of the error of these measurements was 0.50% with a standard deviation of $\pm 11.67\%$. The individual mean and standard deviation for each magnification range at high accelerating voltage is shown in Fig. 15b. In comparison, Fig. 16a represents box plots of the data obtained from the lowest accelerating voltage reported from each instrument. In this figure, the mean of the error of these measurements was 1.65% with a standard deviation of $\pm 11.21\%$. The individual mean and standard deviation for each magnification range for low accelerating voltage is shown in Fig. 16b. Comparison of these data for high keV operation (Fig. 15) to that for low keV operation (Fig. 16) demonstrates that the error increases overall at the low accelerating voltages. This is expected since NIST SRM 484 is commonly used at high accelerating voltage and no NIST low voltage SEM magnification calibration sample is currently available.

These data can be separated even further in order to determine the magnification calibration performance of the semiconductor industry participants to other non-semiconductor related laboratories. Figure 17 represents the data obtained from semiconductor industry participants and Fig. 18 represents data from other non-semi-

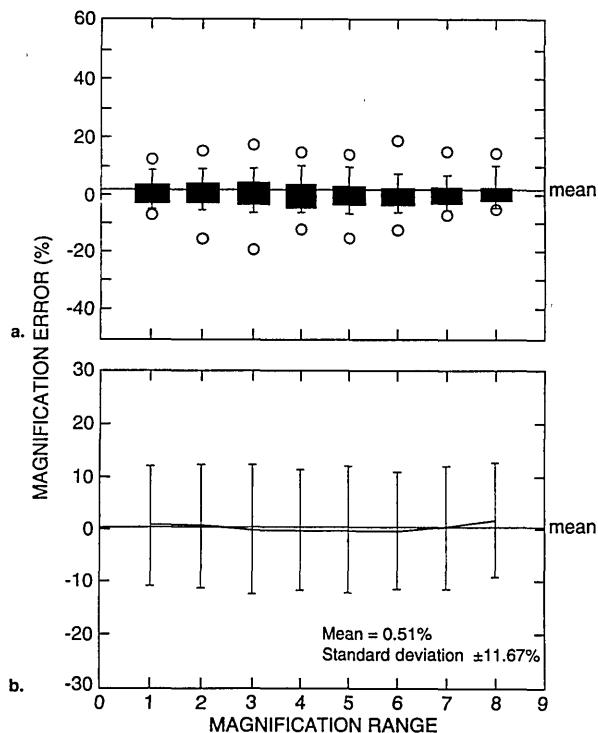


Fig. 15. Magnification calibration error as related to accelerating voltage. (a) Box plots and (b) scatter plots of the magnification error for the highest reported accelerating voltages.

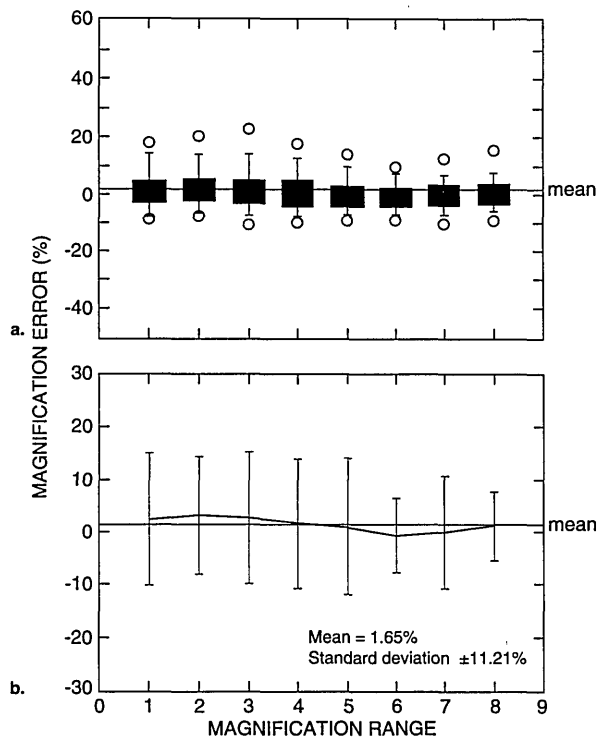


Fig. 16. Magnification calibration error as related to accelerating voltage. (a) Box plots and (b) scatter plots of the magnification error for the lowest reported accelerating voltages.

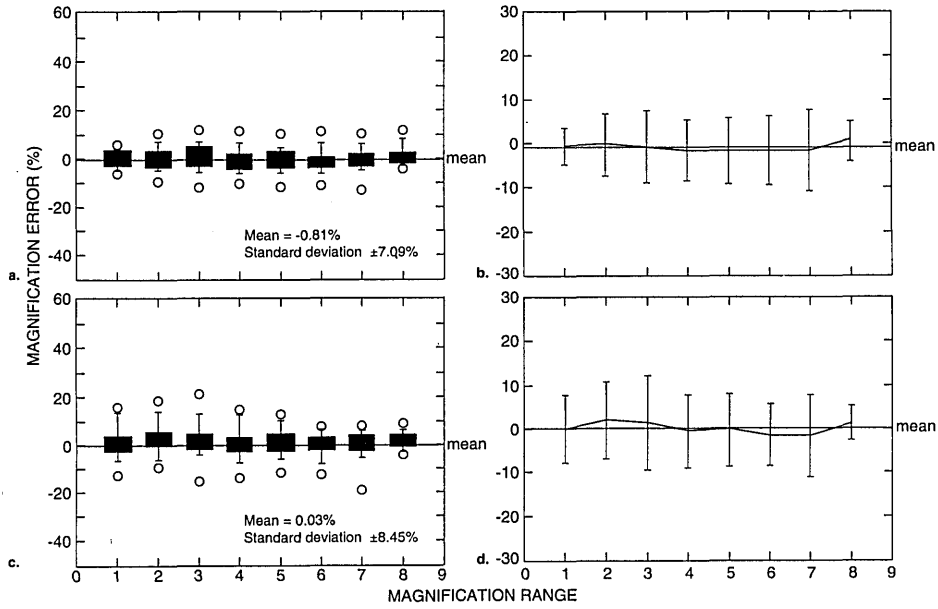


Fig. 17. Magnification calibration error as related to type of laboratory and accelerating voltage. (a) Box plots and (b) scatter plots of the magnification error for semiconductor related laboratories for the highest accelerating voltages reported. (c) Box plots and (d) scatter plots of the magnification error for semiconductor related laboratories for the lowest accelerating voltages reported.

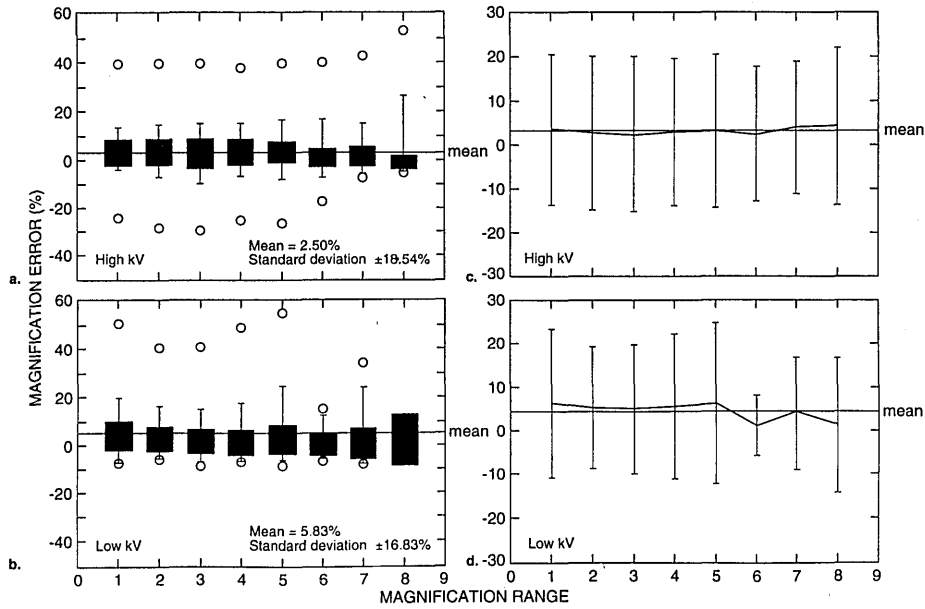


Fig. 18. Magnification calibration error as related to type of laboratory and accelerating voltage. (a) Box plots and (b) scatter plots of the magnification error for nonsemiconductor related laboratories for the highest accelerating voltages reported. (c) Box plots and (d) scatter plots of the magnification error for nonsemiconductor related laboratories for the lowest accelerating voltages reported.

conductor related laboratories. Figure 17a is box plots representing the data from the semiconductor related laboratories of the highest accelerating voltages reported from each instrument. In this figure, the mean of the error of these measurements was -0.81% with a standard deviation of $\pm 7.09\%$. The individual mean and standard deviation for each magnification range for the high accelerating voltage performance is shown in Fig. 17b. Figure 17c is box plots representing the lowest accelerating voltage reported from each instrument from these laboratories. In this figure, the mean of the error of these measurements was 0.03% with a standard deviation of $\pm 8.45\%$. The individual mean and standard deviation for each magnification range for the high accelerating voltage performance is shown in Fig. 17d. These data are contrasted to the performance of the “other” participants. Figure 18a is box plots representing the highest accelerating voltage reported from each instrument from the nonsemiconductor related laboratories. In this figure, the mean of the error of these measurements was 2.50% with a standard deviation of $\pm 18.54\%$. The individual mean and standard deviation for each magnification range for the high accelerating voltage performance is shown in Fig. 18b. Figure 18c is a box plot representing the lowest accelerating voltage reported from each instrument. In this figure, the mean of the error of these measurements was 5.83% with a standard deviation of $\pm 16.83\%$. The individual mean and standard deviation for each magnification range for the low accelerating voltage performance is shown in Fig. 18d. It should be noted that the “other” category included the data from the applications laboratories from three SEM manufacturers and, thus the overall error was somewhat reduced. Results from all of the data sets including the maximum error reported is found in Table 3.

3.3 Accelerating Voltage Compensation

An analysis of the performance of the instrument accelerating voltage compensation circuitry was also obtained from the supplied data. It is assumed by most operators that when the accelerating voltage is changed, the magnification compensation circuitry adjusts for this change and the magnification is correctly adjusted. Many factors which are outside of this study complicate this process. However, one major factor contributing to variations in the magnification between accelerating voltages is lens hysteresis. Many newer instruments have mechanisms such as degaussing circuitry to compensate or correct for this problem. Figure 19a shows the performance of an older instrument at four separate accelerating voltages. Note that there is at least a 5% error spread between each accelerating voltage range. Figure 19b demonstrates the results from a newer instrument from the same laboratory. Note the tight spread of results. With this instrument, consistent results between accelerating voltages were obtained. The lens compensation effect is also related to the X-Y squareness of the low magnification image as shown in Fig. 20. In this figure, a comparison of the error of the X and Y measurement as related to the expected value is compared for several accelerating voltages for the *same* instrument. As with Fig. 8, perfect X and Y compensation would place the boxes representing the data points in the center of the graph (0,0).

3.4 “Linewidth Measurements”

The NIST prototype SEM sample is designed to be used for calibration of the SEM magnification to a known pitch. This sample is not designed nor is meant to be used as a “linewidth” calibration sample. The reasons for this distinction have been

Table 3. Error Summary

Type of error measurement	Mean	Standard deviation	Maximum error
Micrometer bar	2.23%	$\pm 13.01\%$	-43.42%
Magnification	1.77%	$\pm 12.03\%$	63.08%
All high kV	0.50%	$\pm 11.67\%$	57.71%
All low kV	1.65%	$\pm 11.21\%$	63.08%
Semiconductor high kV	-0.81%	$\pm 7.09\%$	18.12%
Other high kV	2.50%	$\pm 18.54\%$	57.71%
Semiconductor low kV	0.03%	$\pm 8.45\%$	33.70%
Other low kV	5.83%	$\pm 16.83\%$	63.08%
Commercial high kV	5.02%	$\pm 4.04\%$	9.76%
Commercial low kV	2.64%	$\pm 5.20\%$	10.90%

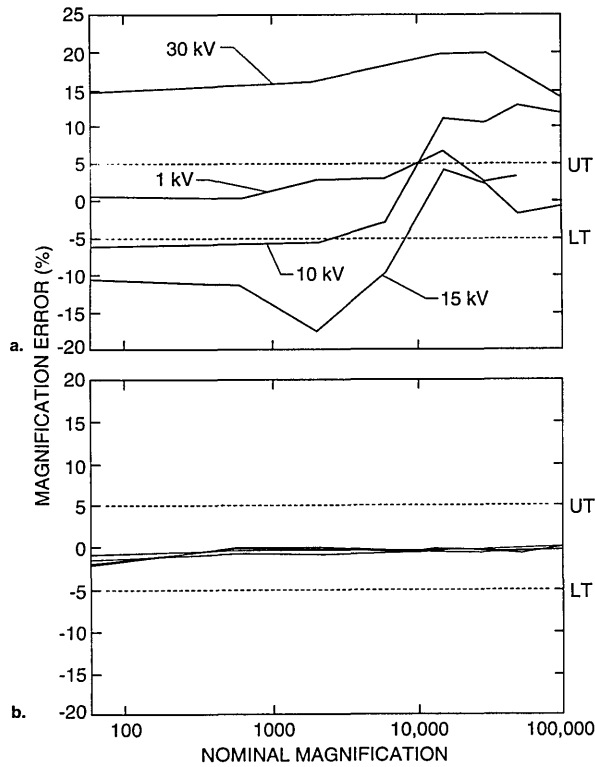


Fig. 19. Comparison of the error of the accelerating voltage compensation as related to magnification for two different instruments. (a) Four different accelerating voltages on instrument 1 showing poor compensation for accelerating voltage changes. (b) Four different accelerating voltages on instrument 2 showing excellent accelerating voltage compensation.

discussed extensively in the literature. However, one exercise requested of the participants was to report their “best-guess” of the width of the $0.2 \mu\text{m}$ nominal lines. Comparison measurements from one of the NIST samples were performed on the NIST metrology instrument at high accelerating voltage (the current configuration of the instrument) using the laser interferometer stage. The laser interferometer measurement of one of the samples reported an average pitch of 401 nm and an average linewidth of 204 nm. Multiple lines were used to obtain the average since it was unknown which lines were measured by the participants. Using the NIST metrology SEM, plots of the video to the laser data representing 24 000 data points for the backscattered electron image are shown in Fig. 21. Measurements were obtained using an arbitrary 50% threshold crossing algorithm. These measurements compare within 3 nm of another set of data submitted by one of the participants using a similar laser interferometer based metrology instrument. The average measure-

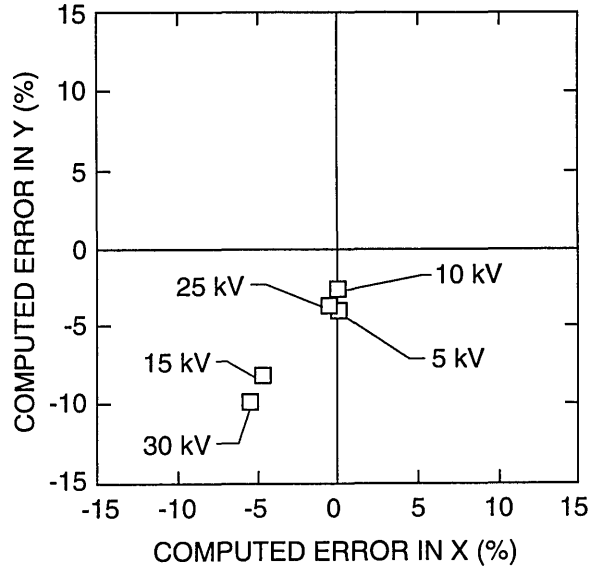


Fig. 20. X-Y Compensation error as related to accelerating voltage. A comparison of the error of the X to the Y measurement as related to the expected value is compared for several accelerating voltages for the same instrument. Perfect X and Y calibration would place the boxes representing the data points in the center of the graph (0,0) and perfect compensation correction would overlay each of the boxes at each accelerating voltage.

ment of these lines was used as the “standard nominal” measurement and the data supplied by the participants was compared to that number and the error plotted (Fig. 22). In some instances, measurements of the same lines using the same fundamental instrument conditions but a variation in accelerating voltage by the participants metrology instruments demonstrated differences of as large as 31 nm (315 nm at 1 keV and 284 nm at 2 keV). This variation in measurement results, especially between different accelerating voltage is expected and has been demonstrated on other types of samples [11]. Other possibilities for variation include: electron beam interaction effects, differences between secondary and backscattered electron measurements, electron beam diameter differences between instruments, the effect of sample contamination, the differences between measurement algorithms and sample variability. For example two common algorithms used for the determination of the data for this work were the threshold crossing algorithm and the linear approximation algorithm. Figure 23 shows a comparison between measurements made between the two methods. Clearly, a “standard” measurement algorithm should be developed. This algorithm should be designed so it can be used on any SEM

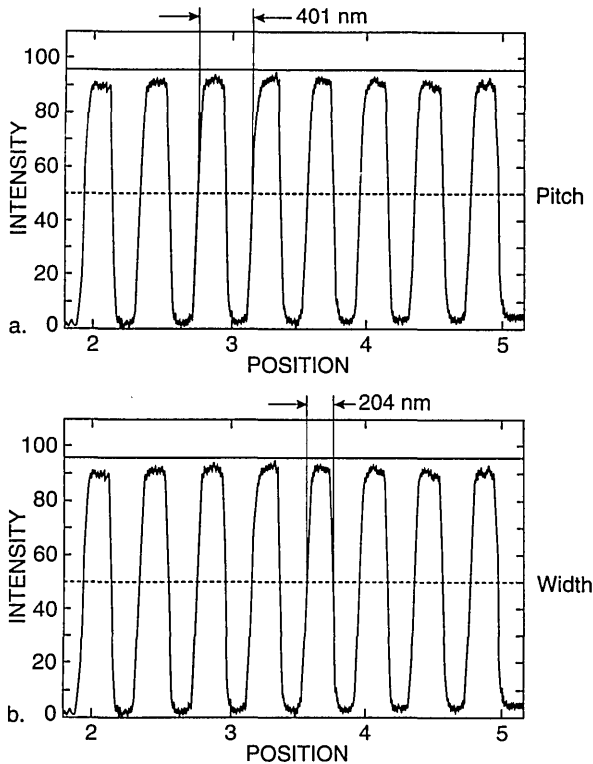


Fig. 21. NIST laser interferometer-based metrology instrument measurement scan data. (a) Pitch of 401 nm. (b) Width of 204 nm. Measurements are based on an arbitrary 50% threshold crossing algorithm and have been measured from the collected backscattered electron signal.

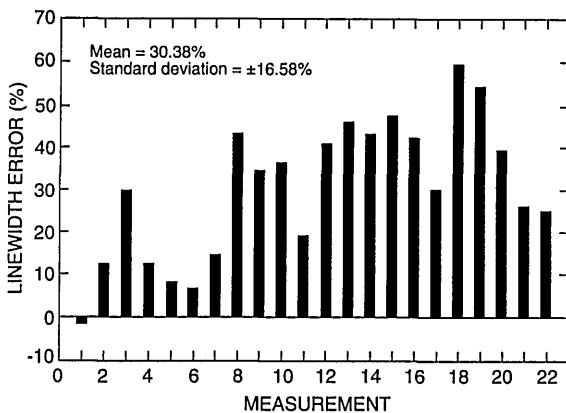


Fig. 22. Plot of the error of reported “linewidth” to that measured by the NIST metrology instrument for the 22 separate measurements reported.

linewidth measurement instrument. Using this algorithm, the measurement data would be handled in an identical manner irregardless of the instrument for comparison purposes. The differences reported for “linewidth” underscores the fact that

the magnification cannot be “point calibrated” to a linewidth type sample, and a magnification type sample cannot be used as a “linewidth” calibration sample unless electron beam interaction modeling is capable of predicting the accurate location of the edges, within some uncertainty, for various instrument and sample conditions.

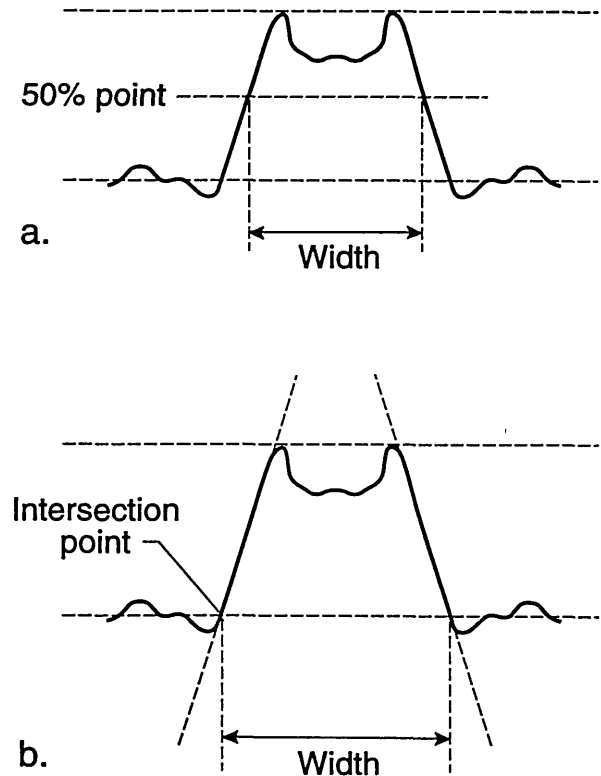


Fig. 23. Diagrammatic Comparison of the difference between two common measurement algorithms on the reported width measurement (a) Threshold crossing algorithm. (b) Linear approximation algorithm.

3.5 Specimen Contamination

Sample contamination is inevitable. Contamination results from sample handling, the environment and the instrument. Hydrocarbons interact with the electron beam and form a layer on the surface. The speed at which this deposition occurs varies with the amount of hydrocarbon (or other contaminant) available to interact, as well as, the operational conditions of the instrument.

In this study, few fully dry-pumped SEMs were used to examine the samples. Dry pumped in this instance is defined as a system equipped with a magnetically levitated turbomolecular pump which is backed by a molecular drag type pump as well as

a molecular drag-type roughing pump on the sample exchange chamber. In one controlled instance, a sample from the first round, (therefore un-examined), was directly inspected in the dry pumped system with no resulting contamination deposition on the surface. The same sample was placed into another "clean" but, non-dry pumped system and rapid sample contamination resulted. From this experience it became apparent that a cleaning procedure was needed. With the assistance of Mr. Aldo Pelillo of Digital Equipment Corporation a successful cleaning procedure was developed. The samples were cleaned in oxygen plasma in intervals using power output ranging from 100-250 W, depending upon the contamination level. It was demonstrated that most of the contamination is removed within the first two cleaning cycles. With the higher wattage, some of the samples tested tended to oxidize requiring a follow-up wet cleaning of the surface in dilute hydrofluoric acid (10:1— $\text{DiH}_2\text{O}:\text{HF}$ for 1.5 min). This procedure was applied to samples measured in their laboratory with great success. Samples measured and returned by some of the participants were inspected at low accelerating voltage at NIST and then sent to be cleaned. The resulting micrographs are shown in Fig. 24.

4. Conclusion

The results of the NIST interlaboratory SEM study underscores that each SEM must be considered as an individual unit. Calibration and adjustment is necessary and must be checked and re-checked periodically in order to make sure that the data obtained from the instrument are correct.

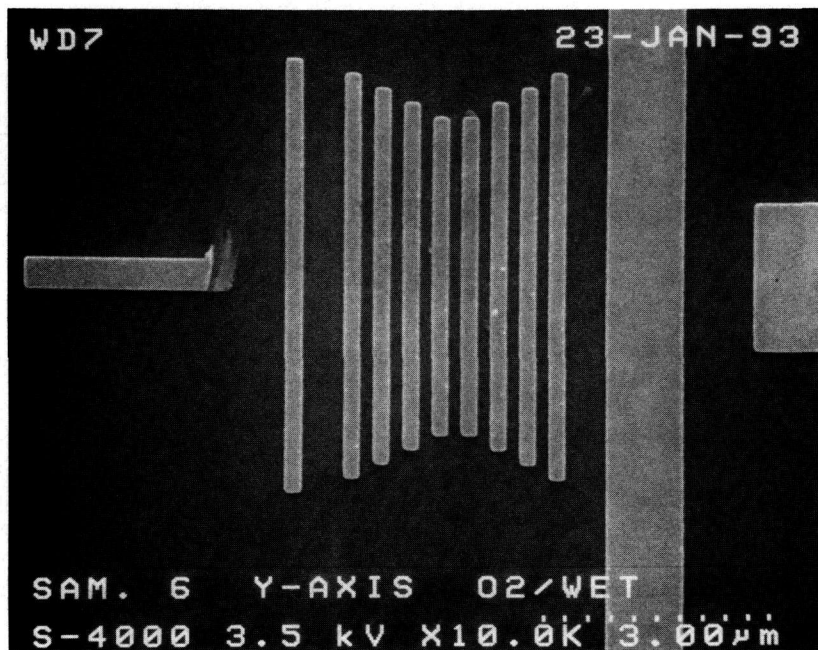
Throughout this study, it became apparent that the magnification calibration capability for the current, more modern instrumentation is far better than for the older instruments. However, the sensitivity of this adjustment should be far finer. Calibration potentiometers which are quite often "5-turn" variable resistors, do not have sufficient sensitivity to properly adjust the transition points adequately for the precision needed for modern SEM operation, especially those used for metrology. Changing these variable resistors to 10 or 20 turn potentiometers would be a step in the right direction, but this is only part of the story. The entire calibration/scan system of the SEM should be redesigned for improved precision for both magnification calibration and accelerating voltage compensation. The 10% rule no longer applies and we should strive for the 0.5% or better rule.

The applicability of the SEM prototype sample has been proven through this study. The prototype sample, as previously described and published, or a sample identical to the test samples used in this study could be issued as an SRM. However, several excellent suggestions made by the participants during the course of the study will be incorporated in the final standard. The first suggestion is that there be more calibration patterns available since contamination (even with the availability of the cleaning procedure) is inevitable. A newly designed pattern including four fine calibration patterns, two in X and two in Y has been designed. It is planned that NIST will certify one pattern in X and one pattern in Y. It will then be up to the user to secondarily calibrate and use the other patterns. The lines have also been lengthened somewhat. Another improvement is that an array of the focusing and astigmatism correction marks has been included near to the fine patterns.

NIST does not, at the current time, have a semiconductor processing facility capable of manufacturing the new proposed SEM magnification sample. NIST does however, have the measurement capability to measure and certify the new standard. Therefore, NIST must rely on commercial state-of-the-art semiconductor processing facilities to fabricate the samples. Until recently only a small number of these facilities were capable of making the standard and a smaller number of those were willing to undertake the challenge. A similar situation occurred with the manufacture of the Optical Photomask Standards SRM 473, 474, and 475. All of these standards push the state-of-the-art of device fabrication to the limit. Specifications for wall verticality and edge roughness are extremely tight and place demands on the fabrication facility that are not required by normal chip production. For the SEM magnification sample, the NNF of Cornell University has been extremely cooperative in assisting in the fabrication of the samples for this and the previous study—but they are not a production facility. The task of the NNF was to prove the sample could be made and they succeeded in that task, but it was not their task to produce it in production quantities. NIST/Cornell demonstrated the concept of this magnification standard in 1988, but it has taken until just recently to identify commercial companies interested and capable of making the standard. Currently there are at least three companies interested in fabricating the standard and procurement is currently underway.



a



b

Fig. 24. Contamination micrographs. (a) Micrograph demonstrating the condition of a sample as received from one participant of the study. (b) Micrograph of the same sample after cleaning. (Micrographs courtesy of Al Pelillo, Digital Equipment Corporation).

Sample contamination is inevitable and a cleaning procedure has been developed with the cooperation of Digital Equipment Corporation. Contamination results from sample handling, packaging, the environment, and the instrument. Hydrocarbons from whatever source interact with the electron beam and form a layer on the surface. The speed at which this deposition occurs varies with the amount of hydrocarbon (or other contaminant) available to interact, as well as the operational conditions of the instrument. Many of the participants of the study commented about the contamination rate of the prototype sample. Some participants were able to cycle the sample successfully through as many as six instruments whereas others stated that the "sample contaminated instantly." Participants of the first round received virgin samples directly from the wafer fabrication facility. Yet, in all but the fully dry pumped scanning electron microscopes, sample contamination proved to be an issue. Was the contamination being deposited on the sample calibration structures from the packaging, handling or instrument? This is unknown, but, it seems to be an area which should be studied further by all interested parties. Participants of the second round were, unfortunately, working under a hardship since the sample each received was viewed by another participant, and the sample was also checked by NIST before being sent out the second time. If more test samples had been available, this recycling of samples would not have been necessary.

Acknowledgments

The authors would like to thank all the participants of the study for their interaction suggestions and assistance. Because of the sensitivity of the results of the study the participants will remain anonymous. The authors would also like to thank Dr. Michael Mort of Signal Analytics for his assistance in the software program modifications, the National Nanofabrication Facility at Cornell University and especially Richard Tiberio for their work in fabricating the prototype standard used in this study, Mr. Aldo Pelillo of Digital Equipment Corporation for his assistance in developing the sample cleaning procedure, and Mr. Raymond Mele of the NIST Program Office for his graphics arts work.

6. References

- [1] M. T. Postek and R. C. Tiberio, Low Accelerating Voltage SEM Magnification Standard Prototype, G. W. Bailey, ed., Proc. EMSA, San Francisco Press, CA (1988) pp. 198-199.
- [2] M. T. Postek, Scanning Electron Microscope-based Metrological Electron Microscope System and New Prototype Scanning Electron Microscope Magnification Standard, Scanning Microscopy 3 (4), 1087-1099 (1989).
- [3] M. T. Postek, J. R. Lowney, A. E. Vladar, W. J. Keery and E. Marx, X-ray Mask Metrology: The Development of Linewidth Standards for X-ray Lithography SPIE Proceedings (1993) in press.
- [4] M. T. Postek, Low Accelerating Voltage SEM Imaging and Metrology Using Backscattered Electrons, Rev. Sci. Instrum. 61 (12) 3750-3754 (1990).
- [5] Isaac Specifications: Apple Macintosh IIfx computer equipped with 8 MB RAM, two (1.2 & 1.44 MB) floppy drives, a 200 MB hard disk, a 650 MB magneto-optical drive, a Sharp JX-320 color scanner (max. 600×600 dpi and 256 gray level resolution) and an Apple LaserWriter IIs laser printer.
- [6] Perceptics Co. P.O. Box 22991 Pellissippi Parkway, Knoxville TN 37933-0991. The frame grabber card is a full size NuBus board with four independent, software controlled, RS-170 or PAL standard inputs; the display rate is 30 frame/s (real time video on the computer screen); the spatial resolution is 640×480 pixels with 256 gray levels.
- [7] Signal Analytics Co. 374 Maple Ave. East Suite #204, Vienna VA, 22180.
- [8] Wayne Rasband, National Institutes of Health, Internet, BitNet: wayne@helix.nih.gov).
- [9] Documentation supplied with NIST SRM 484.
- [10] M. T. Postek and D. C. Joy, Submicrometer Microelectronics Dimensional Metrology: Scanning Electron Microscopy, J. Res. Natl. Bur. Stand. (U.S.) 92 (3), 205-228 (1987).
- [11] M. T. Postek, W. J. Keery, and R. D. Larrabee, The Relationship Between Accelerating Voltage and Electron Detection Modes to Linewidth Measurement in an SEM, Scanning 10, 10-18 (1987).

About the authors: Michael Postek is a physical scientist and the project leader for scanning electron microscope metrology in the Microelectronics Dimensional Metrology Group of the Precision Engineering Division at NIST. His main interest is the development of dimensional standards for the scanning electron microscope. Andras Vladar is an electrical engineer and Guest Scientist from the Research Institute for Technical Physics of the Hungarian Academy of Sciences currently working in the Microelectronics Dimensional Metrology Group. Samuel Jones is a member of the Microelectronics Dimensional Metrology group of the Precision engineering Division and is currently working on submicrometer metrology with the SEM. William Keery, now retired from NIST, is an electronics engineer and currently a Guest Scientist in the Microelectronics Dimensional Metrology Group. The National Institute of Standards and Technology is an agency of the Technology Administration, U.S. Department of Commerce.

Phase Equilibria and Crystal Chemistry in Portions of the System SrO-CaO-Bi₂O₃- CuO, Part IV—The System CaO-Bi₂O₃-CuO

Volume 98

Number 4

July–August 1993

**B. P. Burton, C. J. Rawn,
and R. S. Roth**

National Institute of Standards
and Technology,
Gaithersburg, MD 20899-0001

and

N. M. Hwang

The Korea Standards Research
Institute, Taedok Science Town,
Taejon, Chungnam, 305-606
Republic of Korea

New data are presented on the phase equilibria and crystal chemistry of the binary systems CaO-Bi₂O₃ and CaO-CuO and the ternary CaO-Bi₂O₃-CuO. Symmetry data and unit cell dimensions based on single crystal and powder x-ray diffraction measurements are reported for several of the binary CaO-Bi₂O₃ phases, including corrected compositions for Ca₄Bi₆O₁₃ and Ca₂Bi₂O₅.

The ternary system contains no new ternary phases which can be formed in air at ~700–900 °C.

Key words: calcium bismuth copper oxide; crystal chemistry; experimental phase relations; phase equilibria.

Accepted: May 3, 1993

1. Introduction

The discovery of superconductivity in cuprates by Bednorz and Müller [1], and its confirmation by Takagi et al. [2] as being due to the phase La_{2-x}Ba_xCuO₄, led to a world-wide search for other compounds with higher T_c 's. Identification of the superconducting phase Ba₂YCu₃O_{6+x} [3], with a critical temperature $T_c \sim 90$ K [4], has resulted in hundreds of published reports on the properties of this and related phases.

Phases with still higher T_c 's were found in the systems SrO-CaO-Bi₂O₃-CuO and BaO-CaO-Tl₂O₃-CuO [5,6]. These phases belong mostly to a homologous series A₂Ca_{n-1}B₂Cu_nO_{2n+4} (A = Sr, Ba; B = Bi, Tl). In the Bi⁺³ containing systems a phase with $n = 2$ and $T_c \sim 80$ K is easily prepared. The exact single-phase region of this phase is not well known, and a structure determination has not been completed because of very strong incommensurate diffraction that is apparently due to a modulation of

the Bi positions. Higher n (and higher T_c) phases have not been prepared as single-phase bulk specimens (without PbO). We undertook a comprehensive study of phase equilibria and crystal chemistry in the four component system SrO-CaO-Bi₂O₃-CuO in the hope that such a study will define the optimum processing parameters for reproducible synthesis of samples with useful properties.

A prerequisite to understanding the phase equilibria in the four component system is adequate definition of the phase relations in the boundary binary and ternary systems. The ternary system SrO-CaO-CuO was the first to be investigated [7,8], followed by the ternary system SrO-Bi₂O₃-CuO and its binary subsystems [9,10,11,12]. Preliminary versions have been published of the systems CaO-Bi₂O₃-CuO and SrO-CaO-Bi₂O₃ [13], and the details of the system SrO-CaO-Bi₂O₃ will appear in the near future [14]. The experimental details,

phase relations, and crystal chemistry of the binary CaO-Bi₂O₃ and the ternary system CaO-Bi₂O₃-CuO are the subject of this publication.

In the following discussion of phase equilibria and crystal chemistry, the oxides under consideration will always be given in the order of decreasing ionic radius, largest first, e.g., CaO:1/2Bi₂O₃:CuO. The notation 1/2Bi₂O₃ is used so as to keep the metal ratios the same as the oxide ratios. The "shorthand" notation is used to designate the phases with C=CaO, B=1/2Bi₂O₃ and Cu=CuO. Thus compositions may be listed simply by numerical ratio e.g., the formula Ca₄Bi₆O₁₃ can be written as C₂B₃ or simply 2:3.

2. Experimental Procedures

In general, about 3.5 g specimens of various compositions in binary and ternary combinations were prepared from CaCO₃, Bi₂O₃ and CuO. Neutron activation analyses of the starting materials indicated that the following impurities (in µg/g) were present: in CuO-3.9Cr, 2.8Ba, 28Fe, 410Zn, 0.09Co, 1.9Ag, 0.03Eu, 14Sb; in Bi₂O₃-2.1Cr, 0.0002Sc, 26Fe, 21Zn, 0.6Co, 0.5Ag, 0.0008Eu, 0.2Sb; in CaCO₃-1.1Cr, 6Ba, 160Sr, 0.0001Sc, 5Fe, 14Zn, 0.14Co, 0.01Ag, 0.0005Eu, 0.02Sb. The constituent chemicals were weighed on an analytical balance to the nearest 0.0001 g and mixed either dry or with acetone in an agate mortar and pestle. The weighed specimen was pressed into a loose pellet in a stainless steel die and fired on an MgO single crystal plate, or on Au foil, or on a small sacrificial pellet of its own composition. The pellets were then calcined several times at various temperatures from ~600 to 850 °C, with grinding and re-pelletizing between each heat treatment. Duration of each heat treatment was generally about 16–20 h. For the final examination a small portion of the calcined specimen was re-fired at the desired temperature (1–8 times), generally overnight, either as a small pellet or in a small 3 mm diameter Au tube, either sealed or unsealed. Too many heat treatments in the Au tube generally resulted in noticeable loss of Cu and/or Bi.

When phase relations involving partial melting were investigated, specimens were contained in 3 mm diameter Au or Pt tubes and heated in a vertical quench furnace. This furnace was heated by six MoSi₂ hairpin heating elements with a vertical 4 in diameter ZrO₂ tube and a 1 in diameter Al₂O₃ tube acting as insulators. The temperature was measured separately from the controller at a point within approximately 1 cm of the specimen by

a Pt/90Pt10Rh thermocouple, calibrated against the melting points of NaCl (800.5 °C) and Au (1063 °C). After the appropriate heat treatment, the specimen was quenched by being dropped into a Ni crucible, which was cooled by He flowing through a copper tube immersed in liquid N₂.

In order to approach equilibrium phase boundaries by different synthesis routes, many specimens were prepared from pre-made compounds or two phase mixtures as well as from end members. These were weighed, mixed, and ground in the same way as for the previously described specimens. Also, some specimens were: 1) annealed at temperature (T_1) and analyzed by x-ray powder diffraction; 2) annealed at a higher or lower temperature (T_2) where a different assemblage of phases was observed; 3) returned to T_1 to demonstrate reversal of the reaction(s) between T_1 and T_2 . All experimental details are given in Tables 1a and 1b. Phase identification was made by x-ray powder diffraction using a high angle diffractometer with the specimen packed into a cavity 0.127 or 0.254 mm deep in a glass slide. The diffractometer, equipped with a theta compensator slit and a graphite diffracted beam monochromator, was run at 1/4° 2θ/min with CuKα radiation at 40 KV and 35 MA. The radiation was detected by a scintillation counter and solid state amplifier and recorded on a chart with 1°/2θ = 1 in. For purposes of illustration and publication, the diffraction patterns of selected specimens were collected on a computer-controlled, step scanning goniometer and the results plotted in the form presented.

Equilibrium in this system has proven to be so difficult to obtain that a few specimens were prepared by utilizing lactic acid in an organic precursor route to obtain more intimate mixing at low temperatures [9]. This procedure yielded an essentially single phase amorphous precursor for the composition that contains 66.7 mol % Bi₂O₃. At higher Bi contents, pure Bi metal was formed by carbothermic reduction under even the lowest temperature drying procedures in air.

Specimens for solidus and liquidus determinations in the CaO-CuO system were prepared by dissolving mixtures of cupric nitrate and calcium nitrate in distilled water and then drying. The specimens were calcined two or three times between 500 and 700 °C with intermittent grinding. Samples of Ca_{1-x}CuO₂ were heated in a horizontal tube furnace for 36 to 120 h in air or in oxygen. In determining the *exact* stoichiometry of the compound previously reported as "CaCuO₂" [7], however, a citrate synthesis route was used [15]. Dried

anhydrous calcium carbonate and basic cupric carbonate ($\text{Cu}(\text{OH})_2:\text{CuCO}_3$) were dissolved in dilute nitric acid and complexed with excess citric acid monohydrate. After drying, the resulting friable, low-density material was calcined at 700 °C either

in air or in a flowing oxygen atmosphere until x-ray diffraction revealed the presence of fewer than three phases. It took 18 to 84 h for these synthesis reactions to reach completion.

Table 1a. Experimental data for the system $\text{CaO-Bi}_2\text{O}_3\text{-CuO}$

Spec. no.	Composition mole percent			Heat treatment ^b			Phys. obser. ^c	Results of x-ray diffraction ^d
	CaO	$1/2\text{Bi}_2\text{O}_3$	CuO	Initial	temp °C final	Time h		
	100	0	0	500 600 600 × 2				CaCO_3 $\text{CaO} + \text{CaCO}_3$ CaO
	66.7	0	33.3	700 850 1000 × 3				C_2Cu
	60	0 <i>nitrates</i>	40	500	750 700 } 800 }	48 24 } 12 }		$\text{CaO} + \text{CuO}$ $\text{CaO} + \text{CuO} + \text{C}_{1-x}\text{Cu}$ $\text{CuO} + \text{CaO} + \text{C}_2\text{Cu}$
				750 × 2	900 745 800 875 × 2 }	2.0 – O_2		$\text{C}_2\text{Cu} + \text{CuO}$ $\text{C}_2\text{Cu} + \text{CuO}$ $\text{C}_2\text{Cu} + \text{CuO}$
					950 980 990 990 1000 1000 × 2 1000 × 3 1007 1011 1014	16 0.66 14.0		$\text{C}_2\text{Cu} + \text{CuO}$ $\text{C}_2\text{Cu} + \text{CuO}$ $\text{C}_2\text{Cu} + \text{CuO} + \text{CCu}_2$ $\text{C}_2\text{Cu} + \text{CCu}_2$ $\text{C}_2\text{Cu} + \text{CCu}_2$ $\text{C}_2\text{Cu} + \text{CCu}_2$
	50	0	50			0.16 1.0 0.5		$\text{C}_2\text{Cu} + \text{Cu}_2\text{O} + \text{CCu}_2$ $\text{C}_2\text{Cu} + \text{Cu}_2\text{O}$
#1		<i>ppt. hydrox-carb.</i>		450	740 740 800	6.0 15.0 16.0		$\text{C}_{1-x}\text{Cu} + \text{CaO} + \text{CuO}_{\text{tr}}$ $\text{C}_{1-x}\text{Cu} + \text{CaO}$ $\text{C}_{1-x}\text{Cu} + \text{CaO}$ $\text{C}_2\text{Cu} + \text{CuO}$
#2		<i>ppt. hydrox-carb.</i>		500	550 600 650 700 740 740 760 780 800	62.5		$\text{CuO} + \text{C}_{1-x}\text{Cu}$ $\text{CuO} + \text{C}_{1-x}\text{Cu} + \text{CaO}$ $\text{C}_{1-x}\text{Cu} + \text{CaO} + \text{CuO}$ $\text{C}_{1-x}\text{Cu} + \text{CuO} + \text{CaO}$ $\text{C}_{1-x}\text{Cu} + \text{CuO} + \text{Ca}(\text{OH})_2$ $\text{C}_{1-x}\text{Cu} + \text{CaO} + \text{CuO}$ $\text{C}_{1-x}\text{Cu} + \text{CaO} + \text{C}_2\text{Cu}_{\text{tr}}$ $\text{C}_{1-x}\text{Cu} + \text{CaO} + \text{CuO}$ $\text{C}_{1-x}\text{Cu} + \text{CaO} + \text{CuO}$ $\text{C}_{1-x}\text{Cu} + \text{CaO} + \text{CuO}_{\text{tr}}$

Table 1a. Experimental data for the system CaO-Bi₂O₃-CuO—Continued

Spec. no.	Composition mole percent			Heat treatment ^b			Phys. obser. ^c	Results of x-ray diffraction ^d
	CaO	1/2Bi ₂ O ₃	CuO	Initial	temp °C final	Time h		
#3				600				CuO + CaO + CaCO ₃ + C _{1-x} Cu
				600 × 2				CuO + CaO + CaCO ₃ + C _{1-x} Cu
				600 × 3				CuO + CaO + CaCO ₃ + C _{1-x} Cu
				600 × 4				CuO + CaO + CaCO ₃ + C _{1-x} Cu
				675				CuO + CaO + C _{1-x} Cu
				675 × 5				C _{1-x} Cu + CaO + CuO
				675 × 11				C _{1-x} Cu + CaO + CuO
				675 × 16				C _{1-x} Cu + CaO + CuO
				675 × 21				C _{1-x} Cu + CaO + CuO
				675 × 26				C _{1-x} Cu + CaO + CuO
				675 × 31				C _{1-x} Cu + CaO + CuO
				675 × 36				C _{1-x} Cu + CaO + CuO
				750 × 2				CaO + CuO + C ₂ Cu
				850				CaO + CuO + C ₂ Cu
				900				C ₂ Cu + CuO + CaO
				600				C ₂ Cu + CuO + CaO
				750				C ₂ Cu + CuO + CaO
				900	675	70		C ₂ Cu + CuO + CaO
					675 × 4			C ₂ Cu + CuO + CaO
	#4		<i>nitrates</i>		500			
				600				
					995	1.0		C ₂ Cu + CuO + CCu ₂
					1007	10.0		C ₂ Cu + CCu ₂ + Cu ₂ O
					1011	1.0		C ₂ Cu + Cu ₂ O + CCu ₂
					1013	1.0		C ₂ Cu + Cu ₂ O + CCu _{2tr}
					1007	10	}	C ₂ Cu + Cu ₂ O + CuO + CCu _{2tr}
					1013	24		
					1014	0.5		C ₂ Cu + Cu ₂ O + CuO + CCu _{2tr}
					1018	0.5		C ₂ Cu + Cu ₂ O + CuO + CCu _{2tr}
					1022	0.5	n.m.	C ₂ Cu + Cu ₂ O + CuO + CCu _{2tr}
					1028	0.5	p.m.	C ₂ Cu + Cu ₂ O + CCu _{2tr}
					1032	0.5	p.m.	C ₂ Cu + Cu ₂ O + CCu _{2tr}
					1036	0.5	p.m.	CaO + C ₂ Cu + Cu ₂ O + CCu _{2tr}
				1040	0.5	p.m.	CaO + C ₂ Cu + Cu ₂ O + CCu _{2tr}	
#5		<i>citrates</i>			700	22		C _{1-x} Cu + CaO
					700	18-O ₂		C _{1-x} Cu + CaO
	47.37	0 (9:10) <i>citrates</i>	52.63					
					700	18		C _{1-x} Cu + CaO
					700	78-O ₂		C _{1-x} Cu + CaO
	45.45	0 (5:6) <i>citrates</i>	54.54					
					700	18		C _{1-x} Cu
					700	21-O ₂		C _{1-x} Cu + CaO
					700	39-O ₂		C _{1-x} Cu + CaO
					700	78-O ₂		C _{1-x} Cu + CaO
	45.33	0 <i>citrates</i>	54.67					
					700	86-O ₂		C _{1-x} Cu
45.20	0 <i>citrates</i>	54.80						
				700	16			
				700	24-O ₂		C _{1-x} Cu	

Table 1a. Experimental data for the system CaO-Bi₂O₃-CuO—Continued

Spec. no.	Composition mole percent		Heat treatment ^b			Phys. obser. ^c	Results of x-ray diffraction ^d
	CaO	1/2Bi ₂ O ₃	CuO	Initial	temp °C final		
	44.95	0 <i>citrate</i> s	55.05	700	16 700	24-O ₂	C _{1-x} Cu + CuO _{ir}
	44.70	0 <i>citrate</i> s	55.30	700	16 700	24-O ₂	C _{1-x} Cu + CuO
	40	0 <i>citrate</i> s	60	700	60		C _{1-x} Cu + CuO
				700 800	18-O ₂		C _{1-x} Cu + CuO
	33.3	0	66.7	800 875 × 2	965 1000 1000 × 2	25.0 19.0	C ₂ Cu + CuO C ₂ Cu + CuO CCu ₂ + C ₂ Cu + CuO CCu ₂ + C ₂ Cu + CuO
#1	30	0 <i>nitrate</i> s	70	500 750 770			CuO + CaO CuO + CaO CuO + CaO
				750 × 2 990			CuO + CaO + C ₂ Cu CuO + C ₂ Cu
				500	980 990 1000 1010 1014 1016	16.0 22.0 16.0 0.5 0.5 24.0	CuO + C ₂ Cu CCu ₂ + CuO + C ₂ Cu CCu ₂ + Cu ₂ O _{ir} + C ₂ Cu _{ir} CCu ₂ + Cu ₂ O + C ₂ Cu _{ir} Cu ₂ O + C ₂ Cu + CCu ₂ Cu ₂ O + C ₂ Cu + CCu _{2ir}
#2		<i>citrate</i> s			700	86-O ₂	
#1	25	0	75	600 750	950 975 1000 1025		CuO + C ₂ Cu CuO + C ₂ Cu CCu ₂ + CuO + Cu ₂ O + C ₂ Cu Cu ₂ O + C ₂ Cu + CuO
#2		<i>nitrate</i> s		500 600	450		CuO + CaO
				750 770 780 790 800 820 830 840	72-O ₂ 48-O ₂ 68-O ₂ 30-O ₂ 36-O ₂ 42-O ₂ 72-O ₂ 36-O ₂	CuO + C _{1-x} Cu CuO + C _{1-x} Cu CuO + C _{1-x} Cu CuO + C _{1-x} Cu + CaO _{ir} CuO + C _{1-x} Cu CuO + C _{1-x} Cu CuO + C _{1-x} Cu + C ₂ Cu _{ir} CuO + C _{1-x} Cu + C ₂ Cu	

Table 1a. Experimental data for the system CaO-Bi₂O₃-CuO—Continued

Spec. no.	Composition mole percent		Initial	Heat treatment ^b		Phys. obser. ^c	Results of x-ray diffraction ^d
	CaO	1/2Bi ₂ O ₃		temp °C	Time h		
				880	36-O ₂		CuO + C ₂ Cu
				750	54		CuO + CaO + C _{1-x} Cu
				760	120		CuO + C ₂ Cu
				780	120		CuO + C ₂ Cu
				800	20		CuO + C ₂ Cu + CaO
				840	64		CuO + C ₂ Cu
				1012	1.0	p.m.	Cu ₂ O + C ₂ Cu + CCu ₂
				1020	0.5	p.m.	Cu ₂ O + C ₂ Cu + CCu ₂ + CaO
20	0	80					
	<i>nitrates</i>		500				
			600				
				1007	1.0		CuO + CCu ₂ + Cu ₂ O _{tr}
				1011	1.0		CCu ₂ + Cu ₂ O + CuO
				1014	0.16	p.m.	CCu ₂ + Cu ₂ O + CuO
				1016	0.5	p.m.	Cu ₂ O + C ₂ Cu + CuO + CCu ₂
				1020	0.5	c.m.	Cu ₂ O + C ₂ Cu + CuO + CCu ₂
15	0	85					
	<i>nitrates</i>		500				
			600				
				1016	0.16	p.m.	CuO + Cu ₂ O + CCu ₂
				1020	0.33	c.m.	Cu ₂ O + CuO + CCu ₂
10	0	90					
	<i>nitrates</i>		500				
			600				
				1020	0.16	p.m.	Cu ₂ O + CCu ₂ + CuO
5	0	95					
	<i>nitrates</i>		500				
			600				
				1016	0.16	p.m.	CuO + Cu ₂ O + CCu ₂
				1020	0.16	p.m.	CuO + Cu ₂ O + CCu ₂
10	90	0					
			700				
			750				rhomb + fcc'
				850	0.33	s.m.	rhomb + fcc' + fcc''
				860	0.33	p.m.	
				870	0.33	c.m.	fcc' + rhomb _{tr}
20	80	0					
			700				
			750				rhomb
				650			rhomb
				835	0.33		rhomb + fcc'
				875	0.33	s.m.	rhomb + fcc'
				875	0.66	s.m.	rhomb + fcc'
				890	0.33	c.m.	rhomb + fcc'
				700→875	} at 3°/h		rhomb + C ₅ B ₁₄
				875→650			
				750→870	} at 1°/h		rhomb
				870→845			

Table 1a. Experimental data for the system CaO-Bi₂O₃-CuO—Continued

Spec. no.	Composition mole percent			Heat treatment ^b			Phys. obser. ^c	Results of x-ray diffraction ^d							
	CaO	1/2Bi ₂ O ₃	CuO	Initial	final °C	Time h									
23	77	0	700 800					rhomb + C ₂ B ₃							
								rhomb + C ₂ B ₃							
								fcc'							
								n.m.							
								n.m.							
								n.m.							
								n.m.							
								c.m.							
								850							
								750 × 2							rhomb
25	75	0	700 750					rhomb + CB ₂ + C ₅ B ₁₄							
								rhomb + C ₅ B ₁₄							
								rhomb							
								rhomb							
								rhomb							
								rhomb							
								fcc'							
								rhomb							
								rhomb							
								850							
750 × 2							rhomb								
26	74	0	700 750					rhomb + C ₂ B ₃							
								fcc' + rhomb _{tr}							
								fcc' + bcc _{tr}							
								fcc'							
								rhomb							
26.32	73.68 (5:14)	0	750 650					C ₅ B ₁₄ + rhomb + C ₂ B ₃							
								rhomb + C ₂ B ₃ + C ₅ B ₁₄							
								fcc' + bcc _{tr}							
								C ₅ B ₁₄							
#1			750 × 2 650 × 5 750 × 3					rhomb + C ₂ B ₃ + CB ₂							
								rhomb + CB ₂ + C ₅ B ₁₄							
								rhomb + C ₅ B ₁₄ + CB _{2tr}							
#3			750 750 × 2 925 750 × 3					rhomb + C ₂ B ₃							
								fcc'							
								rhomb + CB ₂ + C ₅ B ₁₄							
								fcc'							
								c.m.							
								c.m.							
								c.m.							
								925	0.33						
								1000	1.0						
								650	16						
650	336														
750 × 5							C ₅ B ₁₄								
							C ₅ B ₁₄								
							rhomb + CB ₂ + C ₅ B ₁₄								
			700		100 MPa			rhomb							

Table 1a. Experimental data for the system CaO-Bi₂O₃-CuO—Continued

Spec. no.	Composition mole percent			Heat treatment ^b			Phys. obser. ^c	Results of x-ray diffraction ^d
	CaO	1/2Bi ₂ O ₃	CuO	Initial	temp °C final	Time h		
	27.27	72.72 (3:8)	0	750	650			rhomb + CB ₂ + C ₂ B ₃ + C ₅ B ₁₄
				750 × 5	750	16.0		CB ₂ + C ₅ B ₁₄ + rhomb CB ₂ + rhomb + C ₅ B ₁₄
				850				
				750 × 2				C ₅ B ₁₄ + CB ₂ + rhomb _{1r}
	28	72	0	700				
				750	860	0.33		fcc'
					870	0.33	n.m.	fcc'
					880	0.33	p.m.	fcc'
					900	0.66	c.m.	fcc'
	30	70	0	750				
					650			CB ₂ + C ₅ B ₁₄ + C ₂ B ₃ + rhomb
				750 × 5	750	1.33		CB ₂ + C ₅ B ₁₄ + rhomb CB ₂ + C ₅ B ₁₄ + rhomb
				850				
				750 × 2				CB ₂ + C ₅ B ₁₄ + rhomb
#1	33.33 (1:2)	66.67	0	800				
				1000	0.166		c.m.	
				750				C ₂ B ₃ + C ₅ B ₁₄ + CB ₂
					750	16.0		C ₂ B ₃ + C ₅ B ₁₄ + rhomb
#2				700				
				750				CB ₂ + C ₅ B ₁₄ + C ₂ B ₃ + rhomb
					65	96		CB ₂ + C ₅ B ₁₄ + C ₂ B ₃
					850	16		fcc' + bcc _{1r} fcc' + C ₂ B ₃
				800				
				850				
				750 × 2				CB ₂ + rhomb + C ₅ B ₁₄
				1000		1.75	c.m.	fcc' + bcc _{1r}
				650		16		CB ₂ + C ₂ B _{31r}
#3				750 × 5				CB ₂ + rhomb + C ₂ B _{31r}
					750	1.33		CB ₂ + rhomb
					925	0.13	c.m.	CB ₂ + C ₂ B ₃ †
					700	312		
					1000	1.0	c.m.	CB ₂ + C ₅ B ₁₄ + C ₂ B ₃
					650	17		
				650 × 4				CB ₂ + C ₂ B _{31r} + C ₅ B _{141r}
				650 × 5				CB ₂ + C ₅ B ₁₄ + C ₂ B _{31r}
				700				CB ₂
				750 × 3				C ₂ B ₃ + rhomb
				750				CB ₂ + C ₂ B _{31r}
				750 × 3				CB ₂ + C ₂ B _{31r}
				750 × 5				CB ₂ + C ₂ B ₃
					650	100 MPa		CB ₂ + C ₂ B ₃

Table 1a. Experimental data for the system CaO-Bi₂O₃-CuO—Continued

Spec. no.	Composition mole percent			Heat treatment ^b			Phys. obser. ^c	Results of x-ray diffraction ^d			
	CaO	1/2Bi ₂ O ₃	CuO	Initial	final temp °C	Time h					
#5	<i>lactate</i>			450							
				650 × 3				CB ₂ + C ₅ B ₁₄			
				650 × 4				CB ₂ + C ₅ B ₁₄			
					700			CB ₂ + C ₅ B ₁₄			
					750			CB ₂ + C ₂ B ₃ + rhomb + C ₅ B _{14tr}			
				35	65	0	750				C ₂ B ₃ + rhomb + fcc
								770	60		C ₂ B ₃ + rhomb + fcc'
								790	0.66		C ₂ B ₃ + rhomb + fcc
								820	0.33		C ₂ B ₃ + fcc' + rhomb _{tr}
								830	0.33		C ₂ B ₃ + fcc'
					830	8.0		C ₂ B ₃ + fcc' + bcc _{tr}			
					840	0.33		C ₂ B ₃ + fcc' + bcc _{tr}			
					840	13.0		bcc			
					850	0.33		bcc + fcc' + unknown			
					850	1.0		bcc			
					920	0.16		bcc + fcc'			
							p.m.				
		37.5	62.5 (3:5)	0	750				C ₂ B ₃ + CB ₂ + C ₅ B ₁₄		
					650				C ₂ B ₃ + CB ₂		
					750 × 5						
	40	60 (2:3)	0								
#1				750							
				650				C ₂ B ₃ + CB ₂ + C ₅ B ₁₄ + CB + CaO			
				750 × 5				C ₂ B ₃			
#2				750							
				650							
				750 × 5				C ₂ B ₃			
				800				C ₂ B ₃			
				850				C ₂ B ₃			
				900	1.0		bcc				
#3				700							
				700 × 5				C ₂ B ₃			
				850				C ₂ B ₃			
				900				bcc + C-mon + unknown			
					750			C ₂ B ₃			
#4				700							
				800							
				900 × 2				C ₂ B ₃ + unknown			
				750				C ₂ B ₃			
					700	240		C ₂ B ₃			
					875	16		bcc			
					1000 } 700 }	1.0 240		C ₂ B ₃			

Table 1a. Experimental data for the system CaO-Bi₂O₃-CuO—Continued

Spec. no.	Composition mole percent			Heat treatment ^b			Phys. obser. ^c	Results of x-ray diffraction ^d
	CaO	1/2Bi ₂ O ₃	CuO	Initial	temp °C final	Time h		
#5				700				
				850				
				900 × 2				
				825				C ₂ B ₃
#6				700				
				750				
					860	0.33		bcc
					935	0.33	n.m.	bcc
					950	0.33	p.m.	bcc
	41.18	58.82 (7:10)	0					
				750				
				650				C ₂ B ₃ + CB ₂ + CB + CaO
					825	17		C ₂ B ₃ + CB
					900	20		bcc + C-mon + fcc'
				750 × 5				C ₂ B ₃ + CB
	42.86	57.14 (3:4)	0					
			700					
			750					
			850				C ₂ B ₃ + CB	
45	55	0						
			700					
			750				C ₂ B ₃ + CB + CB ₂ + CaO	
				650	96		C ₂ B ₃ + CB + CaO	
				850	16		C ₂ B ₃ + CB + CaO	
				870	0.66		bcc + CB	
				890	0.33		bcc + C-mon + CB	
				900	0.33		bcc + C-mon + CB _{1r}	
				900	1.00		bcc + C-mon	
				940	1.00		bcc + CB + C-mon	
				880	1.00			
				950	0.33	p.m.	bcc + C-mon _{1r}	
				1000	1.75	c.m.	bcc	
48	52	0						
			700					
			800				CB + bcc	
			900				C-mon + bcc + CaO	
				955	0.33		bcc + C-mon + CaO	
				960	0.33			
				940	0.33			
				970	0.33	p.m.	bcc + CaO	
#1	50	50	0					
				700				
				750				CB + C ₂ B ₃ + CaO
					650	96		CB + C ₂ B ₃ + CaO
					850	16		CB + C ₂ B ₃
					900	1.0		CB
				900				
					940	1.0		C-mon
				940 } 2.0				
				820 } 15			CB + Czmon	
				1000	1.0	c.m.	bcc + CaO	

Table 1a. Experimental data for the system CaO-Bi₂O₃-CuO—Continued

Spec. no.	Composition mole percent			Heat treatment ^b			Phys. obser. ^c	Results of x-ray diffraction ^d
	CaO	1/2Bi ₂ O ₃	CuO	Initial	temp °C final	Time h		
#2				750				C ₂ B ₃ + CB + CaO
					860	10.0		CB
					880	1.0		CB + unknown + CaO
					940	0.33		C-mon
					940	2.0		C-mon
					950	0.25		C-mon
					960	0.5	n.m.	C-mon + bcc + CaO
					970	0.33	p.m.	bcc + CaO
				940		2.0		C-mon
					850	3.0		C-mon
					880	11.0		CB
					1000 } 940 }	0.16 24.0		bcc + CaO
	#3				700			
				800				
				900				CB
				825				CB
					940			CB
#4				700				
				750 × 4				
				850				CB
				900				CB
#1	53.85	46.15 (7:6)	0	750				
				650				C ₂ B ₃ + rhomb + CB + CaO
				750 × 5				CB + CaO
#2				750				
				650				
				900				CB + CaO
#3				700				
				800				
				900				CB + CaO
				825				CB + CaO
					940	16.0		CB + CaO
#1	54	46	0	750				
				650				
					930	2.0	n.m.	C-Mon + CaO
					940	2.0		
					920	2.0		C-Mon + CaO
#1	57.14	42.86 (4:3)	0	750				
				850				CB + CaO + C ₂ B _{31r}
				900				CB + CaO

Table 1a. Experimental data for the system CaO-Bi₂O₃-CuO—Continued

Spec. no.	Composition mole percent			Heat treatment ^b			Phys. obser. ^c	Results of x-ray diffraction ^d
	CaO	1/2Bi ₂ O ₃	CuO	Initial	temp °C final	Time h		
#1	60	40	0	900				CB + CaO
				900 × 2				CB + CaO
#2				750				
				650				CB + C ₂ B ₃ + CaO
				750 × 5				CB + CaO
	66.67	33.33	0	750 × 2				CB + CaO
					920	0.33	n.m.	CB + CaO
					930	0.33	n.m.	C-Mon + CaO
					940	0.33	n.m.	C-Mon + CaO
					950	0.33	n.m.	C-Mon + CaO
					960	0.33	n.m.	bcc + CaO
	71.43	28.57 (5:2)	0	750 × 5				CB + CaO
	11.11	44.44	44.44	700				
				750			rhomb + CuO + B ₂ Cu	
				750 × 5			rhomb + CuO + B ₂ Cu	
	20	40	40	700				
				750			CuO + rhomb + CB ₂	
				750 × 5			CuO + CB ₂ + rhomb	
	33.33	33.33	33.33	700				
				750			CB + C ₂ B ₃ + CuO	
				750 × 5			CB + C ₂ B ₃ + CuO	
	44.02 <i>Ca₄Bi₆O₁₃ + Ca₂Bi₂O₅ + C_{1-x}CuO₂</i>	7.14	48.84 1:1:10	700				C _{1-x} Cu + C ₂ B ₃ + CB
				700 × 2			C _{1-x} Cu + CB + C ₂ B ₃	
				700 × 3			C _{1-x} Cu + CB + C ₂ B _{3tr}	
				700 × 4			C _{1-x} Cu + CB	
				700 × 4			C _{1-x} Cu + CB	
	44.44 <i>Ca₂CuO₃ + Bi₂CuO₄</i>	22.22	33.33 2:1	700				C ₂ Cu + B ₂ Cu
				700 × 2			C ₂ Cu + C ₂ B ₃ + B ₂ Cu + CuO	
				700 × 3			C ₂ Cu + C ₂ B ₃ + B ₂ Cu + CuO + CB C ₂ Cu + C ₂ B ₃ + CuO + CB + B ₂ Cu ^e	
	45	45	10	700				
				750				
					920	0.33	p.m.	bcc + C-mon + CaO
			940	0.33	c.m.	bcc + CaO + C-mon _{tr}		

Table 1a. Experimental data for the system CaO-Bi₂O₃-CuO—Continued

Spec. no.	Composition mole percent			Heat treatment ^b			Phys. obser. ^c	Results of x-ray diffraction ^d
	CaO	1/2Bi ₂ O ₃	CuO	Initial	temp °C final	Time h		
49	49	2	700	900	0.33	0.33	p.m.	CB
			750					
			910					
			915					
50	25	25	700	800	0.33	p.m.	CB	
			750					
			750×5					
			750×5					
54	23	23	700	700	6		CB + CaO + CuO + C _{1-x} Cu	
			750×6					
54.95 <i>Ca₄Bi₆O₁₃ + Ca₂CuO₃ + C_{1-x}CuO₂</i> 1:7:3	14.63	30.41	700	700	2		C ₂ B ₃ + C ₂ Cu + C _{1-x} Cu	
			700×2					
			700×3					
			700×3					
56	24	20	700	700	3	O ₂	C ₂ B ₃ + C ₂ Cu + C _{1-x} Cu + CB	
			700×2					
			700×3					
			700×3					
#1	<i>Ca₄Bi₆O₁₃ + Ca₂CuO₃</i> 1:5		700	700	2		C ₂ Cu + C ₂ B ₃	
			700×2					
#2			700	750	2		C ₂ Cu + C ₂ B ₃ + CB	
			700×2					
#3	+ C _{1-x} Cu _{tr}		700	700	2		C ₂ Cu + CB + C ₂ B ₃ + CB + CuO	
			700×2					
#4	+ C _{1-x} Cu(more)		700	700	2		C ₂ Cu + CB + C ₂ B ₃ + CuO	
			700×2					
57.14 <i>Ca₂CuO₃ + Bi₂CuO₄</i> 6:1	9.52	33.33	700	700	3		C ₂ Cu + CB + C ₂ B ₃ + C _{1-x} Cu	
			700×2					
			700×3 ^f					
			700×4 ^f					
			700×5 ^f					
60	20	20	700	700	2		C ₂ Cu + B ₂ Cu	
			750					
			750×5					
			750×9					
60	20	20	700	700	2		C ₂ Cu + B ₂ Cu + C ₂ B ₃ + CuO	
			750					
			750×5					
			750×9					
60	20	20	700	700	2		C ₂ Cu + CB + C ₂ B ₃ + CuO	
			750					
			750×5					
			750×9					

Table 1a. Experimental data for the system CaO-Bi₂O₃-CuO—Continued

Spec. no.	Composition mole percent			Heat treatment ^b			Phys. obser. ^c	Results of x-ray diffraction ^d
	CaO	1/2Bi ₂ O ₃	CuO	Initial	temp °C final	Time h		
61.29	19.35	19.35						
	<i>Ca₂CuO₃ + Ca₇Bi₆O₁₆</i>							
	6:1							
				750 × 2				
					700	336		CB + C ₂ Cu + CaO CB + C ₂ Cu + CaO _{tr}
70	15	15						
				700				
				750 × 5				
					800			CaO + CB + Ca _{1-x} Cu + CuO
					850			CaO + CB + Ca _{1-x} Cu + CuO
					900			CaO + CB + C ₂ Cu
					900			CaO + C-mon + C ₂ Cu
					750			CaO + CB + C ₂ Cu
					900			CaO + Czmon + C ₂ Cu
					750			CaO + Czmon + C ₂ Cu
					900 × 7,126			

^a Starting materials CaCO₃, Bi₂O₃, CuO except when listed in italics. Compositions given in italics were formulated from the listed pre-reacted compounds or compositions.

^b Specimens were given all previous heat treatments listed in the initial column, sequentially, and held at temperature 16–24 h, with grinding in between, for the number of times shown and then reheated at the final temperature for the indicated number of hours. (if hours are not specified heat treatment was overnight). O₂ = heat treatment in one atmosphere of purified oxygen.

^c p.m. = partially melted, c.m. = completely melted, n.m. = no melting, s.m. = slightly melted.

^d Compounds are listed in order of estimated amounts, most prevalent first.

tr = trace, just barely discernable.

C₂Cu = Ca₂CuO₃

C_{1-x}Cu = Ca_{1-x}CuO₂

CCu₂ = CaCu₂O₃

rhomb = rhombohedral solid solution

fcc = face centered cubic solid solution; symmetry often distorted and generally with superstructure

fcc' - very slight rhombohedral distortion of cubic symmetry, with incommensurate superstructure perpendicular to the hexagonal *c** (corresponding to α', of [20].

fcc'' - metastable phase with larger rhombohedral distortion of cubic

symmetry, with superstructure equal to 42 and faint incommensurate

superstructure perpendicular to the hexagonal [*h*0*l*] plane.

bcc = body centered cubic solid solution; symmetry often distorted and generally with superstructure.

C₅Bi₁₄ = Ca₅Bi₁₄O₂₆

CB₂ = CaBi₂O₄

C₂B₃ = Ca₄Bi₆O₁₃

CB = Ca₂Bi₂O₅ (triclinic)

C-mon = metastable C-centered monoclinic phase near Ca₆Bi₇O_{16.5}.

^e Although Ca₄Bi₆O₁₃ has formed during first 700 °C heat treatment, further heating and grinding resulted in formation of Ca₂Bi₃O₅, which increased with the third heat treatment, indicating that the 2:3 phase was formed metastably but the 1:1 compound is the stable phase.

^f Amount of 2:3 decreasing and amount of Ca_{1-x}CuO₂ may be increasing very slightly.

Table 1(b). Experimental conditions for crystal growth experiments

Charge	Flux	Container	Temperature cycle	Results
CaO:1/2Bi ₂ O ₃ 1:6 90 wt%	(KNa)Cl 10 wt%	Small dia Au sealed	700 °C 595 h	biaxial xtals Rhomb (Orth)
CaO:1/2Bi ₂ O ₃ 1:4		Small dia Au sealed	700→875 °C @ 10 °C/h 875→650 °C @ 3 °C/h	
CaO:1/2Bi ₂ O ₃ 5:14 20 wt%	(KNa)Cl 80 wt%	Large dia Pt sealed	750 °C→645 °C @ 1 °C/h 645 °C 64 h	
CaO:1/2Bi ₂ O ₃ 5:14 20 wt%	(KNa)Cl 80 wt%	large dia Pt	750 °C→645 °C @ 1 °C/h 645 °C 64 h	
CaO:1/2Bi ₂ O ₃ 5:14	10 μL H ₂ O	Small dia Au sealed	Hydrothermal unit 700 °C 100 MPa	
CaO:1/2Bi ₂ O ₃ 5:14 80 wt%	(KNa)Cl 20 wt%	Large dia Au sealed	650 °C→750 °C @ 10 °C/h 750 °C→640 °C @ 1 °C/h	
CaO:1/2Bi ₂ O ₃ 5:14	None	Small dia Au open Small dia Au open	900 °C, 20 min. quenched (liq N ₂ cooled He cup) crushed 780 °C 67.5 h quenched (liq N ₂ cooled He cup)	fcc'
CaO:1/2Bi ₂ O ₃ 5:14	None	Small dia Au sealed Small dia Au open	925 °C→850 °C @ 3 °C/h 850 °C 24 h quenched (liq N ₂ cooled He cup) 650 °C 2 weeks	Ca ₅ Bi ₁₄ O ₂₆
CaO:1/2Bi ₂ O ₃ 5:14	None	Small dia Au sealed Small dia Au open	925 °C→850 °C @ 3 °C/h 650 °C 16 h	
CaO:1/2Bi ₂ O ₃ 3:8	None	Small dia Au open Small dia Au open	900 °C 22 h quenched (liq N ₂ cooled He cup) crushed –800 °C 3 d quenched (liq N ₂ cooled He cup) –760 °C 15 min pulled from furnace –800 °C 1 h quenched (liq N ₂ cooled He cup) –760 °C 10 min quenched (liq N ₂ cooled He cup)	fcc''

Table 1(b). Experimental conditions for crystal growth experiments—Continued

Charge	Flux	Container	Temperature cycle	Results
CaO:1/2Bi ₂ O ₃ 33:67 80 wt%	(KNa)Cl 20 wt%	Small dia Au sealed	775 °C (18h)→645 °C @ 1 °C/h	
CaO:1/2Bi ₂ O ₃ 33:67 20 wt%	(KNa)Cl 80 wt%	Small dia Au sealed	775 °C(18h)→645 °C @ 1 °C/h	CaBi ₂ O ₄
CaO:1/2Bi ₂ O ₃ 33:67 50 wt%	(KNa)Cl 50 wt%	Small dia Au sealed	775 °C(18h)→645 °C @ 1 °C/h	CaBi ₂ O ₄
CaO:1/2Bi ₂ O ₃ 1:2 20 wt%	(KNa)Cl 80 wt%	Large dia Pt sealed	750 °C→645 °C @ 1 °C/h 645 °C 64 h	
CaO:1/2Bi ₂ O ₃ 1:2 20 wt%	(KNa)Cl 80 wt%	Large dia Pt	750 °C→645 °C @ 1 °C/h 645 °C 64 h	
CaO:1/2Bi ₂ O ₃ 1:2 20 wt%	(KNa)Cl 80 wt%	vycor cruc.	675 °C 144 h	
CaO:1/2Bi ₂ O ₃ 1:2	None	Small dia Au sealed	925 °C→850 °C @ 3 °C/h 850 °C 24 h quenched (liq N ₂ cooled He cup) crushed	
		Small dia Au open	500 °C→700 °C @ 3 °C/h 700 °C 168 h	
CaO:1/2Bi ₂ O ₃ 1:2	None	Small dia Au sealed	925 °C→850 °C @ 3 °C/h	
		Small dia Au open	650 °C 16 h	
CaO:1/2Bi ₂ O ₃ 1:2 80 wt%	(KNa)Cl 20 wt%	Large dia Au sealed	650 °C→750 °C @ 10 °C/h 750 °C→640 °C @ 1 °C/h	
CaO:1/2Bi ₂ O ₃ 1:2	10 μL H ₂ O	Small dia Au sealed	Hydrothermal unit 700 °C 100 MPa	
CaO:1/2Bi ₂ O ₃ 1:2	None	Large dia Au sealed	750 °C→875 °C @ 25 °C/h 875 °C→845 °C @ 1 °C/h	
CaO:1/2Bi ₂ O ₃ 1:2	None	Small dia Au sealed	925 °C 10 min quenched (liq N ₂ cooled He cup) crushed to a fine powder	
		Small dia Au open	500 °C→700 °C @ 3 °C/h	

Table 1(b). Experimental conditions for crystal growth experiments—Continued

Charge	Flux	Container	Temperature cycle	Results
CaO:1/2Bi ₂ O ₃ 2:3	None	Small dia Au sealed	1000 °C→900 °C @ 1 °C/h crushed	
		Small dia Au sealed	825 °C 190 h furnace cooled	
CaO:1/2Bi ₂ O ₃ 2:3	None	Small dia Au sealed	1000 °C 1 h quenched (liq N ₂ cooled He cup) 875 °C 260 h	Ca ₄ Bi ₆ O ₁₃
CaO:1/2Bi ₂ O ₃ 2:3 98 wt%	(KNa)Cl 2 wt%	Large dia Au sealed	840 °C→640 °C @ 1 °C/h	
CaO:1/2Bi ₂ O ₃ 2:3 80 wt%	(KNa)Cl 20 wt%	Large dia Au sealed	840 °C→640 °C @ 1 °C/h	
CaO:1/2Bi ₂ O ₃ 2:3 50 wt%	(KNa)Cl 50 wt%	Large dia Au sealed	840 °C→640 °C @ 1 °C/h	
CaO:1/2Bi ₂ O ₃ 2:3 20 wt%	(KNa)Cl 80 wt%	Large dia Au sealed	840 °C→640 °C @ 1 °C/h	
CaO:1/2Bi ₂ O ₃ 7:10 20 wt%	(KNa)Cl 80 wt%	Large dia Pt sealed	750 °C→645 °C @ 1 °C/h 645 °C 64 h	Ca ₄ Bi ₆ O ₁₃
CaO:1/2Bi ₂ O ₃ 7:10 20 wt%	(KNa)Cl 80 wt%	Large dia Pt	750 °C→645 °C @ 1 °C/h	
CaO:1/2Bi ₂ O ₃ 6:7 80 wt%	CaCl ₂ 20 wt%	Large dia Au open	900 °C 20 h	
CaO:1/2Bi ₂ O ₃ 1:1 80 wt%	(KNa)Cl 20 wt%	Small dia Au sealed	650 °C→950 °C @ 100 °C/h 950 °C→900 °C @ 1 °C/h	
CaO:1/2Bi ₂ O ₃ 1:1 50 wt%	(KNa)Cl 50 wt%	Small dia Au sealed	650 °C→950 °C @ 100 °C/h 950 °C→900 °C @ 1 °C/h	
CaO:1/2Bi ₂ O ₃ 1:1 20 wt%	(KNa)Cl 80 wt%	Small dia Au sealed	650 °C→950 °C @ 100 °C/h 950 °C→900 °C @ 1 °C/h	
CaO:1/2Bi ₂ O ₃ 7:6 20 wt%	(KNa)Cl 80 wt%	Large dia Pt sealed	750 °C→645 °C @ 1 °C/h 645 °C 64 h	Ca ₂ Bi ₂ O ₅

Table 1(b). Experimental conditions for crystal growth experiments—Continued

Charge	Flux	Container	Temperature cycle	Results
CaO:1/2Bi ₂ O ₃ 7:6 20 wt%	(KNa)Cl 80 wt%	Large dia Pt	750 °C→645 °C @ 1 °C/h	
CaO:1/2Bi ₂ O ₃ 7:6 80 wt%	(KNa)Cl 20 wt%	Large dia Au sealed	900 °C 19.5 h	

3. Experimental Results and Discussion

Most of the experiments performed on the binary and ternary mixtures of CaO-Bi₂O₃-CuO are reported in Table 1a. Additional experiments specifically designed in an attempt to obtain crystals large enough for x-ray single crystal studies are detailed in Table 1b. Crystallographic data for various phases are reported in Table 2.

3.1 The System Bi₂O₃-CuO

A phase diagram for this system was already published [16], and was redrawn as Fig. 6392 in Phase Diagrams for Ceramists (PDFC) [17]. It apparently contains only one compound Bi₂CuO₄ (B₂Cu). No attempt was made to reinvestigate the melting relations of this system because it does not have any great effect on the phase equilibria of the ternary system with CaO.

3.2 The System CaO-CuO

Although a revised phase diagram for this system was previously reported [7], further experimental evidence (Table 1a) was accumulated in this study and the diagram was revised again [18] as shown in Fig. 1. The CaCu₂O₃ compound, which was reported to be stable only above 950 °C [19], was found to be stable between 985 and 1018 °C. Previously determined temperatures, 1020 and 1013 °C [20,7] for the decomposition of CaCu₂O₃(CCu₂) and for eutectic melting, respectively, are within experimental error of the new values, 1018 ± 2 °C and 1012 ± 2 °C.

3.2.1 Ca₂CuO₃ The Ca₂CuO₃(C₂Cu) compound decomposes into CaO plus liquid above 1034 ± 2 °C, which is slightly above the previous estimate of 1030 °C [20,7]. The composition of the eutectic reaction is 20CaO–80CuO ± 5%, as determined from the presence or absence of the

Ca₂CuO₃ phase in samples of varying compositions that were quenched from 1020 °C.

3.2.2 Ca_{1-x}CuO₂ Samples prepared with an original Ca:Cu ratio of 45.33:54.67 contained no detectable CaO or CuO after heating in oxygen at 700 °C, as demonstrated by x-ray diffraction (Fig. 2 and Table 3). Compositions with original Ca:Cu ratios of 45.20:54.80 and 45.45:54.54 (≈5:6) yielded x-ray patterns which indicated the presence of excess CuO and excess CaO, respectively. Therefore, the Ca:Cu ratio for this compound is 0.453:0.547 or Ca_{1-x}CuO₂ with the composition Ca_{0.828}CuO₂ (x = 0.172) at 700 °C in oxygen. The single phase region for this phase probably varies with temperature and partial pressure of oxygen. The composition and structural analyses of this phase have been recently reported [15]. The x-ray powder diffraction pattern for Ca_{1-x}CuO₂ is shown in Fig. 2 and the indexed data is given in Table 3. This compound decomposes into Ca₂CuO₃ plus CuO above 755 °C in air and 835 °C in oxygen. In Fig. 1, the experiments conducted in air and those conducted in an oxygen atmosphere are indicated by the dashed line and the crosses, respectively. At 675 °C, Ca_{1-x}CuO₂ can be synthesized from CaCO₃ plus CuO but the run product never fully equilibrates to a single- or two-phase assemblage. Rather, the metastable three-phase assemblage Ca_{1-x}CuO₂ + CaO + CuO persists: after five cycles of heating with intermittent grinding the relative proportions of phases were Ca_{1-x}CuO₂ > CaO > CuO and they remained that way for an additional overnight heat treatments. Because of its great persistence, Ca_{1-x}CuO₂ is interpreted as being an equilibrium phase, but it should be noted that reversal of its decomposition (synthesis from CuO + Ca₂CuO₃) was not successfully demonstrated.

Table 2. Crystal structure data

Chemical formula	Symmetry phase (T °C)	a (Å)	b (Å)	c (Å)	α degrees	β degrees	γ degrees
$\text{Ca}_{1-x}\text{CuO}_2$ $x=0.172$	Fmmm ^a $T \sim 700$ °C	2.8047 ^b (7)	6.321 (2)	10.573 (2)			
$\text{CaO}:1/2\text{Bi}_2\text{O}_3$ 1:6	$R\bar{3}$	3.9448 (8)		27.8400 (8)			
	$T \sim 750$ °C						
	Cmmm	6.8188 (3)	3.9531 (2)	27.830 (1)			
$\text{CaO}:1/2\text{Bi}_2\text{O}_3$ 3:8	$R\bar{3}$	7.7427 (9)		9.465 (1)			
	α' ($T \sim 780$ °C)						
	B2/m	15.5819 (3)	3.8077 (1)	10.8955 (3)		91.829 (2)	
$\text{Ca}_5\text{Bi}_{12}\text{O}_{41}$	$P\bar{1}$	9.934 (1)	15.034 (2)	15.008 (2)	82.65 (1)	85.27 (1)	
CaBi_2O_4	$C2/c$	16.6295 (8)	11.5966 (5)	14.0055 (6)		134.036 (3)	
$\text{Ca}_4\text{Bi}_6\text{O}_{13}$	$C2mm$	17.3795 (5)	5.9419 (2)	7.2306 (2)			
$\text{CaO}:1/2\text{Bi}_2\text{O}_3$ 9:10	"bcc"	4.2458 (1)					
	$T \sim 1000$ °C						
$\text{Ca}_2\text{Bi}_2\text{O}_5$	$P\bar{1}$	10.1222 (7)	10.146 (6)	10.4833 (7)	116.912 (5)	107.135 (6)	92.939 (6)
$\text{Ca}_{6+x}\text{Sr}_{6-x}\text{Bi}_{14}\text{O}_{33}$ $x \rightarrow 6$	C-centered monoclinic	21.295 (4)	4.3863 (8)	12.671 (2)		102.74 (1)	

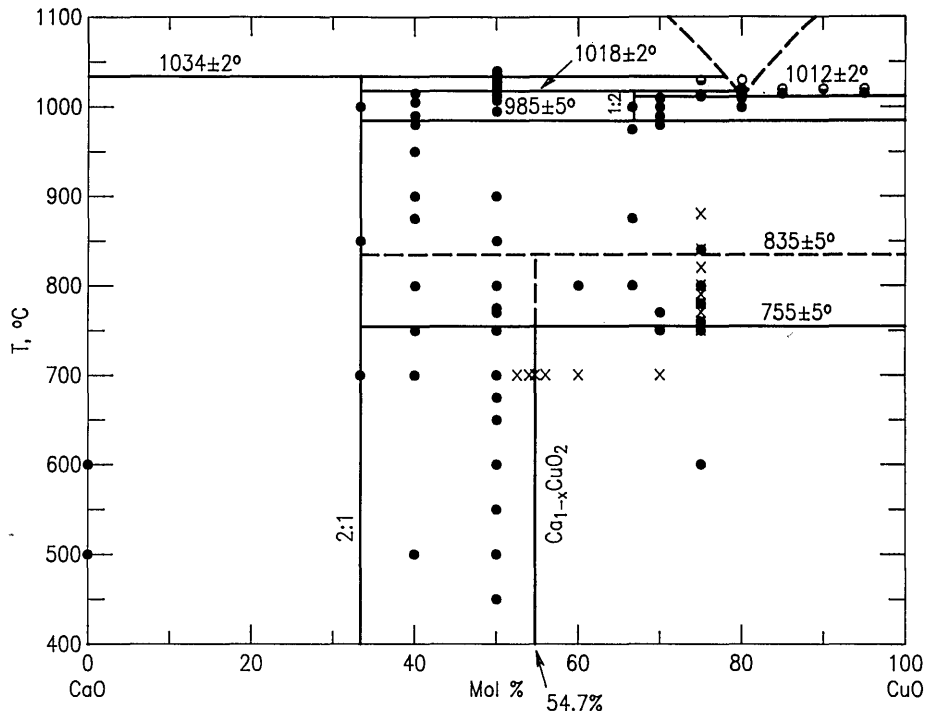
^a Indicates a subcell.^b Numbers in parentheses indicate uncertainties in final digits.

Fig. 1. CaO-CuO phase diagram.

Table 3. X-ray powder diffraction data for the compound $\text{Ca}_{1-x}\text{CuO}_2$

<i>d</i> obs (Å)	Rel <i>I</i> (%)	2θ obs	2θ calc ^a	<i>hkl</i>
5.273	13	16.80	16.76	002
3.1554	21	28.26	28.21	002
3.0994	1	28.78 ^b		
2.8914	6	30.90	30.91	1-δa,1,1-δc
2.8245	3	31.65	31.66	1-δa,1,1+δc
2.7106	100	33.02	32.99	022
2.6407	22	33.92	33.89	004
2.4887	23	36.06	36.02	111
2.3218	6	38.75	38.77	1-δa,1,3-δc
2.2207	7	40.59	40.60	1-δa,1,3+δc
2.0720	61	43.65	43.62	113
1.7666	4	51.70	51.72	1-δa,3,1-δc
1.7613	6	51.87	51.84	600
1.7571	6	52.00	51.95	1-δa,1,5-δc
1.7527	8	52.14	52.21	1-δa,3,1+δc
1.6840	2	54.44	54.39	1-δa,1,5+δc
1.6632	10	55.18	55.16	131
1.6306	29	56.38	56.36	115
1.6088	2	57.21	57.23	1-δa,3,3-δc
1.5802	12	58.35	58.34	040
1.5397	18	60.04	60.06	026
1.5200	16	60.90	60.90	133
1.4811	1	62.67 ^b		
1.4545	1	63.95 ^b		
1.4467	1	64.34 ^b		
1.4129	1	66.07 ^b		
1.4025	6	66.63	66.64	200
1.3702	1	68.41	68.42	1-δa,1,7-δc
1.3565	12	69.20	69.21	044
1.3471	2	69.75 ^b		
1.3208	13	71.35	71.33	1-δa,1,7+δc
1.3186	15	71.49	71.55	135
1.3018	5	72.56	72.59	117
1.2819	5	73.87	73.87	220

^a Calculated on the basis of an orthorhombic subcell, Fmmm, $a = 2.8047$ (7), $b = 6.321$ (2), and $c = 10.573$ (2) Å.

^b Superstructure probably not accounted for by δ-vectors.

3.2.3 Cu_2O in the Binary System Cu_2O , which is known to be stable in air only above 1026 °C, was found in this system above 1012 °C. Therefore, Cu^+ and Cu^{2+} must have coexisted in the samples that were quenched in air from temperatures between 1012 and 1026 °C. The Cu_2O observed in samples that were quenched from below 1026 °C is probably formed during solidification of the liquid phase; i.e., an oxygen deficiency in the liquid may result in the solidification of Cu_2O as well as CuO .

3.3 The System $\text{CaO-Bi}_2\text{O}_3$

The phase equilibria diagram for the system $\text{CaO-Bi}_2\text{O}_3$ was reported in [21] and redrawn as Fig. 6380 in PDFC [17]. It is reproduced here as

Fig. 3 with the scale changed to $1/2\text{Bi}_2\text{O}_3\text{-CaO}$ instead of $\text{Bi}_2\text{O}_3\text{-CaO}$, to maintain consistency with the other phase diagrams in this report. An interpretation of the experimental results recorded in Table 1 was published in [19] and it is shown in Fig. 4 (cf. Fig. 3). The major differences between our new diagram and the one presented in [21] are: 1) the composition of “ $\text{Ca}_7\text{Bi}_{10}\text{O}_{22}$ ” [21,22] is revised to $\text{Ca}_4\text{Bi}_6\text{O}_{13}$ (2:3) and its crystal structure is reported in [23]; 2) the composition of “ $\text{Ca}_7\text{Bi}_6\text{O}_{16}$ ” [21,22] is now reported as $\text{Ca}_2\text{Bi}_2\text{O}_5$, and its crystal structure is given in [24]; 3) a metastable phase $\sim\text{Ca}_6\text{Bi}_7\text{O}_{16.5}$ was formed at about 925 °C on the CaO-rich side of $\text{Ca}_2\text{Bi}_2\text{O}_5$, but at about 885 °C on the CaO-poor side; 4) melting relations have been determined in the region of 20–50 mol % CaO.

3.3.1. Rhombohedral Solid Solution (Sillen Phase-Rhomb) The rhombohedral solid solution was first reported by Sillen [25]. Phase relations in the CaO-rich region of the Sillen phase field were previously [20] represented as exhibiting a congruent transition to the fcc solid solution, and the present experiments indicate such a point at (~22 mol % CaO, ~835 °C). Conflant et al. [21] reported a phase transition from one rhombohedral phase to another at about 735–740 °C. Differential thermal analysis of a 1:6 ratio $\text{CaO}:1/2\text{Bi}_2\text{O}_3$ specimen confirms the presence of a reversible transition at about 735 °C. Samples quenched from ~750 °C are clearly rhombohedral as previously reported [21,22], but x-ray patterns (Figs. 5a, 5b; Tables 4, 5, 6) from samples that were quenched from ≤ 735 °C exhibit peak splitting and faint superstructure reflections (Fig. 5b). The diffraction patterns for both the high and low temperature forms are much sharper if the specimens are not ground after quenching. Apparently, it is easy to induce mechanical deformation in these samples by grinding. The peak splitting can be indexed with an orthorhombic cell $a = 6.8188$ (3), $b = 3.9531$ (2), and $c = 27.830$ (1) Å, which is most easily observed in the rhombohedral (0,2,13) and (3,0,9) reflections corresponding to (2,2,13)+(4,0,13) and (3,3,9)+(6,0,9), respectively, in the orthorhombic indexing (Figs. 5a, 5b, and Tables 5, 6). Dimensionally the unit cell is orthorhombic, but the symmetry cannot be higher than monoclinic because it is the derivative of a rhombohedral (rather than hexagonal) high symmetry phase. Single crystals prepared at 700 °C with a salt eutectic flux (Table 1b) give a biaxial interference figure, in polarized light, parallel to the pseudo-rhombohedral *c* axis.

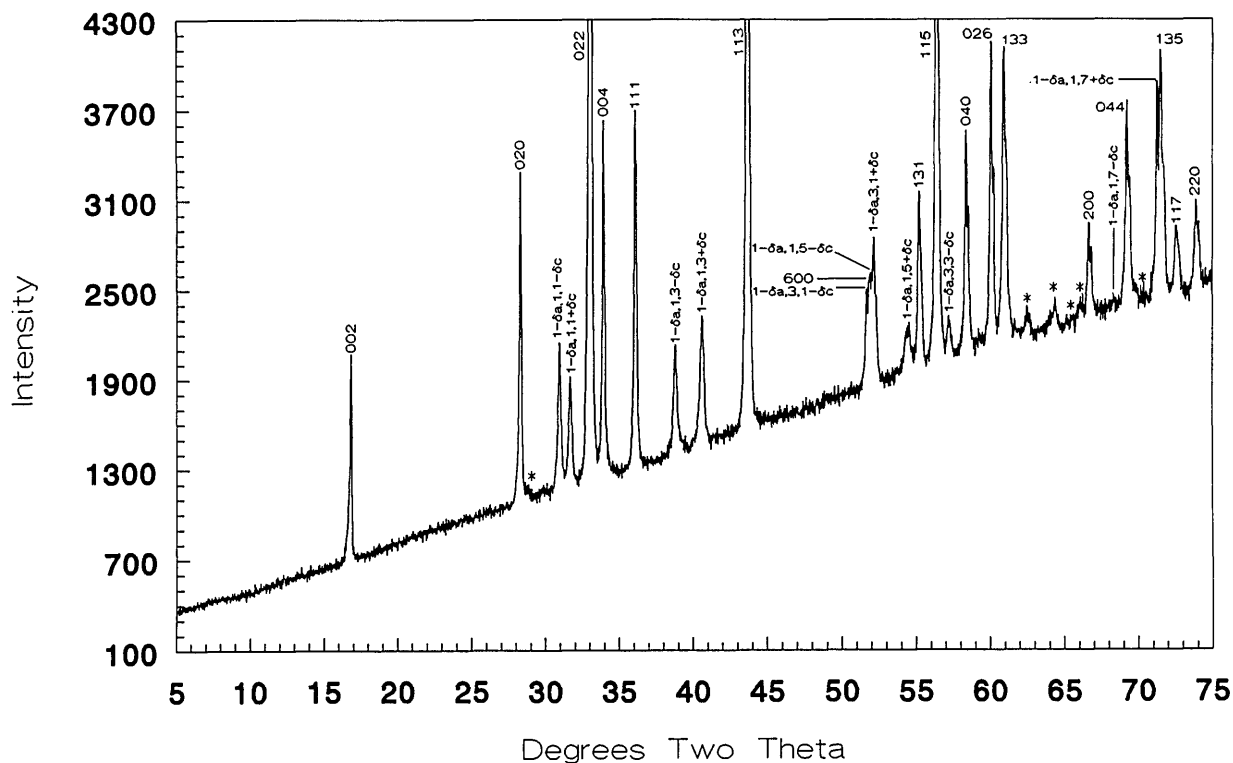


Fig. 2. $\text{Ca}_{1-x}\text{CuO}_2$ x-ray diffraction powder pattern (CaO:CuO 45.328:54.672).

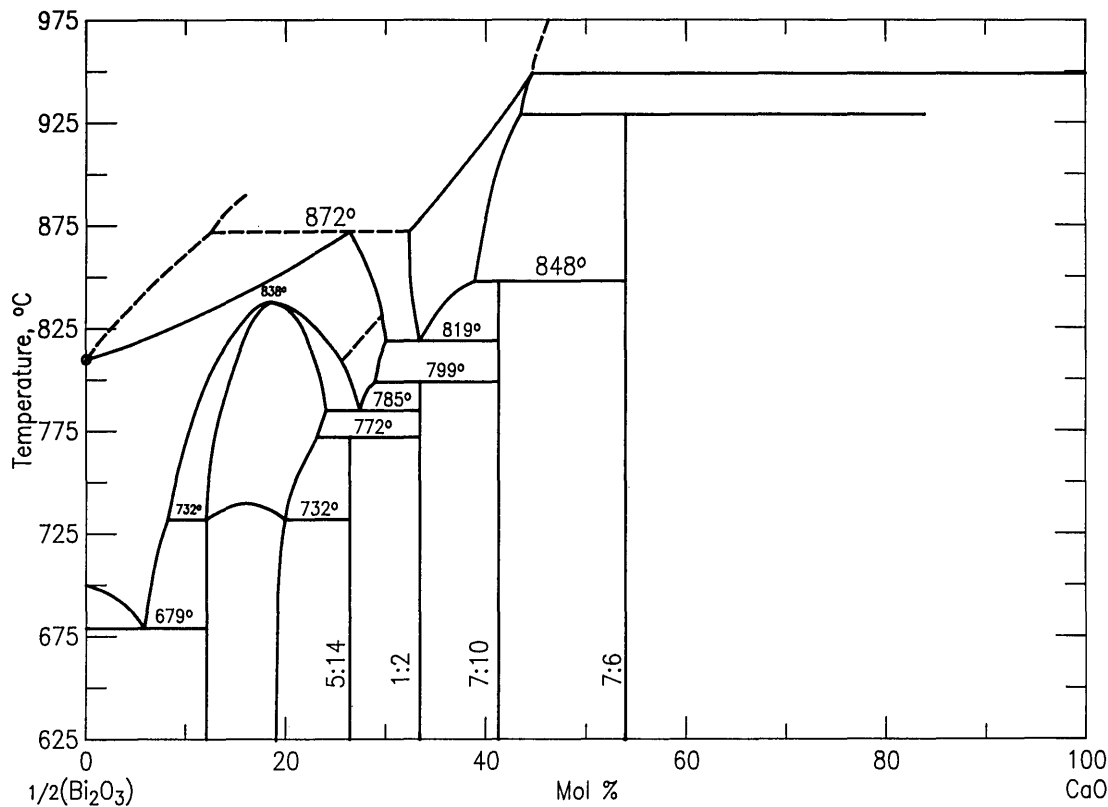


Fig. 3. $\text{CaO}-1/2\text{Bi}_2\text{O}_3$ phase diagram as changed from PDFC 6380-Conflant et al.

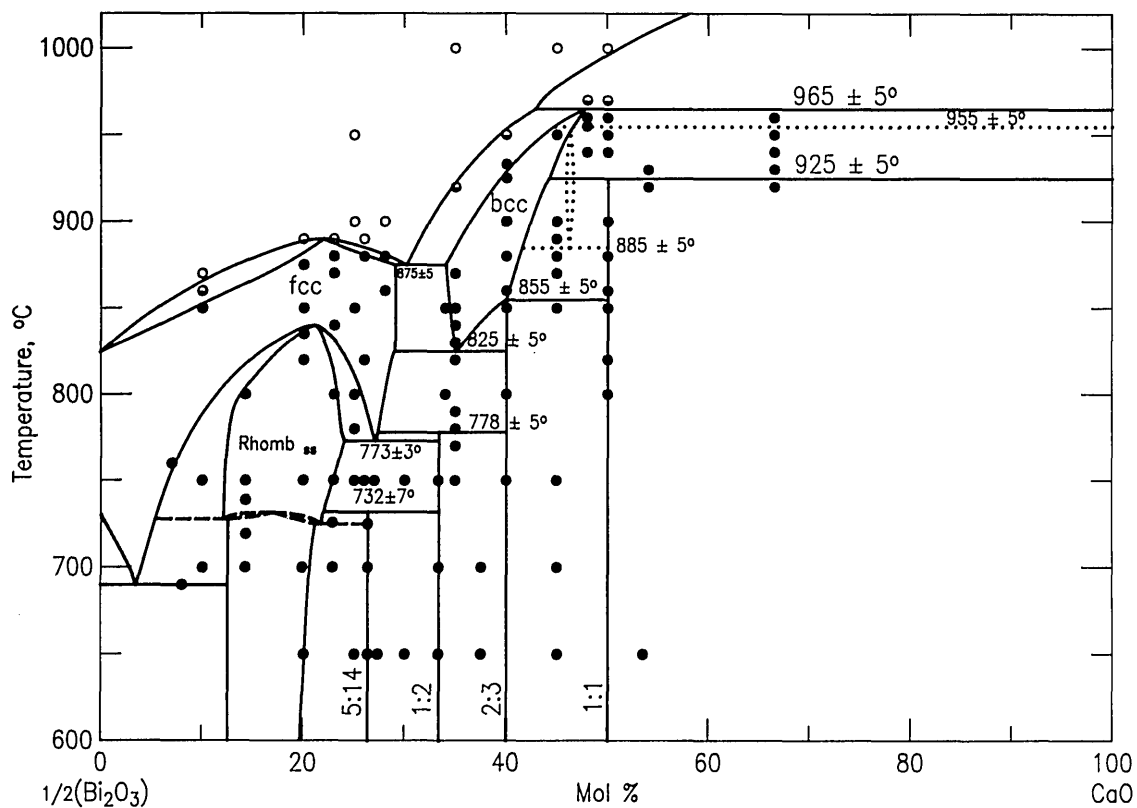


Fig. 4. CaO- $1/2\text{Bi}_2\text{O}_3$ —present phase diagram.

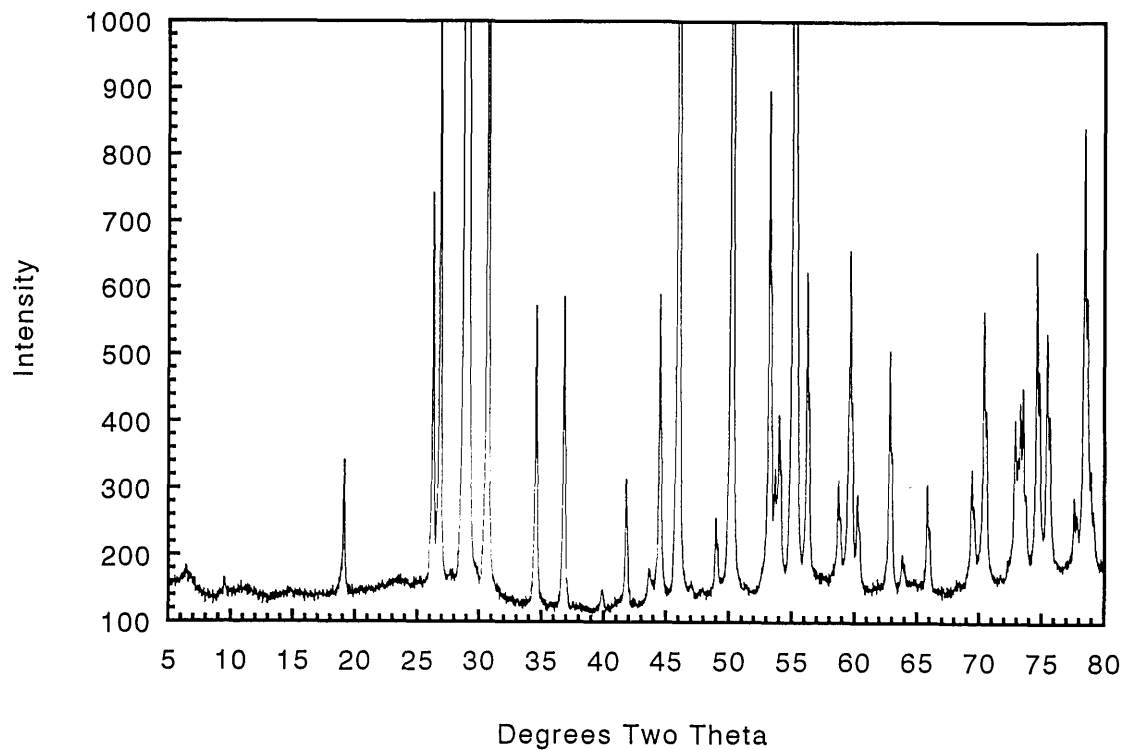


Fig. 5a. X-ray powder diffraction pattern CaO: $1/2\text{Bi}_2\text{O}_3$ 1:6 quenched from 740 °C.

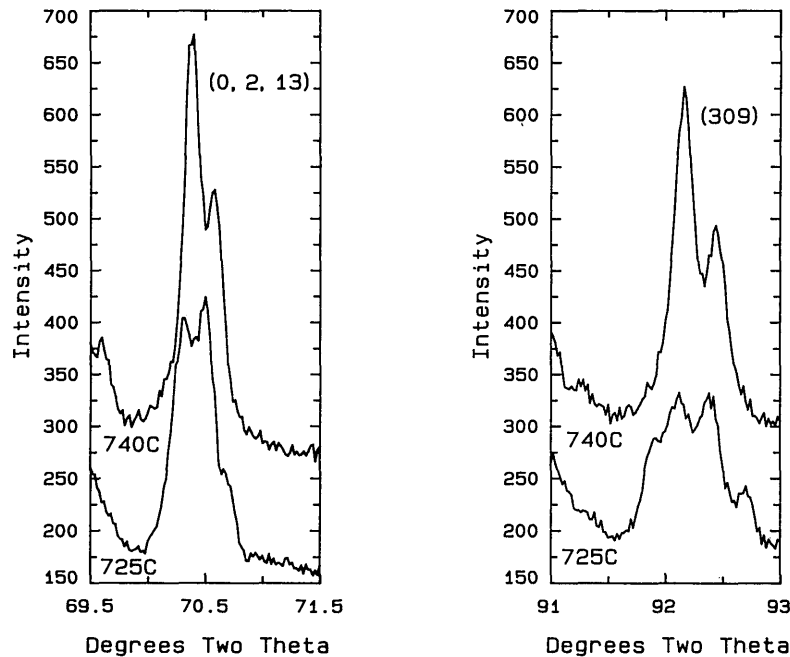


Fig. 5b. X-ray powder diffraction pattern of CaO:1/2Bi₂O₃ 1:6 quenched from 740 °C (rhombohedral indexing) and 725 °C (orthorhombic indexing).

Table 4. X-ray powder diffraction data for the high temperature rhombohedral (Sillen phase) indexing of CaO:1/2Bi₂O₃ 1:6

<i>d</i> obs (Å)	Rel <i>I</i> (%)	2 <i>θ</i> obs	2 <i>θ</i> calc ^a	<i>hkl</i>
9.254	4	9.55	9.52	003
4.633	8	19.14	19.11	006
3.3897	23	26.27	26.26	101
3.3166	31	26.86	26.85	012
3.0922	93	28.85	28.84	009
3.0651	100	29.11	29.09	104
2.9099	56	30.70	30.68	015
2.5896	16	34.61	34.58	107
2.4372	17	36.85	36.84	018
	2	39.90 ^b		
2.1578	10	41.83	41.82	1,0,10
	2	43.67 ^b		
2.0326	17	44.54	44.52	0,1,11
1.9726	57	45.97	45.98	110
1.9283	1	47.09	47.07	113
1.8554	12	49.06	49.04	0,0,15
1.8149	57	50.23	50.22	116
			50.24	1,0,13
1.7188	24	53.25	53.26	0,1,14
1.7043	8	53.74	53.72	021
1.6953	10	54.05	54.05	202
1.6629	72	55.19	55.19	119
1.6333	16	56.28	56.29	205
1.5694	6	58.79	58.79	027
1.5500	10	59.60	59.58	1,0,16
1.5467	18	59.74	59.74	0,0,18
1.5334	6	60.31	60.31	208
1.4770	12	62.87	62.88	0,1,17
1.4561	2	63.88	63.89	0,2,10
1.4157	6	65.93	65.92	2,0,11

Table 4. X-ray powder diffraction data for the high temperature rhombohedral (Sillen phase) indexing of CaO:1/2Bi₂O₃ 1:6—Continued

<i>d</i> obs (Å)	Rel <i>I</i> (%)	2 <i>θ</i> obs	2 <i>θ</i> calc ^a	<i>hkl</i>
1.3516	7	69.49	69.49	1,1,15
1.3355	12	70.45	70.46	0,2,13
1.2956	8	72.96	72.95	2,0,14
1.2891	10	73.39	73.39	0,1,20
1.2856	11	73.62	73.61	122
1.2693	15	74.73	74.71	214
1.2579	13	75.52	75.53	125
1.2280	4	77.70	77.69	217
1.2171	21	78.53	78.53	1,1,18
1.2105	5	79.04	79.03	128
1.1868	14	80.94	80.95	1,0,22
1.1823	9	81.31	81.33	2,0,17
1.1712	2	82.25	82.24	2,1,10
1.1598	3	83.24	83.22	0,0,24
1.1503	5	84.08	84.09	1,2,11
1.1407	8	84.95	84.93	0,1,23
1.1386	12	85.15	85.13	300
1.1122	1	87.67	87.68	0,2,19
1.1059	13	88.30	88.30	306
			88.31	2,1,13
1.0828	7	90.70	90.68	1,2,14
1.0790	2	91.11	91.10	2,0,20
1.0686	10	92.25	92.24	309
1.0587	2	93.37	93.36	1,0,25
1.0368	2	95.97	95.95	2,1,16
1.0309	7	96.70	96.67	0,0,27
1.0217	8	97.86	97.86	0,1,26
1.0169	8	98.49	98.50	0,2,22
1.0141	9	98.86	98.87	1,2,17

Table 4. X-ray powder diffraction data for the high temperature rhombohedral (Sillen phase) indexing of $\text{CaO}:1/2\text{Bi}_2\text{O}_3$ 1:6—Continued

<i>d</i> obs (Å)	Rel <i>I</i> (%)	2 θ obs	2 θ calc ^a	<i>hkl</i>
0.9999	3	100.77	100.78	1,1,24
0.9876	3	102.52	102.52	2,0,23
0.9863	4	102.70	102.72	220
0.9707	1	105.04	105.05	3,0,15
0.9469	4	108.88	108.87	131
0.9454	4	109.14	109.15	312
0.9394	8	110.16	110.13	229
0.9341	4	111.10	111.11	315
0.9330	3	111.31	111.33	0,2,25
0.9243	2	112.90	112.91	0,1,29
0.9218	3	113.36	113.38	137
0.9171	7	114.27	114.28	3,0,18
0.9141	10	114.84	114.83	318
0.9076	3	116.14	116.15	2,2,12
0.9072	3	116.22	116.22	2,0,26
0.9038	7	116.92	116.93	2,1,22
0.8970	1	118.35	118.36	1,3,10
0.8875	2	120.45	120.47	3,1,11
0.8832	3	121.43	121.45	1,2,23
0.8686	6	124.95	124.97	1,0,31
0.8665	7	125.50	125.49	1,3,13
0.8554	4	128.46	128.46	3,1,14

^aCalculated on the basis of a rhombohedral unit cell, $R\bar{3}$, $a = 3.9448(8)$ and $c = 27.8400(8)$ Å.

^bApparently due to an unidentified structure.

Table 5. X-ray powder diffraction data for the low temperature orthorhombic indexing of $\text{CaO}:1/2\text{Bi}_2\text{O}_3$ 1:6

<i>d</i> obs (Å)	Rel <i>I</i> (%)	2 θ obs	2 θ calc ^a	<i>hkl</i>
9.283	1	9.52	9.53	003
4.6405	10	19.11	19.12	006
	1	25.15 ^b		
3.3922	17	26.25	26.23	111
3.3190	24	26.84	26.82	112
3.0911	100	28.86	28.85	009
3.0703	84	29.06	29.07	114
2.9127	47	30.67	30.66	115
2.5911	14	34.59	34.57	117
2.4391	13	36.82	36.82	118
2.4359	14	36.87	36.88	208
	1	38.29 ^b		
	1	38.90 ^b		
	1	40.76 ^b		
2.1588	7	41.81	41.81	1,1,10
2.1563	7	41.86	41.87	2,0,10
	1	43.01 ^b		
2.0339	15	44.51	44.51	1,1,11
2.0326	1	44.54	44.56	2,0,11
1.9775	25	45.85	45.87	020
1.9726	40	45.97	46.00	021
	1	47.17 ^b		
	1	48.20 ^b		
1.8550	5	49.07	49.06	0,0,15
1.8152	51	50.22	50.24	1,1,13
1.8142	49	50.25	50.27	316
	1	51.92 ^b		
	1	52.07 ^b		
	2	52.90 ^b		

Table 5. X-ray powder diffraction data for the low temperature orthorhombic indexing of $\text{CaO}:1/2\text{Bi}_2\text{O}_3$ 1:6—Continued

<i>d</i> obs (Å)	Rel <i>I</i> (%)	2 θ obs	2 θ calc ^a	<i>hkl</i>
1.7188	22	53.25	53.26	1,1,14
1.7174	15	53.30	53.30	2,0,14
1.7070	6	53.65	53.66	221
1.7011	5	53.85	53.84	401
1.6976	6	53.97	53.98	222
1.6924	5	54.15	54.16	402
1.6660	34	55.08	55.10	029
1.6618	54	55.23	55.23	319
1.6607	47	55.27	55.28	224
1.6563	28	55.43	55.45	404
1.6343	10	56.24	56.23	225
1.6298	9	56.41	56.41	405
	1	56.98 ^b		
	2	58.34 ^b		
1.5704	4	58.75	58.73	227
1.5662	4	58.92	58.90	407
1.5464	18	59.75	59.76	0,0,18
1.5348	5	60.25	60.26	2,2,18
1.5309	3	60.42	60.43	408
	1	61.15 ^b		
1.4764	10	62.90	62.89	1,1,17
1.4753	9	62.95	62.93	2,0,17
1.4567	1	63.85	63.84	2,2,10
	2	63.90 ^b		
1.4532	1	64.02	64.00	4,0,10
1.4164	3	65.89	65.87	2,2,11
1.4139	3	66.02	66.03	4,0,11
1.3526	4	69.43	69.42	0,2,15
1.3506	4	69.55	69.54	3,1,15
1.3362	9	70.41	70.41	2,2,13
1.3335	10	70.57	70.57	4,0,13
	1	71.22 ^b		
1.2964	6	72.91	72.91	2,2,14
1.2942	6	73.05	73.06	4,0,14
1.2889	9	73.40	73.40	1,1,20
1.2852	7	73.65	73.64	422
1.2719	6	74.55	74.54	134
1.2694	8	74.72	74.73	424
1.2678	9	74.83	74.84	514
1.2603	6	75.35	75.36	135
1.2575	7	75.55	75.55	425
1.2562	7	75.64	75.66	515
	2	77.45 ^b		
1.2263	3	77.83	77.83	517
1.2167	17	78.56	78.58	3,1,18
1.1866	13	80.96	80.97	1,1,22
1.1862	12	80.99	81.01	2,0,22
1.1734	2	82.06	82.08	1,3,10
1.1699	1	82.36	82.37	5,1,10
1.1594	2	83.27	83.25	0,0,24
1.1496	3	84.14	84.12	4,2,11
1.1409	6	84.93	84.95	1,1,23
1.1404	7	84.98	84.99	2,0,23
1.1399	7	85.03	85.02	330
1.1364	5	85.35	85.35	600
	2	85.60 ^b		
1.1266	1	86.27	86.25	5,1,12
	1	87.50 ^b		
1.1075	4	88.14	88.16	1,3,13
1.1070	5	88.19	88.18	336
1.1054	6	88.35	88.34	4,2,13
1.1045	7	88.44	88.45	5,1,13

Table 5. X-ray powder diffraction data for the low temperature orthorhombic indexing of CaO:1/2Bi₂O₃ 1:6—Continued

<i>d</i> obs (Å)	Rel <i>I</i> (%)	2 θ obs	2 θ calc ^a	<i>hkl</i>
1.1039	6	88.50	88.51	606
1.0842	3	90.55	90.53	1,3,14
1.0827	4	90.71	90.71	4,2,14
1.0818	4	90.80	90.82	5,1,14
1.0793	3	91.07	91.07	2,2,20
1.0780	3	91.22	91.22	4,0,20
1.0694	5	92.16	92.14	339
1.0666	6	92.47	92.46	609
1.0586	2	93.38	93.39	1,1,25
1.0356	2	96.11	96.10	5,1,16
1.0306	5	96.74	96.72	0,0,27
1.0216	5	97.88	97.89	1,1,26
1.0170	6	98.48	98.48	2,2,22
1.0157	6	98.65	98.62	4,0,22

^aCalculated on the basis of an orthorhombic unit cell, Cmmm, *a* = 6.8188(3), *b* = 3.9531(2), and *c* = 27.830(1) Å.

^bApparently due to an unidentified structure.

Table 6. X-ray powder diffraction data for the high temperature rhombohedral (Sillen phase) indexing versus the orthorhombic indexing of CaO:1/2Bi₂O₃ 1:6

2 θ obs	Rhombohedral		Orthorhombic
	<i>hkl</i> ^a	<i>hkl</i> ^b	2 θ obs
9.55	003	003	9.52
19.14	006	006	19.11
			25.15 ^b
26.27	101	111	26.25
26.86	012	112	26.84
28.85	009	009	28.86
29.11	104	114	29.06
30.70	015	115	30.67
34.61	107	117	34.59
36.85	018	118	36.82
		208	36.87
			38.29 ^b
			38.90 ^b
39.90 ^b			40.76 ^b
41.83	1,0,10	1,1,10	41.81
		2,0,10	41.86
			43.01 ^b
43.67 ^b			
44.54	0,1,11	1,1,11	44.51
		2,0,11	44.54
		020	45.85
45.97	110	021	45.97
47.09	113		47.17 ^b
			48.20 ^b
49.06	0,0,15	0,0,15	49.07
50.23	116	1,1,13	50.22
	1,0,13		
		316	50.25
			51.92 ^b
			52.07 ^b
			52.90 ^b
53.25	0,1,14	1,1,14	53.25
		2,0,14	53.30

Table 6. X-ray powder diffraction data for the high temperature rhombohedral (Sillen phase) indexing versus the orthorhombic indexing of CaO:1/2Bi₂O₃ 1:6—Continued

2 θ obs	Rhombohedral		Orthorhombic
	<i>hkl</i> ^a	<i>hkl</i> ^b	2 θ obs
		221	53.65
53.74	021	401	53.85
		222	53.97
54.05	202	402	54.15
		029	55.08
55.19	119	319	55.23
		224	55.27
		404	55.43
56.28	205	225	56.24
		405	56.41
			56.98 ^b
			58.34 ^b
58.79	027	227	58.75
		407	58.92
59.60	1,0,16		
59.74	0,0,18	0,0,18	59.75
		2,2,18	60.25
60.31	208		
		408	60.42
			61.15 ^b
62.87	0,1,17	1,1,17	62.90
		2,0,17	62.95
63.88	0,2,10	2,2,10	63.85
			63.90 ^b
		4,0,10	64.02
65.93	2,0,11	2,2,11	65.89
		4,0,11	66.02
		0,2,15	69.43
69.49		1,1,15	
		3,1,15	69.55
70.45	0,2,13	2,2,13	70.41
		4,0,13	70.57
			71.22 ^b
72.96	2,0,14	2,2,14	72.91
		4,0,14	73.05
73.39	0,1,20	1,1,10	73.40
73.62	112	422	73.65
		134	74.55
74.73	214	424	74.72
		514	74.83
		135	75.35
75.52	125	425	75.55
		515	75.64
			77.45 ^b
77.70	217		
		517	77.83
78.53	1,1,18	3,1,18	78.56
79.04	128		
80.94	1,0,22	1,1,22	80.96
		2,0,22	80.99
81.31	2,0,17		
		1,3,10	82.06
82.25	2,1,10	5,1,10	82.36
		0,0,24	83.27
83.24	0,0,24		
84.08	1,2,11	4,2,11	84.14
84.95	0,1,23	1,1,23	84.93

Table 6. X-ray powder diffraction data for the high temperature rhombohedral (Sillen phase) indexing versus the orthorhombic indexing of CaO:1/2Bi₂O₃ 1:6—Continued

2 θ obs	Rhombohedral		Orthorhombic 2 θ obs
	<i>hkl</i> ^a	<i>hkl</i> ^b	
85.15	300	330	85.03
		600	85.35 85.60 ^b
		5,1,12	86.27 87.50 ^b
87.67	0,2,19	1,3,13	88.14
		336	88.19
88.30	306 2,1,13	4,2,13	88.35
		5,1,13	88.44
		606	88.50
		1,3,14	90.55
90.70	1,2,14	4,2,14	90.71
		5,1,14	90.80
91.11	2,0,20	2,2,20	91.07
		4,0,20	91.22
92.25	309	339	92.16
		609	92.47
93.37	1,0,25	1,1,25	93.38
95.97	2,1,16		
96.70	0,0,27	5,1,16	96.11
		0,0,27	96.74
97.86	0,1,26	1,1,26	97.88
98.49	0,2,22	2,2,22	98.48
		4,0,22	98.65
98.86	1,2,17		

^a Calculated on the basis of a rhombohedral unit cell, R $\bar{3}$, $a = 3.9448(8)$ and $c = 27.8400(8)$ Å.

^b Calculated on the basis of an orthorhombic unit cell, Cmmm, $a = 6.8188(3)$, $b = 3.9531(2)$, and $c = 27.830(1)$ Å.

^c Apparently due to an unidentified superstructure.

3.3.2. “Face-Centered-Cubic” Solid Solution (“fcc”) Levin and Roth [26] demonstrated that the solidus temperature of fcc Bi₂O₃ (α_1 in [21]) increases with additions of CaO. Conflant et al. [21] depicted its homogeneity range as extending to temperatures above the rhombohedral Sillen phase, and they did not include a congruent melting point. The present work and [18], however, indicate that there is a congruent melting point between 20 and 23 mol % CaO at about 885 °C. The phase diagram in [21] includes a dashed line which defines a small α_1' region in the CaO-rich, low temperature portion of the fcc field. Present results are essentially in agreement with this finding; i.e., all x-ray diffraction patterns from quenched “fcc” samples that contain at least 20 mol % CaO exhibit the superstructure peaks described in [21] plus a very slight splitting of

cubic diffraction maxima that was not described in [21] (Fig. 6, Table 7). The observed splitting of substructure peaks of α_1' fits rhombohedral symmetry with $a_H = 7.7427(9)$, $c_H = 9.465(1)$ Å, $c/a = 1.2224$. The complete field, extending to about 30 mol % CaO, is labeled “fcc” because neither the data presented here nor that in [20] provides a sound basis for drawing definitive phase boundaries. The minimum shown in Fig. 4 at ~ 773 °C for the CaO-rich end of this solid solution is in relatively good agreement with the value of 785 °C which can be interpreted from [21] (Fig. 3). When a single-phase specimen of composition near this minimum (5:14:3:8, CaO:1/2Bi₂O₃) is quenched after 10 min annealing at ~ 760 °C (~ 13 °C below the equilibrium minimum), the rhombohedral splitting of cubic maxima was greatly enhanced; this is the α_1'' phase of [21] (Fig. 6; Table 8). As with the rhombohedral Sillen-type phases, these rhombohedrally distorted fcc phases are highly susceptible to mechanical damage during routine grinding, therefore the line splitting of α_1' can only be seen if the quenched specimen is not ground. X-ray analysis of this sample yielded $a_H = 7.616$, $c_H = 9.6477$, $c/a = 1.2668$, whereas hexagonal indexing of a truly cubic pattern would give $c/a = 1.2247$; $[1,1,1]_c = [0,0,0,3]_H$ and $[2,2,0]_c = [2,2,4,0]_H$. Thus, the rhombohedrally distorted phase that was quenched from the stable “fcc” region (α_1') had a c/a ratio that was slightly smaller than the cubic value, but the metastable lower-temperature phase (α_1'') that was quenched from below the “fcc” region had a c/a ratio that was considerably larger than the cubic value. Single crystal x-ray precession patterns from the α_1'' phase (Fig. 7) can be indexed with either a monoclinic or a rhombohedral cell with $a = 4a_{\text{sub}}$ as shown in Table 8.

3.3.3. The “Body-Centered-Cubic” Solid Solution (“bcc”) The phase referred to as body-centered-cubic (“bcc”) solid solution was reported as a high temperature phase in [21]. In the present study this phase was found to extend from about 35 to 45 mol % CaO. The exact boundaries of the two-phase “fcc-bcc” region were not determined because the compositions of coexisting phases were not consistently reproduced. Just as with the “fcc” phase the “bcc” phase also exhibits line splitting and superstructure. Distortions from cubic symmetry (Fig. 8, Table 9), seem to be greatest in samples that are quenched from the region near the decomposition point of the 2:3 phase, (Fig. 9, Table 10). Single crystal x-ray diffraction precession data (Fig. 10) confirm the distortion recorded in Fig. 9 and Table 10 and indicate the nature of the superstructure.

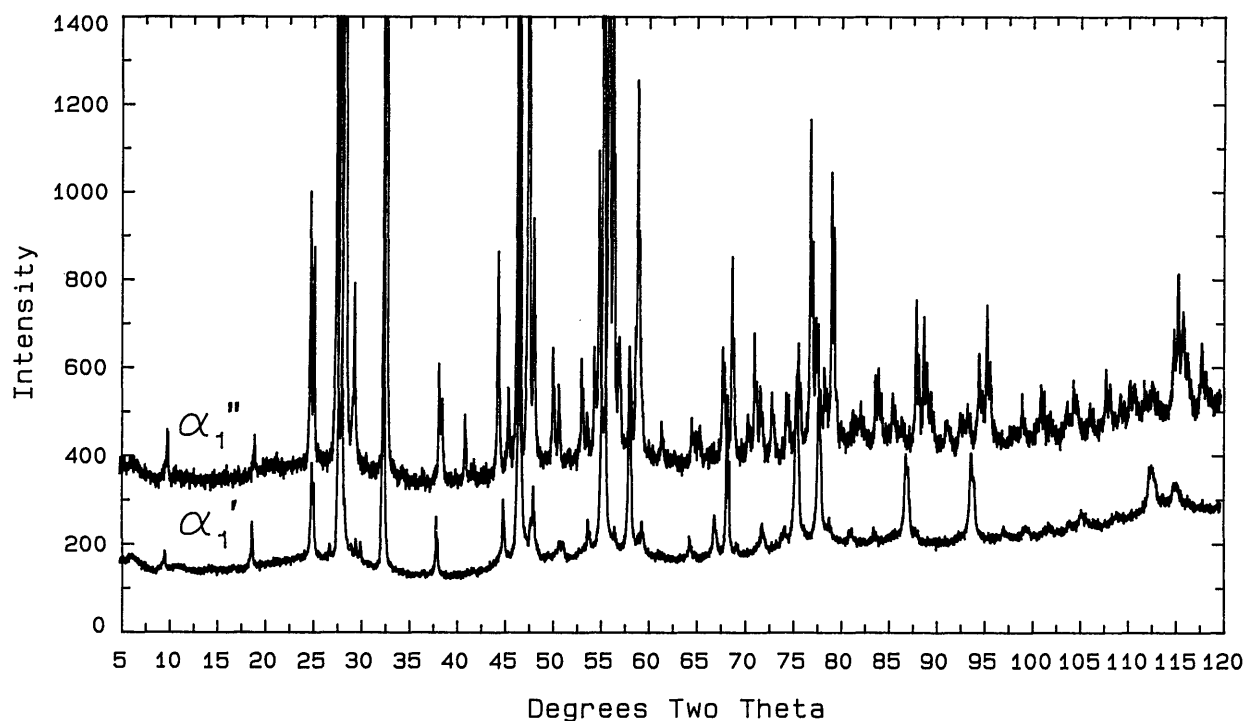


Fig. 6. X-ray powder diffraction pattern of the fcc phase showing splitting and superstructure of α_1' and α_1'' .

CaO-rich phase boundaries of the “bcc” field have not been precisely determined in part because of complications arising from the presence in many experiments of a metastable phase (see “C-mon” below). This bcc-type phase was found to be stable down to a minimum temperature of 825 ± 5 °C (Fig. 4) which is in good agreement with the value of 819 °C interpreted from [20] (see Fig. 3).

Table 7. X-ray powder diffraction data for the α_1' phase (CaO:1/2Bi₂O₃ mol ratio 3:8, 780 °C quench, sample not ground)

d obs (Å)	Rel I (%)	2θ obs	2θ calc ^a	hkl
8.990	2	9.83		
4.669	4	18.99		
3.5296	7	25.21		
3.5050	6	25.39		
3.1565	100	28.25	28.26	003
2.9946	2	29.81		
2.9492	1	30.28		
2.7339	58	32.73	32.71	202
2.3510	4	38.25		
2.0031	5	45.23		
1.9517	3	46.49		
1.9341	54	46.94	46.96	024
1.8882	2	48.15		
1.8801	5	48.37		
1.7875	1	51.05		
1.7752	2	51.43		
1.6940	1	54.09		

Table 7. X-ray powder diffraction data for the α_1' phase (CaO:1/2Bi₂O₃ mol ratio 3:8, 780 °C quench, sample not ground) – Continued

d obs (Å)	Rel I (%)	2θ obs	2θ calc ^a	hkl
1.6492	51	55.69	55.72	205
1.6184	1	56.84		
1.5799	5	58.36	58.35	042
1.5770	5	58.48	58.46	006
1.5666	1	58.90		
1.5482	2	59.67		
1.4401	1	64.67		
1.3906	2	67.27		
1.3680	6	68.54	68.55	404
1.3515	1	69.49		
1.3078	2	72.17		
1.2762	1	74.25		
1.2581	1	75.50		
1.2558	8	75.67	75.66	241
1.2537	8	75.82	75.80	027
1.2231	8	78.07	78.09	226
1.2089	1	79.16		
1.1828	1	81.27		
1.1796	1	81.53		
1.1528	1	83.85		
1.1174	5	87.16	87.15	600
1.1155	4	87.35	87.33	208
1.0533	5	94.00	94.03	425
1.0245	7	97.50		
1.0077	7	99.70		

^a Calculated on the basis of a rhombohedral unit cell, $R\bar{3}$, $a = 7.7427(9)$ and $c = 9.465(1)$ Å.



Fig. 7. X-ray precession photograph of the fcc α_1'' phase (Mo radiation).

Table 8. X-ray powder diffraction data for the α_1'' phase (CaO:1/2Bi₂O₃ mol ratio 3:8, 760 °C quench, not ground)

d obs (Å)	Rel I (%)	2θ obs	2θ calc ^a	hkl ^a	2θ calc ^b	hkl ^b
8.812	<2	10.03	10.05	300	10.05	101
4.631	1	19.15	19.16	051	19.16	301
	<1	21.41	2:3		2:3	
3.5618	15	24.98	24.99	502	24.99	10 $\bar{3}$
3.5120	11	25.34	25.35	701	25.35	11 $\bar{1}$
3.2156	27	27.72	27.72	003	27.72	40 $\bar{2}$
3.1208	100	28.58	28.58	081	28.58	40 $\bar{2}$
	2	29.38	2:3		2:3	
3.0225	7	29.53	29.55	303	29.55	30 $\bar{3}$
	1	30.80 ^c				
	<1	31.09 ^c				
	1	32.27 ^c				
2.7226	55	32.87	32.87	802	32.87	004
	<1	34.39 ^c				
	<1	34.57 ^c				
2.5817	<1	34.72	34.73	381	34.73	113
2.3417	4	38.41	38.41	832	38.41	511
2.3265	3	38.67	38.65	0,11,1	38.66	503
2.3231	3	38.73	38.73	850	38.74	313
2.1934	2	41.12	41.12	054	41.12	701
2.1707	<1	41.57	41.56	244	^d	
2.1485	1	42.02	42.00	514	42.04	105
2.0322	8	44.55	44.57	704	44.56	51 $\bar{3}$
1.9866	4	45.63	45.64	13,0,1	45.65	305
1.9466	28	46.62	46.62	084	46.62	800
1.9039	34	47.73	47.73	880	47.73	020

Table 8. X-ray powder diffraction data for the α_1' phase (CaO:1/2Bi₂O₃ mol ratio 3:8, 760 °C quench, not ground)—Continued

<i>d</i> obs (Å)	Rel <i>I</i> (%)	2 θ obs	2 θ calc ^a	<i>hkl</i> ^a	2 θ calc ^b	<i>hkl</i> ^b
8.812	<2	10.03	10.05	300	10.05	101
4.631	1	19.15	19.16	051	19.16	301
	<1	21.41	2:3		2:3	
1.9866	4	45.63	45.64	13,0,1	45.65	305
1.9466	28	46.62	46.62	084	46.62	800
1.9039	34	47.73	47.73	800	47.73	020
1.8828	9	48.30	48.29	853	48.30	115
					48.30	711
1.8382	<1	49.55	49.54	235	^d	
1.8125	4	50.30	50.31	505	51.31	505
1.7929	3	50.89	50.90	384	50.90	31 $\bar{5}$
1.7613	<1	51.87	51.88	13,3,1	51.89	31 $\bar{5}$
					51.89	32 $\bar{1}$
1.7176	4	53.29	53.29	075	53.29	713
1.7008	1	53.86	53.86	0,11,4	53.87	901
1.6786	4	54.63	54.62	3,13,2	54.62	12 $\bar{3}$
1.6652	12	55.11	55.10	805	55.10	40 $\bar{6}$
1.6384	34	56.09	56.09	883	56.09	422
1.6253	20	56.58	56.58	16,0,1	56.58	40 $\bar{6}$
1.6102	4	57.16	57.14	11,5,3	57.14	32 $\bar{3}$
					57.15	52 $\bar{1}$
1.6079	4	57.25	57.25	006	57.25	80 $\bar{4}$
1.5821	4	58.27	58.29	306	58.28	70 $\bar{5}$
					58.29	90 $\bar{3}$
1.5650	4	58.97	58.94	835	58.95	91 $\bar{1}$
1.5602	13	59.17	59.17	0,16,2	59.17	024
					59.17	804
1.5526	4	59.49	59.48	13,0,4	59.48	10 $\bar{7}$
1.5490	2	59.64	59.63	295	^d	
1.5033	1	61.65	61.64	11,0,5	61.64	30 $\bar{7}$
	<1	62.58 ^c		*		
1.4738	<1	63.02	63.03	16,3,1	63.03	523
1.4382	1	64.77	64.78	13,3,4	64.78	11 $\bar{7}$
					64.79	72 $\bar{1}$
1.4303	1	65.17	65.18	16,1,3	65.18	913
1.4218	1	65.61	65.63	8,13,1	65.63	715
1.3773	3	68.01	68.01	13,8,2	68.01	317
1.3743	3	68.18	68.18	19,0,1	68.18	325
1.3614	6	68.92	68.93	16,0,4	68.93	008
					68.93	820
1.3338	1	70.55	70.56	18,0,3	70.57	11,0, $\bar{3}$
1.3221	4	71.27	71.27	856	71.27	51 $\bar{7}$
					71.27	11,1, $\bar{1}$
1.3127	2	71.86	71.86	3,13,5	71.86	52 $\bar{5}$
1.2942	2	73.05	73.04	707	73.03	70 $\bar{7}$
					73.04	915
1.2717	2	74.56	74.55	11,11,3	74.56	12,0, $\bar{2}$
			74.57	087	74.57	81 $\bar{6}$
1.2687	2	74.77	74.79	16,3,4	74.80	921
1.2536	4	75.83	75.83	0,16,5	75.84	12,0,2
1.2360	11	77.10	77.09	8,16,1	77.09	426
1.2285	4	77.66	77.66	886	77.66	82 $\bar{4}$
1.2256	4	77.88	77.89	387	77.88	71 $\bar{7}$
1.2168	3	78.55	78.56	11,5,6	78.56	92 $\bar{3}$
1.2065	8	79.35	79.33	16,8,2	79.34	824
1.2011	2	79.78	79.78	10,15,1	79.79	10,0, $\bar{6}$
			79.79	208		

Table 8. X-ray powder diffraction data for the α_1' phase (CaO:1/2Bi₂O₃ mol ratio 3:8, 760 °C quench, not ground)—Continued

<i>d</i> obs (Å)	Rel <i>I</i> (%)	2 θ obs	2 θ calc ^a	<i>hkl</i> ^a	2 θ calc ^b	<i>hkl</i> ^b
1.1798	1	81.52	81.51	3,16,5	81.51	32 $\bar{7}$
1.1703	1	82.33	82.34	21,0,3	82.34	309
1.1526	2	83.87	83.88	13,8,5	83.87	11 $\bar{9}$
1.1489	2	84.21	84.23	078	84.23	11,1,5
1.1402	1	85.00	84.99	18,6,3	85.00	234
			85.00	13,0,7	85.00	50 $\bar{9}$
					85.00	630
					85.00	13,1,1
1.1331	2	85.66	85.67	16,1,6	85.66	31 $\bar{9}$
					85.67	52 $\bar{7}$
1.1272	1	86.22	86.23	0,19,5	86.24	11,2,1
					86.24	13,0,3
1.1226	1	86.66	86.69	11,13,4	86.69	53 $\bar{3}$
1.1074	5	88.15	88.16	8,16,4	88.16	028
					88.16	43 $\bar{4}$
					88.16	12,1,4
1.0990	4	88.96	88.97	24,0,0	88.98	808
1.0922	2	89.70	89.69	16,10,3	88.69	228
			89.70	13,3,7	89.69	51 $\bar{9}$
					89.69	10,2,4
					89.70	11,2,3
1.0768	1	91.35	91.38	5,19,4	91.38	335
1.0641	1	92.75	92.76	309	92.75	11,0,7
					92.75	13,0,5
1.0575	1	93.51	93.51	16,0,7	93.50	4,0,10
					93.51	12,2,2
1.0468	3	94.76	94.74	16,8,5	94.74	832
					94.74	12,2,2
1.0402	4	95.55	95.56	24,0,3	95.56	4,0,10
			95.57	7,12,7	95.56	12,0,6
1.0343	1	96.28	96.27	2,12,8	^d	
1.0212	<1	97.93	97.93	4,15,7	^d	
1.0203	<1	98.05	98.06	639	^d	
1.0115	1	99.20	99.22	21,8,1	99.22	719
1.0002	1	100.73	100.72	3,13,8	100.72	15,1,1
0.9968	1	101.21	101.19	16,13,3	101.19	329
					101.20	11,2,5
0.9946	1	101.52	101.50	8,13,7	101.50	15,1,1
0.9898	1	102.20	102.20	26,1,1	102.18	15,0,3
0.9781	1	103.92	103.90	19,0,7	103.90	52 $\bar{9}$
0.9733	2	104.64	104.64	859	104.64	15,1,3
0.9622	1	106.37	106.37	0,2,10	106.36	14,0,6
0.9520	2	108.03	108.02	16,16,0	108.03	828
					108.04	040
0.9432	1	109.51	109.52	5,25,1	109.54	16,1,0
0.9371	1	110.57	110.58	21,8,4	110.58	3,1,11
0.9332	1	111.26	111.27	26,2,3	111.29	935
0.9289	1	112.05	112.05	11,5,9	112.05	11,2,7
0.9258	1	112.61	112.60	0,25,5	112.62	15,0,5
0.9242	1	112.91	112.91	2,7,10	112.92	2,3,
			112.92	2,24,5		
0.9127	2	115.13	115.11	3,20,7	115.11	12,2,6
0.9104	5	115.58	115.56	0,19,8	115.57	15,2,1
					115.57	17,0,1
0.9074	3	116.19	116.17	24,0,6	116.18	12,3,0
			116.21	9,13,8	116.18	16,0,4

Table 8. X-ray powder diffraction data for the α_1'' phase (CaO:1/2Bi₂O₃ mol ratio 3:8, 760 °C quench, not ground)—Continued

d obs (Å)	Rel I (%)	2θ obs	2θ calc ^a	hkl ^a	2θ calc ^b	hkl ^b
0.8984	2	118.05	118.06	20,4,7	118.07	12,3, $\bar{2}$
0.8939	1	119.02	119.00	29,0,2	119.01	7,0,11
0.8780	1	122.64	122.66	29,2,0	^d	
0.8755	1	123.25	123.23	5,24,5	123.23	1,2,11
					124.24	139
0.8738	1	123.66	123.66	13,11,8	123.66	11,3, $\bar{5}$
0.8732	1	123.80	123.81	21,13,2	123.79	139
					123.80	74 $\bar{1}$
0.8710	1	124.35	124.37	5,18,8	^d	
0.8665	1	125.49	125.49	27,6,0	^d	

^a Calculated on the basis of a rhombohedral unit cell, $R\bar{3}$, $a = 30.4640(5)$ and $c = 9.6477(2)$ Å.

^b Calculated on the basis of a monoclinic unit cell, $B2/m$, $a = 15.5819(3)$, $b = 3.8077(1)$, $c = 10.8955(3)$ Å, and $\beta = 91.829(2)^\circ$.

^c Apparently due to an unidentified superstructure.

^d Not indexable by the monoclinic all.

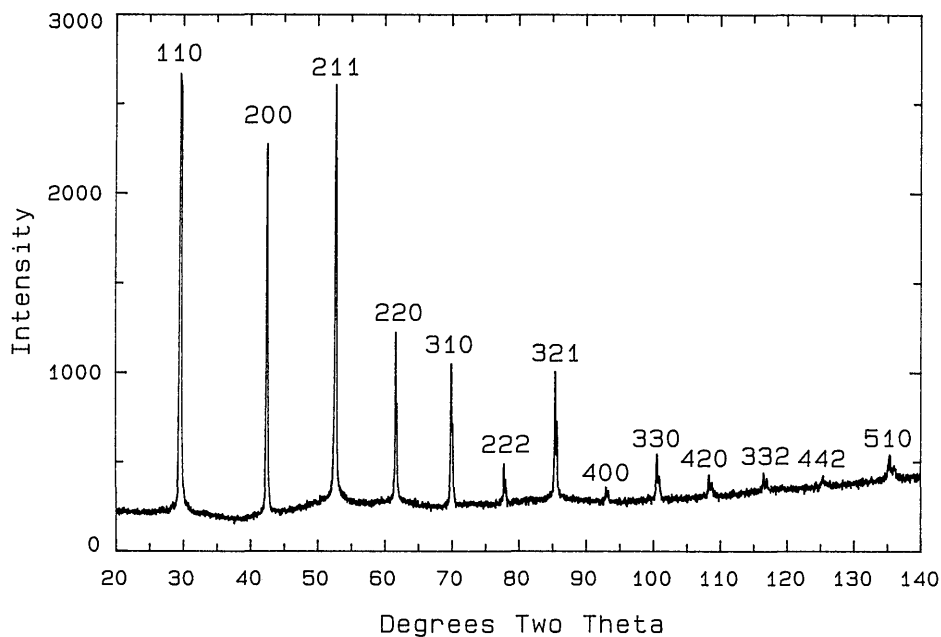
**Fig. 8.** X-ray powder diffraction pattern for the bcc phase.

Table 9. X-ray powder diffraction data for the body centered cubic phase (CaO:1/2Bi₂O₃ mol ratio 9:10, 1000 °C quench)

<i>d</i> obs (Å)	Rel <i>I</i> (%)	2 θ obs	2 θ calc ^a	<i>hkl</i>
3.0006	100	29.75	29.73	110
2.1239	34	42.53	42.52	200
1.7330	51	52.78	52.77	211
1.5011	14	61.75	61.75	220
1.3430	12	70.00	70.02	310
1.2255	3	77.89	77.88	222
1.1346	10	85.52	85.51	321
1.0617	1	93.03	93.06	400
1.0008	3	100.65	100.66	330
0.9494	2	108.45	108.46	420
0.9052	1	116.64	116.63	332
0.8667	1	125.43	125.45	422
0.8326	2	135.39	135.37	510

^a Calculated on the basis of a body centered cubic cell with $a = 4.2458(1)$ Å.

Table 10. X-ray powder diffraction data for the distorted body centered cubic phase with line splitting and superstructure (CaO:1/2Bi₂O₃ mol ratio 2:3, 860 °C)

<i>d</i> obs (Å)	Rel <i>I</i> (%)	2 θ obs	2 θ calc ^a	<i>hkl</i>
8.699	1	10.16		
7.950	1	11.12		
7.783	1	11.36		
4.828	3	18.36		
4.635	1	19.13		
4.460	1	19.89		
4.2267	2	21.00		
4.1698	1	21.29		
4.0826	1	21.75		
3.9849	1	22.29		
3.8868	1	22.86		
3.5379	1	25.15		
3.4714	3	25.64		
3.3997	2	26.19		
3.3164	1	26.86		
3.2291	1	27.60		
3.1410	1	28.39		
3.0972	3	28.80		
3.0015	100	29.74	29.73	110
2.8841	4	30.98		
2.8245	2	31.65		
2.7801	1	32.17		
2.7526	1	32.50		
2.7184	1	32.92		
2.5924	1	34.57		
2.5467	1	35.21		
2.5300	1	35.45		
2.4859	1	36.10		
2.4609	1	36.48		
2.4143	1	37.21		
2.3901	1	37.60		
2.3218	1	38.75		
2.3012	1	39.11		
2.2861	2	39.38		
2.2800	2	39.49		
2.1621	4	41.74		

Table 10. X-ray powder diffraction data for the distorted body centered cubic phase with line splitting and superstructure (CaO:1/2Bi₂O₃ mol ratio 2:3, 860 °C)—Continued

<i>d</i> obs (Å)	Rel <i>I</i> (%)	2 θ obs	2 θ calc ^a	<i>hkl</i>
2.1233	23	42.54	42.52	200
2.0531	2	44.07		
2.0187	1	44.86		
1.9815	2	45.75		
1.9746	2	45.92		
1.9270	1	47.12		
1.8897	1	48.11		
1.8440	2	49.38		
1.8253	1	49.92		
1.8111	1	50.34		
1.7908	1	50.95		
1.7720	4	51.53		
1.7524	7	52.15		
1.7335	49	52.76	52.77	211
1.6990	3	53.92		
1.6871	2	54.33		
1.6673	3	55.03		
1.6626	3	55.20		
1.6502	1	55.65		
1.6252	1	56.28		
1.6078	1	57.25		
1.5278	1	60.55		
1.5111	3	61.29		
1.5025	9	61.68	61.75	220
1.4951	3	62.02		
1.3651	2	68.70		
1.3532	1	69.39		
1.3481	10	69.69	70.02	310
1.3356	2	70.44		
1.3235	1	71.18		

^a Calculated on the basis of a body centered cubic cell with $a = 4.2458(1)$ Å.

3.3.4. “Ca₅Bi₁₄O₂₆” (C₅B₁₄-5:14) A compound with the composition Ca₅Bi₁₄O₂₆ was previously reported [21,22] as stable up to at least 650 °C. We have no contrary evidence and indeed an apparently single phase x-ray diffraction pattern can be obtained for the 5:14 ratio (26.32% CaO; Fig. 11, Table 11) by annealing a quenched liquid of this composition overnight at 650 °C. The exact composition should be regarded as provisional, however, pending a crystal structure determination. The x-ray pattern in Table 11 corresponds well with that published in [22] except for a small but consistent shift in observed *d* amounting to $\sim 1/4^\circ 2\theta$ for CuK α radiation. Apparently the earlier work had an unrecognized deviation in calibration of the diffraction data. The diffraction pattern has not yet been indexed even with the aid of some single crystal data (Fig. 12). The complexity of the pattern and consideration of the single crystal data suggests triclinic symmetry.

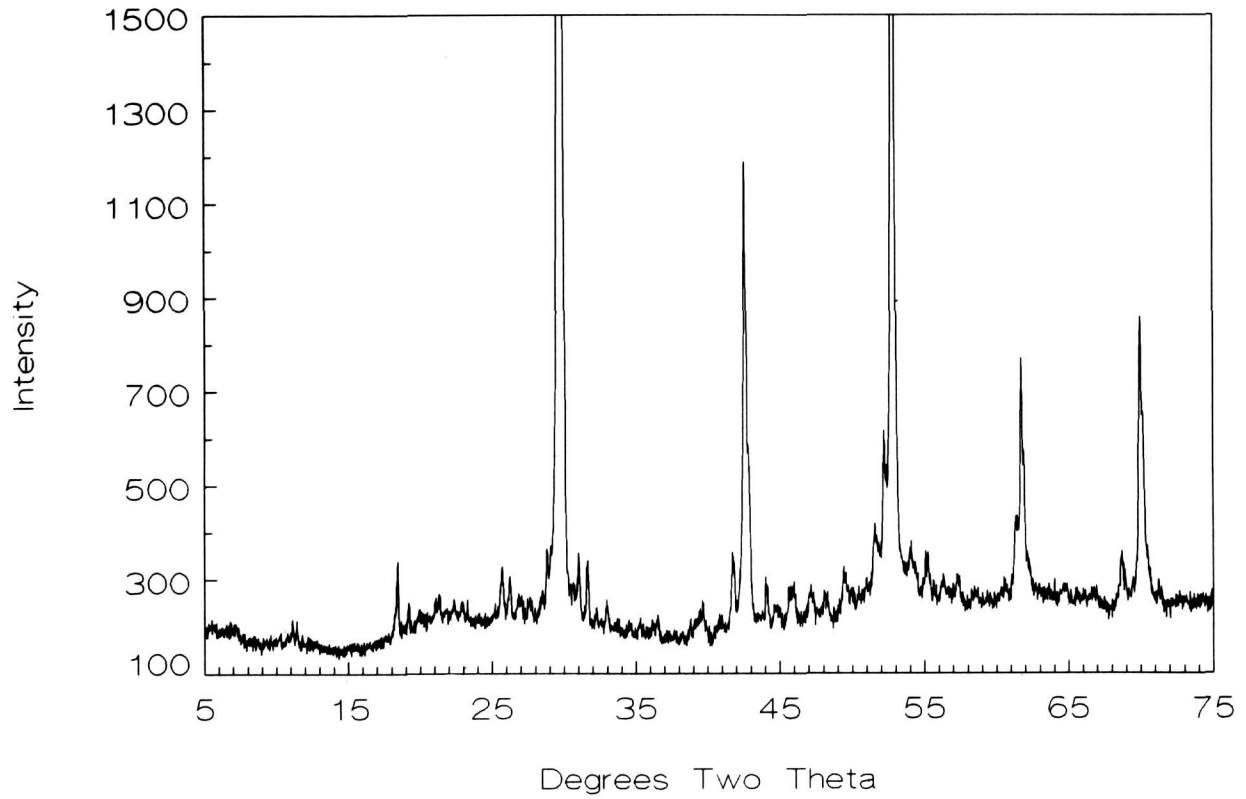


Fig. 9. X-ray powder diffraction pattern for the distorted bcc phase with line splitting and superstructure ($\text{CaO:1/2Bi}_2\text{O}_3$ 2:3 860 °C).

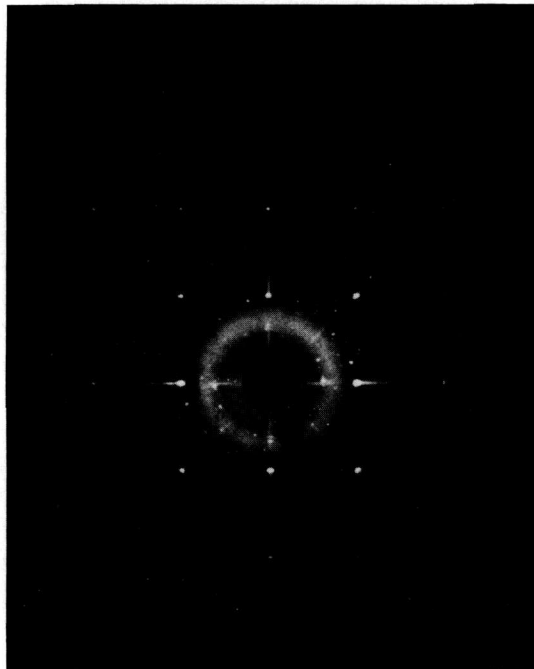


Fig. 10. X-ray precession photograph of the bcc distorted phase (Mo radiation).

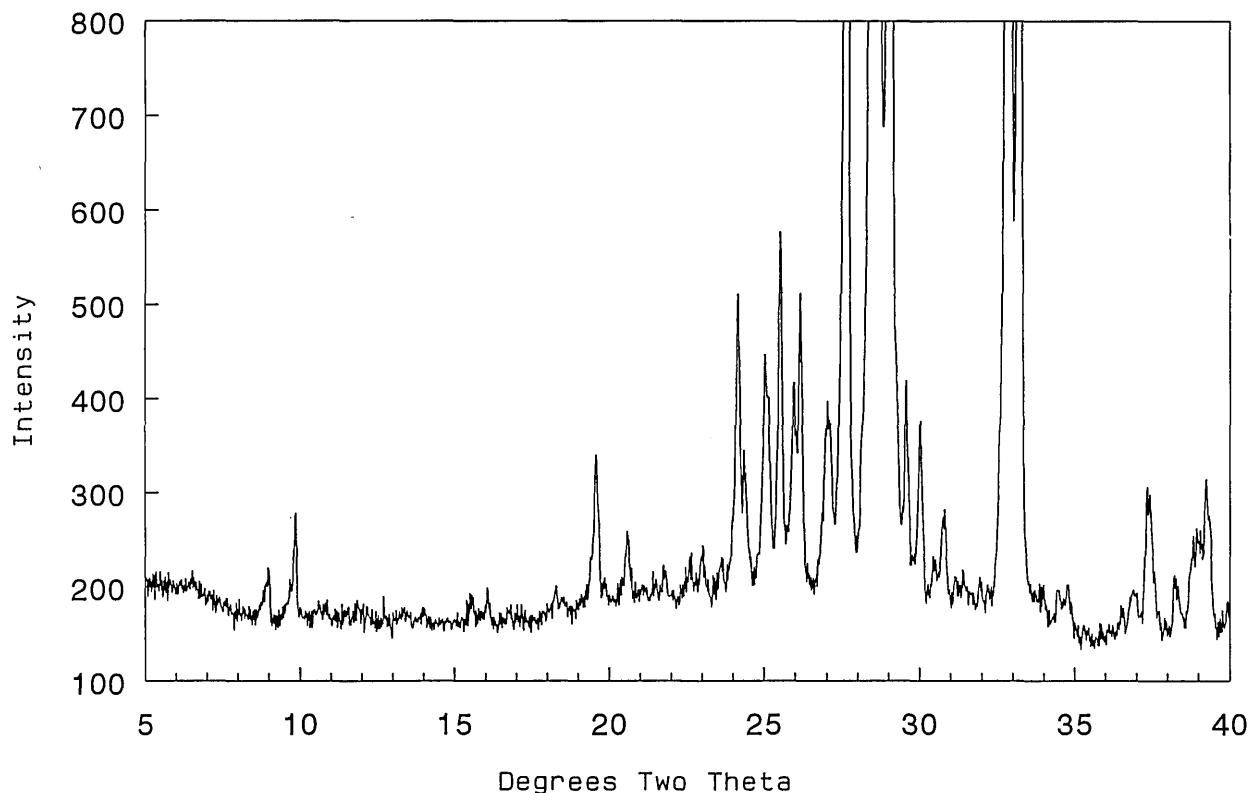


Fig. 11. X-ray powder diffraction pattern for the $\text{Ca}_5\text{Bi}_{14}\text{O}_{26}$ compound.

At $732 \pm 7^\circ\text{C}$ the 5:14 phase decomposes to a mixture of the rhombohedral phase plus CaBi_2O_4 (1:2). This equilibrium was demonstrated by both the breakdown of single phase material after heating above this range, and by nucleation of 5:14 in a two phase mixture of rhombohedral + 1:2 below it. This is considerably lower than the value of 772°C which may be interpreted from [21] (Fig. 3).

3.3.5. CaBi_2O_4 (CB_2 -1:2) The compound CaBi_2O_4 was synthesized at 650°C [22] and reported as stable up to about 800°C [21] where it was shown (Fig. 3) to decompose to fcc plus 2:3. Apparently inconsistent data in our own work required us to determine the decomposition temperature by simultaneous quenching of single phase 1:2, originally prepared by annealing at 650°C , and reheating a sample of quenched liquid from which fcc plus 2:3 was synthesized. These experiments suggest that the 1:2 phase is not stable above $778 \pm 5^\circ\text{C}$. This may be compared with the value of 799°C which can be interpreted from [21] (Fig. 3).

The 1:2 phase often occurs along with other phases in samples that are air quenched from temperatures greater than about 800°C . The x-ray powder diffraction pattern of the 1:2 phase Fig. 13, Table 12, corresponds well with that reported in [22] except for the observed shift in 2θ mentioned in section 3.3.4. Several attempts were made to synthesize single crystals of the 1:2 phase (see Table 1b), but the only procedure that succeeded was to anneal single phase 1:2 + a 50/50 NaCl/KCl flux (50/50 flux/charge) at 775°C and then cool at 1°C/h to 645°C . The single crystal x-ray diffraction precession data are shown in Fig. 14. The x-ray powder diffraction pattern was indexed on the C-centered monoclinic cell $\text{C}2/c$ obtained from the single-crystal precession data. The lattice parameters refined by least-squares analysis with the aid of calculated structure factors and the calculated powder pattern based on single crystal structure determination are $a = 16.6295(8)$, $b = 11.5966(5)$, $c = 14.0055(6)$ Å, and $\beta = 134.036(3)^\circ$.

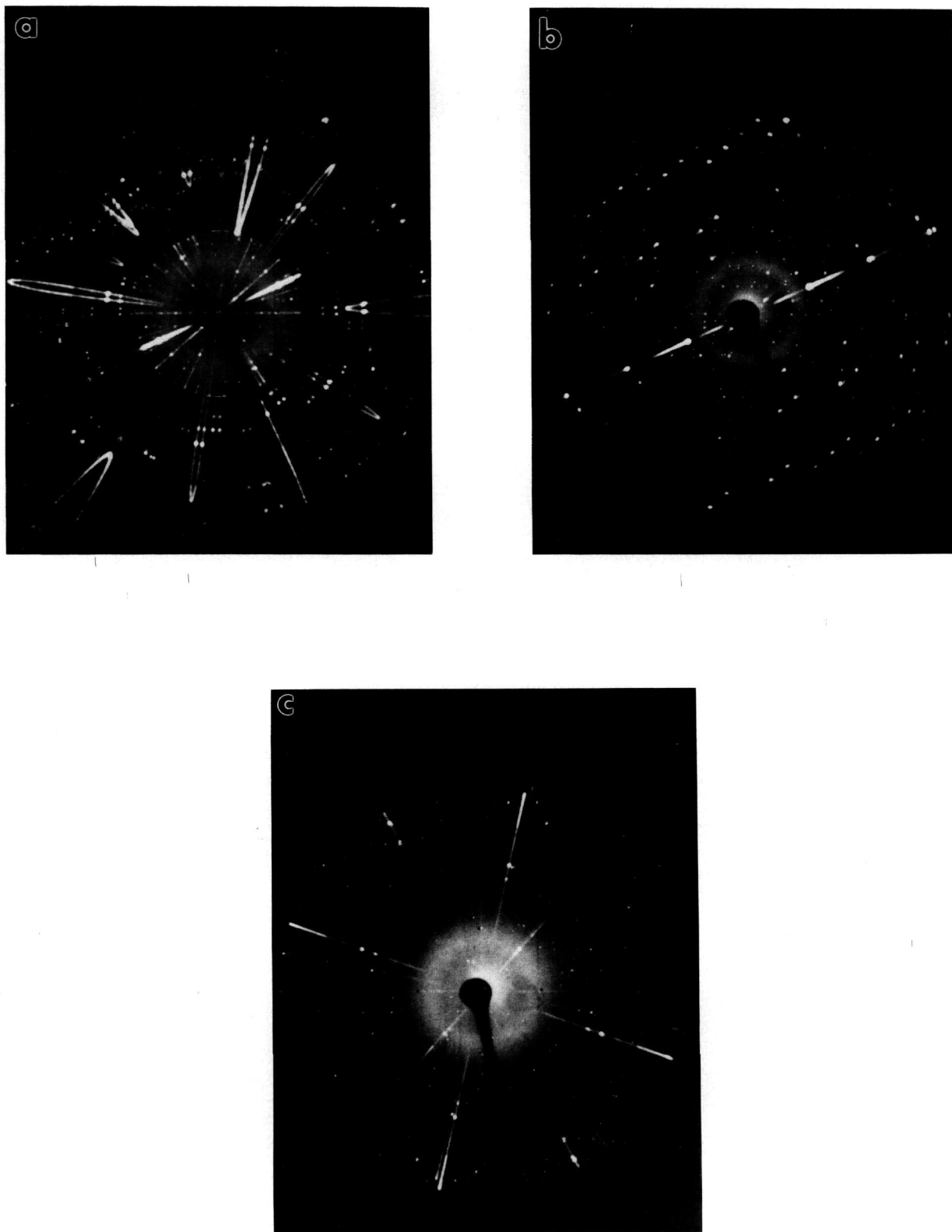


Fig. 12. X-ray precession photographs of $\text{Ca}_5\text{Bi}_{14}\text{O}_{26}$ (Mo radiation) (a) $(h0l)$ unfiltered $\mu = 10^\circ$, (b) $(h0l)$ Zr filter (c) alternate plane, unfiltered.

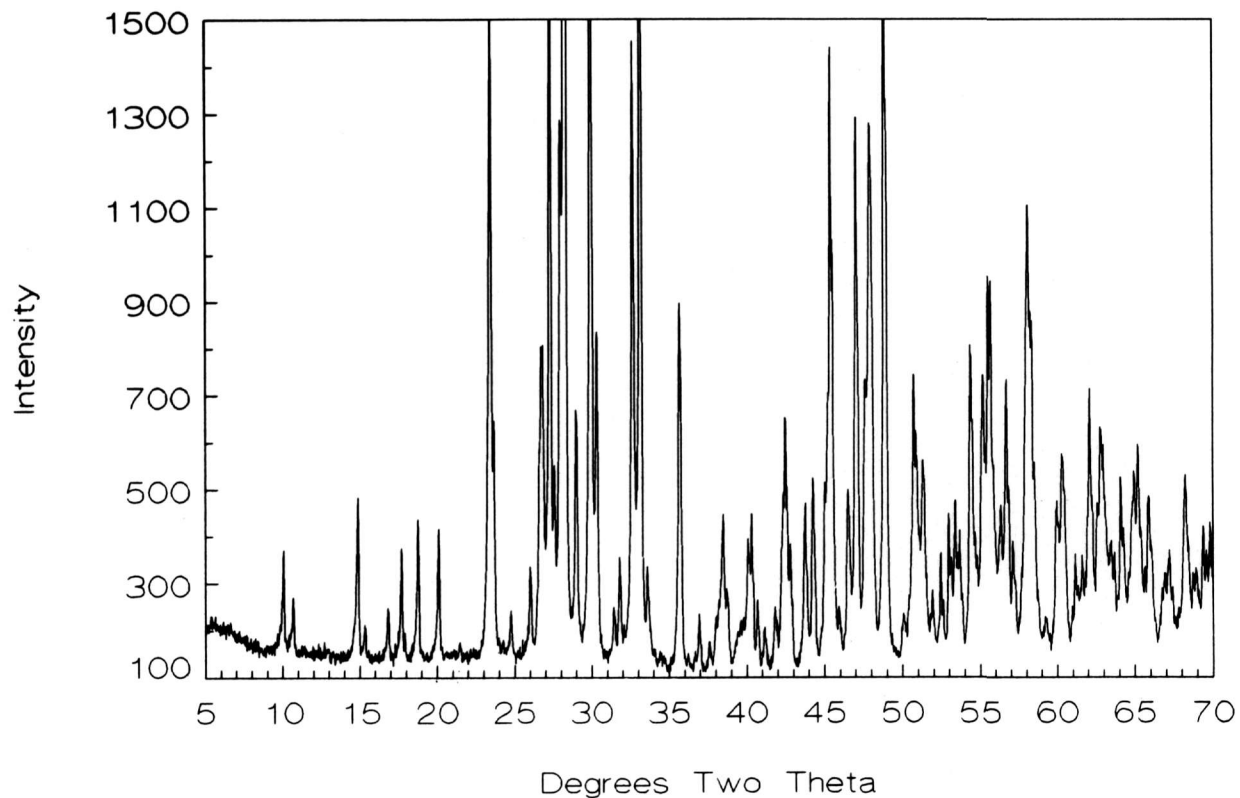


Fig. 13. X-ray powder diffraction pattern of the CaBi_2O_4 compound.

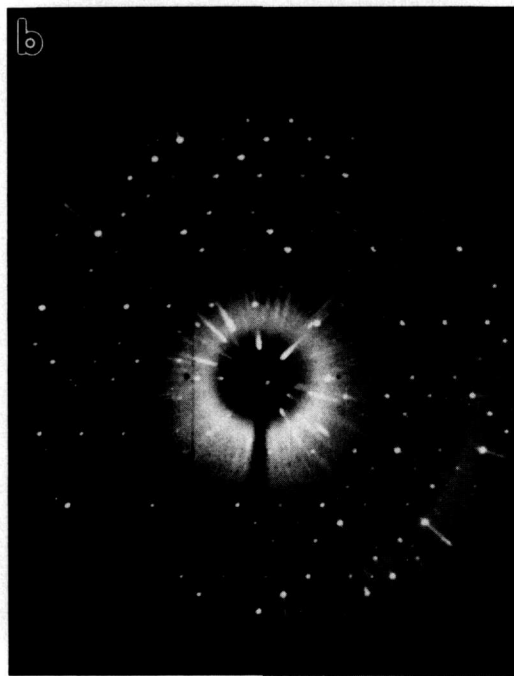
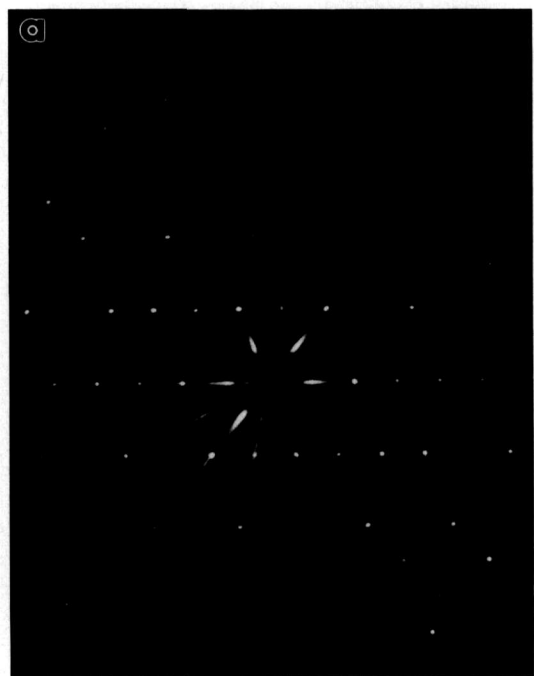


Fig. 14. X-ray precession photographs of CaBi_2O_4 (Mo radiation) (a) ($h0l$), (b) (hll).

Table 11. X-ray powder diffraction data for the compound $\text{Ca}_5\text{Bi}_{14}\text{O}_{41}$

d obs (Å)	Rel I (%)	2θ obs	2θ calc ^a	hkl
9.840	3	8.98	8.96	011
8.972	4	9.85	9.83	110
8.316	1	10.63	10.62	101
8.133	1	10.87	10.85	111
7.419	1	11.92	11.90	002
7.279	1	12.15	12.14	020
6.932	1	12.76	12.74	012
6.632	1	13.34	13.33	$\bar{1}11$
6.549	1	13.51	13.49	$\bar{1}11$
6.334	1	13.97	13.97	012
6.307	1	14.03	14.03	$\bar{1}21$
5.690	1	15.56	15.55	121
5.521	1	16.04	16.04	022
4.849	1	18.28	18.26	030
4.800	1	18.47	18.46	211
4.782	1	18.54	18.56	031
4.593	2	19.31	19.29	$\bar{1}22$
4.537	7	19.55	19.54	$01\bar{3}$
			19.55	$2\bar{1}1$
4.467	1	19.86	19.85	031
4.3143	3	20.57	20.58	$\bar{1}03$
4.2429	1	20.92	20.94	123
4.2150	1	21.06	21.08	$\bar{1}22$
4.1298	1	21.50	21.49	$11\bar{3}$
4.0736	2	21.80	21.81	222
3.9277	2	22.62	22.60	$21\bar{2}$
3.8620	2	23.01	22.99	230
3.7652	2	23.61	23.63	$\bar{2}12$
3.6838	13	24.14	24.11	141
			24.16	$\bar{2}20$
			24.16	$\bar{2}2\bar{2}$
3.6525	5	24.35	24.33	$\bar{2}2\bar{2}$
3.5576	11	25.01	24.99	203
3.5534	9	25.04	25.06	223
3.4903	16	25.50	25.51	142
3.4308	8	25.95	25.97	$\bar{1}32$
3.4063	13	26.14	26.15	104
3.3336	2	26.72	26.71	$21\bar{3}$
3.3178	4	26.85	26.85	$\bar{2}22$
3.2997	8	27.00	27.00	310
3.2877	8	27.10	27.11	033
3.2293	75	27.60	27.61	$\bar{1}33$
3.1347	100	28.45	28.47	042
3.1272	72	28.52	28.53	034
3.1112	97	28.67	28.69	214
3.0744	94	29.02	29.02	$32\bar{1}$
3.0539	8	29.22	29.24	$\bar{1}24$
3.0195	9	29.56	29.55	$\bar{1}42$
2.9743	7	30.02	30.01	$\bar{2}23$
2.9361	2	30.42	30.41	$3\bar{1}1$
2.9323	2	30.46	30.44	$\bar{2}23$
			30.48	115
2.9285	2	30.50	30.51	$31\bar{2}$
2.9053	4	30.75	30.74	$\bar{2}32$
2.8662	2	31.18	31.17	025
2.8422	1	31.45	31.47	$\bar{2}14$
2.8212	1	31.69	31.69	$31\bar{2}$
2.7997	2	31.94	31.94	$05\bar{1}$
2.7777	2	32.20	32.19	$\bar{1}43$
2.7718	2	32.27	32.25	303
2.7250	96	32.84	32.84	$11\bar{5}$
			32.86	252

Table 11. X-ray powder diffraction data for the compound $\text{Ca}_5\text{Bi}_{14}\text{O}_{41}$ —Continued

d obs (Å)	Rel I (%)	2θ obs	2θ calc ^a	hkl
2.6971	50	33.19	33.21	$32\bar{1}$
2.6369	2	33.97	33.99	$\bar{3}03$
2.5976	2	34.50	34.52	$\bar{2}24$
2.5766	2	34.79	34.79	253
2.5426	1	35.27	35.27	$\bar{3}13$
2.5371	1	35.35	35.36	$\bar{2}42$
2.4861	1	36.10	36.10	154
2.4584	2	36.52	36.54	420
2.4391	2	36.82	36.81	061
2.4276	3	37.00	36.99	$\bar{2}34$
			37.01	060
2.4057	6	37.35	37.34	261
2.4001	5	37.44	37.41	422
2.3964	4	37.50	37.48	$0\bar{1}6$
			37.51	053
2.3523	3	38.23	38.24	$\bar{2}2\bar{5}$
2.3185	4	38.81	38.78	$\bar{3}32$
2.3088	4	38.98	39.00	$\bar{4}3\bar{1}$
2.3008	3	39.12	39.11	216
2.2952	6	39.22	39.20	$\bar{2}25$
2.2929	6	29.26	39.29	$\bar{4}11$
2.2896	3	39.32	39.32	$\bar{1}26$
			39.32	423
2.2868	5	39.37	39.38	$\bar{2}53$

^a Calculated on the basis of a triclinic cell, $P\bar{1}$, $a = 9.934(1)$, $b = 15.034(2)$, $c = 15.008(2)$ Å, $\alpha = 82.65(1)$, $\beta = 85.27(1)$, and $\gamma = 77.17(1)^\circ$.

Table 12. X-ray powder diffraction data for the compound CaBi_2O_4 (CaO:1/2Bi₂O₃ 33:67)

d obs (Å)	Rel I (%)	2θ obs	2θ calc ^a	hkl	$ F $ calc
8.847	4	9.99	9.98	$11\bar{1}$	35
8.324	2	10.62	10.62	110	27
5.977	7	14.81	14.81	200	79
5.802	2	15.26	15.27	020	32
5.282	2	16.77	16.77	111	32
5.029	5	17.62	17.60	002	15
5.018	5	17.66	17.64	021	46
4.957	1	17.88	17.85	$31\bar{2}$	14
4.7413	6	18.70	18.70	$22\bar{1}$	56
4.4316	6	20.02	20.03	$\bar{2}2\bar{2}$	57
			21.44 ^{2,3}		
3.8179	20	23.28	23.27	$11\bar{3}$	78
3.8018	31	23.38	23.38	022	130
3.7700	11	23.58	23.59	310	79
3.6808		24.16	24.18	130	
3.6029	2	24.69	24.68	112	31
3.4308	5	25.95	25.95	$40\bar{4}$	79
3.3546	9	26.55	26.53	$42\bar{2}$	58
3.3385	14	26.68	26.67	314	81
3.3312	15	26.74	26.77	$13\bar{2}$	78
3.3190	8	26.84	26.83	221	42
3.2723	42	27.23	27.24	204	247
3.2374	8	27.53	27.52	131	72
3.1941	22	27.91	27.89	$51\bar{3}$	117
3.1631	100	28.19	28.21	332	276

Table 12. X-ray powder diffraction data for the compound CaBi_2O_4 ($\text{CaO}:1/2\text{Bi}_2\text{O}_3$ 33:67)—Continued

d obs (\AA)	Rel I (%)	2θ obs	2θ calc ^a	hkl	$ F $ calc
3.0859	12	28.91	28.92	$33\bar{1}$	78
3.0817	12	28.95	28.96	$42\bar{1}$	59
		29.33 ^{2,3}			
2.9879	48	29.88	29.87	400	289
2.9503	16	30.27	30.25	$33\bar{3}$	87
			30.28	311	74
2.9053	2	30.75	30.76	023	14
2.8970	1	30.84	30.82	040	5
2.8502	2	31.36	31.67	$22\bar{4}$	43
2.8178	5	31.73	31.75	$11\bar{4}$	65
2.7853	14	32.11	32.10	041	16
2.7769	17	32.21	32.24	330	22
2.7470	30	32.57	32.57	$60\bar{4}$	234
2.7058	44	33.08	33.07	132	209
2.6705	5	33.53	33.53	$24\bar{2}$	46
			33.53	$51\bar{5}$	38
2.6559	2	33.72	33.71	420	31
2.6559	6	33.90	33.92	222	17
2.6422	5	33.96	33.97	$31\bar{5}$	18
2.6086	1	34.35	34.35	240	24
2.5882	1	34.63	34.61	$33\bar{4}$	18
2.5567	1	35.07	35.04	$60\bar{2}$	23
2.5198	18	35.60	35.58	$42\bar{5}$	106
2.5185	15	35.62	35.64	004	135
2.4821	1	36.16	36.15	$62\bar{4}$	22
2.4552	1	36.57	36.56	$53\bar{2}$	15
2.4494	1	36.66	36.63	$24\bar{3}$	19
2.4359	3	36.87	36.89	$53\bar{4}$	49
2.3933	1	37.55	37.53	331	41
2.3708	2	37.92	37.93	$44\bar{2}$	43
2.3618	2	38.07	38.06	312	28
2.3571	3	38.15	38.14	241	42
2.3411	6	38.42	38.42	$62\bar{2}$	77
2.3271	5	38.66	38.67	$71\bar{4}$	59
2.3014	1	39.11	39.11	$22\bar{5}$	23
2.2957	1	39.21	39.23	$40\bar{6}$	40
2.2857	2	39.39	39.67	$15\bar{1}$	32
2.2762	2	39.56	39.55	150	42
2.2669	2	39.73	39.73	$44\bar{1}$	46
2.2500	5	40.04	40.02	133	68
2.2377	6	40.27	40.27	$53\bar{5}$	91
2.2177	3	40.65	40.64	$33\bar{5}$	58
2.1934	2	41.12	41.11	043	50
2.1598	3	41.79	41.78	151	59
2.1393	5	42.21	42.21	114	75
2.1339	7	42.32	42.32	$42\bar{6}$	67
2.1272	10	42.46	42.46	$62\bar{6}$	104
2.1225	6	42.56	42.58	$62\bar{1}$	53
2.1130	5	42.76	42.77	$35\bar{1}$	81
2.0693	8	43.71	43.73	$35\bar{3}$	98
2.0466	9	44.22	44.21	332	118
		44.67 ^{2,3}			
2.0236	2	44.75	44.75	$73\bar{4}$	26
2.0137	7	44.98	44.97	$44\bar{5}$	80
2.0112	6	45.04	45.02	$15\bar{3}$	63
2.0061	9	45.16	45.17	$80\bar{6}$	49
2.0049	12	45.19	45.20	350	90
1.9986	28	45.34	45.35	$53\bar{6}$	173
1.9936	17	45.46	45.49	600	134
1.9767	3	45.87	45.88	$73\bar{3}$	57
1.9526	8	46.47	46.46	$82\bar{5}$	98

Table 12. X-ray powder diffraction data for the compound CaBi_2O_4 ($\text{CaO}:1/2\text{Bi}_2\text{O}_3$ 33:67)—Continued

d obs (\AA)	Rel I (%)	2θ obs	2θ calc ^a	hkl	$ F $ calc
1.9330	24	46.97	46.98	060	170
			46.98	$71\bar{7}$	126
1.9119	12	47.52	47.52	422	104
1.9100	13	47.57	47.58	$22\bar{6}$	100
1.8987	24	47.87	47.85	$33\bar{6}$	117
			47.89	061	117
1.8953	19	47.96	47.95	204	176
1.8650	33	48.79	48.79	$73\bar{2}$	231
1.8611	24	48.90	48.93	$26\bar{2}$	77
1.8459	1	49.33	49.32	$35\bar{1}$	29
1.8244	2	49.95	49.93	$11\bar{6}$	42
1.8217	2	50.03	50.00	$91\bar{5}$	35
1.8200	2	50.08	50.06	$42\bar{7}$	40
1.8105	2	50.36	50.36	243	52
		50.44 ^{2,3}			
1.8038	5	50.56	50.54	062	66
1.7991	10	50.70	50.69	$44\bar{6}$	123
1.7805	8	51.27	51.25	$26\bar{3}$	109
1.7785	7	51.33	51.35	153	91
1.7610	3	51.88	51.89	$33\bar{3}$	54
1.7438	6	52.43	52.43	$60\bar{8}$	118
1.7282	6	52.94	52.94	$71\bar{8}$	103
1.7156	6	53.36	53.37	$80\bar{8}$	143
1.7067	5	53.66	53.66	$46\bar{1}$	102
1.6869	12	54.34	54.32	$91\bar{3}$	110
			54.34	$84\bar{5}$	109
1.6784	4	54.64	54.64	844	66
			54.65	006	48
1.6744	4	54.78	54.76	063	63
1.6640	11	55.15	55.15	$26\bar{4}$	116
1.6544	16	55.50	55.48	$93\bar{6}$	164
1.6503	15	55.65	55.62	314	108
			55.68	$84\bar{6}$	95
1.6413	4	55.98	55.95	640	70
1.6357	5	56.19	56.18	408	71
			56.20	$91\bar{8}$	60
1.6335	5	56.27	56.29	$75\bar{3}$	66
1.6319	6	56.33	56.35	$93\bar{4}$	66
1.6227	10	56.68	56.67	460	146
1.6118	5	57.10	57.09	026	110
1.6023	1	57.47	57.46	$93\bar{7}$	38
1.5959	3	57.72	57.73	171	57
1.5874	18	58.06	58.06	532	139
			58.07	154	82
1.5834	12	58.22	58.21	$75\bar{6}$	43
1.5807	12	58.33	58.33	$66\bar{4}$	130
			58.35	$66\bar{3}$	87
1.5704	2	58.75	58.77	$91\bar{2}$	37
1.5595	1	59.20	59.20	$53\bar{8}$	30
1.5573	1	59.29	59.28	$37\bar{3}$	42
1.5425	6	59.92	59.93	$66\bar{2}$	95
1.5343	7	60.27	60.25	$31\bar{8}$	117
1.5330	8	60.33	60.33	064	82
1.5311	6	60.41	60.43	$26\bar{5}$	73
1.5188	2	60.95	60.94	$93\bar{8}$	58
1.5150	4	61.12	61.12	461	84
1.5055	3	61.55	61.58	$35\bar{3}$	81
1.4969	5	61.94	61.93	$75\bar{7}$	85
1.4941	8	62.07	62.06	800	134
			62.08	$11,1,7$	131
1.4851	4	62.49	62.52	263	75

Table 12. X-ray powder diffraction data for the compound CaBi_2O_4 ($\text{CaO}:1/2\text{Bi}_2\text{O}_3$ 33:67)—Continued

d obs (Å)	Rel I (%)	2θ obs	2θ calc ^a	hkl	$ F $ calc
1.4836	4	62.56	62.58	404	153
1.4793	8	62.76	62.76	62 $\bar{9}$	89
1.4753	8	62.95	62.97	622	93
1.4715	5	63.13	63.12	51 $\bar{9}$	65
1.4692	4	63.24	63.24	572	66
1.4649	4	63.45	63.46	574	78
1.4606	4	63.66	63.65	247	51
			63.68	11,1, $\bar{8}$	61
1.4520	6	64.08	64.06	046	110
			64.10	20 $\bar{8}$	136
1.4414	3	64.61	64.60	73 $\bar{9}$	42
1.4374	5	64.81	64.83	84 $\bar{1}$	78
1.4346	6	64.95	64.94	081	116
1.4299	8	65.19	65.18	10,2, $\bar{9}$	103
1.4295	8	65.21	65.24	357	105
1.4216	3	65.62	65.61	954	80
1.4170	6	65.86	65.88	136	130
1.4090	1	66.28	66.28	864	28
			66.29	533	25
1.4027	1	66.62	66.61	10,0, $\bar{2}$	37
			66.63	957	39
1.4010	2	66.72	66.71	11,1, $\bar{9}$	67
1.3984	2	66.85	66.86	462	58
1.3977	3	66.89	66.91	266	57
1.3942	3	67.08	67.07	065	65
1.3923	3	67.18	67.21	866	91
1.3820	1	67.75	67.73	283	49
1.3802	1	67.85	67.85	11,3, $\bar{5}$	42
1.3750	5	68.14	68.13	750	84
1.3736	6	68.22	68.23	558	73
			68.23	12,0, $\bar{8}$	138
1.3657	2	68.67	68.67	372	63
1.3631	2	68.82	68.80	10,2, $\bar{2}$	63
1.3614	3	68.92	68.92	467	43
			68.92	931	37
1.3610	3	68.94	68.95	8,2, $\bar{10}$	56
1.3540	5	69.35	69.34	354	82
			69.38	264	78
1.3465	4	69.79	69.79	481	69
1.3457	5	69.84	69.83	867	68
			69.85	958	67

^a Calculated on the basis of a monoclinic unit cell, space group $C2/c$, $a = 16.6295(8)$, $b = 11.5966(5)$, $c = 14.0055(6)$ Å, and $\beta = 134.036(3)^\circ$.

3.3.6. $\text{Ca}_4\text{Bi}_6\text{O}_{13}$ ($\text{C}_2\text{B}_3\text{-2:3}$) The compound “ $\text{Ca}_7\text{Bi}_{10}\text{O}_{22}$ ”, (41.176 mol % CaO) was reported in [22] and [21], and the phase diagram shown in [21] can be interpreted as indicating that it decomposes at about 848 °C. (Fig. 3 in [20]). Experiments performed in the present work (Table 1) indicate that the composition of this phase is really 2:3 (40 mol % CaO) rather than 7:10, but the decomposition temperature (Table 1 and Fig. 4) of 855 ± 5 °C is in good agreement with [21]. The x-ray powder diffraction pattern of this phase is shown in Fig. 15

and recorded in Table 13. These results agree well with those in [22] (except for the shift in 2θ previously mentioned). Single crystals of $\text{Ca}_4\text{Bi}_6\text{O}_{13}$ were grown both by utilizing a 50/50 NaCl/KCl flux and by reannealing a quenched liquid. The compound is orthorhombic $a = 17.3795(5)$, $b = 5.9419(2)$, $c = 7.2306(2)$ Å, with a C-centered space group, as determined from single crystal x-ray precession photographs (Fig. 16) and x-ray diffraction data refined by least squares. A complete crystal structure determination [23] including single crystal x-ray analysis, neutron diffraction Rietveld analyses, and measurements of second harmonic generation, proved that the true space group is the non-centrosymmetric $C2mm$. The crystal structure was reported in [23] from data collected on crystals prepared in this study. A complete discussion of the indexing of this phase with comparison to the calculated powder pattern is given in [27]. The crystal structure determination [23] reveals that Bi^{+3} occurs in two coordination types with 2/3 of the Bi^{+3} ions five-coordinate and 1/3 of the Bi^{+3} ions only three-coordinate, by oxygen. Determinations of the crystal structures of more of these phases will perhaps result in a better understanding of the role played by Bi^{3+} coordination in 3- and 4-component superconductors.

3.3.7. $\text{Ca}_2\text{Bi}_2\text{O}_5$ ($\text{C}_2\text{B}_2\text{-1:1}$) The compound “ $\text{Ca}_7\text{Bi}_6\text{O}_{16}$ ”, (53.846 mol % CaO) was reported in [22] and [21], and the phase diagram in [21] (redrawn as Fig. 3) can be interpreted as indicating that it decomposes at about 929 °C. Experiments performed in the present work (Table 1) combined with a structure determination performed on crystals prepared in this study [24] indicate that the composition of this phase is really 1:1 (50 mol % CaO) rather than 7:6. The x-ray powder diffraction pattern of the phase shown in Fig. 17 and Table 14 agrees well with that reported in [22] (except for the shift in 2θ noted above). Single crystal x-ray diffraction precession photographs (Fig. 18) indicate that the 1:1 compound is triclinic, and powder x-ray diffraction data [27] yield least squared values of $a = 10.1222(7)$, $b = 10.146(6)$, $c = 10.4833(7)$ Å, $\alpha = 116.912(5)$, $\beta = 107.135(6)$, $\gamma = 92.939(6)^\circ$. The indexing of this pattern out to high angles in 2θ could only be accomplished with the aid of calculated structure factors and the calculated powder pattern based on the single crystal structure determination reported in [24]. The structure determination reveals a unique Bi^{+3} coordination of U-shaped Bi_3O_{11} groups with one five-fold coordinated Bi^{+3} bridging two four-fold “saw-horse” shaped polyhedra [24].

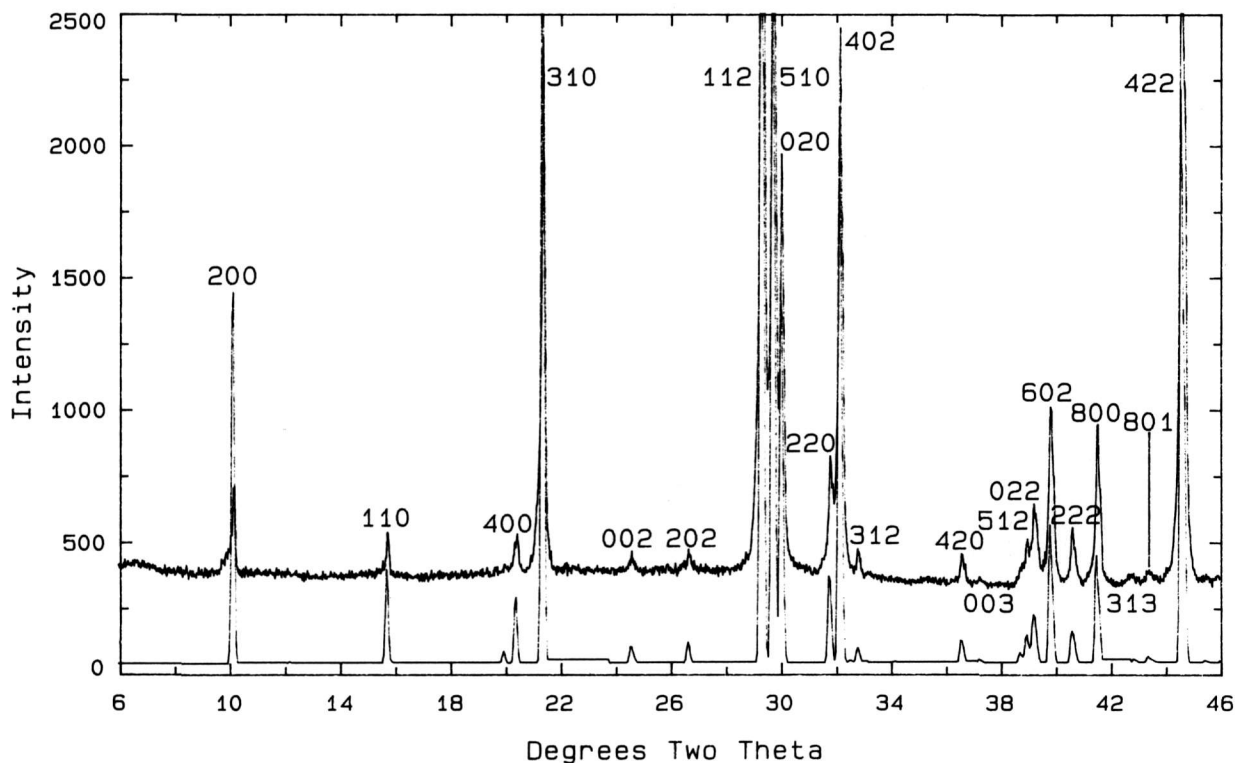


Fig. 15. X-ray powder diffraction pattern of the $\text{Ca}_4\text{Bi}_6\text{O}_{13}$ compound.

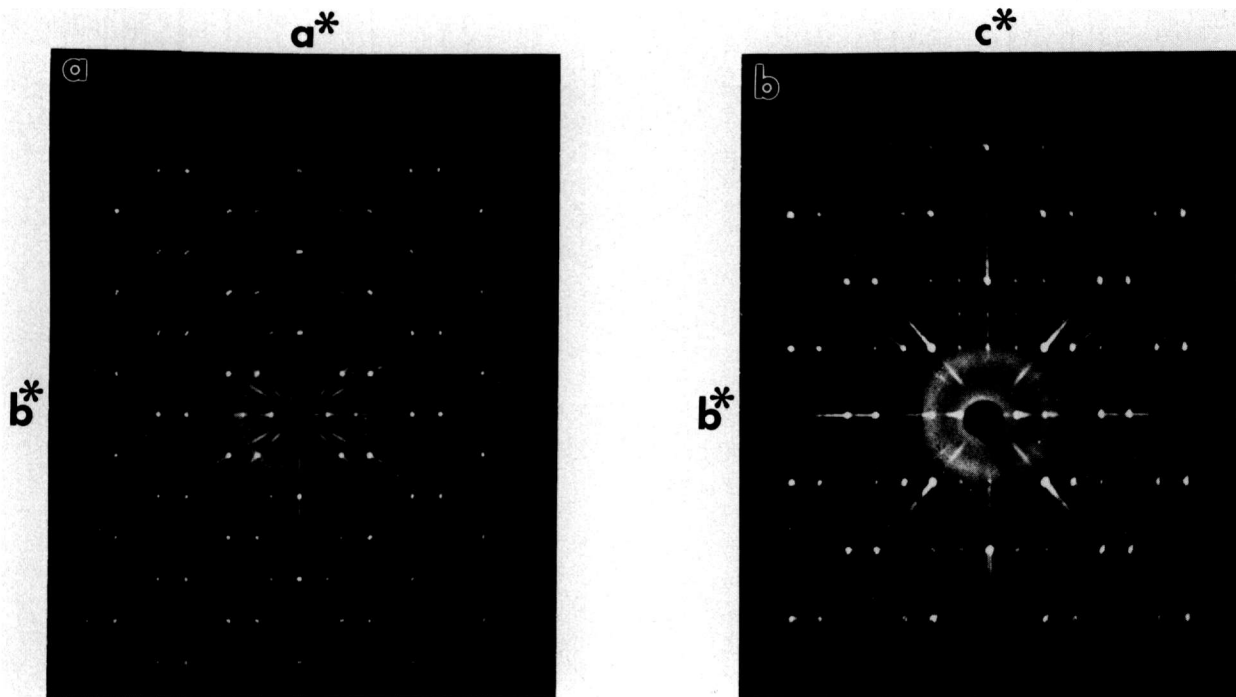


Fig. 16. X-ray precession photographs of $\text{Ca}_4\text{Bi}_6\text{O}_{13}$ (Mo radiation), (a) $(hk0)$, (b) $(0kl)$.

Table 13. X-ray powder diffraction data for the compound $\text{Ca}_4\text{Bi}_6\text{O}_{13}$

d obs (Å)	Rel I (%)	2θ obs	2θ calc ^a	hkl	$ F $ calc
8.708	13	10.15	10.17	200	250
5.629	4	15.73	15.75	110	136
4.434	1	20.01	19.99	111	45
4.346	5	20.42	20.42	400	217
4.145	47	21.42	21.40	310	571
3.614	52	24.61	24.60	002	138
3.338	52	26.68	26.69	202	118
3.0386	100	29.37	29.35	112	748
2.9987	68	29.77	29.75	510	893
2.9694	31	30.07	30.05	020	829
2.8117	8	31.80	31.81	220	306
2.7794	44	32.18	32.18	402	766
2.7250	2	32.84	32.84	312	93
2.4519	2	36.62	36.61	420	187
2.4107	1	37.27	37.28	003	103
2.3225	1	38.74	38.74	203	116
			38.74	421	45
2.3088	3	38.98	38.98	512	158
2.2952	5	39.22	39.22	022	263
2.2918	3	39.28	39.90	710	185
2.2609	12	39.84	39.85	602	501
2.2187	3	40.63	40.62	222	165
2.1717	13	41.55	41.54	800	667
2.0847	1	43.37	43.39	313	85
2.0815	1	43.44	43.46	801	35
2.0733	1	43.62	43.61	620	64
2.0291	53	44.62	44.61	422	846
1.9686	1	46.07	46.09	130	159
1.9357	4	46.90	46.92	712	227
1.8744	7	48.53	48.54	330	437
1.8625	1	48.86	48.87	802	182
1.8368	2	49.59	49.60	910	189
1.8288	1	49.82	49.79	223	81
1.8078	14	50.44	50.44	004	917
1.7991	12	50.70	50.71	622	466
1.7699	2	51.60	51.60	204	195
1.7537	11	52.11	52.11	820	602
1.7376	9	52.63	52.62	10,0,0	679
1.7285	23	52.93	52.93	132	607
1.7206	18	53.19	53.18	114	141
			53.18	530	769
1.6688	1	54.98	54.97	404	197
1.6640	2	55.15	55.16	332	149
1.6574	10	55.39	55.40	314	423
1.6373	31	56.13	56.13	912	804
1.5782	1	58.43	58.45	822	170
1.5670	1	58.89	58.92	10,0,2	93
1.5533	2	59.46	59.44	532	183
1.5486	21	59.66	59.67	514	696
			59.67	730	142
1.5446	10	59.83	59.84	024	675
1.5265	1	60.61	60.59	11,1,0	141
1.5206	3	60.87	60.88	224	232
1.5004	7	61.78	61.79	10,2,0	599
1.4857	5	62.46	62.47	040	682
1.4645	2	63.47	63.48	240	332
1.4552	1	63.92	63.93	424	185
1.4462	1	64.37	64.37	005	112
1.4262	1	65.38	65.37	205	120
1.4233	3	65.53	65.53	732	321
1.4064	2	66.42	66.41	11,1,2	221
1.4060	2	66.44	66.46	440	235
1.3896	6	67.33	67.33	804	528
1.3831	1	67.69	67.71	930	197
1.3738	1	68.21	68.20	042	210

Table 13. X-ray powder diffraction data for the compound $\text{Ca}_4\text{Bi}_6\text{O}_{13}$ — Continued

d obs (Å)	Rel I (%)	2θ obs	2θ calc ^a	hkl	$ F $ calc
1.3574	1	69.15	69.16	242	168
1.3445	3	69.91	69.91	12,0,2	406
1.3314	1	70.70	70.71	134	150
1.3102	10	72.02	72.03	442	593
1.3041	6	72.41	72.40	13,1,0	618
1.3008	9	72.62	72.61	334	355
1.2914	9	73.24	73.24	932	615
1.2739	1	74.41	74.43	10,2,3	67
1.2588	5	75.46	75.47	824	490
1.2530	3	75.87	75.88	10,0,4	545
1.2466	9	76.33	76.34	534	619
1.2418	4	76.68	76.71	642	375
1.2354	1	77.15	77.17	11,3,0	142
1.2261	4	77.84	77.83	840	506
1.2249	3	77.93	77.94	12,2,2	344
1.1856	1	81.04	81.04	150	162
1.1783	5	81.65	81.64	116	472
1.1740	4	82.01	82.00	14,0,2	615
1.1690	2	82.44	82.46	11,3,2	239
1.1643	2	82.84	82.86	350	411
1.1614	3	83.10	83.11	406	527
			83.11	842	176
1.1544	4	83.71	83.71	10,2,4	494
1.1476	3	84.32	84.32	044	565
1.1378	3	85.22	85.22	244	260
1.1374	3	85.26	85.28	15,1,0	386
1.1291	2	86.04	86.03	10,4,0	466
1.1265	4	86.28	86.28	152	455
1.1243	2	86.49	86.48	550	501
1.1168	1	87.22	87.23	026	213
1.1126	1	87.63	87.63	606	323
1.1082	3	88.07	88.08	13,3,0	566
			88.08	352	149
			88.08	934	191
1.0983	1	89.07	89.08	934	191
1.0918	6	89.74	89.73	14,2,2	579
1.0863	1	90.32	90.33	16,0,0	167
1.0817	5	90.82	90.83	426	551
1.0736	1	91.70	91.68	552	220
1.0578	4	93.47	93.48	13,1,4	520
1.0420	1	95.34	95.34	626	303
1.0370	1	95.94	95.95	12,4,0	154
1.0277	6	97.10	97.10	136	415
1.0200	1	98.08	98.06	16,2,0	245
1.0148	3	98.77	98.77	844	426
1.0074	4	99.75	99.73	916	556
1.0001	1	100.75	100.75	15,3,0	332
0.9968	2	101.21	101.21	12,4,2	353
0.9903	1	102.13	102.13	060	478
0.9841	1	103.03	103.05	260	254
0.9787	2	103.82	103.82	354	342
0.9745	6	104.45	104.44	952	496
0.9704	3	105.08	105.06	17,1,2	405
0.9655	2	105.85	105.84	18,0,0	557
0.9627	2	106.28	106.31	15,1,4	322
0.9576	2	107.10	107.09	10,4,4	396
0.9549	3	107.55	107.56	554	431
0.9446	3	109.27	109.25	13,3,4	484
0.9327	3	111.35	111.33	462	420
0.9263	1	112.52	112.51	12,0,6	275
0.9210	3	113.52	113.50	14,4,2	473
0.9182	3	114.05	114.04	18,2,0	516
0.9148	3	114.71	114.70	446	433

^a Calculated on the basis of an orthorhombic unit cell, space group $C2mm$, $a = 17.3795(5)$, $b = 5.9419(2)$, and $c = 7.2306(2)$ Å.

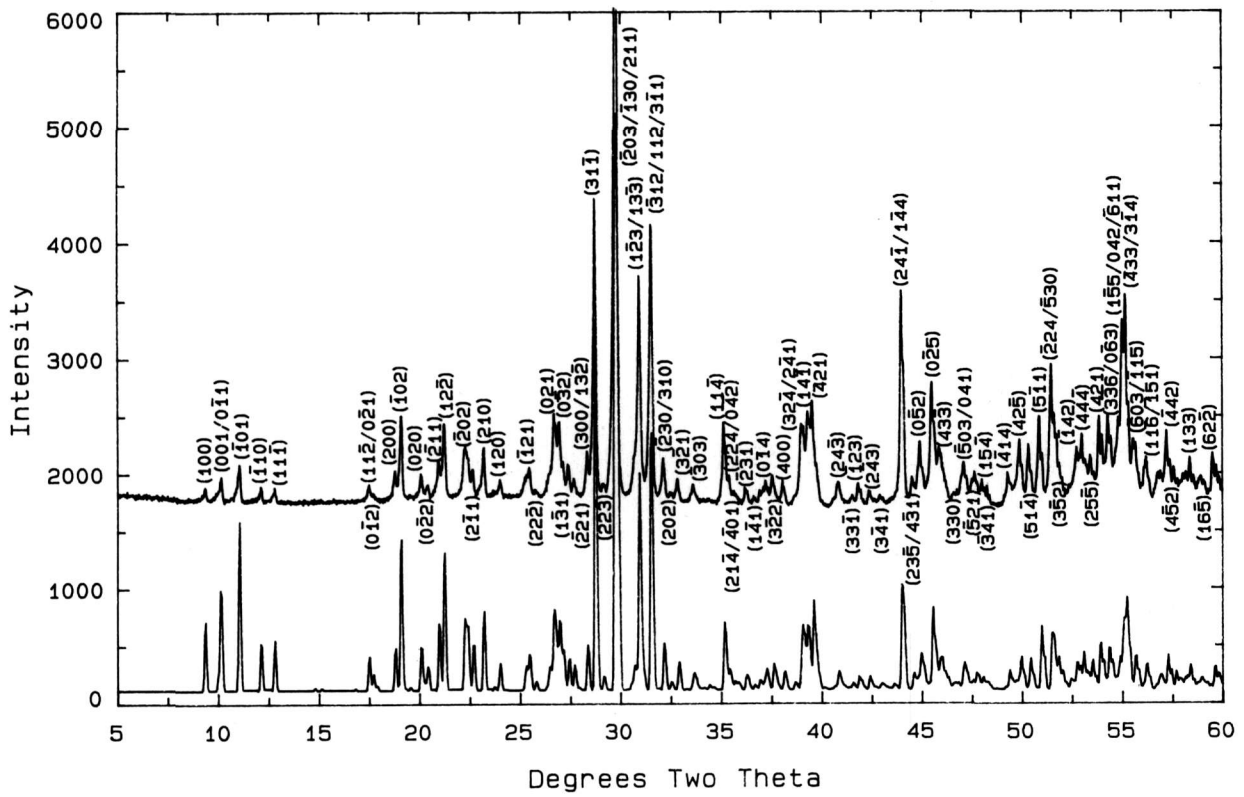


Fig. 17. X-ray powder diffraction pattern of the $\text{Ca}_2\text{Bi}_2\text{O}_5$ compound.

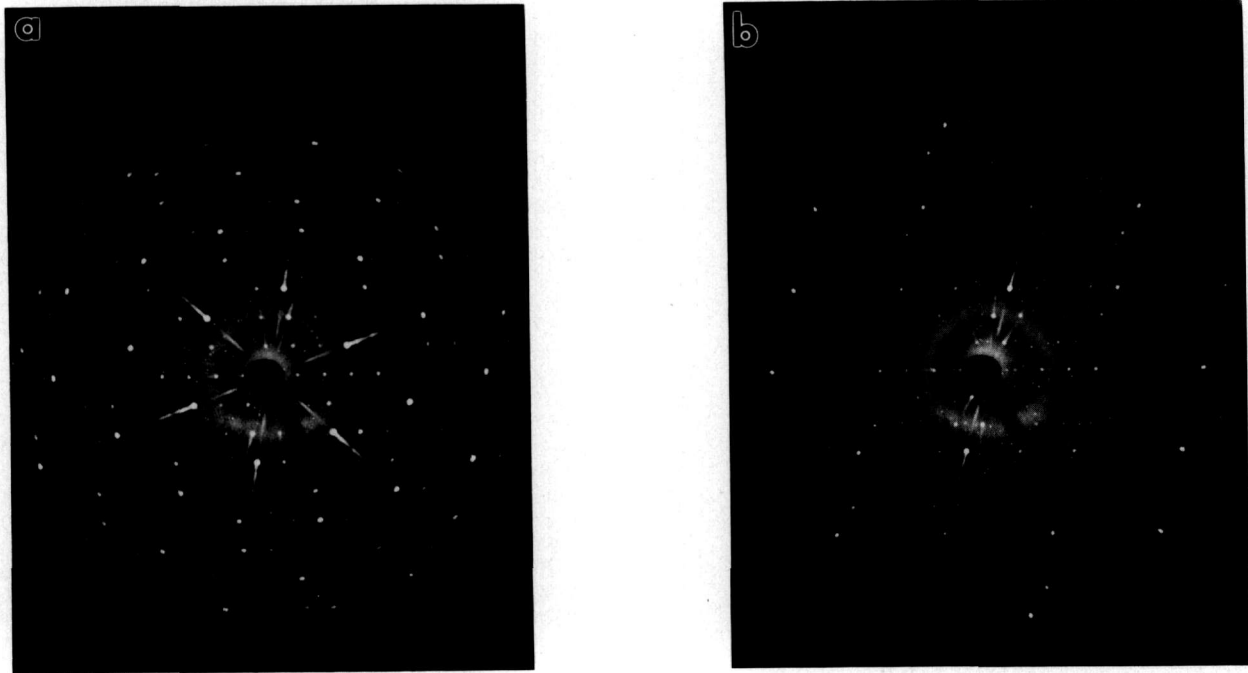


Fig. 18. X-ray precession photographs of $\text{Ca}_2\text{Bi}_2\text{O}_5$ (Mo radiation) (a) $(hk0)$, (b) $(h0l)$.

Table 14. X-ray powder diffraction data for the compound $\text{Ca}_2\text{Bi}_2\text{O}_5$

d obs (Å)	Rel I (%)	2θ obs	2θ calc ^a	hkl	$ F $ calc
9.461	4	9.34	9.36	100	59
8.717	7	10.14	10.12	001	56
			10.16	0 $\bar{1}$ 1	63
8.001	11	11.05	11.07	101	109
7.303	4	12.11	12.14	$\bar{1}$ 10	66
6.916	4	12.79	12.81	11 $\bar{1}$	70
5.069	4	17.48	17.49	11 $\bar{2}$	40
			17.49	0 $\bar{2}$ 1	71
5.013	2	17.68	17.69	0 $\bar{1}$ 2	56
4.965	1	17.85	17.87	201	31
4.721	4	18.78	18.78	200	98
4.648	16	19.08	19.09	$\bar{1}$ 02	191
4.421	6	20.07	20.09	020	93
4.352	3	20.39	20.41	0 $\bar{2}$ 2	79
4.237	8	20.95	20.97	$\bar{2}$ 11	141
4.182	19	21.23	21.23	1 $\bar{2}$ 2	206
3.9940	10	22.24	22.24	$\bar{2}$ 02	146
3.9746	7	22.35	23.33	1 $\bar{1}$ 2	104
			22.42	111 ^b	120
3.9209	7	22.66	22.65	2 $\bar{1}$ 1	130
3.8341	11	23.18	23.19	210	169
3.7480	1	23.72	23.69	122	38
3.7065	4	23.99	24.00	120	103
3.5243	3	25.25	25.23	2 $\bar{2}$ 1	81
3.5120	3	25.34	25.33	102	82
3.4957	6	25.46	25.48	$\bar{1}$ 21	127
3.4530	2	25.78	25.79	2 $\bar{2}$ 2	65
3.3834	2	26.32	26.31	221	37
3.3696	3	26.43	26.43	$\bar{3}$ 01	98
3.3571	3	26.53	26.52	12 $\bar{3}$	76
3.3361	14	26.70	26.69	021	197
3.3226	8	26.81	26.80	$\bar{2}$ 12	88
			26.83	012	115
3.3045	11	26.96	26.96	032	192
3.2806	6	27.16	27.13	0 $\bar{1}$ 3	135
			27.18	023	60
3.2501	5	27.42	27.41	131	133
3.2179	4	27.70	27.70	$\bar{2}$ 21	117
3.1456	8	28.35	28.33	300	127
			28.35	13 $\bar{2}$	102
3.1059	54	28.72	28.74	31 $\bar{1}$	471
3.0600	3	29.12	29.15	2 $\bar{2}$ 3	97
3.0006	100	29.75	29.73	203	427
			29.74	$\bar{1}$ 30	410
			29.77	211	116
2.9938	57	29.82	29.82	22	469
2.9099	5	30.70	30.69	003	132
2.8989	9	30.82	30.82	033	111
2.8897	36	30.92	30.93	123	83
			30.93	133	380
			31.09	$\bar{3}$ 20 ^b	122
2.8361	36	31.52	31.49	312	228
			31.53	112	391
			31.55	3 $\bar{1}$ 1	82
2.7828	7	32.14	32.13	230	172
			32.17	310	99
2.7519	2	32.51	32.50	202	81
2.7234	5	32.86	32.84	321	155
2.6620	3	33.64	33.63	$\bar{3}$ 03	101
2.6049	1	34.40	34.38	32 $\bar{3}$	68
2.5510	12	35.15	35.14	114	259

Table 14. X-ray powder diffraction data for the compound $\text{Ca}_2\text{Bi}_2\text{O}_5$ —Continued

d obs (Å)	Rel I (%)	2θ obs	2θ calc ^a	hkl	$ F $ calc
2.5336	4	35.40	35.40	224	91
			35.41	042	95
2.5171	2	35.64	35.64	214	68
			35.65	401	72
2.5055	1	35.81	35.83	024	86
2.4761	2	36.25	36.24	$\bar{2}$ 31	117
2.4500	1	36.65	36.63	141	73
2.4333	2	36.91	36.92	013	106
2.4182	2	37.15	37.13	412	84
2.4132	3	37.23	37.24	014	122
2.3921	5	37.57	37.55	322	177
2.3805	1	37.76	37.75	$\bar{3}$ 13	79
2.3594	4	38.11	38.09	400	144
2.3271	2	38.66	38.64	314	93
2.3116	6	38.93	38.95	332	107
2.3071	10	39.01	38.99	324	138
			39.02	241	245
2.3003	9	39.13	39.14	413	139
			39.15	420	133
2.2896	12	39.32	39.31	141	259
2.2857	11	39.39	39.39	230	158
2.2757	13	39.57	39.56	221	348
2.2658	4	39.75	39.76	124	163
2.2484	1	40.07	40.06	332	55
2.2192	1	40.62	40.61	134	69
2.2083	4	40.83	40.83	243	116
2.1722	2	41.54	41.55	331	94
2.1578	3	41.83	41.84	203	146
2.1311	3	42.38	42.40	123	146
2.1055	2	42.92	42.95	243	85
2.0765	1	43.55	43.55	341	96
2.0558	24	44.01	44.00	241	400
			44.01	144	207
2.0536	24	44.06	44.06	140	140
2.0326	3	44.54	44.54	235	149
			44.54	431	198
2.0206	4	44.82	44.81	1141	39
2.0167	7	44.91	44.90	052	159
2.0154	5	44.94	44.95	502	149
			44.95	332	137
2.0087	2	45.10	45.10	321	123
1.9911	18	45.52	45.50	025	396
1.9841	4	45.69	45.72	325	180
1.9763	4	45.88	45.87	343	168
1.9722	6	45.98	45.96	433	202
			46.11	512 ^b	117
1.9490	2	46.56	46.54	330	103
1.9322	3	46.99	46.98	412	123
1.9287	4	47.08	47.05	503	104
			47.10	041	158
			47.12	5123 ^b	109
1.9081	3	47.62	47.64	521	164
1.9043	3	47.72	47.74	434	95
1.8946	3	47.98	47.99	154	124
1.8850	1	48.24	48.26	341	124
1.8462	5	49.32	49.34	414	204
			49.82	305 ^b	102
1.8261	7	49.90	49.90	425	266
1.8112	6	50.34	50.36	514	270
1.7939	13	50.86	50.87	511	396
1.7743	16	51.46	51.46	224	368

Table 14. X-ray powder diffraction data for the compound $\text{Ca}_2\text{Bi}_2\text{O}_5$ —Continued

d obs (Å)	Rel I (%)	2θ obs	2θ calc ^a	hkl	$ F $ calc
1.7660	6	51.72	51.47	$\bar{5}30$	266
1.7569	3	52.01	51.73	$3\bar{5}2$	280
1.7459	3	52.36	52.01	$3\bar{3}3$	176
1.7418	2	52.49	52.36	$5\bar{2}1$	156
1.7388	4	52.59	52.47	$4\bar{4}\bar{3}$	107
1.7349	8	52.72	52.58	$0\bar{5}\bar{5}$	100
1.7306	3	52.86	52.73	$1\bar{4}2$	261
1.7267	7	52.99	52.88	$40\bar{5}$	127
1.7200	4	53.21	53.01	$4\bar{4}\bar{4}$	300
			53.23	$2\bar{5}4$	177
			53.26	$3\bar{2}2^b$	109
			53.38	$4\bar{3}\bar{3}^b$	145
1.7135	4	53.43	53.45	$2\bar{5}\bar{5}$	223
1.7017	12	53.83	53.84	$4\bar{2}1$	377
			54.12	$3\bar{5}\bar{3}^b$	104
			54.12	$3\bar{5}\bar{3}^b$	118
1.6883	9	54.29	54.27	$3\bar{3}\bar{6}$	250
			54.28	$0\bar{6}\bar{3}$	248
1.6846	4	54.42	54.40	$2\bar{1}\bar{5}$	108
			54.41	$1\bar{4}\bar{6}$	128
			54.62	$2\bar{3}2^b$	113
			54.66	$4\bar{1}\bar{3}^b$	151
1.6738	7	54.80	54.78	$1\bar{6}\bar{3}$	269
			54.95	$1\bar{6}2^b$	142
1.6682	16	55.00	54.98	$1\bar{5}\bar{5}$	305
			54.99	$0\bar{4}\bar{2}$	242
			54.99	$6\bar{1}\bar{1}$	117
			55.06	$2\bar{1}\bar{6}^b$	213
			55.07	$4\bar{1}2^b$	128
1.6643	15	55.14	55.13	$4\bar{3}\bar{3}$	183
			55.14	$3\bar{1}4$	386
1.6596	3	55.31	55.32	$2\bar{2}\bar{3}$	128
1.6530	5	55.55	55.55	$60\bar{3}$	260
1.6503	5	55.65	55.63	$1\bar{1}\bar{5}$	217
			55.95	$6\bar{1}2^b$	101
			56.06	$0\bar{4}6^b$	147
1.6370	4	56.14	56.14	$1\bar{1}\bar{6}$	105
1.6357	5	56.19	56.18	$1\bar{5}\bar{1}$	231
1.6248	1	56.60	56.58	$2\bar{6}\bar{2}$	110
			56.71	$4\bar{5}\bar{1}^b$	119
1.6201	2	56.78	56.77	$1\bar{6}\bar{4}$	106
1.6172	2	56.89	56.89	$10\bar{5}$	161
1.6092	7	57.20	57.21	$4\bar{4}\bar{2}$	313
1.5997	4	57.57	57.56	$4\bar{5}\bar{2}$	242
1.5919	2	57.88	57.87	$5\bar{3}\bar{5}$	154
1.5884	2	58.02	58.00	$6\bar{1}\bar{1}$	150
1.5846	2	58.17	58.16	$2\bar{6}\bar{1}$	152
1.5797	2	58.37	58.35	$1\bar{3}\bar{3}$	266
			58.74	$5\bar{3}\bar{1}^b$	111
1.5694	1	58.79	58.81	$1\bar{3}\bar{6}$	129
1.5672	2	58.88	58.88	$1\bar{6}\bar{5}$	145
1.5621	1	59.09	59.11	$2\bar{5}\bar{5}$	133
1.5523	6	59.50	59.51	$6\bar{2}\bar{2}$	300
1.5453	2	59.80	59.82	$1\bar{2}\bar{4}$	159

^a Calculated on the basis of a triclinic unit cell, space group $\text{P}\bar{1}$, $a = 10.1222(7)$, $b = 10.1466(6)$, $c = 10.4833(7)$ Å, $\alpha = 116.912(5)$, $\beta = 107.135(6)$, and $\gamma = 92.939(6)^\circ$.

^b Calculated $|F|$ greater than 100 but cannot be distinguished from nearby peaks.

3.3.8 “C-mon” Metastable Phase
 $\sim \text{Ca}_{6+x}\text{Sr}_{6-x}\text{Bi}_{14}\text{O}_{33}$ ($x \rightarrow 6$) When the 1:1 phase is heated between 885 and 925 °C for 20 min to 3 h a metastable C-centered monoclinic phase is formed which may be nearly single phase [$a = 21.295(4)$, $b = 4.3863(8)$, $c = 12.671(2)$ Å, and $\beta = 102.74(1)^\circ$]. After overnight heat treatments, however, this phase decomposes to a “bcc” plus CaO assemblage. Comparison of the X-ray powder diffraction patterns (Fig. 19, Table 15) for this phase and for $\text{Ca}_{6+x}\text{Sr}_{6-x}\text{Bi}_{14}\text{O}_{33}$ ($x \sim 4.8$) indicates that it is the metastable end member extension of the stable ternary solid solution.

3.4 The System $\text{CaO-Bi}_2\text{O}_3\text{-CuO}$

Ternary phase relations of the system $\text{CaO-1/2Bi}_2\text{O}_3\text{-CuO}$ have been studied at temperatures between 700 and 900 °C. No ternary compounds were discovered, but new data on the $\text{CaO-1/2Bi}_2\text{O}_3$ and CaO-CuO binaries have been incorporated. The ternary phase relations at 700–750 and 750–800 °C are shown in Figs. 20 and 21 respectively. There remains some uncertainty about the equilibrium phase relations involving $\text{Ca}_{1-x}\text{CuO}_2$.

To verify that the three-phase equilibria inferred from synthesis runs (products of a synthesis from CaCO_3 , Bi_2O_3 , and CuO) reflected equilibrium phase assemblages, various three phase mixtures of pre-made binary compounds were reacted isothermally. For example, such experiments demonstrate that a mechanical mixture of $\text{Ca}_4\text{Bi}_6\text{O}_{13} + 7\text{Ca}_2\text{CuO}_3 + 3\text{Ca}_{4.533}\text{Cu}_{5.467}\text{O}_{10}$ (bulk composition 51.80: 9.84: 38.36) is metastable with respect to a mixture of $\text{Ca}_2\text{Bi}_2\text{O}_5 + \text{Ca}_2\text{CuO}_3 + \text{Ca}_{4.533}\text{Cu}_{5.467}\text{O}_{10}$ at 700 °C. Because the nucleation (or increase in volume fraction) of $\text{Ca}_{1-x}\text{CuO}_2$ from binary compounds was never demonstrated at 700 °C (see Sec. 3.2.2) the possibilities of three phase equilibria including Ca_2CuO_3 (and/or $\text{Ca}_{1-x}\text{CuO}_2$) plus $\text{Bi}_6\text{Ca}_4\text{O}_{13}$ can not be ruled out. For example, the mechanical mixture $5\text{Ca}_2\text{CuO}_3 + \text{Ca}_4\text{Bi}_6\text{O}_{13}$ which has a bulk composition of 56:24:20 shows no convincing evidence of $\text{Ca}_{1-x}\text{CuO}_2$ even after six heating/grinding treatments at 700 °C.

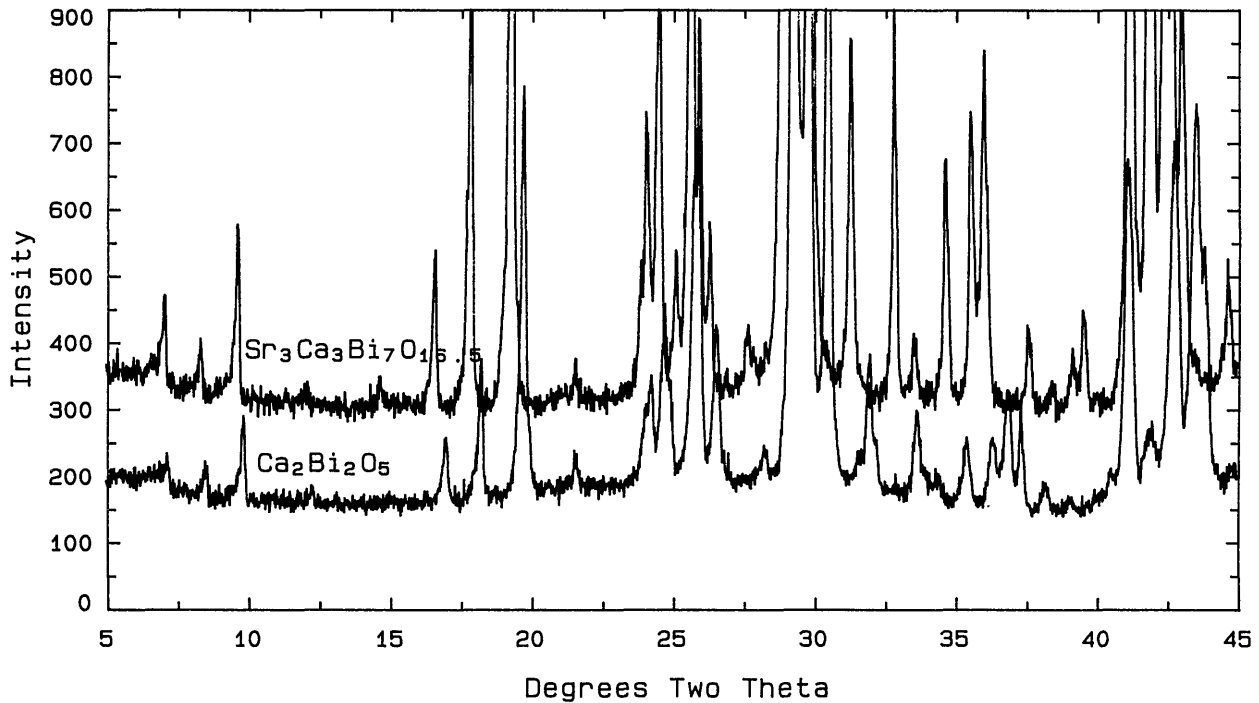


Fig. 19. X-ray powder diffraction pattern comparing the "C-mon" metastable phase $\sim\text{Ca}_{6+x}\text{Sr}_{6-x}\text{Bi}_{14}\text{O}_{33}$ $x \rightarrow 6$ to the ternary $x \rightarrow 0$.

Table 15. X-ray powder diffraction data for the "C-mon" Metastable Phase

d obs (Å)	Rel I (%)	2θ obs	2θ calc ^a	hkl
12.405	2	7.12	7.15	001
10.419	3	8.48	8.51	200
9.009	6	9.81	9.83	$20\bar{1}$
7.219	1	12.25	12.27	$20\bar{1}$
5.221	4	16.97	16.99	$40\bar{1}$
4.865	11	18.22	18.24	202
4.489	27	19.76	19.74	$40\bar{2}$
4.447	4	19.95	19.94	401
	1	20.62 ^b		
4.109	2	21.61	21.59	$11\bar{1}$
3.7049	4	24.00	24.00	310
	5	24.07 ^b		
3.6718	8	24.22	24.23	$31\bar{1}$
3.6044	11	24.68	24.69	402
			24.69	$11\bar{2}$
3.5730	6	24.90	24.93	203
3.4491	22	25.81	25.79	112
3.4360	23	25.91	25.88	311
3.3583	11	26.52	26.53	$31\bar{2}$
3.3521	11	26.57	26.57	$60\bar{2}$
3.1576	2	28.24	28.24	601
3.1565	2	28.25	28.24	$20\bar{4}$
3.0922	3	28.85	28.87	004
3.0457	74	29.30	29.31	$51\bar{1}$
3.0406	88	29.35	29.34	$11\bar{3}$
3.0265	97	29.49	29.51	312
3.0056	100	29.70	29.59	510
			29.60	$60\bar{3}$
2.9267	69	30.52	30.50	403
2.8299	2	31.59	31.61	511

Table 15. X-ray powder diffraction data for the "C-mon" Metastable Phase—Continued

d obs (Å)	Rel I (%)	2θ obs	2θ calc ^a	hkl
2.7989	11	31.95	31.96	204
	4	32.17 ^{CaO}		
2.6605	6	33.66	33.64	$80\bar{1}$
2.6101	2	34.33	34.35	$60\bar{4}$
2.6042	1	34.41	34.38	313
2.5976	1	34.50	34.52	800
2.5336	5	35.40	35.40	$20\bar{5}$
2.4715	6	36.32	36.31	005
2.4359	9	36.87	36.88	801
	9	37.34 ^{CaO}		
2.3541	2	38.20	38.19	$51\bar{4}$
2.3036	1	39.07	39.07	$71\bar{3}$
2.2463	2	40.11	40.10	$80\bar{4}$
			40.11	314
2.2234	3	40.54	40.51	802
2.1919	25	41.15	41.13	020
2.1593	5	41.80	41.80	021
2.1534	6	41.92	41.93	712
2.1470	5	42.05	42.08	220
2.1225	7	42.56	42.58	$11\bar{4}$
2.1102	29	42.82	42.80	$20\bar{6}$
2.0783	25	43.51	43.51	$40\bar{6}$
2.0760	27	43.56	43.54	10,0,0
2.0630	17	43.85	43.86	405
2.0223	3	44.78	44.79	421

^a Calculated on the basis of a monoclinic unit cell, C2/m, $a = 21.295(4)$, $b = 4.3863(8)$, $c = 12.671(2)$ Å, and $\beta = 102.74(1)^\circ$.

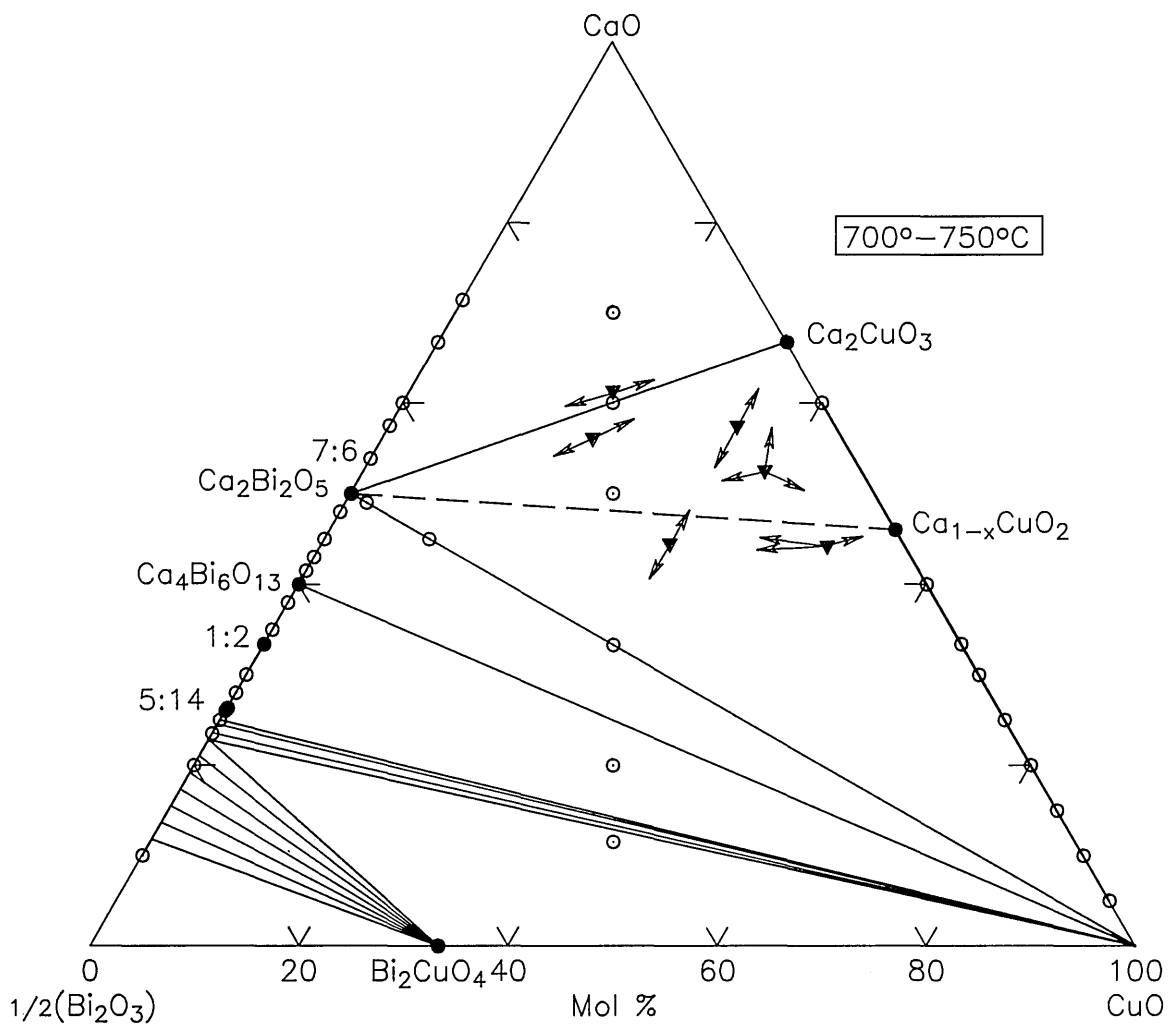


Fig. 20. CaO-Bi₂O₃-CuO 700–750 °C phase diagram.

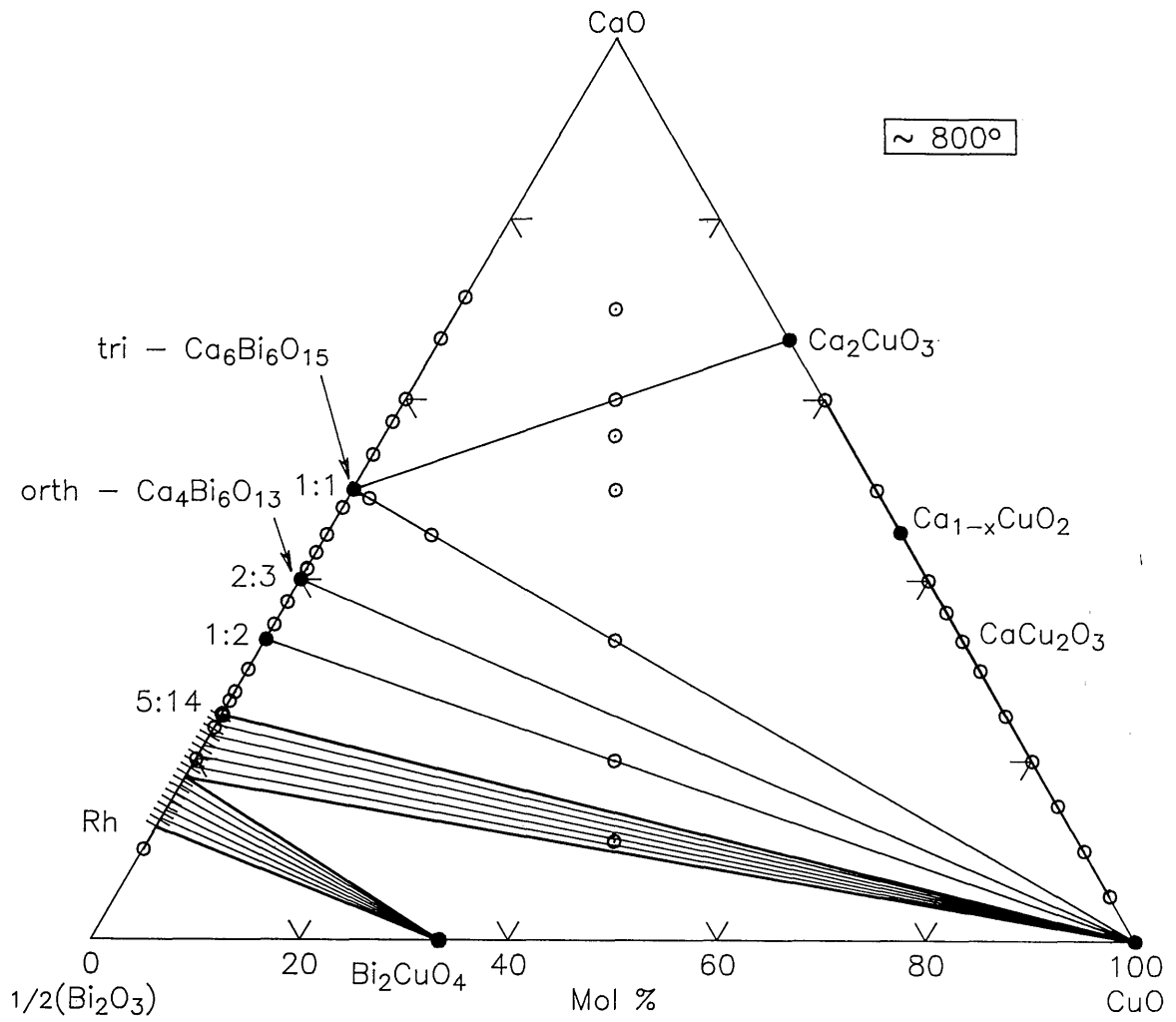


Fig. 21. CaO-Bi₂O₃-CuO 750-800 °C phase diagram.

4. Summary

A new phase diagram is presented for the system CaO-CuO with the composition of the phase $\text{Ca}_{1-x}\text{CuO}_2$ corresponding to a Ca:Cu ratio of 45.33: 54.67. This compound decomposes at $\sim 755^\circ\text{C}$ in air and 835°C in O_2 . The phases previously reported as “ $\text{Ca}_7\text{Bi}_{10}\text{O}_{20}$ ” and “ $\text{Ca}_7\text{Bi}_6\text{O}_{16}$ ” [21,22] are really $\text{Ca}_4\text{Bi}_6\text{O}_{13}$ and $\text{Ca}_2\text{Bi}_2\text{O}_5$ respectively. X-ray powder and single crystal data are reported for almost all of the binary phases encountered. No ternary phases were found in the system $\text{CaO}-1/2\text{Bi}_2\text{O}_3\text{-CuO}$. Above 775°C CuO is in equilibrium with all of the binary CaO-Bi₂O₃ phases, and this is probably true below 775°C as well.

Acknowledgments

Phase diagrams were computer drafted by T. Green, American Ceramic Society Associate of the Phase Diagrams for Ceramists, Data Center at NIST. Sibel P. Bayracki, under the guidance of J. J. Ritter, determined the stoichiometry of $\text{Ca}_{1-x}\text{CuO}_2$ using the citrate route.

5. References

- [1] J. G. Bednorz and K. A., Müller, *Z. Phys. B-Condensed Matter* **64**, 189 (1986).
- [2] H. Takagi, S. Uchida, K. Kitazawa, and T. Tanaka, *Jpn. J. Appl. Phys. Lett.* **26**, L123 (1987).
- [3] R. J. Cava, B. Batlog, R. B. VanDover, D. W. Murphy, S. A. Sunshine, T. Siegrist, J. R. Remeika, E. A. Rietman, A. Zahurak, and G. P. Espinosa, *Phys. Rev. Lett.* **58**, 1676, (1987).
- [4] M. K. Wu, Jr., J. R. Asburn, C. J. Torng, P. H. Hor, R. L. Meng, L. Gao, Z. J. Huang, Y. Q. Wang, and C. W. Chu, *Phys Rev. Lett.* **58**, 908 (1987).
- [5] H. Maeda, Y. Tanaka, A. Fukutomi, and T. Asano, *Jpn. J. Appl. Phys.* **27**, L209-10 (1988).
- [6] Z. Z. Sheng and A. M. Hermann, *Nature* **332**, 55-57 (1988).
- [7] R. S. Roth, C. J. Rawn, J. J. Ritter, and B. P. Burton, *J. Am. Ceram. Soc.* **72**, 1545 (1989).
- [8] T. Siegrist, S. M. Zahurak, D. W. Murphy, and R. S. Roth, *Nature* **334**, 231-232 (1988).
- [9] R. S. Roth, C. J. Rawn, B. P. Burton, and F. Beech, *J. Res. Natl. Inst. Stand. Technol.* **95**, 291 (1990).
- [10] R. S. Roth, C. J. Rawn, J. D. Whitley, C. K. Chiang, and W. K. Wong-Ng, *J. Am. Ceram. Soc.* **72** (3) 395-99 (1989).
- [11] T. Siegrist, L. F. Schneemeyer, S. A. Sunshine, J. V. Waszczak, and R. S. Roth, *Mat. Res. Bull.* **23**, 1429-1438, (1988).
- [12] R. S. Roth, C. J. Rawn, and L. A. Bendersky, *J. Mater. Res.* **5**, 46 (1990).
- [13] R. S. Roth, B. P. Burton, and C. J. Rawn, in *Superconductivity and Ceramic Superconductors*, K. M. Nair and E. A. Giess, eds., *Ceram. Trans.* **13**, 23 (1990).
- [14] C. J. Rawn, R. S. Roth, B. P. Burton, and M. D. Hill, *J. Am. Ceram. Soc.*, to be published.
- [15] T. Siegrist, R. S. Roth, C. J. Rawn, and J. J. Ritter, *Chem. Mat.* **2**, 192 (1990).
- [16] B. G. Kakhan, V. B. Lazarev, and I. S. Shaplygin, *Zh. Neorg. Khim* **24** (6) 1663-68 (1979) *Russ. J. Inorg. Chem. (Engl. Transl.)* **24** (6) 922-925 (1979).
- [17] R. S. Roth, J. R. Dennis, and H. F. McMurdie, eds., *Phase Diagrams for Ceramists*, Vol. 6, Am. Ceram. Soc., Westerville, OH (1987).
- [18] R. S. Roth, N. H. Hwang, C. J. Rawn, B. P. Burton, and J. J. Ritter, *J. Am. Ceram. Soc.* **74** (9), 2148 (1991).
- [19] Powder Diffraction File, Card No. 34-284. Joint Committee on Powder Diffraction Standards, Swarthmore, PA (1984).
- [20] A. M. M. Galla and J. White, *Trans. Br. Ceram. Soc.* **65**, 181 (1966).
- [21] P. Conflant, J. C. Boivin, and D. J. Thomas, *Solid State Chem.* **18**, 133 (1976).
- [22] P. Conflant, J. C. Boivin, and G. Tridot, *C. R. Acad. Sci. Paris* **279**, 457 (1974).
- [23] J. B. Parise, C. C. Torardi, H. N. Whangbo, C. J. Rawn, R. S. Roth, and B. P. Burton, *Chem. Mater.* **2**, 454 (1990).
- [24] J. B. Parise, C. C. Torardi, C. J. Rawn, R. S. Roth, B. P. Burton, and A. Santoro, *J. Solid State Chem.* **102**, 132 (1993).
- [25] L. G. Sillen and B. Z. Aurivillius, *Krist.* **101**, 483 (1943).
- [26] E. M. Levin, and R. S. Roth, *Natl. Bur. Stands. (U.S.)*, *J. Res. Phys. Chem* **68**, 197 (1964).
- [27] C. J. Rawn, R. S. Roth, and H. F. McMurdie, *Powder Diffraction* **7** (2), 109 (1993).

About the authors: Benjamin P. Burton is a Physical Scientist in the Ceramics Division of the NIST Materials Science and Engineering Laboratory. Claudia J. Rawn is currently a graduate student at the University of Arizona, and was formerly in the Ceramics Division of the NIST Materials Science and Engineering Laboratory. Robert S. Roth is currently under contract at NIST, and was formerly in the Ceramics Division of the NIST Materials Science and Engineering Laboratory. N. M. Hwang is with the Korea Science and Engineering Foundation, Daejeon Chunynam, Korea, and was a Guest Scientist at NIST. The National Institute of Standards and Technology is an agency of the Technology Administration, U.S. Department of Commerce.

Conference Report

COMPASS '93, EIGHTH ANNUAL CONFERENCE ON COMPUTER ASSURANCE Gaithersburg, MD June 14–17, 1993

Report prepared by

**Dolores R. Wallace and
Elizabeth B. Lennon**

Computer Systems Laboratory,
National Institute of Standards and Technology,
Gaithersburg, MD 20899-0001

1. Introduction

Cosponsored by the IEEE Aerospace and Electronics Systems Society and the IEEE National Capital Area Council, in cooperation with the British Computer Society, COMPASS is an organization which advances the theory and practice of building computer assurance into critical systems. NIST's Computer Systems Laboratory hosted the Eighth Annual Conference on Computer Assurance (COMPASS '93) on June 14–17, 1993, and served as cosponsors with the following industry and government organizations: Arca Systems, Inc.; ARINC Research Corporation; Control Systems Analysis, Inc.; CTA, Inc.; IBM; Logicon, Inc.;

Naval Research Laboratory; Naval Surface Warfare Center; Systems Safety Society; TRW Systems Division; and the U.S. General Accounting Office. COMPASS '93 attracted more than 130 participants from government, industry, academia, and foreign countries such as the United Kingdom, Italy, and Taiwan. This year's theme, "Practical Paths to Assurance," highlighted the need to use a pragmatic and realistic approach when providing assurance in a computer system.

2. Tutorials

COMPASS '93 featured tutorials for conference participants who wanted an in-depth discussion of two relevant topics. John Rushby and Patrick Lincoln, SRI International, provided an introduction to formal methods with special focus on the use of automated support tools such as PVS, a Prototype "next generation" Verification System that attempts to provide the benefits of powerful and effective automation for an expressive specification language. Worked examples were demonstrated "live" and included examples from hardware design, fault tolerance, and real-time systems. Janet Cugini, NIST, gave a second tutorial on the draft Federal Criteria for Information Technology Security which covered background, protection profiles, Trusted Computing Base (TCB) functional components, development assurance requirements, evaluation assurance requirements, and future work.

The first full day of the conference opened with welcoming remarks by James Burrows, CSL Director; Judith Bramlage, COMPASS '93 General Chair; and John Marciniak, COMPASS '93 Program Chair.

3. Myths of Dependable Computing

Peter Neumann, SRI International, keynoted the first day of the conference with a talk entitled "Myths of Dependable Computing: Shooting the Straw Herrings in Midstream." Citing the belief that most users are doing what they can to assure dependable computing, Neumann identified five problem areas: unsecured PCs; distributed systems which do not back up well; standards and criteria which are useful but inadequate; the lack of use of software engineering and fault tolerance; and the fact that the state-of-the-art in software engineering is not being used in critical systems. Stating that myths tend to be true in the small view, false in the larger picture, he discussed the reliability, security, and safety of software systems, and proposed solutions through research, development, and education. Neumann challenged organizations to do it right in the first place, to make hard decisions, and to look at assurance in the context of the larger picture.

4. Verification Technology

Moderated by Connie Heitmeyer, Naval Research Laboratory, this session featured three papers. Sidney Bailin and Scott Henderson, CTA Incorporated, presented a talk on "A Tool for Reasoning About Software Models" which described the Formal Interconnection Analysis Tool (FIAT). Supporting formal reasoning about software systems via their specification diagrams, FIAT decomposes the specification into a diagram of interconnected lower-level components and uses this information to establish some automated verification results.

Chung-Ming Huang, National Cheng Kung University, Tainan, Taiwan, described a protocol verification method which could use ESTELLE and SDL verification tools to assure the correctness of communication protocols. Current verification protocol techniques utilize a global state reduction technique to allow the use of ESTELLE and SDL; the new technique reduces global states to a single state for live variables having the same value, making the incremental protocol model applicable in the ESTELLE and SDL verification tools.

The third presenter was Farn Wang of the University of Texas. Building off the successful use

of propositional temporal logic in the verification of digital circuits, Wang and co-author Aloysius K. Mok proposed a technique called Asynchronous Register Temporal Logic (ARTL) to address the verification of distributed real-time software systems. ARTL uses a multi-clock model, utilizes reasoning about items which have more than binary values normally found in digital circuits, and uses a freezing modal operator for fixing register contents. Results are promising for using the verifier for larger benchmarks.

5. Special Topics

Peter Neumann, session moderator, introduced Carol Taylor, National Security Agency (NSA), who spoke on "Global Protection against Limited Strikes (Trusted Software Methodology)." In a joint effort with General Electric and AT&T, NSA's task was to solve the information security problems for the Strategic Defense Initiative (SDI). Taylor stressed that in the process of identifying threats and developing safeguards and countermeasures, 85 percent of the methodology was simply good software engineering practices. She identified three requirements for security: the environment to control separation of duties; the trusted process; and vigilance to ensure the integrity of the environment and the process. Increased costs for up-front efforts were largely recovered in the code and test phase.

John McHugh, University of North Carolina, and Greg Chisholm, Argonne National Laboratory, presented a paper on the "Application of the High Trust Process Model to Complexity Management and System Architecture in the SDI." Despite the expenditure of large amounts of time, money, and effort, the lack of a definitive, detailed architecture indicates the difficulty of the problem. The authors described a risk-driven approach which utilizes a product model and a process model, concluding that prototyping is the primary risk mitigation process and success is more a matter of accident than design.

"Using Ada in Secure Systems" was the topic of a paper by Roberta Gotfried and David J. Naiditch, Hughes Aircraft Company. Gotfried gave an overview of research into applications of Ada to real-time systems, concluding that Ada has advantages for trusted systems implementations generally lacking in other programming languages.

6. The Government Accounting Office (GAO) Perspective

Rona Stillman, Chief Scientist, GAO, gave the second-day keynote address on the task at GAO to ensure that the taxpayer is well served by federal information systems. Are systems performing their intended functions and are they performing well? Problems to be addressed include the poor understanding of software as a product; the difficulty in measuring security; the software development process; and security lapses, both physical and operational. GAO is working on defining methodologies for audits. Assurance will be more difficult in the future with the expansion of the national information infrastructure.

7. Reliability Measurement

Moderator Reginald Meeson, Institute for Defense Analysis, introduced Herb Hecht, SoHaR, Inc., who spoke on “Rare Conditions—An Important Cause of Failures.” Hecht’s premise was that rarely executed code has a much higher failure rate than frequently executed code during the early operational period. The inability to handle multiple rare conditions is a prominent cause of program failure in well-tested systems. Problem-solving approaches include correcting identified deficiencies; conducting stress testing in accordance with specified procedures; and conducting testing in a high-workload environment with scenarios that emphasize computer and peripheral equipment failures.

Jeffrey Voas, Jeffrey Payne, and Christoph Michael, Reliable Software Technologies Corporation, and Keith Miller, College of William and Mary, presented a paper entitled “Experimental Evidence of Sensitivity Analysis Predicting Minimum Failure Probabilities.” They presented a theoretical statistical technique complementary to black-box testing known as “sensitivity analysis.” While black-box testing establishes an upper limit on the probability of failure, software sensitivity analysis sets a lower limit on the likelihood of failure. Together, these estimates can establish confidence that software does not contain faults.

“Assigning Probabilities for Assurance in Multi-Level Secure (MLS) Database Design” was the subject addressed by Lucian Russell, Argonne National Laboratory. Russell considered the problem in

computer assurance that exists when a MLS application is designed using a MLS database. A system of assigning risks to the release of data collections allows database design to be quantified by a risk factor, resulting in reduced costs. A security policy based upon such a rational approach is more likely to gain acceptance for the system.

8. System Safety

Michael Brown, Naval Surface Warfare Center, served as session moderator. He introduced Ron Bell, Health and Safety Executive, United Kingdom, who spoke on “Risk and System Integrity Concepts for Safety-Related Control Systems.” Bell gave an overview of the concepts of risk and safety-integrity in relation to safety-related electrical/electronic/programmable electronic systems. Co-authored by D. Reinert of Germany, the presented paper was an abridged version of Annex A of the emerging International Electrotechnical Commission (IEC) Standard “Functional safety of electrical/electronic/programmable electronic systems.” Bell discussed the standards work on the safe utilization of programmable electronic systems (PES) being done in the U.K., Germany, the European Community, and the United States, the major objective of which is the achievement of international standardization.

“Identifying Generic Safety Requirements” was the topic addressed by Jan Filsinger, Booz-Allen & Hamilton, and Jody Heaney, MITRE Corporation. They proposed a four-step approach to identify generic safety requirements: identification of the safety application domains; analysis of the identified domains; a policy and guidance review; and the review of existing tools, techniques, and methodologies. The approach builds upon lessons learned from the security engineering field to provide tentative answers for several outstanding questions in the safety field.

Keith Gallagher, NIST and Loyola College, and James Lyle, NIST, addressed the issue of “Software Safety and Program Slicing.” They proposed a method that uses program slicing to locate all code that contributes to the value of variables that might be part of a safety critical component. They described how slicing-based techniques can be used to validate functional diversity. The researchers are prototyping this method as part of a NIST research project.

9. Management and Developmental Issues

Session moderator Charles Payne, NRL, introduced the first paper by Qi Shi, J. A. McDermid, and J. D. Moffett of the University of York. "Developing Secure Systems in a Modular Way" presented a new technique for the development and verification of secure systems in a modular way. At the heart of the technique is a general approach for coping with the composition of modules. The dependencies among modular security requirements are analyzed and used to locate the modules affected by changes, thus avoiding unnecessary security reevaluation of other modules.

James Freeman, CTA, Inc., spoke on security policy modeling. He stressed the production of a formal security policy model as an important element in the development of a secure system. It is important to produce first a system-specific security policy that explicitly identifies only those portions of the system to be modeled. This separation helps to clarify what needs to be specified and reduces ambiguity.

Stephen Cha, Aerospace Corporation, addressed the "Management Aspect of Software Safety." Cha contended that more immediate and significant effects on current safety-critical projects can be realized by addressing the management aspects first and then the technical ones. Management policies and decisions are critical to software safety because management has the ultimate control over how and when to spend the limited available resources.

10. Developing Standards and Issues

Dolores Wallace, NIST, moderated this session. Robin Bloomfield presented an overview of the many draft standards evolving in the European community. The European community is attempting to replace national standards with international standards but has found the process to be time-consuming. There are various standards organizations ranging from those working generically, such as the ISO IEC SC65A working groups 9 and 10 for Functional Safety of Programmable Electronic Systems, to those who are developing application-specific standards, including the nuclear, avionics, and railway signaling industries. The issues of allowing "best practices" or having strong requirements have not been resolved. Another issue is validating that a standard is effective.

The ISO 9000 Standards for Quality, as described by Taz Daughtrey of Babcock and Wilcox, establish

requirements for quality management systems for many industries. In Europe, companies must meet ISO 9000 requirements and be registered by an official Registration Accreditation Board in order to market selected products.

Dr. Raghu Singh, of the Navy SPAWAR Command, discussed the draft of the new Military Standard 498, Software Development and Documentation, which harmonizes the previous standards for both weapons systems and information systems. The document has been reviewed by industry, the Department of Defense and other federal agencies and comments have been reconciled into the document. Dr. Singh plans to have approval of the standard by September 30, 1993.

Michael Brown of the Naval Surface Warfare Center reported on the Military Standard 882C, System Safety Program Requirements, and described how it differs from its predecessor, MIL-STD-882B, in both positive and negative aspects. He concluded by stating that while the new standard is an improvement over its predecessor, it may be difficult to apply to projects involving only software.

11. Results of Workshops/Studies

Session moderator H. O. Lubbes, Naval Research Laboratory, introduced Chuck Howell, MITRE, who discussed the MITRE Critical Assurance Workshop of September 1992. The workshop indicated a need for risk reduction, a national repository for research problems, personnel exchange, standards development, and equipping developers and certifiers to deal with the formal method.

Susan Gerhart, National Science Foundation, reviewed the International Survey of the Industrial Applications of Formal Methods conducted by NIST in conjunction with the Naval Research Laboratory and the AECB of Canada. The survey concluded that there are significant applications of formal methods, there is evidence of "best practice," and advanced tools can be used without excessive costs. The survey cited many limitations, however, including inadequate cost models.

Eugene Troy reported on the Federal Criteria Workshop held at Turf Valley, Maryland, on June 2–3, 1993. The workshop concluded that the replacement of the Orange Book should address distributed systems, networks, encryptions, and PC security. Protection profiles should provide more flexibility and the evaluation and certification process were deemed important issues. There is

now a Common Criteria Editorial Board comprised of the European community whose three representatives are from the U.K., France and Germany, and Canada and the United States with one representative each from NIST and NSA. The Board's objective is to align the three existing IT security criteria documents into a common set of criteria.

12. Evening Sessions

COMPASS '93 also held two social/business activities. On the first evening, two roundtable parallel sessions gave participants the opportunity to discuss issues on Processes (Capability Maturity Model [CMM]) and Standards for Formal Methods. John Baumert, Computer Sciences Corporation, led a discussion on the CMM and explained the differences between the CMM usage and software process assessments where improvement is the principal objective. Roger Fujii, Logicon, proposed different types of formal methods for requirements, design, code and test activities and asked participants to discuss the state-of-the-art of these methods relative to maturity for standardization.

Following the COMPASS banquet the next evening, Dr. Dorothy Denning, Georgetown University, described the Clipper chip, the government-developed "key escrow" chip cryptographic technology, and how it would be used with respect to phone-tapping. Dr. Denning fielded many difficult questions from her audience who were concerned with issues ranging from individual privacy rights to export controls to production of the chip by a single company.

13. COMPASS '94

COMPASS '94 will be held June 27–30, 1994, at NIST in Gaithersburg, Maryland. The deadline for papers submitted for COMPASS '94 is January 15, 1994. For the first time, the COMPASS organization will give a special award for the best paper that uses technology presented at a previous COMPASS conference; the paper may be research-based or application-oriented. For information about COMPASS '94 or how to obtain the proceedings of COMPASS '93, contact Dolores Wallace, Computer Systems Laboratory, National Institute of Standards and Technology, Building 225, Room B266, Gaithersburg, MD 20899-0001; telephone (301) 975-3340 or fax (301) 926-3696.

Conference Report

WORKSHOP ON AGING, DIMENSIONAL STABILITY, AND DURABILITY ISSUES IN HIGH TECHNOLOGY POLYMERS Gaithersburg, MD May 28–29, 1992

Report prepared by

Cynthia Arnold-McKenna

White House Office of Science
and Technology Policy,
Old Executive Office Building, Room 427,
Washington, DC 20500

and

Gregory B. McKenna

National Institute of Standards and Technology,
Gaithersburg, MD 20899-0001

1. Introduction

The expected functional life of polymers and polymer-based composites subjected to a set of environments and stress conditions is often determined by issues of aging, dimensional stability and durability. The complexity of these issues leads not only to a need for further research developments

but also improved methods of application of current physical and chemical knowledge to the design, manufacture, and use of materials. The knowledge base required to attain improvements in materials performance requires a “high technology” approach across the entire spectrum of industries that critically depend upon materials.

Problems associated with the lifetime and performance of polymers and polymer-based composites are manifest in many products and industries ranging from automotive and aerospace to photographic and imaging applications and electronic packaging. In some cases, the product design is necessarily conservative to compensate for the lack of understanding of the base materials. In other cases, the developments required to advance into new markets are constrained because testing methodologies are unavailable to benchmark material performance. Furthermore, materials design cannot advance in the absence of a fundamental understanding of the mechanical performance of materials.

Materials suppliers, end-users, and government experts were brought together at a workshop sponsored by the Materials Science and Engineering Laboratory of the National Institute of Standards and Technology, held at NIST on May 28-29, 1992. The purpose of the workshop was to provide inputs and advice into the programs at NIST involved in the study of the mechanical performance of polymers. The participants in the workshop began a dialogue on the possible mechanisms of interaction between industry and government, viz., NIST, to address these problems in a mutually beneficial way. The long term goal is to enhance the knowledge base associated with materials performance, with the result of improving the competitiveness of U.S. industries that critically depend upon materials performance.

In this conference report, we highlight the presentations made at the workshop in a format that first presents a scientific perspective on the issues, then highlights manifestations of the problems experienced across industries, indicating the ubiquitous nature of the relevant phenomena. Finally, we summarize the technological difficulties in the application of polymers and polymer-based composites that need to be addressed and surmounted in order to positively affect the industries involved.

2. The Science Base of Performance Issues

The implications of the process of physical aging on long-term performance of polymeric glasses were outlined in an introductory presentation by Dr. G. McKenna (NIST), who highlighted the research on physical aging that has been an ongoing activity at NIST for about the past decade. In Fig. 1, the thermodynamic basis for physical aging is delineated. When a glass-forming polymer is quenched from above to below its glass transition (T_g), it becomes essentially trapped in a non-equilibrium state [1,2]. (This is an event which occurs in the manufacture of nearly all polymers.) With time, the glass evolves towards equilibrium, and this volume recovery results in the process known as physical aging [3]. The importance of physical aging can be put into perspective in that it affects many, if not all properties of materials, such as dimensional stability, creep compliance, the relaxation modulus, yield strength, and fracture and failure resistance.

McKenna discussed the work carried out at NIST on aging of epoxy resins in the context of the classical [3] time-aging time superposition concept. Thus, as depicted in Fig. 2, the relaxation modulus for an amine-cured epoxy evolves with aging time, t_e , after a quench. All of the curves can be overlaid to form a single "master curve" by shifting them along the horizontal axis. The amount of displacement required for each curve to overlay on the master curve is called the "shift factor," denoted a_{te} . The ability to shift each curve is referred to as time-aging time superposition and is important in developing mathematical models of the process. In Fig. 3, the "shift factor" is plotted as a function of the aging time. Importantly, near the glass transition, aging eventually stops as the glass attains equilibrium. However, far below T_g , aging continues for extremely long times *at the same rate* — a factor that is important in long term applications of polymers.

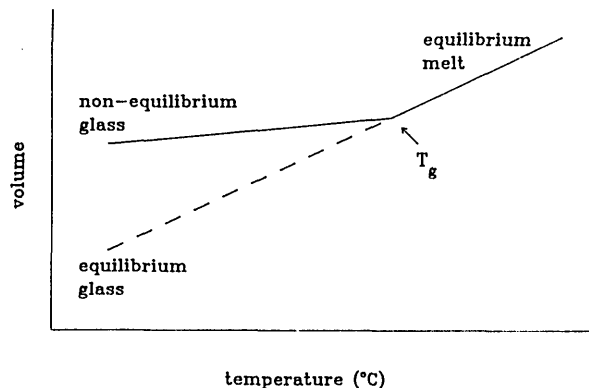


Fig. 1. Schematic representation of volume-temperature behavior of a glass forming material.

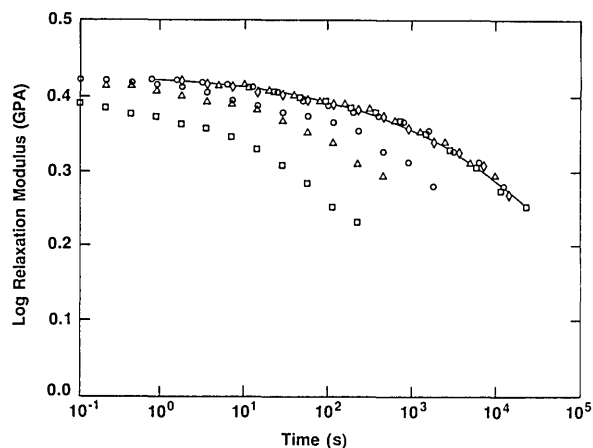


Fig. 2. Relaxation modulus vs time at different aging times for an epoxy glass quenched from above the glass transition temperature to 25 °C below it. Aging times after the quench are (□) 28 min; (Δ) 125 min; (○) 503 min; (◇) 4026 min. Solid line depicts curve obtained from time-aging time-superposition. (After Ref. [4])

Although the linear response of polymeric glasses to physical aging is readily understood within the context of time-aging time superposition principles, the same cannot be said of the nonlinear response that is relevant to material behavior in fatigue and fracture (large deformations at crack tips), residual stresses in composites, and yield of engineering resins. The current controversy has strong implications for the development of nonlinear constitutive equations for polymeric materials and the physical basis for the mathematical functions upon which these are based.

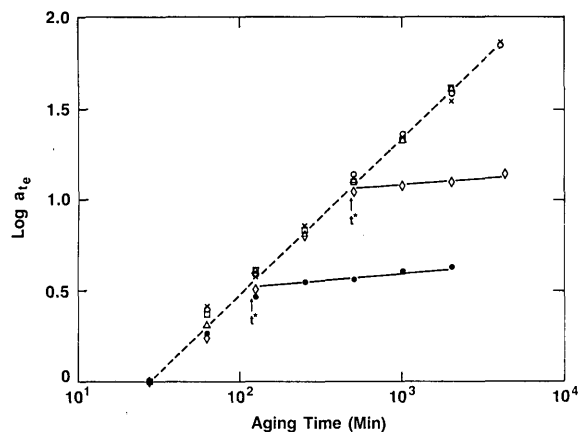


Fig. 3. Double logarithmic representation of aging time shift factor (a_{te}) vs aging time (t_e) for an epoxy glass quenched from above T_g to different temperatures below T_g . T: (●) 66 °C; (◇) 62 °C; (△) 57 °C; (○) 42 °C. Note that near to $T_g = 72$ °C the aging virtually ceases at t^* . (After Ref. [4])

According to L. C. E. Struik [3], large stresses and deformations “erase” the prior aging or “rejuvenate” the glass. Struik argued that the large mechanical stimuli cause the thermodynamic state of the glass to be changed to one that looks more freshly quenched. The evidence for this was that the slope of the logarithmic plots of a_{te} vs t_e (see Fig. 3) was reduced when the aging was probed using large stresses.

McKenna described two types of experiment performed at NIST that contradict Struik’s hypothesis. First, by working close to the glass transition, the kinetics of aging could be characterized not only by the value of $\mu = d \log a_{te} / d \log t_e$, as had Struik, but also by the value of t^* , the time required for the viscoelastic properties to cease evolving. As shown in Fig. 4, t^* is independent of the applied stress [5], whereas the Struik hypothesis [3] would have demanded that t^* increase as stress increases.

In the second set of experiments a torsional dilatometer was used to simultaneously measure the volumetric and mechanical response subsequent to a quench from above to below T_g . Again contradictory to Struik [3], the application of the mechanical deformation did not affect the time evolution of the volume of the glass towards equilibrium. Rather, the volume recovery which causes aging affects the nonlinear response (large stress) of the glass less than it does the linear response (small stress).

The implications for the above evidences are that the glassy structure has a large effect on the mechanical response, in particular, in the small

deformation regime. The effects of glassy structure on the non-linear response are less important. However, large mechanical stimuli do not alter the underlying structure of the glass. This is an important conclusion because it simplifies greatly the description of the viscoelastic response of glasses and the constitutive equations needed to model the properties of materials.

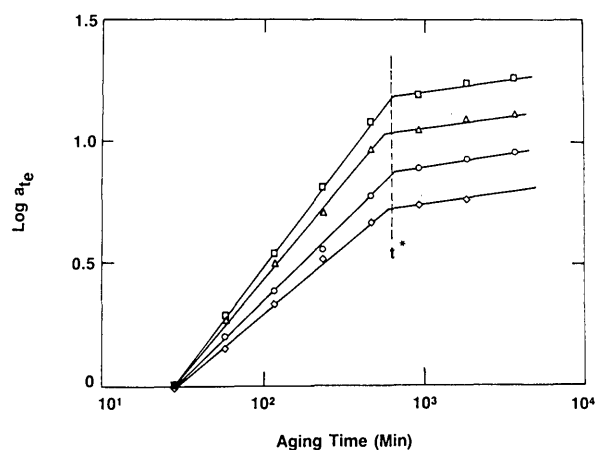


Fig. 4. Double logarithmic representation of aging time shift factor (a_{te}) vs aging time (t_e) for an epoxy glass quenched to 5 °C below its glass transition and probed by different magnitude stresses. (□) 1 MPa; (△) 5 MPa; (○) 10 MPa; (◇) 15 MPa. Note that t^* does not vary with the magnitude of the applied stress, although the slopes of the data prior to t^* do. (After Ref. [5])

Dr. D. VanderHart (NIST) discussed the use of nuclear magnetic resonance (NMR) spectroscopy to characterize structural features and the kinetics of their formation in glassy polymer blends. NMR offers advantages over small angle x-ray scattering, which is ineffective if the electron densities of the phases are similar. It can also provide chemical information about the individual phases. Spin diffusion NMR was used to obtain structural information, e.g., phase size and stoichiometry. In a study of the high temperature behavior of poly(etherimide)–polybenzimidazole (PEI/PBI) blends, VanderHart showed the importance of the kinetics of the glass transition phenomenon on the long term phase stability of these blends. In Fig. 5 is plotted the spin diffusion results for different thermal treatments as ΔM_s (the difference in the magnetization from the equilibrium magnetization) vs time for the PEI phase aliphatic protons. The time for ΔM_s to return to zero provides an estimate of the domain size. The

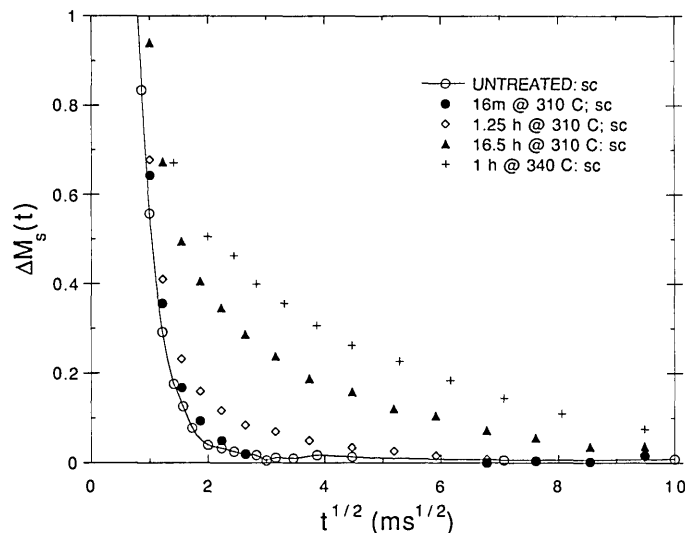


Fig. 5. NMR spin diffusion results for a PEI/PBI blend that was initially homogeneous (untreated) showing effects of aging time and temperature on phase separation. (See text for discussion). (D. L. VanderHart, NIST.)

untreated, homogeneous system shows a very rapid decay to zero as the spins equilibrate rapidly due to the intimate mixing of the PEI and PBI chains. As the aging time gets longer or the temperature higher, the decay time gets longer because spin equilibration occurs due to diffusion from the PEI phase to the PBI phase, consistent with the phase separation of the system. This occurs even though these experiments were performed well below T_g for the blend of 347 °C. Such results have serious implications for the long term performance of materials because the fundamentally kinetic nature of the glass transition implies that short term results are not readily extrapolated to long times. Thus, blends can apparently phase separate at long times well below T_g .

Clearly, much fundamental information is known about the time-dependent properties of polymers. Incorporating this knowledge into adequate descriptive models by the engineering design community has not kept pace. Therefore, predictive models for the long-term in-service performance of polymers and polymer-based composites that are needed by materials suppliers and end-users are lacking. The science base also needs to be advanced. Chemical and physical mechanistic changes which are associated with a loss of performance and failure, such as plasticization, recrystallization, degradation of molecular weight, and stress cracking, affect the bulk state. These com-

plex relationships must be defined, as failure is not obviously related to singular changes in the bulk state. The models must deal with the additional complexities of heterogeneous structures that are process dependent; the synergistic effects of aging, load, temperature, and solvents; and the added dimension of time scales.

3. Approaches to Addressing Performance Problems

While the scientific understanding of some aspects of aging, dimensional stability, and durability of polymers and polymer-based composites is well in hand, there are other areas in which such is not the case. The range of approaches to these issues represented by the workshop speakers demonstrates this. In some instances, the complexity of the issues (in particular, synergism of effects of nonlinearity of the phenomena) makes even parametric approaches appear virtually incomprehensible. In other instances, the application of fundamental understanding to specific problems can help solve them, post-facto. Overall, the trend that becomes apparent is that not only is there a need for more fundamental science, but there is a need for better application of the fundamental science early in the design process to avoid later stage problems in the manufacturing and service stages of material lifetimes.

3.1 Identification of General Needs

Some key technical issues in bringing new polymers and polymer-based composites into market applications were examined by representatives from a materials end-user, a materials supplier and a government agency. Mr. D. Grande from Boeing Company discussed the implications of aging and durability for meeting the materials requirements for composite structural applications in the high speed civil transport (HSCT). Mr. Grande identified the key technical barriers to the commercialization of this second generation supersonic transport as the understanding of aging effects in polymer-based composites and the need for low cost design and manufacture of composite structures. The demanding service environment of the aircraft requires durability for 12,000 supersonic hours under cyclic loads and temperatures up to 175 °C. Ideally, under these conditions, material properties will not change. However, noting the time-dependent nature of polymer properties, particularly in aggressive mechanical, thermal and chemical environments, the prediction of lifetime performance becomes mandatory. The aging issue is shown schematically in Fig. 6. For materials development to be successful, the seven year lead required for real-time testing of components must give way to successful accelerated testing methodologies and predictive models. Thus, for an HSCT to be given a “go-ahead” in the year 2000, real time testing of current (1993) materials must already be

underway. Accelerated testing would allow the introduction of improved materials as late as 1997. As current materials are already known to be inadequate to meet the demanding performance requirements of the HSCT, the lack of models for long-term performance of polymer-based composites will delay the commercialization of the aircraft. Data in the absence of fundamental knowledge leads to a trial and error development cycle that is prohibitively costly. The heterogeneous nature of composite systems and synergies of the multivariate environmental exposures further complicate the development of coherent test methodologies and predictive models for composite performance. Finally, a fundamental understanding of the manufacturing processes has not been established.

The problems which these circumstances present to a materials supplier were highlighted by Dr. C. Carlson (DuPont). The lack of understanding of the aging process and its effects on materials properties result in serious economic ramifications. The development of high technology polymers must be science-based and include the analytical tools and methods, and modeling and simulations capabilities, to avoid, as Mr. Grande suggested, the trial and error materials development which otherwise results. A knowledge of the applications and global market needs also contribute to successful, timely development of materials. However, the development cycle time must be minimized, as it is difficult to attract and sustain resources throughout a long

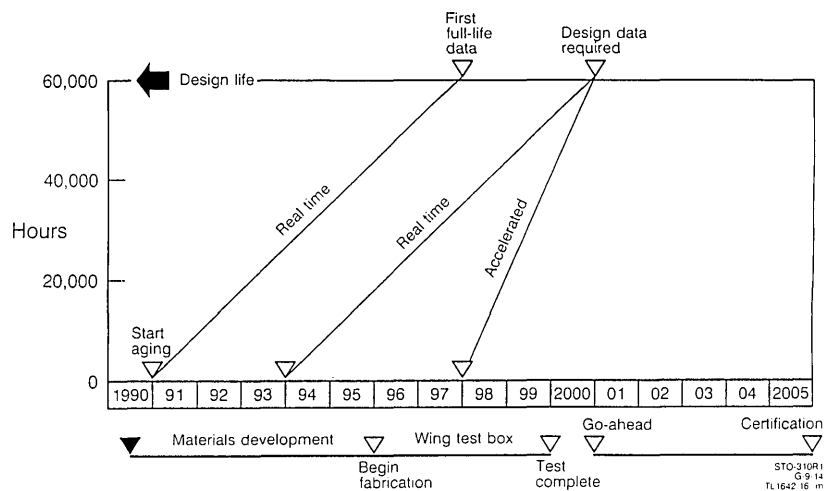


Fig. 6. Representation of the schedules for development of HSCT and how real-time materials testing and accelerated testing methodologies (currently non-existent) affect HSCT go-ahead for manufacturing commitment. (D. Grande, Boeing Company.)

development-to-commercialization cycle. For example, DuPont's Avimid K-3 polyimide series, first developed in 1982, has not been utilized in production; opportunities for large-scale commercialization will be available no sooner than 1997—at least 15 years after the initial development. Currently, product validation requires real-time testing. Accelerated testing methodologies and predictive models for materials performance need to be developed for pure materials, composites, and structures.

While the modeling needs and lack of adequate accelerated testing methodologies in advanced materials are obvious in the above, the same problems also occur in lower performance polymers and their composites in other industries. The high technology needs in automotive applications were outlined by Dr. J. Eberhardt of the U.S. Department of Energy. He noted that many materials properties change with time due to the mechanical, environmental, and thermal service environment, which is delineated in Table 1 for various automotive applications. Many modes of damage are experienced: impact, fatigue, temperature-induced creep, delamination, chemical attack, and importantly, synergism among the modes. Coupon tests provide data on singular effects, but synergistic effects are not duplicated with coupons. Adhesive durability is also an issue. Recognizing that the average age of the American automobile has increased almost 40% since 1970, Dr. Eberhardt expressed that the major needs for understanding lifetime performance issues in these applications are realistic accelerated and application-specific test methods. His concerns and interests were reiterated by the industrial representatives to the workshop.

3.2 Semi-Empirical Approaches

The important need for test methodologies and predictive models was highlighted in several presentations in which semi-empirical approaches were described which addressed immediate problems in design, application and manufacturing. Currently, prediction of long-term performance of materials is frequently done by straight-line extrapolation of short-term data, gathered from tests which simulate, as closely as possible, the actual in-service environment. For example, Dr. D. Houston from Ford Motor Company indicated that test coupons of materials for automotive applications are currently tested by mounting them on undersides of trucks in various cities in the United States with widely different climates, such as Phoenix and Detroit, and driving them for various times. After such in-service exposure, the physical/mechanical properties are determined and incorporated into the design criteria.

Without insight into the physical and chemical processes that are occurring, some of which are nonlinear, semi-empirical approaches can lead to erroneous predictions of performance. For instance, Mr. M. Greenwood (Owens-Corning Fiberglass) discussed the need and approaches of the civil engineering community for accelerated tests and failure prediction. In Fig. 7, an apparent change in mechanism(s) influences the stress at rupture for a composite rod exposed to an aggressive environment during testing. The degradation rate increases dramatically at times longer than 100 h. Thus, long term performance could not be predicted by a simple (straight-line) extrapolation of the short term data. For improved prediction of

Table 1. Applications and operating environments for polymers and composites in automotive applications (J. Eberhardt, DOE)

Operating environment	Mechanical	Environmental	Thermal
Materials application			
Interior materials	Vibration	UV and visible radiation	Solar heat load
Exterior materials	Impact loads Vibration Structural weight	UV radiation Ozone Chemicals	Outside temp. Direct sun
Underhood and under chassis	Cyclic loads Impact loads Vibration	Chemicals Ozone	Hot engine Solar heat load

durability, other considerations, such as sample preconditioning prior to testing, should be included in the methodology.

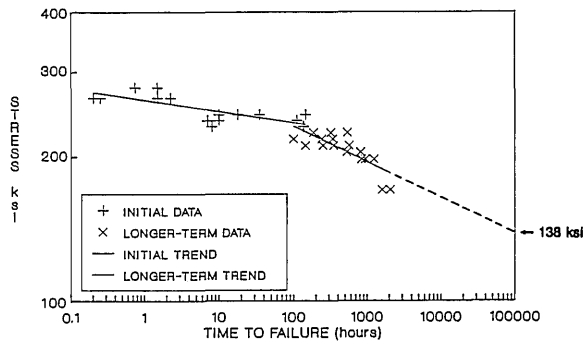


Fig. 7. Stress at rupture vs time to failure for a composite rod showing how short time data (<100 h) could not be extrapolated to predict long term performance. (M. Greenwood, Owens-Corning.)

The discussion by Drs. N. Kakarala (General Motors), Houston and Greenwood indicated that tests are frequently performed in more severe environments than the average service environment in order to simulate long-term exposure in short times. Without insight into degradative mechanisms, the development of such tests is severely flawed. Furthermore, statistical uncertainty in the measurements leads to overly conservative designs. Some desirable criteria for developing test methodologies were delineated: to reflect the service conditions; for samples to be representative of the product with regards to the materials and manufacturing “quality”; and test and service failure modes should be the same.

Different aspects of the complexity of predicting the performance of polymeric materials were illustrated in the work on electronic packaging materials discussed by Dr. C. Lee of the MCC Packaging and Interconnect Program. He tabulated a variety of property data as a function of processing (cure) conditions. Property measurements included residual stress, the glass transition, and the coefficient of thermal expansion (CTE). These were affected by the curing temperature and rate, and the annealing temperature. The limitations of such a semi-empirical approach can be seen from the following example given by Dr. Lee. In one instance, the CTE of packaging material was found to have a minimum when aged near T_g , while another system was found to either have an increase or a decrease upon aging, depending on the exact nature of the curing process. Such results are confusing when the fundamental relationships between the properties, in this case CTE and the

process history, have not been adequately developed. In particular, complex interactions between the chemistry of curing systems and the aging process need to be considered in detail if one is to successfully predict properties that are relevant to device performance.

The specific effect of physical aging on the creep of the engineering polymers Noryl—a blend of poly(phenylene oxide) and high impact polystyrene—and polycarbonate was studied by Dr. G. Tryson of General Electric. Given that creep is moderated by physical aging, Tryson noted that a product may be overdesigned if physical aging is not considered in the design process. In attempting to develop a meaningful correlation between aging and creep performance, he noted some variables that were difficult to evaluate: fillers, additives, fibers, and other modifiers; non-constant loads and temperatures; residual stress of the component; and the effects of aging on the creep rupture performance.

3.3 Science-Based Approaches to Problem Solving

As discussed in Sec. 2, there is a considerable, albeit incomplete, science base to our understanding of the problems of aging and dimensional stability of polymeric materials. As a result, several of the workshop speakers were able to present approaches used in their companies that took into account the science of aging to improve manufacturing or to resolve specific problems once they had arisen.

Dr. G. Pearson of the Eastman Kodak Company gave an extensive overview of the importance of aging in both cellulose triacetate and poly(ethylene terephthalate) in photographic films.

In addition to showing that aging affects a variety of engineering properties, such as the ANSI curl number (a measure of the viscoelastic set of a film) as shown in Fig. 8, Pearson also described how learning to control aging became important for the manufacturing of films as Kodak moved towards tighter inventory control and just-in-time inventory/delivery procedures. The shortening of the holding time between manufacture and actual delivery of films makes control of the film properties and dimensions more important. Where previously films sat in warehouses long enough to age or stabilize, the rapid turnover could lead to “unaged” or “partially aged” films being delivered. The difference in aging could result in a variable product. Having developed a fundamental understanding of the relationships between aging and the properties of interest, the manufacturing parameters could be modified to assure that high quality products were consistently delivered.

Some of the problems involved in epoxy-novolac encapsulants for integrated circuit devices were described by Dr. H. Bair of AT&T Bell Laborato-

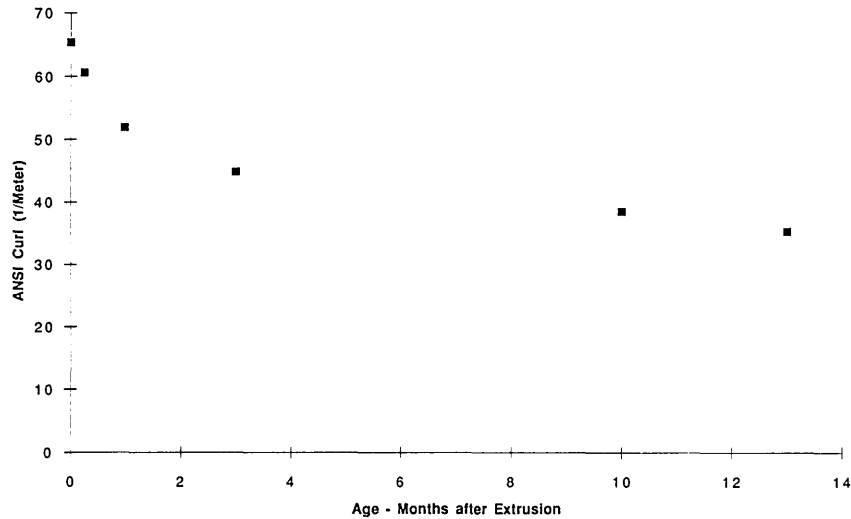


Fig. 8. ANSI curl number vs aging time for extruded poly(ethylene terephthalate). (G. Pearson, Eastman Kodak Company.)

ries. He discussed the importance of keeping moisture away from the resins during cure. High moisture content resulted in large decreases in T_g and the extent of cure. In addition, upon exposure to elevated temperatures, greater permanent changes in encapsulant dimensions (expansion) occurred when the encapsulant was cured in the presence of moisture than when dry. By processing in the absence of moisture, the final properties of the system could be controlled and the quality of the products guaranteed. Improvements in dimen-

sional and property stability could be obtained by using encapsulants with higher glass transitions or by using resins where cure chemistry was less moisture-sensitive.

Dr. W. Prest of the Xerox Corporation discussed the effects of physical aging on the optical, electrical, and mechanical properties of imaging components. The densification that accompanies aging increases the polarizability per unit volume, producing corresponding changes in the index of refraction of optical components. Fig. 9 illustrates

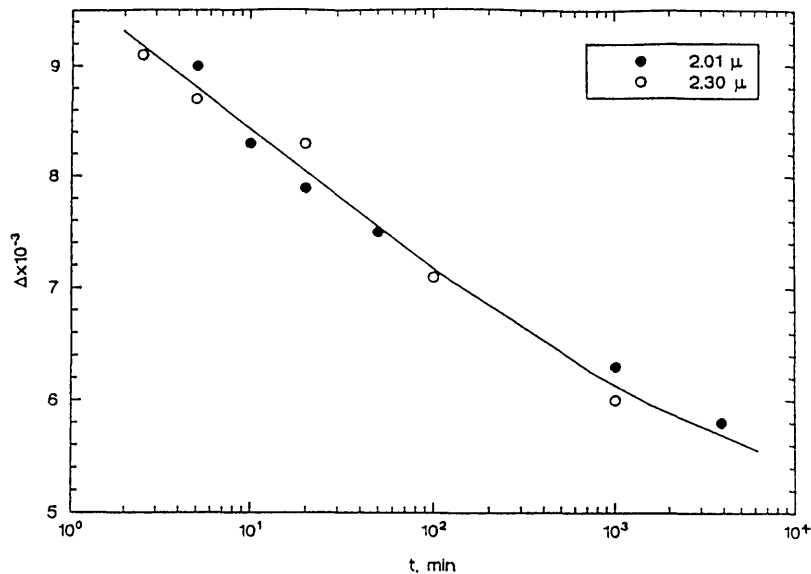


Fig. 9. Birefringence of an oriented polycarbonate material as a function of time after processing at 411 K. (W. Prest, Xerox Corporation.)

the change in the birefringence as a function of aging time. However, the anisotropy stops changing before the index of refraction. The densification also increases charge mobility, as the inter-site hopping distance between dispersed electrically active species is decreased. The accompanying aging induced restriction in molecular mobility (aging rate) gives rise to changes in the yield and fracture behavior of the polymeric glasses, affecting durability and the modes of failure; brittle fracture is associated with long aging time, for instance.

3.4 Science-Based Predictive Approaches

Dr. R. Chambers from Sandia National Laboratories in Albuquerque presented results from finite element analyses that he has performed on model glass/metal seals. The goal here is to design systems in which the glass, after processing at a high temperature to form the seal, is in a state of compression at low temperatures. Residual tensile stresses can lead to failure of the seal. Chambers applied the Narayanaswamy [7] nonlinear model of volume recovery of glass-forming materials in his finite element analysis and compared it to simple linear models of thermo-viscoelasticity. Chambers showed that the nonlinear modeling indicates a tensile stress in the glass during cooling while the linear analysis predicted compressive stresses. (See Fig. 10.) This correlated well with the observation of cracking due to tensile stresses during the processing of real glass to metal seals that had been designed on the basis of a linear thermoelastic model.

The importance of the Chambers modeling is that it takes the current knowledge of physical aging of glass-forming materials (Narayanaswamy's volume recovery model) and applies it to a composite system (glass/metal seal) in the framework of the design engineer (finite element analysis). Although the model itself was simple, it points the direction to be taken for more complicated fiber-reinforced composites. Chambers also noted the need for materials property data for volume recovery of materials used in composites, as well as better constitutive models to describe the nonlinear mechanical response of glass-forming materials. Further experimental work is needed to validate finite element models of more complex systems.

The science base of durability issues was addressed by Dr. C. Bosnyak (of the Dow Chemical Company). Reiterating the needs identified by the

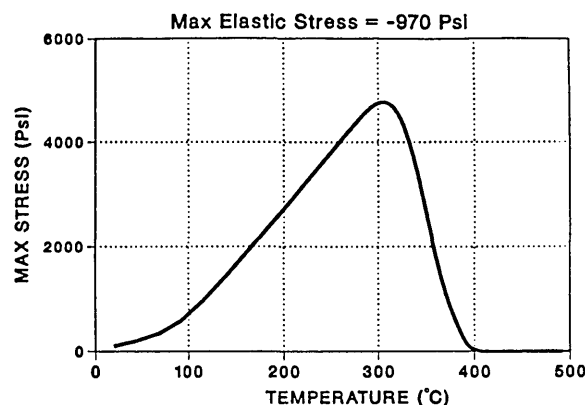


Fig. 10. Stress in the glass in a glass/metal seal upon cooling as calculated using a finite element analysis incorporating volume recovery of the glass. Note that the stresses go through a tensile maximum at approximately 300 °C. Linear thermo-elasticity predicted a compressive stress throughout the thermal cycle. (R. Chambers, Sandia National Laboratory.)

preceding speakers, Bosnyak noted that all models of durability require as their basis the fundamental principles and mechanisms of the relevant physical and chemical phenomena, adding that the prediction of durability has not been developed as a technology. For models to be useful, they must be *predictive*, rather than solely descriptive; however, at least one participant remarked that even adequate descriptive models are currently unavailable. Bosnyak highlighted—in agreement with the participants—that models that are derived from databasing and curve-fitting have limited utility to guide the work of materials suppliers, designers, and users. Suppliers have the ability to challenge the utility of models by applying their extensive materials databases to test them; users may also bound the problem by defining the failure criteria, based on the material's application.

Bosnyak identified the scientific criteria necessary for developing lifetime prediction models, starting with an intimate knowledge of the application and materials. The variables that need to be understood are outlined in Table 2. Emphasis was placed on understanding and quantifying the mechanisms of failure, and relating these to the structure of the material. The next step links the results of laboratory tests to performance, yielding the ability to predict in-service performance. This could be accomplished by developing scaling concepts of time and geometry, from which accelerated test methodologies could be used to simulate long-term performance and failure.

Table 2. Key variables in the engineering design for plastics (C. Bosnyak, Dow Chemical Company)

Material	Geometry	Loading	Environment
Molecular wt (MW)	Thickness	Stress level	Temperature
MW distribution	Shape (stress concentration)	Stress rate	Weathering
Morphology		Rate	Chemicals

In his research, Bosnyak examined the role of failure mechanisms in the development of accelerated test methodologies for polycarbonate. He developed a diagram of the stress vs crack initiation time for samples of varying thickness (Fig. 11). As noted by previous speakers, simple data extrapolation would lead to erroneous conclusions, in this case, the crack initiation time. However, by normalizing the stress and “mapping” regions in which different failure mechanisms were exhibited, a useful fatigue crack initiation mechanism map was developed (Fig. 12). Thus, for known geometries, loads, and mechanisms of failure, the crack initiation time is predictable. However, although the mechanism maps represent a significant advance toward understanding durability in polymers, it is only the first step. Further work is ongoing to select appropriate normalization of the axes. Importantly, it should be clearly recognized that durability or toughness cannot be adequately described by a single number.

4. Summary and Conclusions

An industry/NIST workshop brought together industrial and government scientists, engineers, and technical managers to assess the state and application of knowledge in addressing a range of problems associated with aging, dimensional stability, and durability of high-technology polymers. The workshop participants, representing 16 companies, as well as NIST and the Department of Energy, compared experiences and perspectives on a class of problems that are ubiquitous in polymer science and technology and impact a range of products and processes in many industries, from photographic and imaging applications to electronic packaging and composites for automotive and supersonic commercial aviation applications. A process, termed physical aging, in which the dimensions and performance properties of polymers change with time in service, was considered a critical scientific problem that should be addressed in collaborative work between industry and NIST.

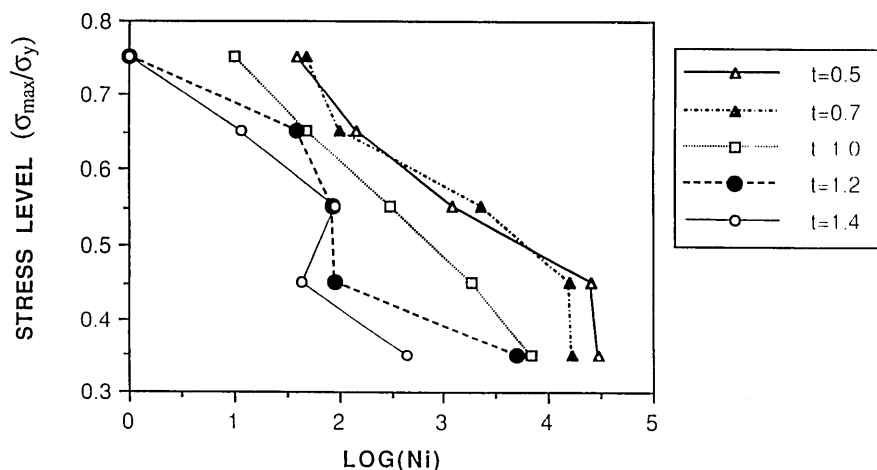


Fig. 11. Stress-crack initiation-cycles diagram for polycarbonate showing how different failure mechanisms intervene depending on the geometry of the specimen. Thickness of specimens is indicated beside diagram. (The crack initiation time (N_i) was defined as the time when the crack length was 0.2 mm on the specimen surface from the V-notch tip under optical microscope observation.) (C. Bosnyak, Dow Chemical Company.)

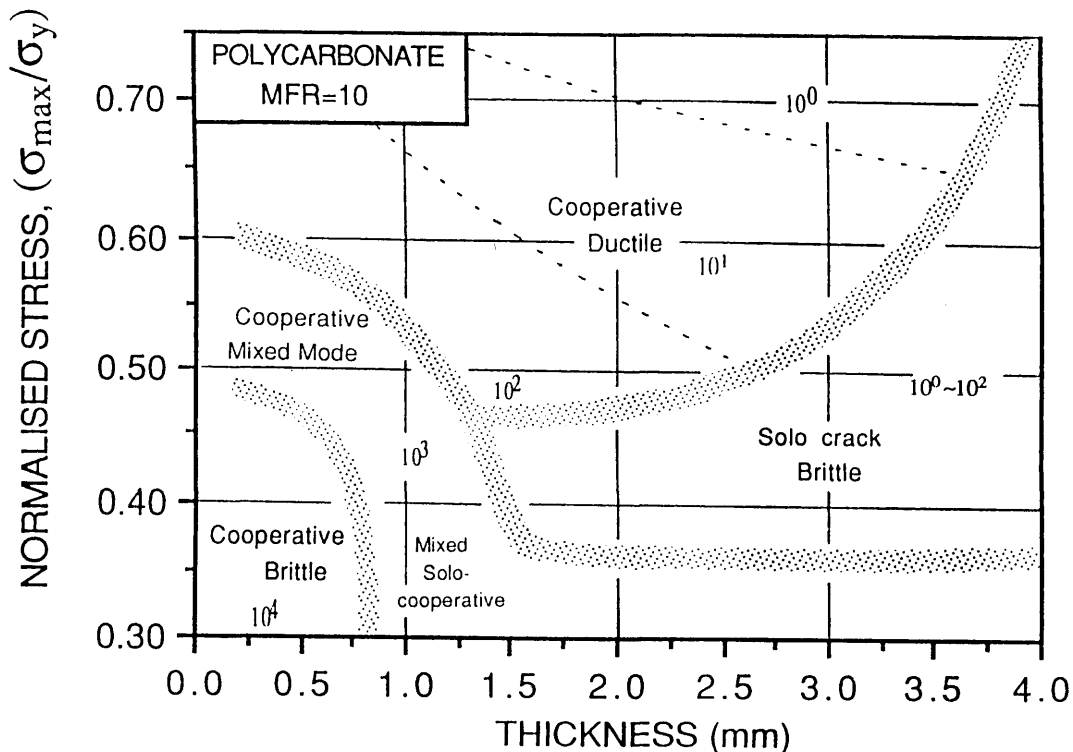


Fig. 12. Fatigue crack initiation mechanism map for polycarbonate showing how failure mode depends on both level of applied stress and the specimen thickness. (C. Bosnyak, Dow Chemical Company.)

The workshop participants noted that although much fundamental information is known about the time-dependent properties of polymers, this knowledge has not, for the most part, been incorporated into adequate descriptive models by the engineering design community. Furthermore, models must be predictive, rather than merely descriptive, in order to be useful to materials suppliers, designers, and users. The development of predictive models is even less advanced, as evidenced by a common approach to the prediction of long-term in-service performance described by several workshop speakers: the straight-line extrapolation of short-term data gathered from tests which simulate, as closely as possible, or intensify the actual in-service environment. This approach frequently fails due to a lack of fundamental physical and chemical mechanistic information, particularly concerning non-linear behavior. The utility of this approach is further limited by the complexities of structural heterogeneities that are process-dependent; the synergistic effects of aging, load, temperature,

and solvents; and the added dimension of time scales. Thus, the basic science associated with performance issues must be advanced; the workshop participants suggested that NIST could play a valuable role by addressing these issues to support the development of predictive models and accelerated test methodologies.

5. References

- [1] A. J. Kovacs, *Fortsch. Hochpolym. Forsch.* **3**, 394 (1963).
- [2] G. B. McKenna, in *Comprehensive Polymer Science*, Vol. 2, Polymer Properties, C. Booth and C. Prize, eds., Pergamon, Oxford, (1989).
- [3] L. C. E. Struik, *Physical Aging in Amorphous Polymers and Other Materials*, Elsevier, Amsterdam (1978).
- [4] A. Lee and G. B. McKenna, *Polymer* **29**, 1812 (1988).
- [5] A. Lee and G. B. McKenna, *Polymer* **31**, 423 (1990).
- [6] D. L. VanderHart, G. C. Campbell, and R. M. Briber, *Macromolecules* **25**, 4734 (1992).
- [7] O. S. Narayanaswamy, *J. Am. Ceram. Soc.* **54**, 4191 (1974).
- [8] R. S. Chambers, F. P. Gerstle, Jr., and S. L. Monroe, *J. Am. Ceram. Soc.* **72**, 929 (1989).

News Briefs

General Developments

Inquiries about News Briefs, where no contact person is identified, should be referred to the Managing Editor, Journal of Research, National Institute of Standards and Technology, Administration Building, A635, Gaithersburg, MD 20899; telephone: 301/975-3572.

ELECTRICAL POTENTIAL: ISRAEL, UNITED STATES AGREE ON STANDARD

The unit of electrical potential, the volt, is the same in Israel and the United States, according to an agreement recently signed by representatives of the two countries' national standards laboratories. The agreement formally recognizes that the U.S. volt, as measured by NIST, and the Israeli volt, as measured by the Israeli National Physical Laboratory, are equivalent to at least one part in 10 million. Both countries measure volts in accord with the definitions of the International System of Units (SI). The agreement between NIST and INPL is the latest in a series of NIST collaborations with international standards organizations in order to facilitate trade.

CRADA PARTNERS FOCUS ON IMPROVING LASER LENSES

A significant obstacle blocking the development of new, more powerful lasers may soon be removed, thanks to a collaborative effort between NIST and a private company. In recent years, physicists have been trying to generate more focused laser beams through techniques such as frequency doubling, frequency summing, and optical parametric amplification. These techniques would be more efficient if researchers could change the geometry of the

beams using cylindrical lenses for improved focusing. However, there currently is no way to measure lens quality and determine whether a beam is focused properly. The private company has produced an instrument which can perform such measurements by characterizing a beam's integrated errors. Representatives from the private company will work with a NIST physicist at the Joint Institute for Laboratory Astrophysics, to explore the use of this machine for evaluating cylindrical and other non-spherical lenses for applications in non-linear optics. For more information, contact Linda Wilbourn at (916) 888-5017 or John Hall at (303) 492-7843. JILA is jointly operated by NIST and the University of Colorado at Boulder.

NIST OBSERVES ONE ELECTRON IN 10 BILLION

For more than 2 decades, advances in superconductivity have been made by studying the behavior of bound pairs of electrons. But if there is an odd number of electrons, what does the unpaired, "odd-man out" do? NIST researchers have taken the first step in answering this question. NIST scientists and a guest worker from the Center for Nuclear Studies, Saclay, France, are attempting to count individual electrons in order to improve electrical standards for capacitance or current. An early success for the project is the detection of a single excited electron above a condensed ground state of 10 billion superconducting electrons. To make their discovery, the researchers used an electrometer composed of two ultra-small tunnel junctions on a superconducting "island" flanked by two normal-state outer electrodes. The dimensions of the "island" were used to determine the 10 billion figure for the number of superconducting electrons involved.

RESEARCH PARTNERS SEEK BETTER INFRARED RADIOMETRY

NIST and a private research company are working together to improve infrared radiation measurements for the aerospace and defense industries. These measurements ensure accuracy in sensors from simple light meters to complex missile detectors. Under terms of a recently signed cooperative research and development agreement, the private company will provide data enabling NIST scientists to improve the institute's Low Background Infrared Calibration Facility. The facility calibrates blackbodies, objects which absorb all incident radiation and reflect none. At a fixed temperature, blackbodies emit radiant energy within a specific spectrum. Aerospace and defense manufacturers can calibrate infrared detectors with these constant radiant emissions, so the LBIR Facility serves as a site to check the accuracy of their measurements. Another part of the agreement involves a absolute cryogenic radiometer manufactured by a private company, present in the LBIR Facility. The device measures radiant energy in a chamber maintained at a temperature of 20 K. Personnel from the private company will assist NIST scientists in modeling how changes in the instrument may improve its future performance.

CRADA PARTNERS TO EVALUATE ADVANCED INSULATIONS

Innovative insulation systems are being developed to replace foam insulations manufactured with chlorofluorocarbons and to meet more stringent energy-use standards. These insulation systems include vacuum powder-filled panels, low-conductivity gas-filled panels, and vacuum insulation panels. However, current test methods cannot properly measure their thermal resistance or R-value. Under a new cooperative research and development agreement, NIST and a private U.S. company are collaborating on the creation of the necessary thermal resistance tests. The company will supply NIST researchers with evacuated insulation panels of varying sizes and materials. The project is expected to take about 3 years. For more information, contact Hunter Fanney, B322 Building Research Building, NIST, Gaithersburg, MD 20899-0001, (301) 975-5864.

STANDARD ADDRESSES CNC PERFORMANCE EVALUATIONS

Consistent and reliable performance by computer numerically controlled machining centers is critical in manufacturing products for the defense, aero-

space, automotive and other industries. With assistance from NIST, a new standard for assessing the effectiveness of CNC machining centers has been developed by the American Society of Mechanical Engineers. The standard, "Methods for Performance Evaluation of Computer Numerically Controlled Machining Centers" (ASME B5.54-1992), establishes requirements and methods for specifying and testing machining centers. It also attempts to facilitate performance comparisons between machines by unifying terminology, general machine classification and the treatment of environmental effects. For technical information on the standard, contact Denver Lovett, Chairman, ASME Standards Committee B5, 136 Shops Building, NIST, Gaithersburg, MD 20899-0001, (301) 975-3503. A printed copy of ASME B5.54-1992 may be obtained by writing ASME, 22 Law Drive, Fairfield, NJ 07007, or by calling (800) 843-2763. Cost is \$44 prepaid; order by N14492.

INTEGRATED OPTIC LASER EMITTING AT 905, 1057, AND 1356 nm

NIST scientists, working with private industry researchers, have developed a new integrated optic laser. NIST and the private industry have signed a cooperative research and development agreement to develop new integrated optic lasers and amplifiers for optical telecommunication networks. Another NIST scientist is providing materials characterization. The joint research has already produced the first neodymium integrated optic laser that produces light at 905 nm. The laser emits over 200 mW of light at 1057 nm, which is the highest power achieved in such a device. One of the scientists reported these results in a post-deadline paper at the Optical Society of America Advanced Solid State Lasers Topical Meeting held early in February. The private company has filed a patent application for the glass used in the laser. This application includes a disclosure of the joint NIST/private company laser and protects the foreign and domestic patent rights of both NIST and the company to this device. A joint patent application for the laser is in progress.

TRAPPED NEUTRAL ATOM METHODOLOGY APPLIED TO HIGH-ACCURACY WAVELENGTH REFERENCE FOR OPTICAL COMMUNICATIONS

NIST scientists are pursuing the application of techniques for cooling and trapping neutral atoms to the development of high-accuracy wavelength standards. NIST played a major role in the develop-

ment of the cooling and trapping methodology, and this wavelength standard work is one of the first applications for trapped neutral atoms. Accurate wavelength standards are important for many of the proposed optical communication schemes involving NIST multiplexing. A goal of the NIST research on optical communication wavelength standards is to produce a highly stable and reproducible primary wavelength reference in the 1.5 μm fiber laser stabilized to narrow resonances in laser-cooled rubidium. In the experiments, neutral rubidium atoms were laser-cooled and confined in a vapor-cell optical trap using 780 nm diode laser light and a weak magnetic field gradient. This arrangement produced a dense sample of cold atoms and reduced the Doppler broadening of the optical transitions to less than the natural linewidth. Spectroscopy of the rubidium $5P_{3/2} \rightarrow 4D_{5/2}$ transition near 1.529 μm was performed using a single-longitudinal-mode erbium-doped fiber laser. Transition linewidths of 10 MHz were observed, and the fiber laser was actively stabilized to the rubidium line.

INDUSTRY, NIST COLLABORATE TO STUDY OVERLAY MEASUREMENTS

Private industry and NIST are collaborating to study overlay measurements. The private company is making space available for a NIST test structure in a “drop-in” test chip to be fabricated along with product on wafers at its Manassas, VA, facility. NIST is supplying the software to produce the test structure and conducting measurements on completed test chips and analysis of the resulting data. Determining accurate registration of multiple lithography steps in semiconductor fabrication is a major problem as minimum device sizes continue to shrink: the Semiconductor Industry Association views overlay as “expected to continue to be the most difficult technical challenge in lithography” through the year 2007. The Modified Offset Alignment Test Structure (MOATS) used in the work was developed by NIST to provide extremely precise measurement (~ 5 nm) of relative locations of parallel features on different mask layers of an integrated circuit wafer.

NIST recently received for evaluation several 100 mm CMOS/bulk wafers from the private company containing the chip. These wafers are unique in that they were fabricated using a “mix-and-match” x-ray lithography technique. Two dimensionally critical layers, diffusion and polysilicon, were patterned using the state-of-the-art x-ray synchrotron source at the private company. All

other steps were performed using traditional photolithography techniques in Manassas. Also incorporated in the drop-in test chip (refers to sites on a wafer at which the product die can be replaced by a test chip) are several other optical and electrical overlay test structures which will allow the group to perform side-by-side comparisons of MOATS with competing techniques. NIST has applied for patent protection for the MOATS (Case Reference 91-0020), which takes the form of a so-called “sliding-wire” potentiometric structure.

NIST PROVIDES LEADERSHIP FOR DARPA INFRARED DETECTOR MATERIALS PROGRAM

A NIST scientist has been asked by the Defense Advanced Research Projects Agency (DARPA) to lead and coordinate the DARPA technical effort in optical characterization of infrared materials. NIST was chosen to lead this effort because of its demonstrated capability to perform high-accuracy semiconductor measurements, to produce Standard Reference Materials, and to function in an unbiased technical role. As one of the first steps, some 20 industry engineers and scientists participated in a workshop held early this year at NIST on techniques being developed for the noninvasive analysis of infrared materials. The participants represented the major contractors in the program. The workshop helped to identify specific metrology needs and requirements; provided a working review of the optical techniques in use such as photorefectance, photoluminescence, and infrared absorption; and identified needs for measurement criteria, calibration procedures, and analysis techniques. The participants placed considerable emphasis on needs for improvements in the absolute accuracy of measurements. In related efforts, NIST is working with DARPA to advance the state of the art in nondestructive analysis and to develop new characterization techniques to address future infrared material needs.

YOUNG'S INTERFERENCE EXPERIMENT USING TWO ATOMS

NIST scientists in collaboration with the Universität Freiburg, have reported the first observation of interference effects in the light scattered from two trapped atoms. The visibility of the fringes can be explained in the framework of Bragg scattering by a harmonic crystal and simple “which path” considerations of the scattered photons. If the light scat-

tered by the atoms is detected in a polarization sensitive way, then it is possible to demonstrate selectively the particle nature or the wave nature of the scattered photons. This is a very vivid demonstration of principles underlying the foundations of quantum mechanics.

The experiments are performed with two trapped $^{198}\text{Hg}^+$ ions. The separation of the ions can be adjusted by changing the potential well of the trap. "Which path" a given photon takes in the experiment (that is, which atom scatters the photon) can, in principle, be determined when σ -polarized light is detected, since a photon with this polarization, when scattered, leaves one of the atoms in a different state. Therefore, when σ -polarization light is detected, no interference is seen because the experimental conditions present the opportunity to determine the photon path. On the other hand, the detection of π -polarized light involves a transition where the initial state and final state of the atom are identical. There is no way to determine which atom scattered a given photon, and in this case interference is observed.

HOLOGRAPHIC MEASUREMENTS OF ATOMIZATION AND SPRAY FORMING

Scientists at NIST recently applied advanced holographic techniques to measure key features in atomization and spray forming processes. The velocities and sizes of droplets formed from the break-up of a molten metal stream of a nickel-based superalloy, Inconel 625, interacting with high-velocity argon gas in the SIGMA system (supersonic inert gas metal atomizer) were investigated. This work was done in collaboration with a private company, which is developing special holographic systems under an SBIR grant from DOC.

Double-pulse techniques with laser pulses, each of 20 ns duration, separated by 3 μs in time allowed direct measurement of droplet velocities soon after droplet formation. This process required superimposing two holographic pictures onto a single holographic plate. Velocities in the range of 50 to 90 m/s were measured for droplet sizes in the range of 20 to 100 μm . Three-dimensional visualizations were obtained both during the initial droplet formation period and near the time of droplet impact onto a substrate.

AMRL SUPPORTS THE METRIC CONVERSION OF AASHTO MATERIALS STANDARDS

The American Association of State Highway and Transportation Officials (AASHTO) is actively pursuing the conversion of its documents to use the International System of units (SI units). This is in coordination with federal government agencies who are implementing Section 5146 of the Omnibus Trade and Competitiveness Act of 1988. The AASHTO Materials Reference Laboratory (AMRL) located at NIST, in its role of providing technical support to the AASHTO Subcommittee on Materials, has completed the task of converting to SI 416 standards for construction materials. These documents will be reviewed by the responsible technical sections of the subcommittee and processed as AASHTO standards. This AMRL support to the AASHTO standards process will speed the conversion and ensure consistency in bringing the standards into compliance with the act.

NEW SRM FOR CALIBRATING INFRARED SPECTROPHOTOMETERS

Spectrophotometers are instruments that spectrally characterize the optical properties of materials. To obtain useful information from these instruments, both the photometric and wavelength (or frequency) scales must be calibrated. Standards are currently available that allow spectrophotometer users to perform such calibrations in the ultraviolet, visible, and near-infrared spectral regions. However, standards have not been readily available for the mid-infrared (IR) spectral region (2–20 μm), in which large numbers of instruments are currently utilized.

Recently, NIST has developed a polystyrene Standard Reference Material (SRM) for calibration of the wavelength scale of spectrophotometers operating in the mid-IR. The SRM provides seven primary reference wavelengths, each with a total uncertainty of less than 0.5 cm^{-1} for the calibration of Fourier transform infrared instruments. In addition, six more secondary wavelengths, each with a total uncertainty of $\approx 1\text{ cm}^{-1}$, are provided.

NIST SPONSORS MAMMOGRAPHY WORKSHOP

NIST held a workshop recently to investigate the issues involved in providing a kilovoltage (kV) standard for diagnostic x-ray systems used in mammography. Mammographic x-ray units operate at a peak voltage of 24 to 32 kV, depending upon the thickness of the compressed breast. The relative attenuation of soft tissue is greater for low-energy x rays, therefore providing more contrast between subtle differences in breast densities. This contrast is needed for detecting calcifications and soft-tissue abnormalities. The need for a kV standard in mammography exists because a change of as little as 1 kV at these low energies affects mammographic film quality, as well as radiation exposure.

Participants in the workshop included representatives of the Center for Devices and Radiological Health of the USFDA, state regulatory agencies, manufacturers of x-ray equipment and kV measuring devices, secondary calibration dosimetry laboratories, and both U.S. and German national standards laboratories. The workshop focused on the present status of, and the impact of future developments on, kV measurements in commercial mammography systems. Kilovoltage measuring field devices were reviewed, as well as the approaches used in laboratories to ensure the quality of the field measurements. Accurate measurement of the kilovoltage is a key step toward improving the quality of diagnostic radiology for the 26 million mammograms taken annually in the United States.

THERMAL CONDUCTIVITY OF HCFC-FILLED POLYMER FOAMS

Polymeric foams expanded with chlorofluorocarbon (CFC) gas are used extensively as thermal insulators in applications ranging from refrigerators and freezers to cryogenic-fuel tanks. New insulation materials are being developed that use more environmentally acceptable hydrogenated chlorofluorocarbon (HCFC) gases. A program to determine the thermal resistance of these foams as a function of temperature, 20 to 330 K, and density, 34 to 50 kg/m³, has been completed at NIST. The effort was supported by a private company and was executed with the aid of a guest researcher. Early results indicate that the temperature dependence of the HCFC-filled foams is similar to that for CFC-filled foams, as expected. This characteristic dependence is a linear rise from nearly zero conductivity at 0 K to a local maximum

at about 220 K, then a drop to a local minimum at 273 K, followed by a linear rise at higher temperatures. The magnitude of the conductivity of the HCFC foams is approximately 5 percent higher than that for CFC foams of the same density and matrix material.

COMPUTER GRAPHICS METAFILE GENERATOR TEST SERVICE INITIATED

In January 1993, NIST expanded its Computer Graphics Metafile (CGM) Validation Test Service to include CGM generator testing. Focusing on metafile conformance testing since its inception in 1991, the service now tests either metafiles or generators for conformance to Federal Information Processing Standard (FIPS) 128, Computer Graphics Metafile (CGM), and the CALS CGM Application Profile (MIL-D-28003A).

Metafiles testing consists of analyzing binary encoded CGM files and verifying that the data stream is syntactically correct. A certificate of validation is issued for conforming metafiles. The cost of testing CGMs varies with the number of metafiles tested. Generator testing uses a NIST-developed test suite from which a set of binary encoded CGMs is generated. The CGMs are analyzed for syntactic and semantic correctness as well as preservation of graphical primitives. Conforming generators receive a certificate of validation. If errors are detected during the validation, a registered report is issued. The base price for generator validation is \$9,000.

All certificates and registered reports are listed in the Validated Products List, which NIST issues quarterly; NISTIR 5103, dated January 1993, is the current publication. Also available is a CGM information pack, which describes the test service and gives pricing information.

NIST/ASA/NSF FELLOW DEVELOPS NEW MODEL FOR CONTROLLING MEASUREMENT PROCESSES

A visiting NIST research fellow has developed a computationally intensive surveillance scheme geared toward quick detection of medium-size changes in ongoing processes. In contrast, Shewhart-type control schemes are geared toward detection of large changes, and CUSUM procedures, while optimal in terms of speed of detection, cannot handle dependent data as easily. Furthermore, the new scheme has the advantage that the baseline for the process need not be known because

nuisance parameters, such as the mean and variance, are eliminated via exploitation of invariant structures inherent in the problem. This work, which included a successful application to data from the mass calibration process at NIST, was performed under the NIST/ASA/NSF Fellowship Program, administered by the American Statistical Association.

NIST PUBLISHES IGES HYBRID MICROCIRCUIT APPLICATION PROTOCOL

NIST has published Technical Note 1295, Initial Graphics Exchange Specification—Hybrid Microcircuit Applications Protocol. This document defines how users, such as developers of design and manufacturing tools, supporting design, production, and marketing functions, are to encode hybrid product data in the Initial Graphics Exchange Specification (IGES) format for exchange among computer-aided design systems and manufacturing systems designed to run in a numerically controlled mode directly from digital data. It also presents proposed extensions to the IGES standard. The use of a neutral data format such as IGES serves as a data “hub” and greatly reduces the number of translators required to interpret data from one system to another, from a maximum of $n(n - 1)$ to a maximum of $2n$, where n is the number of systems. Publication of the document culminates a 3 year standardization effort led by NIST within the Navy MicroCIM program. Industry involvement throughout the MicroCIM program has led to the development of an exchange specification that can be efficiently mapped to a variety of computer-aided design systems in use. Three public forums were held, which resulted in the selection of IGES as the target standard for data representation and exchange. Driven by industry needs, the scope of the application protocol was defined to include information needed for hybrid documentation and manufacturing automation, including relevant military specifications and data required by systems used to design and fabricate hybrids. NIST expects this application protocol to form part of the underlying methodology needed by the electronics industry in the evolution of fully automated design and manufacturing systems for complex products. Technical Note 1295 constitutes the second IGES application protocol and the first one developed supporting electronics. It is available from the National Technical Information Service (order PB93-175404/AS).

IMPROVED METHOD DEVELOPED FOR CHARACTERIZING HgCdTe INFRARED DETECTORS

NIST scientists have developed a new method for measuring and analyzing electrical parameters of passivated layers of HgCdTe infrared detectors. Among other applications, these detectors are the “eyes” of weather satellites such as the National Atmospheric and Oceanic Administration’s Geostationary Observational Environmental Satellites (GOES) series. The method requires access to only the two terminals of each detector element and provides a unique signature. Commercial suppliers of detectors use various methods to passivate the top and bottom surfaces of a detector to produce the thin accumulation layers needed for high performance and stability. The density and mobility of electrons in these layers directly affect the performance of the detector. The method involves exposing a detector to a high magnetic field, which causes splitting of energy levels, in turn leading to detectable quantum magnetotransport phenomena, such as Shubnikov-de Haas oscillations in the magnetoresistance of the accumulation layers. Carrier densities are proportional to the frequencies of these oscillations, periodic as a function of inverse magnetic field. The mobilities are proportional to the relaxation times, which can be obtained from the field dependence of the amplitude of the oscillations. Electron effective masses can be obtained from the temperature dependence of the amplitude of the oscillations.

The scientists found excellent agreement between theoretical predictions and empirical data for a detector having anodically oxidized surfaces. However, they found poor agreement for detectors having heavily accumulated surfaces produced by differing passivation processes. The predicted effective masses were about twice the measured values, and the relaxation times, normally assumed constant below 30 K, were found to vary with temperature. Correcting for this variation brought the measured masses into agreement with the predictions. The scientists suspect that the passivation processes damaged the surfaces.

NIST DEVELOPS IMPROVED SENSOR FOR HIGH AC AND PULSED CURRENTS

A NIST scientist has conceived, implemented, and tested a new design of a sensor for high currents in the form of a machinable Rogowski coil. His design addresses a principal factor limiting accuracy in

conventional Rogowski coils, sensitivity to position of the current-carrying conductor. Rogowski coils are air-core mutual inductors having mutual inductance of $1 \mu\text{H}$ or less and are commonly used to measure very high ac and pulsed currents, generally greater than 1 kA. It is not unusual for the output of commercially available coils to vary several percent with different positions. They also suffer from relatively large temperature coefficients. Although these coils find application where accuracy requirements are not demanding, coils with much better performance are needed. The new machinable Rogowski coil has extremely low positional sensitivity, on the order of ± 0.05 percent, and a temperature coefficient of only $+9 \text{ ppm}/^\circ\text{C}$. The coil is made by laser scribing a coil-turns pattern on a silver-coated precisely machined ceramic torus. Turns symmetry is obtained by the machining process and the compensation turn required in a single-layer Rogowski coil can be precisely located. The coils' excellent symmetry and precisely located compensation turn result in its improved performance in comparison with other Rogowski coils. The coil has a nominal mutual inductance of $0.265 \mu\text{H}$ (a reactance of $100 \mu\Omega$ at a frequency of 60 Hz).

INDUSTRY FOCUSES ON TRACEABILITY NEEDS AT NIST/DOE GEAR METROLOGY WORKSHOP

A workshop was held recently to discuss the development of an improved national infrastructure for gear metrology. The workshop, which was held in Oak Ridge, TN, was attended by some 50 representatives from business and government agencies. One purpose of the workshop was to focus on the needs of the gear industry regarding the re-establishment of traceability to NIST for dimensional measurements of precision gears.

As a result of a previous NIST workshop which identified the need for NIST-traceable gear measurements, NIST and DOE have entered into a collaboration to provide new traceability of gear measurements to NIST through a joint NIST/DOE center being developed at the DOE Y-12 Facilities in Oak Ridge. The 2 day gear workshop gave potential users of the center the opportunity to make their needs known and to interact with industry, university, DOD, Y-12, and NIST principals in gear manufacturing and measurement. A major result was agreement by participants to establish an ad hoc industry-driven council on gear metrology. This council will be charged with developing prior-

ity gear measurement needs to be considered by NIST and Y-12 as part of the proposed gear metrology program.

PHOTOPATTERNING OF ALKYLTHIOL SELF-ASSEMBLED MONOLAYERS

Self-assembled monolayers (SAMs) currently represent the most well-defined organic thin-film system for controlling the molecular architecture of surfaces and interfaces. The ability to control the spatial distribution of these molecular monolayers on surfaces is expected to impact such diverse areas as biosensing, immunoassay diagnostics, DNA sequencing, and molecular electronics. NIST scientists have developed a new, versatile method for photopatterning an alkylthiol SAM on gold and silver surfaces. The patterning method is derived from two recent studies which showed that: 1) adsorbed alkylthiolate molecules (RS^-) in the monolayer are oxidized to the corresponding alkylsulfonate (RSO_3^-) when they are uv irradiated in air; and 2) alkylsulfonates are weakly bound to gold and silver surfaces and, thus, are easily displaced from the surface by subsequent immersion of the sample in an alkylthiol solution. The photopatterning method uses knowledge gained from these two observations.

A pattern of alkylsulfonates is first formed in a SAM by uv irradiation through a mask. The sample is then immersed in a dilute solution of a different alkylthiol. The alkylsulfonates in the exposed areas of the original SAM are displaced, incorporating the second type of alkylthiol into the monolayer. This results in a single monomolecular film composed of two types of alkylthiol in a pattern determined by the mask. Maps of the molecular composition of the films have been made by a NIST scientist. Secondary ion mass spectrometry (SIMS) images confirmed the efficacy of the photopatterning strategy. The advantages of the SIMS method are that physical contact with the sample is not required, and it is generally applicable to mono-layers of any alkylthiol molecule. Pattern features of approximately $10 \mu\text{m}$ have been demonstrated, and work is continuing to determine the ultimate resolution of the photopatterning method.

ATMOSPHERIC SAMPLING IN SAUDI ARABIA

NIST and the Saudi Arabian Ministry of Defence and Aviation (MODA) recently collaborated to collect ambient particulate and gas samples at several

locations in Saudi Arabia. The interest grew from the recent degradation of air quality in the region as a result of the Kuwaiti oil well fires. The sampling team consisted of two NIST researchers and three MODA personnel. The Saudis were trained in collection methods at a 2 week Ground-Based Smoke Sampling Techniques Training Course held at NIST in August 1992.

The team collected samples to demonstrate the operation of portable gas and particulate-sampling instrumentation, including gravimetric measurements, light-scattering cells, size classifiers, battery-powered gas analyzers, and filter sampling trains. The aerosol samples will be used to determine the particulate-size distribution, inhalable particulate fraction, and total particulate mass concentration. Filter and sorbent tube samples will be analyzed to determine polycyclic aromatic hydrocarbon concentrations. At each collection site, the concentrations of carbon dioxide, carbon monoxide, hydrogen sulfide, nitrous oxide, and oxygen were monitored. Approximately half of the samples will be analyzed by the Saudi personnel in Saudi Arabia, while the others were returned to NIST for analysis. Some of the NIST particulate samples will undergo more specialized examination, including electron microscopy and laser microprobe analysis.

COLLABORATIVE RESEARCH ELUCIDATES CARBON MONOXIDE AND SOOT OXIDATION

A joint effort by a NIST scientist and university researchers has explained why soot, always produced inside luminous flames, does not always escape as smoke. The group measured the concentrations of OH radicals in the soot oxidation regions of diffusion flames of methane, a methane/butane mixture, and a methane/1-butene mixture in air at atmospheric pressure. The large, super-equilibrium values observed in the high-temperature reaction zones in the absence of soot particles are greatly reduced in the presence of soot. Their computations of the soot oxidation rates using the concentrations of the pertinent flame species showed that this diminution is primarily attributable to OH reaction, with O₂ making only a small contribution, and their comparison of the soot and CO oxidation rates showed that the soot (with its high-collision efficiency with OH) successfully competes with CO for OH. Thus, large soot concentrations are often accompanied by significant CO emissions. A paper on this research has been submitted to *Combustion and Flame*.

NIST SUPPORTS COMPUTER-AIDED ACQUISITION AND LOGISTIC SUPPORT (CALS) INITIATIVE IN COMPUTER GRAPHICS

In its continuing support of the Department of Defense CALS program, NIST developed a detailed design specification for determining conformance of Computer Graphics Metafile (CGM) interpreter products to the requirements of Federal Information Processing Standard (FIPS) 128, CGM, and the Military Specification MIL-D-28003A. In a three-part effort, researchers first initiated a conformance testing service for CGM metafiles in May 1991. The next phase focused on developing procedures for the testing of CGM generator (writer) products to verify that a product produces conforming metafiles that accurately and correctly define the intended picture; the CGM generator product conformance testing service is scheduled to begin soon.

The last part of the total CGM conformance testing environment is to ensure that a CGM interpreter (reader) product can correctly and completely parse an CGM file and produce the intended picture. NISTIR 5146, Detailed Design Specification for Conformance Testing of Computer Graphics Metafile (CGM) Interpreter Products, describes the CGM interpreter product testing program and makes recommendations for further CGM testing in support of CALS.

SPOKEN LANGUAGE TECHNOLOGY AND APPLICATIONS DAY HELD

Recently NIST cooperated with the Defense Department's Advanced Research Projects Agency (ARPA) to sponsor a showcase event aimed at unveiling spoken language understanding technology. Held at the National Academy of Sciences, the event attracted more than 250 attendees from government, industry, and academia. The goal of the seminar was to catalyze the rapid transfer of the technology into real human-computer interaction systems, including government and military applications. Participating in ARPA spoken language research programs since 1984, NIST developed the benchmark tests that have been used to track the progress of spoken language technology.

"TRAPPED" IONS PROVIDE FIRST VIEW OF LIGHT PROPERTY

In an experiment that demonstrates the wave-particle duality of light, NIST scientists reported in the April 19 *Physical Review Letters* that they had

made the first observation of interference effects in light scattered by two trapped atoms. Quantum theory states that light can act either as a wave or as a particle. Researchers at NIST surmised that if two or more atoms are localized (kept relatively still and close to each other), polarized laser light striking them would be absorbed and then re-radiated by each. Then, a polarization-sensitive analyzer would detect the re-radiated light and measure how the photons (packets of light) interfere. This would indicate if the photons were acting like particles or waves. Most other experiments of this type were unable to adequately localize atoms to within 50 nm (a quarter length of a light wave), and therefore were unable to observe this phenomenon. The NIST team was able to trap two mercury ions in an electromagnetic “well” and selectively demonstrate both the particle nature and the wave nature of the photons. Since publication of the paper describing the experiment, the researchers have observed the interference pattern of three ions. For a reprint of the *Physical Review Letters* article, contact Sarabeth Moynihan, Div. 104, NIST, Boulder, CO 80303-3328, (303) 497-3237. Ask for paper no. 12-93.

PARTNERS PLAN DEVICE FOR CLEARER PROTEIN IMAGES

The Center for Advanced Research in Biotechnology (CARB) and a Rockville, MD firm, are collaborating on a new system to simplify the study of three-dimensional shapes of protein molecules. Defining these complex structures helps pharmaceutical companies design more effective drugs. The new imaging system will be developed under a 2-year cooperative research and development agreement, with support coming from the National Institute of General Medical Sciences. Current imaging techniques involve bombarding a protein crystal with x rays and using the resulting diffraction patterns to decipher its three-dimensional structure. CARB and the Rockville firm seek to develop and test a prototype system that will collect x-ray diffraction patterns more accurately and quickly than commercially available methods. CARB was established in 1984 by NIST, the University of Maryland and Montgomery County, MD, as a unique center for government, academic and industry scientists.

CRADA SEEKS BETTER FACTORY SYSTEMS INTEGRATION

Despite years of product development, truly modular and flexible integrated manufacturing systems are still not prevalent in U.S. industry. Problems include the inability of factories to share information on engineering, production management and control systems, as well as a lack of standards specifying the interactions between such systems. Addressing these problems is the goal of a recently signed cooperative research and development agreement between NIST and a private company. The multiyear collaboration involves the development of computer-aided process planning and integrated manufacturing control systems technology. Specifically, the partners will design or implement information models, communications protocols and prototype software. For more information, contact Steven Ray, A127 Metrology Building, NIST, Gaithersburg, MD 20899-0001, (301) 975-3524.

U.S./HUNGARIAN TEAM TO REFINES pH STANDARDS

NIST and its sister agency in Hungary, the Hungarian National Office of Measures, have been awarded a grant to work toward establishing a more universal pH scale (the acid/base scale). The Board of the U.S.-Hungarian Science and Technology Joint Fund recently approved a 3-year grant for studies on pH and electrolytic conductivity. The grant formalizes more than a decade of cooperation between scientists at NIST and the Hungarian National Office of Measures. Chemists in the two agencies plan to assess similarities in U.S. and Hungarian pH and conductivity standards. Their work will form a foundation for an improved international pH scale and will refine measurements for international conductivity standardization. Such measurements are crucial to diverse industries such as foods, agriculture, medicine, fuel, materials, and semiconductors.

ELEVEN INVENTIONS READY FOR LICENSING

NIST recently announced that the following 11 government-owned inventions are now available for licensing:

- Intermetallic Ti-Al-Nb Alloys Based on Strengthening of the Orthorhombic Phase by Mega-type Phase (Docket No. 90-032);

- High-Speed, Amplitude-Variable Thrust Control (Docket No. 90-035);
- Automated Recognition of Characters Using Optical Filtering with Positive and Negative Functions Encoding Pattern and Relevance Information (Docket No. 92-004);
- Automated Recognition of Characters Using Optical Filtering with Maximum Uncertainty-Minimum Variance (Docket No. 92-005);
- Synthetic Perturbation Tuning of Computer Programs (Docket No. 92-010);
- Method and Materials for the Assay of Several Classes of Enzymes by Light-Scattering Techniques Using Substrate-Coated Colloidal Particles (Docket No. 92-011);
- A Procedure for Digital Image Restoration (Docket No. 92-028);
- Micro-Hotplate Devices and Methods for Their Fabrication (Docket No. 92-045);
- Temperature-Controlled, Micromachined Arrays for Chemical Sensor Fabrication and Operation (Docket No. 92-046);
- Application of Microsubstrates for Materials Processing (Docket No. 92-047); and
- Method and Apparatus for Precisely Measuring Accelerating Voltage Applied to X-Ray Sources (Docket No. 93-023).

For technical and licensing information on these inventions, contact Bruce E. Mattson, B256 Physics Building, NIST, Gaithersburg, MD 20899-0001, (301) 975-3084.

WALL DESIGNERS GET HELP AVOIDING THE "DRAFT"

Poorly designed or constructed exterior walls often leak air and moisture into and out of office buildings. This can lead to uncomfortable occupants, poor indoor air quality, increased energy consumption and even structural safety problems. NIST has developed a set of practical guidelines to help building designers understand air leakage and other thermal performance problems, and, more importantly, learn how to avoid them. The guide is divided into three easy-to-follow sections. The first explains how heat, air and moisture transfer between the inside and outside of a building. This section also explains where and how defects can

occur, and how they can be prevented. The second describes basic design principles and techniques for avoiding problems. The third describes a variety of wall systems and design features crucial to achieving good thermal performance. Envelope Design Guidelines for Federal Office Buildings: Thermal Integrity and Airtightness (NISTIR 4821) is available from the National Technical Information Service, Springfield, VA 22161, (703) 487-4650 for \$27 prepaid. Order by PB 93-183770.

NIST INTENDS TO GRANT EXCLUSIVE DSA LICENSE

In a June 8 Federal Register notice, NIST announced its intent to grant an exclusive worldwide license to a private company for the "Digital Signature Algorithm." NIST has filed a patent application for the algorithm, which forms the basis for a proposed federal information processing standard that will allow federal agencies to verify the integrity of electronic data and the sender's identity. The proposed standard, known as the Digital Signature Standard, adopts a system that uses mathematical formulas to create and verify a digital value called a signature. The prospective license is expected to resolve a patent dispute with the private company concerning the algorithm. The company intends to permit royalty-free use of the algorithm for noncommercial purposes and by U.S. federal, state, and local governments.

AEROSPACE ALLOYS CONSORTIUM LAUNCHED

Seven manufacturers, seven universities, three federal agencies and one industry technical society have committed to join an industry/government program to improve the precision casting of metal alloys commonly used in the aerospace industry. The 18-member consortium will be the largest cooperative research and development program in materials at NIST. The overall goal of the program is to plan and undertake research on high-technology casting so that the planning, research, and technology transfer can be coordinated and brought quickly to manufacturers. The consortium is a cooperative, distributed effort by participants; research will be carried out in-house by members and by NIST. The American Foundrymen's Society will represent the U.S. casting industry. For information, contact Robert J. Schaefer, Office of Intelligent Processing of Materials, B344 Materials Building, NIST, Gaithersburg, MD 20899-0001, (301) 975-5727.

CONSORTIUM TO ADVANCE POLYMER BLENDS PROCESSING

Four manufacturers that produce and use engineering resins and a U.S. national laboratory are joining NIST in a cooperative research and development program to improve the processing of polymer blends and alloys. The consortium is sponsored by NIST to help the U.S. polymers industry retain its technological lead in the international marketplace. The goal of the consortium is to use NIST measurement tools to develop the data and processing models industry needs to produce new and more economical resins. New information will enable producers to make critical in-process measurements that are not now possible. For information, contact H. Thomas Yolken, Office of Intelligent Processing of Materials, B344 Materials Building, NIST, Gaithersburg, MD 20899-0001, (301) 975-5727.

CRADA MAY IMPROVE MICROWAVE MEASUREMENTS

A long-standing problem for measuring microwaves has been providing a meaningful traceability between NIST's primary (six-port) microwave measurement system and automated vector network analyzers used extensively in government and private industry. Existing methods require numerous connections to the six-port system; these connections are time consuming and a major source of measurement error. A new NIST cooperative research and development agreement with a private company calls for the partners to use programmable multistate tuners as a transfer standard. This requires only one connection and should reduce significantly the amount of operator effort needed. NIST will initially evaluate the stability of the company's tuner and then work with the company to develop state-of-the-art statistical methods for uncertainty analysis. For more information, contact Bob Judish of NIST at (303) 497-3380 or Mike Fennelly of ATN Microwave at (508) 667-4200.

ACTIVITIES REPORT HIGHLIGHTS 1992 FOR NIST LAB

From measurement standards for nuclear medicine to ultra-precise time and frequency measurements for telecommunications, NIST provides U.S. industry with technologies that are vital to the nation's health, safety and economic competitiveness. Scientists at NIST frequently collaborate with industry, academia, and other government agencies. A

new report on the technical activities at one of NIST's principal laboratories summarizes these collaborations as well as its recent research and accomplishments. The Physics Laboratory Technical Activities Report for 1992 is available for \$36.50 (print) or \$17.50 (microfiche) prepaid from the National Technical Information Service, Springfield, VA 22161, (703) 487-4650. Order by PB 93-178648.

NEW CRADA TO IMPROVE ON-LINE CVD MONITORING

Many manufacturers use a process known as chemical vapor deposition to fabricate semiconductor devices and other advanced crystalline materials. One such manufacturer and NIST are collaborating to develop an on-line monitoring system that would improve quality control and reduce defects during manufacture. This joint effort is the result of a recently signed cooperative research and development agreement between NIST and the private manufacturer. The partners are developing a system that will identify and measure metalorganics flowing into a CVD reactor. In the CVD process, metalorganics are reacted on a heated substrate to form semiconductor chips and other advanced electronics materials. Based on Fourier transform infrared spectroscopy, the system will provide the ability to continuously monitor the process. Such on-line monitoring will enable reactor operators to adjust the CVD system for optimum quality.

REPORT REVIEWS 1992 ACHIEVEMENTS OF NIST LAB

Whether the need is to find environmentally safe refrigerants or identify contaminants in semiconductor wafers, U.S. industry is increasingly turning to NIST for answers. One of the principal laboratories at NIST provides industry with a variety of collaborative opportunities in areas such as biotechnology, analytical chemistry, chemical kinetics, thermophysics, surface science and process measurements. A complete report covering this laboratory's scientific research and industry connections is now available from the National Technical Information Service. The report, Chemical Science and Technology Laboratory Technical Activities Report for 1992, number PB 93-173482, may be ordered for \$44.50 (print) or \$19.50 (microfiche) prepaid from NTIS, Springfield, VA 22161, (703) 487-4650.

“HASH” STANDARD FOR DIGITAL SIGNATURES APPROVED

Secretary of Commerce Ronald H. Brown recently approved a federal information processing standard that can be used to help verify the integrity of electronic data and the sender's identity. The Secure Hash Standard (FIPS Publication 180) is used to condense a long message or data file to 160 bits. A mathematical technique is then applied to this message “digest” to produce a digital signature. Like a handwritten signature, a digital one can be used to identify and authenticate the originator of the information and to verify that the information has not been altered after it is signed. A hashing function is used because it is faster and more efficient to sign the 160-bit digest than a message that could be thousands of bits. The standard is required for federal government use with the proposed Digital Signature Standard. Copies of FIPS 180 will soon be available from the National Technical Information Service, Springfield, VA 22161, (703) 487-4650.

NEW ALGORITHM SHARPENS IMAGES, DAMPS NOISE

A NIST mathematician has developed an improved algorithm for reducing fuzziness and blur in digital images. The procedure could potentially improve quality for a host of imaging applications, including medical diagnostics, astronomy, satellite mapping, industrial imaging, and low-light imaging. While not applicable to all possible sources of image blurring, the new algorithm is effective at reducing the very broad class of “Gaussian-like” blurs—such as those produced by atmospheric turbulence in a satellite photograph, or x-ray scattering in radiography. Older algorithms exist that technically reduce Gaussian blurring, but with a side effect. The same operations that reduce the blurring tend to magnify any random noise in the image—and there's always noise. Experiments on images that have been artificially blurred confirm theoretical predictions that the improved algorithm achieves better results than the older procedures, while sharply limiting the effects of noise. NIST has applied for a patent on the procedure.

A STEP TOWARD COMPETITIVE “MADE-TO-MEASURE”

A new cooperative research and development agreement could help make tomorrow's custom-designed clothing competitive with today's “ready-to-wear” garments. Specialists from NIST and the Fashion Institute of Technology have joined forces to develop an information model for made-to-measure pattern making that expresses pattern styles and individual body measurements in digital, standardized computer format. FIT, a research leader in the area of apparel design and manufacture, will provide NIST with data requirements for the representation of made-to-measure patterns. Four types of data will be considered for the informational model: two dimensional pattern data, grading information, anthropometric data and constraint information. NIST will develop the information model as a STEP (Standard for the Exchange of Product Model Data) application protocol. The model developed will be incorporated by NIST, FIT and a private company into STEP-based computer software that will modify patterns to reflect individual body measurements. NIST is working with clothing manufacturers and the Defense Logistics Agency to extend STEP into the apparel industry.

PRIMER TELLS WHAT'S COOL (AND TRAPPED) WITH LASERS

Scientists interested in a basic primer on laser cooling and trapping of neutral atoms will want a copy of a new paper by NIST and University of Colorado researchers. Laser Cooling and Trapping for the Masses describes the current techniques for cooling and trapping atoms, offers a history of the research, discusses recent simplifications made possible by the use of diode lasers and the vapor-cell magneto-optical trap, and speculates on future applications for this technology. These include improved atomic clocks, wavelength standards for optical communications, and solutions to problems in basic physics (such as a study of the fundamental weak interaction between quarks and electrons). For a copy of paper 22-93, contact Sarabeth Moynihan, Div. 104, NIST, Boulder, CO, 80303-3328, (303) 497-3237.

EXAMINERS NEEDED FOR 1994 BALDRIGE AWARD

NIST is seeking examiners from all sectors of American business to review and evaluate applications submitted for the 1994 Malcolm Baldrige National Quality Award. Applicants for the award's board of examiners must be experts in quality management and capable of evaluating large/small manufacturing and service businesses. Those selected must take a three-day preparation course based on the Baldrige award examination items, the scoring criteria, and the examination process. The board of examiners currently has 265 quality experts. This number is expected to increase slightly for the 1994 board. Applications will be available in September from the Malcolm Baldrige National Quality Award Office, A537 Administration Building, NIST, Gaithersburg, MD 20899-0001, (301) 975-2036, fax: (301) 948-3716. Completed applications are due Nov. 2, 1993.

NIST MEASUREMENTS CONFIRM QUANTUM HALL DEVICES AS INTRINSIC STANDARDS OF RESISTANCE

NIST scientists have verified that quantum Hall devices can be used as an intrinsic standard of resistance that is independent of the specimen itself to within an accuracy of 2 parts in 10^9 . These measurements were carried out on the quantum Hall effect research system, which permits long-term observations of specimen performance, providing a unique tool for investigating fine-scale effects. The quantum Hall effect has been used as the international practical standard of resistance since Jan. 1, 1990.

The scientists compared specimens made from GaAs/AlGaAs heterostructures by AT&T Bell Laboratories, specimens made from GaAs/AlGaAs heterostructures by Philips LEP for the European Metrology Organization, a silicon MOSFET specimen made at the University of Southampton in Great Britain, and NIST specimens prepared from GaAs/AlGaAs heterostructures grown by NIST's molecular-beam epitaxy system. These measurements were made with a superconducting magnet at temperatures below 0.4 K using an automated high-precision potentiometric comparator. The resistances measured at the 6453.2Ω resistance plateau on all of the devices were found to be the same to within 2 parts in 10^9 .

These results represent an order of magnitude improvement in NIST capabilities and are in agree-

ment with measurements made at other national laboratories, including the National Physical Laboratory in Great Britain, the Bureau International des Poids et Mesures and the Laboratoire Central des Industries Electriques in France, and the Swiss Eidgenossisches Amt Für Messwesen.

NIST WORK ENABLES MICROMACHINE DESIGNERS TO FABRICATE DEVICES THROUGH FOUNDRY PROCESSING

NIST scientists have developed a framework and procedures for producing micromachined semiconductor devices through the MOSIS silicon foundry service. MOSIS (Metal Oxide Semiconductor Implementation Service) is the integrated-circuit fabrication service established by the National Science Foundation and the Advanced Research Projects Agency in support of government research. Considerable technical excitement is being expressed for the potential offered by so-called "micromachined" parts—tiny mass-produced artifacts made in silicon using conventional semiconductor processing technologies until the last step, an etching process to complete the desired electrical and mechanical structures. A single silicon chip can incorporate both the micromachine and an integrated circuit, for example a sensor and signal-processing electronics.

The NIST development permits a micromachine designer to fabricate devices by using a commercially available standard process, followed by an in-house custom etching step requiring only simple, inexpensive equipment. Because their fabrication depends on tested, reliable methods, micromachines offer the promise of low cost. Parts proposed to date include a variety of sensors, electric motors, gear trains, lever mechanisms, and in vivo surgical tools, in addition to NIST projects, including thermal targets, ac-to-dc thermal converters, and chemically specific sensors. To implement the potential for micromachine development which they realized lay in commercially available processing, the NIST scientists added two layers to the MOSIS CMOS process to define a region to be micromachined by customers upon receipt of their MOSIS chips. The "open" layer defines a region of bare silicon, the region to be exposed to the post-processing etchant. The "etch-stop" layer defines an ion-implanted frame around the open layer regions within which the etched silicon is confined. The new capability has been announced to the MOSIS community.

“LIFT-MODE” MAGNETIC-FORCE MICROSCOPY DECONVOLVES MAGNETIC INFORMATION FROM SURFACE TOPOLOGY

NIST scientists have developed a dual-scan form of atomic-force microscopy that solves a problem which has plagued researchers attempting to study the magnetic properties of surfaces at near-atomic levels of resolution. The problem is that the topography of the surface typically affects the measurement. In the new NIST method, the sensing tip, or cantilever, of an atomic-force microscope is coated with a magnetic film, so that the tip will respond to magnetic domains and other magnetic structures on the specimen surface. The tip is first scanned in contact with the surface, and the line-trace signal recorded. A second scan over the same path is taken with the tip lifted a small distance from the surface; a piezodrive using information from the first scan is used to keep this separation distance constant. Magnetic forces cause small deflections of the tip from the predetermined path and are recorded during the second line scan, referred to as “lift mode.” A series of paired contacting and lift-mode scans generates simultaneous topographic and magnetic images of the surface being examined.

The NIST method uses a cantilever that is non-vibrating and responds directly to the force it experiences, rather than to the derivative of force as was the case with previous methods that used vibrating non-contact cantilevers. In addition, since the positioning mechanism can place the tip within a few nanometers of the surface during the lifted scans, resolution and sensitivity are further enhanced. The capability of topographic imaging having a vertical resolution of 0.1 nm and a lateral resolution of 1 nm, with simultaneous magnetic imaging having a force sensitivity of 10^{-12} N and lateral resolutions approaching 10 nm, will provide industry with a valuable tool for developing magnetic nanostructures and microelectronic circuits depending on magnetic phenomena, including memory.

NIST DEVELOPS REFERENCE SPECIMENS TO IMPROVE CRITICAL-CURRENT MEASUREMENTS ON HIGH-TEMPERATURE SUPERCONDUCTORS

A NIST scientist has developed a methodology for producing reference specimens of high-temperature superconductors that yield consistent results for measurements of critical current. By providing a “standard” test specimen to evaluate the perfor-

mance of a measuring system and associated techniques for handling and preparing specimens for measurement, this work addresses the great variability of measurement results experienced by researchers in the high-temperature superconductor field. Confusion surrounding conflicting claims for performance impedes both scientific development and commercialization. Some of this confusion results from the fact that high-temperature superconductors are very susceptible to degradation as a result of mechanical stress, the presence of moisture, thermal cycling, and aging. These factors can create differences between two consecutive measurements of critical current that are as large as 40 percent.

The scientist’s methodology, together with his methods of sample preparation and mounting, can reduce these differences to less than 4 percent—a reduction in variation by a factor of 10. The approach developed by the scientist has demonstrated high repeatability: one specimen was thermally cycled nine times; two of these runs included remounts of the pressure contacts for voltage and current. The overall change in critical current was less than 4 percent from the first run to the ninth run. The NIST reference specimen, also known as the high-temperature superconductor standard reference device (HTS-SRD), is the first such HTS-SRD to be developed.

WORKSHOP ON THERMOCHEMICAL DATA NEEDS FOR CVD MODELING

The proceedings from a joint SEMATECH/NIST Workshop on Chemistry of Chemical Vapor Deposition (CVD) Processes in Semiconductor Manufacturing have been published by SEMATECH. This workshop was held at NIST and was organized by several NIST scientists. There were approximately 50 participants from industry, universities, and other government agencies.

The workshop focused on the chemical kinetic and thermodynamic data requirements for process simulators used in semiconductor manufacturing. These simulators rely on models for the gas phase and surface chemical reactions controlling thin-film deposition processes. Participants in the workshop reviewed the current state of development in gas-phase/surface kinetics modeling, data requirements, and methods to obtain the data necessary to model reliably the chemical reactions controlling CVD. The current state-of-the-art for both experimentally generated and computationally generated thermochemical data were reviewed and discussed,

as were database evaluation and dissemination needs. The rapid advancements in *ab initio* calculational methods provide a means for data estimation of sufficient accuracy to be competitive with experimentally produced values. Recommendations were made for four topical areas: (1) application and use of data by industry, (2) measurement of fundamental thermodynamic and kinetic data, (3) status of present and future data estimation methods, and (4) standardization of input databases.

This workshop was an outgrowth of a previous meeting sponsored by SEMATECH, Sandia, and NIST in 1990 on CVD Reactor Modeling. Two primary needs identified by the 1990 workshop were: (1) reliable fluid dynamic models of reactor geometries and (2) reliable data on the kinetics and thermodynamics of pertinent chemical systems. Future joint workshops in the area of thin-film processing needs of the semiconductor industry are under consideration.

NEW MONOGRAPH OF THERMOCOUPLE REFERENCE FUNCTIONS AND TABLES BASED ON THE ITS-90 NOW AVAILABLE

Temperature-Electromotive Force Reference Functions and Tables for the Letter-Designated Thermocouple Types Based on the ITS-90 (NIST Monograph 175, which supersedes NBS Monograph 125) presents reference functions and tables based on the International Temperature Scale of 1990 (ITS-90) for the eight, ISA letter-designated thermocouple types: noble-metal types B, R, and S and base-metal types E, J, K, N, and T. Also, for these thermocouple types, reference functions and tables of their thermoelements versus the NIST platinum thermoelectric reference standard, Pt-67, are included. The 600-page monograph, which was prepared by several NIST staff members, contains 118 tables, giving tabular values of temperature and thermoelectric voltage in several different formats to satisfy the requirements of various users. The monograph also covers such topics as history of development, special precautions regarding usage, recommended temperature ranges of use, industrial tolerances, and nominal chemical compositions of each thermocouple type. Information

from Monograph 175 was the basis for reference functions and/or tables prepared for: Standard Handbook for Electrical Engineers, ASHRAE Fundamentals Handbook, IEC Standard Publication 584-1, Thermocouples, Part 1: Reference Tables, CRC's Handbook of Chemistry and Physics, ASTM Manual 12 On the Use of Thermocouples in Temperature Measurement, and various ASTM standards.

TECHNOLOGY TO FABRICATE NANOMETER-SIZE SURFACE TEST STRUCTURES DEVELOPED

A number of new techniques have been developed recently that are useful for visualizing surface topography with nanometer or sub-nanometer resolution. Techniques such as scanning tunneling microscopy, electron microscopy, optical interferometry, near-field optical microscopy, and scanning scattering microscopy produce very detailed images of surface topography. Different properties of a surface are probed by each technique, however, and the images can be difficult to compare or interpret quantitatively.

A small company, working with a NIST scientist, has successfully completed work supported by a Department of Commerce Small Business Innovation Research Phase I contract. The company has investigated three test structures that could be used for evaluating the performance of instruments measuring surface topography on the nanometer scale. One test structure, consisting of etched steps in silicon dioxide on silicon, showed particular promise. The company showed that 20 nm wide lines with spacings of 20 nm could be produced on the 15 nm thick thermally grown oxide. Procedures were developed to form steps in increments of 1 nm height by controlled etching. A thin metal layer was deposited over the stepped oxide. Tests made with scanning tunneling microscopy and transmission electron microscopy showed that useful devices with steps of 10 nm height had been fabricated. Improvements in the fabrication procedure have been proposed to produce structures with smaller step heights.

OBSERVATION OF STRAIN-INDUCED MICROCRACKS IN HIGH T_c SUPERCONDUCTOR COMPOSITE WIRE

The use of new high-temperature superconductors in a number of applications is challenged by the difficulty of fabricating wire from a brittle material. One promising cable fabrication process embeds the superconductor as fine filaments in a metal matrix. However, strains in the cables due to bending, or to Lorentz forces associated with large magnetic fields can significantly reduce critical currents.

To investigate the effects of strain on current carrying capability, scientists at NIST, in collaboration with a private company, recently obtained radiographs of strain-induced microcracks in superconducting wires using an x-ray microscope developed and patented by NIST. This unique facility is located on NIST beamline X23A3 at the National Synchrotron Light Source. Microcracks as small as $1\ \mu\text{m}$ were observed non-destructively. The effect of increasing strain was clearly visible by the number and size of cracks. Detailed studies are planned to clarify further the nature of the microcracks.

INCOMMENSURATE SPIN DENSITY WAVES IN METALLIC $V_{2-y}O_3$

Scientists from NIST, another government laboratory, a number of universities, and a private company, in a joint collaboration, have characterized the static and dynamic properties of metallic $V_{2-y}O_3$ in a region of composition, temperature, and hydrostatic pressure near the metal-insulator transition (MIT). Many materials are known to possess such transitions, and various theories and models have been successful in clarifying several mechanisms for their behavior. That several mechanisms are necessary to describe the MIT in different materials reflects the variety of circumstances which the electrons (and holes) experience due to crystalline structure (or lack of it as in amorphous materials), doping conditions, and in general energetics of the interactions. In several materials that exhibit antiferromagnetism in the insulating phase, doping transforms them into a highly correlated metal. Recent theories have suggested the possibility that the metallic state near the MIT

exhibits spiral magnetic order. Until now the extensive search for this effect has been unsuccessful.

In the recent work at the NIST research reactor, the sought-for ordering has been discovered. The static ordering of the moments, measured with neutron diffraction, has been determined to be an incommensurate spin density wave. Utilizing inelastic neutron scattering, the dynamic properties of the moment fluctuations also have been characterized. In addition to providing definitive results that confirm recent theoretical models, the existence of such ordering could be significant in understanding the cuprate superconductors which are related to this general class of materials.

HIGH-SPEED SPATIAL SCANNING PYROMETER DEVELOPED

An accurate high-speed spatial scanning pyrometer has been designed and developed by NIST scientists. The pyrometer measures spectral radiance temperatures at multiple target points along the length of a rapidly heating/cooling specimen in dynamic thermophysical experiments at high temperatures. The design, which is based on a self-scanning linear silicon array containing 1024 elements, enables the pyrometer to measure spectral radiance temperatures (nominally at $0.65\ \mu\text{m}$) at 1024 equally spaced points along a 25 mm target length. The elements of the array are sampled consecutively every $1\ \mu\text{s}$, thereby permitting one cycle of measurements to be completed in approximately 1 ms. The pyrometer output is recorded digitally with a full-scale resolution of 0.025 percent every $1\ \mu\text{s}$. The estimated total uncertainty of radiance temperature measurements is about 4 K at temperatures above 2000 K. This pyrometer, the only one of its kind in the world, has been used successfully in the NIST laboratory as part of a subsecond rapid heating technique for measuring thermal conductivity of tungsten in the range 1800 K–3200 K. Although the pyrometer is designed specifically for thermophysical measurements, it has the potential of having broad applications in various high-temperature technologies related to materials processing and characterization, systems performance, heat transfer diagnostics, and high-temperature research in general.

COMPUTER GRAPHICS METAFILE (CGM) AND POSIX FIPS REVISED

The Secretary of Commerce approved a revision to FIPS 128, CGM, which will be published as FIPS 128-1. The revised standard adopts the redesignated version of the CGM standard known as ANSI/ISO 8632.1-4:1992; adds a requirement for the use of profiles that define the options, elements, and parameters of ANSI/ISO 8632 necessary to accomplish a particular function and to maximize the probability of interchange between systems implementing the profile; and adopts the first such profile as a requirement, the military specification MIL-D-28003A, Nov. 15, 1991, known as the CALS (Computer-aided Acquisition and Logistics Support) CGM Application Profile.

Effective Oct. 15, 1993 FIPS 128-1 is a graphics data interface standard that specifies a file format suitable for the description, storage, and communication of graphical (pictorial) information in a device-independent manner. The standard will facilitate the transfer of graphical information between different graphical software systems, different graphical devices, and different computer graphics installations.

Also revised was FIPS 151-1, POSIX: Portable Operating System Interface for Computer Environments, which will be published as FIPS 151-2. The revision adopts International Standard ISO/IEC 9945-1:1990, Information Technology—Portable Operating System Interface (POSIX)—Part 1: System Application Program Interface (API) [C Language], which defines a C programming interface to an operating system environment. Effective Oct. 15, 1993 FIPS 151-2 will promote the portability of useful computer application programs at the source code level and maximize the return on investment in computer programs by ensuring operating system compatibility.

OVERVIEW OF FIRST TEXT RETRIEVAL CONFERENCE PUBLISHED

NIST Special Publication 500-207, The First Text REtrieval Conference (TREC-1), presents an overview of this conference held recently and attended by about 100 people involved in 25 participating groups. TREC-1 brought research groups together to discuss their work on a new large test collection. Participants reported on a large variety of retrieval techniques, compared the effectiveness of different techniques, and discussed how differences between the systems affected performance. The conference is expected to become an annual event.

NIST SPONSORS USERS' FORUM ON APPLICATION PORTABILITY PROFILE (APP) AND OPEN SYSTEM ENVIRONMENT (OSE)

NIST sponsored the 11th in a series of semi-annual APP/OSE workshops recently, which was attended by about 150 participants. The APP defines a common set of standards and specifications that address the broad functional areas of applications portability and interoperability. The forums provide users and vendors the opportunity to exchange information on NIST's proposals on the evaluation and adoption of an integrated set of standards to support the APP and OSE. A new feature of the users' forum is an introductory half-day tutorial for users with little or no experience with the APP and OSE. The next APP/OSE workshop will be held Nov. 17–18.

NIST EXPLAINS ROLE OF MEASUREMENTS IN THE COMPETITIVE STANCE OF THE U.S. ELECTRONICS INDUSTRY

NIST has explained why measurement capability has such high leverage on the competitiveness of the U.S. electronics industry in a new publication, Measurements for Competitiveness in Electronics, NISTIR 4583. This publication describes the role that measurements play in manufacturing industries, the role that NIST plays in the development of measurement capability for U.S. industry, and the specific measurement needs that are impeding U.S. competitiveness in nine fields of electronics. The nine fields addressed are semiconductors, magnetics, superconductors, microwaves, lasers, optical-fiber communications, optical-fiber sensors, video, and electromagnetic compatibility. This publication is designed to serve both technical and policy-making audiences in Government and industry.

Each chapter on a field of electronic technology contains four basic types of information: (1) a review of the technology; (2) a discussion of world markets and U.S. competitiveness; (3) an outline of the goals that U.S. industry is pursuing to improve its competitiveness; and (4) an assessment of the new measurement capability that U.S. industry needs to meet its own goals. The focus is on measurement capability that is needed widely in the U.S. electronics industry, that will have especially high impact if provided, and that is beyond the resources of the broad range of individual companies to develop. This analysis was developed in cooperation with U.S. industry as a consensus statement of the principal needs. The publication provides the framework for an action plan to correct the shortfall and to advance U.S. competitiveness.

NIST-INDUSTRY COLLABORATION DEVELOPING NEEDED FINE-SCALE TEST STRUCTURES

NIST scientists are leading a collaboration with industry that is intended to extend the design criteria of practical electrical test structures to the subhalf-micrometer linewidth region. At 0.5 μm and below, applying conventional test-structure methodology to make dimensional measurements becomes extremely difficult, as the effects of what were ignorable as perturbations at larger dimensions now need to be understood in detail and accounted for. Industry needs test structures to support lithography advances (such as the use of deep ultraviolet excimer laser wafer steppers) enabling production-line fabrication of features to half-micrometer and below design rules, required for example by next-generation digital logic, including microprocessors. The companies that have collaborated with NIST are a major semiconductor manufacturer, and a manufacturer of test equipment for semiconductor manufacturing.

The semiconductor manufacturer has applied its most advanced developmental line to fabricate wafers bearing test structures designed by the three collaborators. Test structures on these wafers have been used as the basis for an evaluation of electrical, optical, and scanning electron microscope methods for measuring fine-scale linewidth. An important goal was to establish traceability to national standards of length for linewidth-measurement methods in commercial use, work carried out by NIST. Each test chip is composed of a number of areas. Linewidths on the key structures were measured by the three methods: transmitted-light optical microscope, electrical test system (cross-bridge test structures), and scanning electron microscope. The results have been described in two papers presented at SPIE conferences: *Extending Electrical Measurements to the 0.5 μm Regime*, SPIE Vol. 1464 (1991) and *Comparisons of Measured Linewidths of Sub-Micrometer Lines, Using Optical, Electrical, and SEM Metrologies*, SPIE Vol. 1926 (1993), to be published.

PRIVATE LABORATORIES TO USE NIST PRINCETON ENGINE VIDEO SUPERCOMPUTER

NIST and a private laboratory have initiated a new joint research program through the execution of a Cooperative Research and Development Agreement. In this program, the private laboratory will

access the Princeton Engine real-time video supercomputer at NIST to evaluate the efficacy of new image-processing algorithms applied to real-time National Television Systems Committee (NTSC) color video sequences. The Princeton Engine, designed and developed by the David Sarnoff Research Center and provided to NIST by the Department of Defense Advanced Research Projects Agency to promote digital imaging developments, is uniquely suited to this research and is the only one of four similar machines that is accessible to industry and government. The Engine provides real-time video processing capability, accepting and producing a variety of video formats over wideband input and output channels. Because the Engine is programmable, it can be used to evaluate software prototypes of video processing components rapidly at a cost below that of building hardware.

NIST PROVIDES LEADERSHIP IN INTERNATIONAL VAMAS SUPERCONDUCTOR STANDARDS ACTIVITIES

A NIST scientist will serve as the primary U.S. contact for a new VAMAS project on "Characterization and Evaluation of High-Temperature Oxide Superconductors." VAMAS—Versailles Agreement on Advanced Materials and Standards—is an acronym identifying the site at which the program of international standards development was formally established. In addition to NIST, the U.S. organizations participating in the new VAMAS project include two private companies and two universities.

The NIST scientist will carry out nondestructive evaluation (NDE) of the critical current of specimens used in the interlaboratory comparisons. Critical current—a measure of how much current a given superconductor material can carry and remain in the superconducting state—is the single most important parameter determining large-scale application of the high-temperature superconductor materials. The NDE methods developed by the NIST scientist will allow the participating laboratories to measure specimens using their own techniques with a minimum of residual influence from the pre-testing. Other topics which will be explored in the VAMAS project include the evaluation of reliable measurement methods for critical temperature, upper critical field, and critical-surface; physical properties; and the evaluation of existing theories and terminology.

NIST LEADS TEAM DEMONSTRATING CONCEPT OF ELECTRONIC BUSINESS REPLY CARD

NIST is leading a government/industry team formed to promote, develop and demonstrate implement the electronic transfer of electronic component product data. The team recently conducted a demonstration at the 1993 Design Automation Conference to provide engineers with a hands-on introduction to the concept of the "electronic business reply card." Through the use of one of several computer terminals, conference attendees were asked first to identify themselves and their affiliation and then to indicate their interest in receiving information on electronic components selected from the short demonstration list. If they were interested in learning more about a component than provided by the information appearing on the terminal screen in response to their initial inquiry, they could request data at a finer level of detail. Replacing paper transactions with electronically transmitted messages and information—an electronic marketplace—provides a number of powerful advantages to the potential buyer, as well as reduced costs borne by the potential seller. These include virtually instantaneous response to requests, assurance that the latest data is being presented, and access to a wider range of products.

Other planned features include the potential for placing orders electronically and for downloading engineering data and information directly into the customer engineer's computer-aided design system. Implementing these capabilities will involve both technical and political-administrative issues that will be addressed by the Electronic Commerce of Component Information (ECCI) Program, formed in the context of the industry-government National Initiative for Product Data Exchange in response to urgent needs of the electronics sector. The work led by NIST is part of the ECCI Program; the team plans a major demonstration of the electronic business reply card concept for the 1993 CALS Expo in Atlanta in December.

SENSING SURFACE FINISH ULTRASONICALLY

The NIST Quality in Automation program has been active in the development of sensor techniques to assure the quality of manufactured parts. One sensor technique under development has been an ultrasound-based approach to assess the surface finish of turned metal parts.

The basic concept is to direct ultrasound to the part surface, and then monitor the reflected/scattered wave signature in a "pulse-echo" mode. The machine coolant and lubricant fluid provides a convenient coupling medium to support the high frequency waves (nominally 10 MHz and above) between the sensor and part surface. Surface features such as nicks, scratches, and the periodic tool marks associated with the cutting of turned parts will produce echo signatures that may be distinguished from those for a smooth surface.

It is an on-going effort to work at shorter wavelengths (higher frequencies) to enhance system sensitivity to finer surface features. It is a significant challenge to simultaneously define and control the ultrasonic beam orientation relative to the surface normal of various part curvatures including cylindrical, tapered, and spherical.

CHROMIUM IN COAL FLY ASH USING MICROWAVE

A microwave oven-based decomposition method for the determination of chromium has been developed by NIST analysts as part of a collaborative effort with a private company and a guest scientist. Chromium is one of the elements considered to be toxic by the EPA. This new method combines the use of sealed vessels, oxidizing acids and a relatively rapid sample decomposition. The procedure yields complete recovery of chromium in NIST SRM 1633a, Coal Fly Ash and its replacement, SRM 1633b. This is a significant improvement over the traditional wet-ash decomposition procedure that can yield low values for total chromium because chromium is either volatilized, especially in samples containing organic matter, or is not completely dissolved.

In this new procedure, sulfuric, nitric and hydrofluoric acids are added to the sample in a sealed vessel, which is then exposed to microwaves. The sample is then evaporated in an open-beaker to remove the nitric and hydrofluoric acids. The chromium values obtained for SRM 1633a using this new technique agreed with the certified value of $(196 \pm 6) \mu\text{g/g}$, and a new certified value of $(202 \pm 7) \mu\text{g/g}$ was determined for its replacement, SRM 1633b. In comparison, previous open-beaker decomposition procedures had yielded a low Cr value of $80 \mu\text{g/g}$ for SRM 1633a. Further work is being carried out to use this new method for determining chromium in other environmental samples.

NIST/SEMATECH GAS FLOW ROUND ROBIN PROGRAM

NIST scientists have completed a SEMATECH-sponsored round-robin program to ascertain measurement discrepancies that exist among the gas flow calibration facilities used in the U.S. Semiconductor Manufacturing Industries (SMI). These SMI calibration facilities provide critical performance data for the Mass Flow Controller (MFC) devices used in semiconductor manufacturing processes.

SMI calibration facilities claim total uncertainties, i.e., inaccuracies, in the range 0.1 to 0.5 percent to try to achieve 1 percent meter performance in process installations. However, reports from MFC users claim performance deviations of 10 to 20 percent or more. In an attempt to resolve this problem, NIST designed, built, and characterized a gas-flow-measurement artifact and test procedure to calibrate the SMI calibration facilities for a selected set of conditions. Nitrogen gas was used for flows in the range from 300 to 800 standard cubic centimeters per minute (sccm). The artifact consists of critical nozzles arranged in tandem to provide redundancy and assurance of performance. The artifact was calibrated at NIST and the calibration data collected were used to specify details of the test procedure. The round robin involved 55 tests performed in 22 laboratories of SEMATECH member companies and related institutions that volunteered to participate.

Results showed that approximately half of the participants had calibration facility inaccuracies of 0.5 percent or less, but approximately one-fourth had inaccuracies of 1 percent or more. Maximum inaccuracies ranged as high as 8 percent. The NIST gas-flow-measurement artifact and test procedure are currently being offered as a NIST calibration service that may be requested in the same manner as that for conventional flowmeter calibrations. Retesting this artifact enables participants either to confirm that their initially satisfactory performance is constant in time or to evaluate improvements made in response to unsatisfactory results.

Successive phases of this program, currently under development, are expected to extend the flow range to $(0.1-3) \times 10^5$ sccm, which is the full range of interest to the semiconductor processing industries. Once the program is completed, the expected significant improvements in SMI gas flow measurement and control should lead to enhanced productivity in these industries.

CRADA WITH PRIVATE COMPANY ON SPRAY FLAMES

NIST recently entered into a cooperative research and development agreement (CRADA) with a private company to determine the feasibility of using high-power acoustic nozzles to generate well-characterized spray flames. A NIST scientist will collaborate with the private company to design more fuel-efficient and environmentally acceptable combustion systems for U.S. industry.

Over the last few years, this program has produced extensive data on droplet sizes, number densities, and velocities in spray flames using non-intrusive optical means such as laser scattering and high-speed cinematography. This work has revealed that droplet sizes and distributions produced by many commercial atomizers are not quantitatively controllable, resulting in poorly defined initial conditions. The polydisperse atomizers used in this study can produce "made-to-order" sprays with known size distributions and number densities which could lead to flames with desirable characteristics. However, although realization of this potential is the central focus of the CRADA, acoustic nozzles have not yet been employed under burning conditions. It is expected that the combination of new spray-production capabilities and NIST spray-flame measurement and control will lead to development of much improved, quantitatively characterized spray-combustion equipment for industrial applications.

X-RAY GONIOMETER DEVELOPED FOR USE IN ULTRA HIGH VACUUM

X-ray diffraction using synchrotron radiation is one of the primary tools to determine the structure of materials during growth or modification in ultra high vacuum (UHV). This has created a demand for an x-ray goniometer stage that will operate under extreme conditions: 10^{-8} Pa, 2 arc second precision, and no conventional lubrication.

A NIST scientist has been collaborating for the last 3 years with private industry to develop just such an instrument. The materials which go into the gears, bearings, and frame of a standard x-ray goniometer are totally unacceptable for use in UHV. New combinations of metals capable of functioning together with the required precision, and without conventional lubrication, have been incorporated into the design. The materials must not outgas significantly during operation. The

goniometer even incorporates a stepping motor that operates inside the vacuum chamber, under UHV conditions.

Most of the testing is being performed at NIST, where a vacuum chamber designed to accommodate this type of goniometer has been constructed. The prototype goniometer stages are being tested for the ability to withstand bakeout, outgassing during rest and operation, accuracy of rotation, and lifetime of the components. While there is a considerable demand for this type of instrument in the synchrotron radiation community, the required testing equipment that is available at NIST is far beyond the resources of a small company. In addition, this Group at NIST is actually doing synchrotron radiation experiments and provides extensive experience in the area of beamline design and construction.

NEW TECHNIQUE REVEALS UNEXPECTED PHENOMENON IN ELECTRON-ION EXCITATION

Excitation of multiply charged ions by electron impact enters intimately into the modeling and diagnostics of high-temperature plasmas such as those encountered in controlled fusion. Measurements of cross sections for electron-impact excitation of Ar^{7+} using a new merged-beams electron-energy-loss technique show that near threshold the inelastically-scattered electrons are ejected primarily in the backward direction. This unusual angular scattering has not been previously observed for atoms or ions and was completely unexpected. The technique has now been used by NIST scientists to observe similar behavior with O^{5+} , strongly suggesting that preferential backscattering may be the rule rather than the exception for multiply-charged ions. The backscattering observed in these measurements was confirmed in subsequent quantum-mechanical calculations and, surprisingly, the effect can be reproduced with a simple semiclassical model. Essential confirmation was obtained from simultaneous measurements of the total (integrated over all scattering angles) cross section over an energy range to 2.2 eV above threshold. To the extent that current models of

electron transport in plasmas of multiply charged ions incorporate the common assumption of strongly forward-peaked excitation, they will have to be revised, or at least revisited, to accommodate this new evidence.

MATERIALS EVALUATION IN SUPPORT OF SUPERCONDUCTING MAGNETIC ENERGY STORAGE

Under a Cooperative Research and Development Agreement (CRADA) with three private companies, NIST will assist in materials evaluation for a Superconducting Magnetic Energy Storage device (SMES). SMES technology could be used to provide power for defense purposes, electrical grid stability, and load leveling energy storage. The proposed SMES and a subscale engineering test model are essentially large superconducting magnetic coils situated in an underground trench. The coils must be supported to withstand both Lorentz forces generated by the magnetic field and thermal contraction. NIST will perform mechanical and thermal tests on candidate coil support materials (fiber-reinforced composites) in the temperature range from liquid helium (4 K) to ambient. Properties to be determined include ultimate strength, fatigue, shear, flexure, creep, thermal conductivity and thermal expansion. NIST has the world's largest mechanical test facility for research at 4 K; modifications to this system are in progress and, when completed, will allow full-scale coil supports to be tested.

NEW Hg SUPERCONDUCTORS

Since the discovery of superconductivity in the copper-oxide systems, the expectation has been that these new materials would make commercial applications of superconductivity viable. However, their anisotropic superconducting properties combined with generally unfavorable mechanical and materials properties, have severely limited progress. Hence the community is excited by the recent announcement of superconductivity in a new series of mercury-containing compounds, with onset superconducting transition temperatures as high as 140 K.

Of critical importance is the determination of the crystal structures and phase diagrams of these new materials. The unique power of neutron powder diffraction profile refinement has been used at NIST to determine the structure for the single-layer material, $\text{HgBa}_2\text{CuO}_{4.06}$. The crystal structure is tetragonal, and is similar in some respects to the electron-superconductor materials, with the same space group ($P4/mmm$). There are a number of interesting features of this new material. One aspect concerns the doping, which is accomplished by adding a small amount of extra oxygen rather than substitutional doping. The doping appears to be similar to the "superoxygenated" $\text{La}_2\text{CuO}_{4+\delta}$ system. In the present case the extra oxygen ions go into the centered position in the Hg plane. The role that the Hg-O layers might play in enhancing the superconducting transition temperature remains to be clarified. This is particularly important considering that the unit cell contains but a single layer of Cu-O, and thus these Cu layers are separated by the rather large distance of 0.95 nm. Yet the superconducting transition temperature is 94 K.

Finally, it is noteworthy that the compound $\text{HgBa}_2\text{CuO}_{4+\delta}$ may be considered as the first member of the homologous series $\text{HgBa}_2\text{R}_{n-1}\text{Cu}_n\text{O}_{2n+2+\delta}$ where R is a rare earth element. With the single-layer material T_c is already 94 K, and higher transition temperatures can be anticipated in the multilayer materials. So far T_c 's up to 140 K have been observed, and the crystallography of these materials is under active investigation.

MEASUREMENTS FOR POLYMER PROCESSING CONSORTIUM

Members of the NIST/Industry consortium, Measurements for Polymer Processing, attended the annual consortium review meeting at NIST recently. Industry representatives from private industry participated in discussions regarding industry requirements for real-time measurements of polymer processing parameters, particularly temperature and viscosity. The NIST measurement program, which is based on optical methods of measurement, utilizes optical fiber probes to monitor the state of polymer resins at specific positions

in the process stream of polymer processing machinery. Discussions of current work focused on progress made to monitor temperature and viscosity using fluorescence spectroscopy. Research topics to be addressed over the next year were prioritized by the industry representatives. Development of a method to measure temperature gradients (the temperature profile through a thickness of polymer resin) during processing was unanimously supported by those present. Industry representatives agreed that accurate knowledge of temperature, temperature gradients, and viscosity are needed in order to understand the physics of polymer processes and to optimize productivity and product performance.

OPTICAL AND ULTRASONIC SENSORS FOR POLYMER PROCESSING

In collaboration with Drexel University, NIST researchers have instrumented a polymer injection molding machine with optical and ultrasonics sensors to monitor the state of the polymer as it is being molded. Optical sensors based on fluorescence spectroscopy can be used to monitor resin temperature, temperature profiles in the mold and time of solidification; ultrasonics sensors are used to measure resin stiffness and density. A pressure transducer was also used to monitor pressure in the mold cavity during the packing phase of the process. Injection molding consists of injecting hot polymer resin into a cold mold under high pressure, holding the resin in the mold under pressure until it solidifies, opening the mold and ejecting the final product, and closing the mold to begin the next cycle. Temperature of the hot resin, pressure of injection, velocity of resin injection into the mold, cooling rate, density, and crystallinity are some of the parameters that determine product quality and the productivity of the process. Controlling the process for the purpose of producing uniform high quality products requires real-time measurements of important resin-process parameters, such as the temperature and stress experienced by the resin during the process. Current practice in the industry is to monitor machine parameters such as temperature of the injection barrel, velocity of the injection ram and pressure of

the hydraulic driving the injection ram, rather than properties of the resin itself. This state of affairs exists because the technology for carrying out real-time resin characterizations does not exist. The development of optical and ultrasonics sensors addresses this technology weakness and provides new tools for the polymer processing industry.

RELIABILITY OF GLASS AIRCRAFT WINDOWS

Researchers from private industry and NIST have developed a reliability assessment methodology for predicting and assuring the safe-life of glass windows intended for use in specialized aircraft. The methodology is based on two concepts: (i) the statistical distribution on window strengths, which are a result of the distribution of the most severe defects in the window surface and/or edge; and (ii) the time-dependent growth of these defects under the simultaneous presence of moisture and in-flight tensile stresses, which result from pressure and thermal gradients across the window. The combined phenomena lead to a statistical distribution of lifetimes for the window. The objective of the analysis was to predict the safe life for specific windows at a given failure probability and confidence level, and under a variety of glass surface conditions.

The relevant materials parameters were determined at NIST from several types of experiments. Strength distributions were measured for test specimens with an as-polished surface finish like that of the actual windows and for various types of simulated in-service "damage": scratches from cleaning and handling, and dust or sand impact damage from environmental or in-flight conditions. Moisture-assisted crack growth properties were determined from the growth characteristics of simulated defects in the glass surface which were produced by controlled indentation with a pyramidal-shaped diamond. The lifetime analysis from these data required an estimate of the 95 percent confidence level that resulted from uncertainties in the experimentally determined parameters. These confidence levels were determined from a non-parametric bootstrap statistical analysis, performed in consultation with scientists from NIST and private industry.

ULTRASONIC RESONANCE SPECTROSCOPY USING EMATS

NIST has developed ultrasonic resonance techniques for measuring elastic constants and damping in cylindrical or spherical metallic samples using noncontacting electromagnetic acoustic trans-

ducers (EMATs). These techniques present advantages over conventional contacting pulsed ultrasonic techniques for the accurate measurement of elastic constants in isotropic materials and for industrial process sensing applications. The non-contacting nature of the transduction mechanism allows the possibility of performing measurements on moving and/or hot materials. By driving samples into resonance, the circuitry can be more easily implemented than with pulsed measurements. With isotropic spherical samples, the elastic constants can be determined from the resonant frequencies with a great accuracy, limited by the uncertainty in the sample diameter. The high resolution in the measurement of resonant frequencies also provides a capability for measuring small deviations from isotropy. For example, the elastic anisotropy associated with texture in wrought alloys and reinforcements in metal-matrix composites can be measured. Variations in case depth have been measured in hardened steel axles.

NIST DEVELOPS BUILDING AND VENTILATION CHARACTERIZATION PROTOCOLS FOR INDOOR AIR QUALITY INVESTIGATIONS

A NIST scientist has developed protocols for characterizing commercial buildings and their ventilation systems for use in indoor air quality investigations. These protocols were developed for use in the U.S. Environmental Protection Agency's Building Assessment Survey and Evaluation (BASE) Program. The BASE Program is a multi-year research effort to collect baseline information on indoor environmental performance of commercial buildings. The development of the protocols involved identifying parameters that characterize a building and its ventilation system and procedures for determining their values. The protocols include checklists for obtaining information in the field and instructions for completing the checklists. The checklists are divided into four areas: descriptive information on the whole building, information on the space within the building that is being tested, design information on the ventilation system serving the space being tested, and performance measurement for the ventilation system. These protocols constitute the first systematic approach to obtaining building and ventilation information, and they will be used within the BASE program and other efforts to obtain indoor air quality information in buildings. The development of these protocols was sponsored by the U.S. Environmental Protection Agency and the U.S. Department of Energy.

EXPERT SYSTEM FOR HIGHWAY CONCRETE
 NIST has completed the development of "HWYCON" (Highway Concrete), an expert system to assist highway departments in making technical decisions concerning concrete. The computerized system provides assistance in three areas: (1) diagnosis of distresses in highway concrete pavements, bridge decks and substructures, (2) the design of concrete for new construction and reconstruction, and (3) selection of materials and procedures for repair and rehabilitation. The focus of the system is on materials-related knowledge and activities. It was developed under the Strategic Highway Research Program's project on the Optimization of Highway Concrete Technology. The system, which is designed to operate on a desktop or portable personal computer, has been tested by potential users in state highway departments and experts in the field of concrete technology. Distribution will be made by the Federal Highway Administration (FHWA) and the Transportation Research Board (TRB). HWYCON contains high-level knowledge, visual, and explanatory information.

NIST AND THE DEPARTMENT OF THE TREASURY SIGN MEMORANDUM OF UNDERSTANDING (MOU) IN INFORMATION TECHNOLOGY SECURITY

As a result of a new MOU with the Department of the Treasury, NIST will develop, prototype, test, and implement computer security standards and procedures to protect sensitive Treasury information from unauthorized access or modification. Areas of cooperation include the research and development of the following as they apply to Treasury's mission: accreditation and certification of sensitive automated information systems (AIS); risk management; security management guidelines; open systems; LAN security; equipment used for switching and interchange of data; security architectures; security criteria and evaluation methods; advanced authentication technology; systems integration; and public and private key cryptographic techniques as applied to electronic data interchange (EDI), electronic funds transfer, electronic mail, and other areas.

REVISION OF FEDERAL INFORMATION PROCESSING STANDARDS (FIPS) FOR DATABASE LANGUAGE SQL

On May 12, 1993 the Secretary of Commerce approved a substantial enhancement of FIPS 127-1, SQL. Effective Dec. 3, 1993 the revised

standard will be published as FIPS 127-2 and replaces FIPS 127-1 in its entirety. FIPS 127-2 is mandatory for all federal procurements of relational model database management systems. The revised SQL standard adds significant new features for schema definition, diagnostics management, integrity constraints, and international character set support, as well as new data types, new table operations, and enhanced data manipulation expressions. A new Information Schema makes all schema data available to applications.

FIPS 127-2 is specified in four separate conformance levels: Entry SQL, Transitional SQL, Intermediate SQL, and Full SQL. Although only Entry SQL is required, initially, for conformance to FIPS 127-2, a higher conformance level may be specified as mandatory in individual procurements.

Available for sale to the public, NIST SQL Test Suite, Version 4.0, provides conformance tests for the Entry SQL level of FIPS PUB 127-2. Future versions of the test suite will evaluate other FIPS SQL conformance levels.

GUIDANCE ON IMPROVING SOFTWARE QUALITY ISSUED

NIST Special Publication 500-209, Software Error Analysis, provides guidance on software error analysis which includes error detection, evaluation, and resolution. The study considers error detection techniques such as those used in software development, software quality assurance, and software verification, validation, and testing activities. Also included are statistical process control techniques and several software reliability models. The document assists the software engineering community in understanding how error analysis can improve the software development process and gives guidance for the evaluation of high-integrity software.

CONFERENCE ON EXTREME VALUE THEORY AND ITS APPLICATIONS

Extreme values control design and policy decisions in a large variety of technological and scientific fields. To assure adequate safety levels, land, ocean and air or space structures must be designed to withstand the effects of extreme loads, and materials and systems used in such structures must exceed certain minimum (extreme) performance levels. Pollutant levels that may be tolerable on the average may attain extremes whose effects would be unacceptable. Statistical extreme value theory provides methods for estimating the probability of extreme events on the basis of a finite set of data.

An international Conference on Extreme Value Theory and Its Applications, cosponsored with Temple University, was held at NIST recently. The Conference attracted 150 researchers from academic, government, and industrial research groups from the United States and abroad. The focus was on the mathematical theory of extremes and applications in the areas of civil engineering, materials sciences, and environmental sciences, although papers in other applications areas such as astronomy, physics, economics were presented as well. A half-day short course before the Conference was well attended and served to acquaint attending scientists and engineers with elements of the modern theory.

A principal goal of the Conference was to assist in the transfer of advances made in the theory of extremes to applications, and to expose the mathematical researchers to the needs of the engineering community. Selected Papers from this conference will be published in a future issue of this Journal.

Standard Reference Materials

TIN-LEAD COATING THICKNESS STANDARDS 60% Sn-40% Pb

The Standard Reference Materials Program announces the release of SRM 2321, Tin-Lead Alloy coating on Copper. This SRM is intended for use in calibrating x-ray fluorescence instruments for the measurement of mass per area and composition of tin-lead alloys deposited on a copper substrate. The SRM consists of a 15 × 15 mm plate of an electroplated tin-lead alloy coating on a polished copper substrate. The plate is mounted in a recessed plastic holder.

The tin-lead alloy coating was characterized using energy dispersive x-ray fluorescence and atomic absorption spectrometry. The SRM is certified for mass per area and the percent tin to within ±5% of the given value at the center of the sample and the average over the entire surface. An approximate thickness of the alloy coating can be estimated from the measured mass per area, the measured composition, and the density.

SRM 2321 is available from the Standard Reference Materials Program, Room 205, Building 202, NIST, Gaithersburg, MD 20899, (301) 975-6776.

STANDARD REFERENCE MATERIAL 886— REFRACTORY GOLD ORE

The gold mining industry depends on highly accurate assays to set the fair market value of its ores. Additionally, selection of the most efficient process for extracting the gold from its matrix requires the determination of concentrations of key matrix elements, such as sulfur and carbon, which can exhibit a deleterious effect on some of the processing methods.

The Standard Reference Materials Program announces the availability of Standard Reference Material (SRM) 886, refractory gold ore. The ore is certified for its gold content, (8.25 ± 0.13) mg/kg. Information values are also reported for carbon at 5.7 weight percent and for sulfur at 1.5 weight percent.

STANDARD REFERENCE MATERIALS 2556 AND 2557—USED AUTOMOBILE CATALYSTS

Automobile catalysts required for emission control use the metals platinum, palladium, and rhodium to catalyze the conversion of pollutant gases in automotive exhaust to harmless compounds. Because of the scarcity and price of these metals, recycling of spent automobile catalysts is routinely undertaken. Highly accurate analyses of the platinum group elements are required to establish the fair market value of the materials being recycled.

The Standard Reference Materials Program announces the availability of Standard Reference Materials 2556 and 2557, used automobile catalysts of the Pellet and Monolith types, respectively. The SRMs were certified by isotope dilution thermal ionization mass spectrometry (Pt, Pd, Pb) and by inductively coupled plasma mass spectrometry (Rh). Instrumental neutron activation analysis and cooperative industry analyses provided corroboration. The certified values for the two materials are:

- SRM 2556
Pt 697 mg/kg; Pd 326 mg/kg; Rh 51.2 mg/kg;
Pb 6228 mg/kg.
- SRM 2557
Pt 1131 mg/kg; Pd 233 mg/kg; Rh 135 mg/kg;
Pb 13,930 mg/kg.

These SRMs were developed in cooperation with the International Precious Metals Institute, whose members provided collaborative analyses. The SRMs are available in units of 70 g of J m powdered material.

Standard Reference Data

RUSSIAN ROCKET-SPACE TECHNOLOGY DATA AVAILABLE

An important collection of reference data originally developed for Soviet rocket/space technology is now available for PCs from NIST. The IVTANTHERMO database includes information on the thermodynamic properties of approximately 2300 individual substances (containing 85 elements and the electron) in the standard state within a wide temperature range. The data are internally consistent within the framework of the principal laws of thermodynamics. The most distinctive feature is that the data are not taken from various references of other databases but calculated using the molecular and thermochemical constants evaluated as a result of expert analysis of all primary data. The data collection was started in the 1950s by the Soviet Academy of Sciences. Through an agreement with an international publisher, NIST is able to make IVTANTHERMO available to users worldwide. NIST Special Database 5, IVTANTHERMO-PC, Version 1.0, is available for \$950 from the Standard Reference Data Program, A320 Physics Building, NIST, Gaithersburg, MD 20899-0001, (301) 975-2208, fax: 926-0416.

DATABASE DETAILS ATOMIC-SCALE SURFACE STRUCTURES

Scientists and researchers in materials, physics, and chemistry now have rapid access to important information on the crystal structures of surfaces. The new Surface Structure Database for PCs, NIST Standard Reference Database 42, is the only complete critical compilation of reliable information on surface crystallographic structures available. It is an important resource for assessing and comparing detailed atomic-scale structures of surfaces and interfaces obtained from low-energy electron diffraction, or LEED, and from other experiments. Nearly 600 structures are included, covering a wide variety of materials of scientific and technological interest, including catalysts. Each structure is covered by extensive tables of numeric data that help the user evaluate how it affects chemical reactivity. The database also contains three-dimensional color graphics that permit the visual inspection of all surface structures. The structures can be rotated and

magnified, and the distance between atoms can easily be determined. The database is available for \$390 from the Standard Reference Data Program, A320 Physics Building, NIST, Gaithersburg, MD 20899-0001, (301) 975-2208, fax: (301) 926-0416.